Universitat Autònoma de Barcelona

Spin-lattice coupling in strongly correlated cobalt oxides investigated by synchrotron and neutron techniques

JESSICA PADILLA PANTOJA

Spin-lattice coupling in strongly correlated cobalt oxides investigated by synchrotron and neutron techniques

by

JESSICA PADILLA PANTOJA

DOCTORAL THESIS SUBMITTED TO THE
DEPARTAMENT DE FÍSICA OF THE FACULTAT DE CIÈNCIES
OF THE UNIVERSITAT AUTÒNOMA DE BARCELONA
FOR THE DEGREE OF
DOCTOR OF MATERIALS SCIENCE

December, 2015

SUPERVISORS

Prof. José Luis García Muñoz

Dr. Javier Herrero Martín

TUTOR

Dr. Xavier Granados García

Universitat Autònoma de Barcelona

Prof. José Luis García Muñoz and Dr. Javier Herrero Martín

CERTIFY

that the work reported in the present by Jessica Padilla Pantoja, entitled, *"Spin-lattice coupling in strongly correlated cobalt oxides investigated by synchrotron and neutron techniques"*, has been done at the Institut de Ciència de Materials de Barcelona (ICMAB-CSIC) with the collaboration of ALBA-CELLS Synchrotron, under their supervision. This works constitutes the Doctoral Thesis Memory submitted by the interested person to the Facultat de Ciències de la Universidad Autònoma de Barcelona to apply for the degree Doctor of Materials Science.

Bellaterra, December 9th, 2015.

Signature:

Prof. José Luis García Muñoz
Research professor at the Institut
de Ciència de Materials de Barcelona
(ICMAB-CSIC)

Signature:

Dr. Javier Herrero Martín
Beamline Scientist at the
ALBA Synchrotron Light
Source in Barcelona

A Paula y Sensi.

….pero quien eres tu tan silenciosa?
Yo tan sólo soy una flor.

Learning is the only thing the mind
never exhausts, never fears,
and never regrets.

Leonardo da Vinci

CONTENTS

List of acronyms used

AFM	Antiferromagnetic
BCO	$Ba_2Co_9O_{14}$
BNS	Belov-Neronova-Smirnova
BVS	Bond Valence Sum
CMR	Colossal Magnetoresistance
C_4	Four-fould symmetry
CSIC	Consejo Superior de Investigaciones Científicas
CT	Charge Transfer
CTM	Charge-Transfer Multiplet
D_{4h}	Tetragonal symmetry
DOS	Density of Occupied States
ECO	$ErCoO_3$
EPR	Electron Paramagnetic Resonance
ESRF	European Synchrotron Radiation Facility
EXAFS	Extended X-ray Absorption Fine Structure
FC	Field-Cooling
FM	Ferromagnetic
FWHM	Full With at Half Maximum
FY	Fluorescence Yield
GBCO	$GdBaCo_2O_{5.50}$
GGA	Generalized Gradient Approximation
GUI	Graphical User Interface
HERFD	High Energy Resolution Fluorescence Detection
HS	High-Spin
ICMA	Instituto de Ciencia de Materiales de Aragón
ICMAB	Institut de Ciència de Materials de Barcelona
ICMM	Instituto de Ciència de Materiales de Madrid
ILL	Institute Laue Langevin
INS	Inelastic Neutron Scattering
IS	Intermediate-Spin
JT	Jahn-Teller
KB	Kirkpatrick-Baez

LCO	$LaCoO_3$
LDA	Local Density Aproximation
LFM	Ligand-Field Multiplet
LS	Low-Spin
ND	Neutron Diffraction
NMR	Nuclear Magnetic Resonance
NPD	Neutron Powder Diffraction
NLSCO	$Nd_{1/3}La_{2/3}Sr0_{.50}CoO_3$
NSCO	$Nd_{0.50}Sr_{0.50}CoO_3$
O_h	Octahedral symmetry
MIT	Metal-Insulator Transition
MS	Magnetostructural
MSG	Magnetic Space Group
PBCO	$PrBaCo_2O_{5.50}$
PBSCO	$Pr_{0.50}Ba_{1-x}Sr_xCoO_3$
PCO	$PrCoO_3$
PCCO	$Pr_{0.50}Ca_{0.50}CoO_3$
PDF	Pair Density Function
PLD	Pulsed Laser Deposition
PPMS	Physical Property Measurement System
PSCO	$Pr_{0.50}Sr_{0.50}CoO_3$
PSD	Position Sensitive Detection
RE	Rare Earth
RT	Room Temperature
SG	Space Group
MSG	Magnetic Space Group
SOFC's	Solid Oxide Fuel Cells
SQUID	Superconducting Quantum Interferometer Device
SS	Spin-State
SST	Spin-State Transition
SXRPD	Synchrotron X-Ray Powder Diffraction
T_d	Octahedral symmetry
TEY	Total-Electron Yield
TFY	Total Fluorescence Yield
TM	Transition metals

YBCO	$YBaCo_2O_{5.50}$
XANES	X-ray Absorption Near-Edge Spectra
XAS	X-ray Absorption Spectroscopy
XES	X-ray Emission Spectroscopy
XMCD	X-ray Magnetic Circular Dichroism
XPS	X-ray Photoelectron Spectroscopy
XRD	X-Ray Diffraction
ZFC	Zero-Field Cooling

Chapter 1

Introduction and motivation

Transition metal (TM) oxides form probably one of the most amazing classes of materials inside the field of strongly correlated systems and functional magnetic compounds, exhibiting a variety of crystal structures, magnetic and transport properties susceptible of multifunctional applications [1–8]. The appealing properties of TM oxides are clearly related to the unique nature of the outer *d*-electrons, leading to the existence of various oxidation states and electronic configurations. In this respect, oxides involving copper (Cu^{2+}/Cu^{3+}), manganese ($Mn^{2+}/Mn^{3+}/Mn^{4+}$), and cobalt ($Co^{2+}/Co^{3+}/Co^{4+}$) have a great potential. In addition, the variety of spin configurations that several of these cations can adopt, especially for cobalt, offer new possibilities.

Copper oxides with layered structure attracted huge attention and produced great impact when in 1986 Bednorz and Muller discovered the superconductivity at "high-temperatures" in $La_{2-x}Ba_xCuO_4$ (T_C ~ 40 K) [9]. Later, the synthesis of $YBa_2Cu_3O_7$ with a higher critical temperature (T_C ~ 92 K) [10] was considered a radical breakthrough. This temperature allows the use of liquid nitrogen, leading to cheaper costs and reducing the environmental impact.

Another interesting group of TMs oxides are manganese oxides with perovskite structure (also called manganites). Some of these compounds present colossal magnetoresistance (CMR) due to their extraordinary capacitance to change their resistance when a magnetic field is

applied and also the coexistence of magnetism and ferroelectricity, known as multiferroicity. One of the most studied series in this family is $Ln_{1-x}A_xMnO_3$ (*Ln*: lanthanide and *A*: alkaline earth) [11, 12]. The large magnetoresistance offers a great potential in Spintronics for the magnetic storage of information and also for the realization of magnetic detectors and actuators. In addition, some Mn oxides exhibit coupled magnetic and thermoelectric properties, offering new technological possibilities as multiferroic materials.

Last but not least, cobalt oxides (cobaltites or cobaltates) have drawn much interest during the last years as promising multifunctional materials for the future, together with their rich physical properties owing to the wide variety of valence and spin-states (SS) Co ions may display. From a scientific perspective, a greater understanding of the complex interplay between the material's lattice, orbital, charge and spin degrees of freedom is fundamental to engineer new multifunctional materials and devices. These materials are being explored as potential candidates for a wide range of applications such as cathodes for solid oxide fuel cells (SOFCs), catalyst systems, oxygen membranes, gas detection sensors, magnetic field sensors, magnetic data storage, read heads, Spintronics and thermoelectric devices.

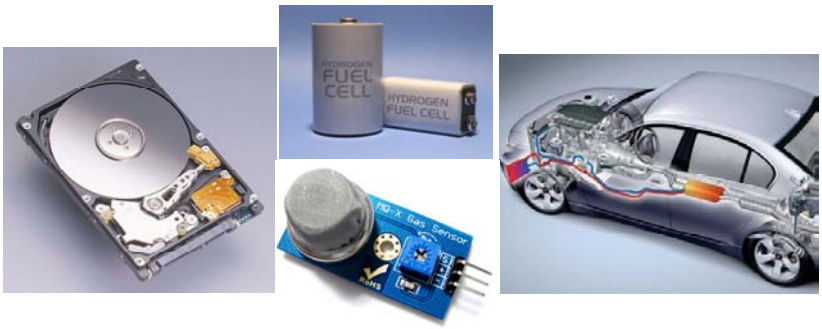

Figure 1. 1. Different devices where cobalt oxides can be suitable for future applications

One of the first and currently best developed applications of cobalt oxides is their use as cathodes for SOFCs. SOFCs convert the chemical energy of the reaction of a fuel (H_2, methanol or carbon monoxide) with oxygen directly into electrical energy. These electrical power generation systems provide important advantages with respect to other energy conversion devices, being highly efficient, ecologically clean, and allowing miniaturization. Great efforts have been devoted in recent decades to enhance the efficiency and service life of solid-state electrochemical devices, and also to reduce their costs using less expensive construction materials. These problems could be partially solved by lowering the SOFC operation temperature [4].

Another interesting perspective for cobalt oxides is their contribution for building thermoelectric devices. Thermoelectric devices can be used for the generation of electricity directly from heat sources. So, they are expected to play an important role in the future from an energetic and environmental point of view, like the direct application on trucks and cars. The closest applicability has been done by the BMW group. In the last years, the BMW group has developed different projects where a thermoelectric generator is integrated in vehicles, thus converting the waste heat into electricity. In this process, a physical phenomenon called the Seebeck effect applies. One of the most studied systems due to its potential application in the field of energy conversion at high temperatures has been the layered cobaltite $NaCo_2O_4$, which shows a high thermoelectric power S_b= +100 μV/K at room temperature (RT) and a low resistivity close to that of a metal ρ = 0.2 mΩ·cm [13, 14].

Another area in which cobalt oxides are being explored as potential multifunctional materials is Spintronics. This field exploits the spin and charge of the electrons to create new technological possibilities and to reduce the energy consumption. Basically, it consists of controlling and manipulating the electronic spins by electric and magnetic fields or electromagnetic radiation.

The last potential application of cobalt oxides that we comment here is their use as materials for gas sensors. Such sensors are required in devices to control chemical processes or monitor the state of the environment, such as, for instance the sensors monitoring the concentration of ammonia (NH_3). Currently used sensors are based in different materials like superconductors, organic compounds, or carbon nanotubes, suffering from a low sensitivity and limited practical applications.

Let us underline to summarize that from a fundamental point of view cobalt oxides present a plethora of very interesting properties like giant magnetoresistance, double-exchange, phase separation, spin-state changes, metal-insulator transitions, high thermoelectric power, oxygen diffusivity, mixed-conduction, charge and orbital ordering or superconductivity among others [15–19]. These properties are interesting not only from a fundamental point of view but also due to their potential applicability in different fields. One very remarkable characteristic of these compounds is the ability of Co ions to present different spin states as a function of temperature [18, 19]. This makes that Co oxides have, in comparison with other transition metal oxides, an extra degree of freedom, namely the spin-state of Co. The physics of cobalt oxides is thus expected to be enriched by the introduction of this new degree of freedom, in fact, it plays a prominent role in the large Seebeck coefficient displayed by different layered cobalt oxides and introduces a new mechanism for drastically changing electronic mobility (inducing metal to insulator transitions). In the current manuscript we investigate the relations and interplay

between the structure and the magnetic and electronic behavior of cobalt based oxides with unconventional properties. In the upcoming sections we will give a brief description of general concepts which are useful to understand these complex oxides.

1.1. Basic structural aspects in perovskites

Perovskites are oxides that have ABO_3 structure, where A is typically a rare earth metal (La, Pr, Sm, Dy, Y…) or an alkaline metal (Sr, Ca, Ba, …) ion, and B is typically a TM ion (in our case Co), and O represents an oxygen anion. Their geometric structure can be represented using a cubic unit cell with A-site ions occupying the (0, 0, 0) position, B-site ions laying at the (½, ½, ½) position, and oxygen ions at (½,½, 0). In general, the space group (S. G.) for cubic Perovskites is *Pm-3m* (No. 221). The structure of these materials varies, but in general, can be described by an octahedron of oxygen atoms surrounding the TM being inside a simple cubic cage of rare earth/alkaline metal cations as Figure 1. 2(a) shows. The result is that A, B and O atoms are in 12, 6 and 8 coordination respectively.

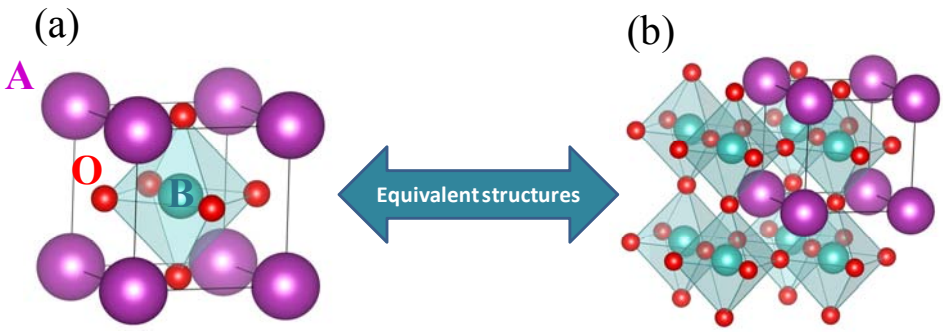

Figure 1. 2. (a) Cubic perovskite unit cell showing the A-site (purple balls), B site (green balls), and oxygen ions (red balls) positions in the lattice. (b) Equivalent cubic structure with corner sharing BO_6 octahedra.

Under the inclusion of different elements in an ideal perovskites structure thus producing changes in the bond-lengths or octahedral tilts, an important term is the Goldschmidt tolerance factor (t) [20]. This factor measures the stability and degree of distortion of a structure from the cubic case ($t \sim 1$) and can be defined by:

$$t = \frac{r_A + r_o}{\sqrt{2}(r_B + r_o)} \qquad \text{(Eq. 1.1)}$$

where r_A refers to the average ionic radii of the A-site, r_B to the average ionic radii of the B-site, and r_o to ionic radii of the oxygen atom.

The bond length ($r_A + r_o$) of cation A to the anion O is $\sqrt{2}$ times larger than the bond length ($r_b + r_o$) of cation B to the anion O for the ideal closed packing structure. A stable perovskite structure is limited to the values $0.78 < t < 1.05$. For $0.78 < t < 0.9$ the orthorhombic crystal symmetry is common, while for $0.9 < t < 1$ the rhombohedral symmetry is favored [21, 22]. When $t < 0.9$ the structure adjusts by decreasing the B-O-B bond angle from 180º and this is seen as a coordinated tilting of the BO_6 octahedra in the lattice.

1.2. Electronic structure of cobaltites

1.2.1. The crystal field splitting

Co ions are TMs with a valence shell formed by (in principle) 5-fold degenerate 3*d* electrons. When in a crystalline solid, the spherical symmetry is violated, the local symmetry is determined by the crystal structure. Thus, if the TM is surrounded by a regular octahedron of O^{2-} anions (the most common situation in the cobaltites), the *d* levels are split into a lower triplet t_{2g} ($3d_{xy}$, $3d_{xz}$, $3d_{yz}$) and an upper doublet e_g ($3d_{x^2-y^2}$ and $3d_{3z^2-r^2}$). The corresponding splitting is caused by the interaction of *d*-electrons with the surrounding ions in the crystal. This is called the crystal field splitting (Δ_{CF}), usually of order of 1 eV. According to the crystal field (CF) theory, the higher energy orbitals are pointing towards the oxygen ligands, while the lower orbitals are pointing in between the oxygen atoms as Figure 1. 3 shows.

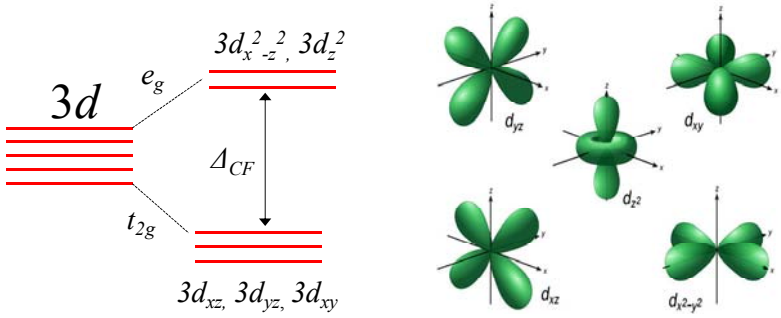

Figure 1. 3. Schematic view of the crystal field effect over the 3*d*-orbitals of TM ions in octahedral coordination (left), and their spatial distribution (right).

1.2.2. The spin state scenarios in Co ions

Depending on the filling mode of the 3*d* orbitals, Co ions show different spin-states. The spin-state degree of freedom arises due to the strong competition between the intra-atomic exchange interaction for spin-up and spin-down levels (Δ_{ex}, Hund's rule coupling), the Jahn-Teller (JT)

distortion, and the crystal-field splitting (Δ_{CF}) [23, 24]. Figure 1. 4 shows the example of a system with six 3*d* electrons (Co^{3+} ion) bonded in a perovskite structure. Depending on the interplay between Δ_{ex} and the Δ_{CF} two different electronic configurations can be found for the Co^{3+} ion in a regular octahedron: (i) when $\Delta_{ex} > \Delta_{CF}$, the Co^{3+} ion takes the high-spin (HS) state ($t_{2g}^{4}\, e_g^{2}$, S=2), or (ii) when $\Delta_{ex} < \Delta_{CF}$ the Co^{3+} ion takes the low-spin (LS) state ($t_{2g}^{6}\, e_g^{0}$, S=0). Moreover, in this case a third electronic configuration is, in principle, also possible: an intermediate spin (IS) state ($t_{2g}^{5}\, e_g^{1}$, S=1). This may result from a JT distortion where the octahedron becomes locally distorted [23, 24].

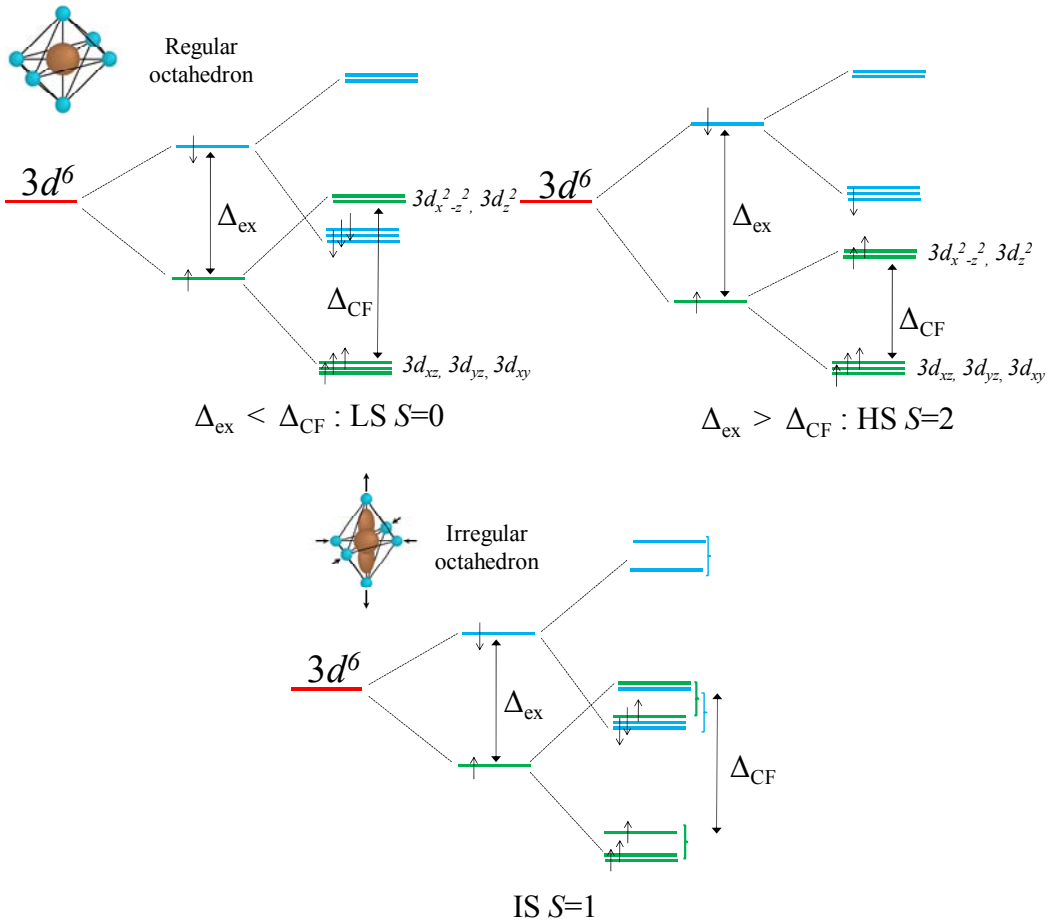

Figure 1. 4. Schematic illustration of the Co^{3+} electronic configuration possibilities (6 *d*-orbital electrons). The intra-atomic exchange splitting for spin-up (green line) and spin-down (blue line) levels of the electronic structure, and the crystal field splitting in octahedra symmetry are also indicated.

The JT effect accounts for the geometrical distortion of molecules and ions associated with a certain electronic configuration. According to the JT theorem [25], any non-linear

molecular system with a degenerated orbital ground level energy is unstable, and so it may undergo a geometrical distortion that removes that degeneracy, because the distortion lowers the overall energy of the species. In general, the orbital degeneracy of the e_g electrons is lifted because of the movement of oxygen ions out of their original positions.

In the Co^{4+} and Co^{2+} ions with 5-*d* and 7-*d* orbital electrons, respectively, different spin-states are possible in the perovskite structures, as shown in Figure 1. 5.

As these specimens are also part of the discussion in the thesis, here we illustrate their different electronic configurations using an easily schematic view.

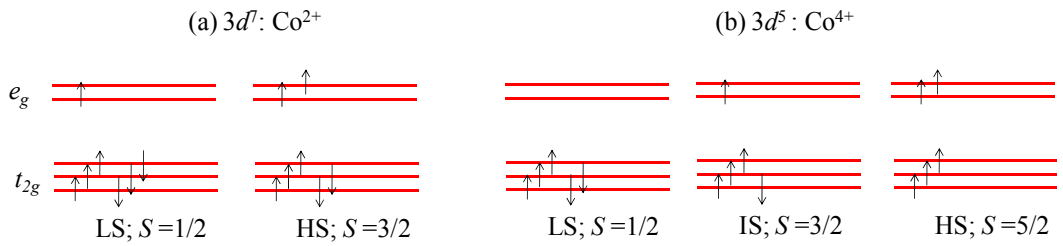

Figure 1. 5. Schematic representation of the t_{2g} and e_g orbitals for a (a) Co^{2+} ($3d^7$) and (b) Co^{4+} ion ($3d^5$)

Since the LS, IS and HS states in Co-perovskites lay close in energy, it is feasible to tune the SS through external parameters such as temperature, hydrostatic pressure, or chemical pressure. One of the best studied examples is $LaCoO_3$ as it will be detailed in Chapter 3. In this material, different efforts to stabilize the LS state have been done using hydrostatic pressure [26, 27]. This external effect increases the CF splitting energy due to the increase in orbital overlap that competes with the Hund's coupling energy, thus stabilizing the LS of Co ions. This effect has been achieved too by doping the A-site cation with smaller rare-earth metals or introducing different cations on the A-site to obtain a mixture of valence states for the Co ion (chemical pressure method), as we will see in Chapter 4. In this way, the CF can be tuned via the modification of the Co-O bond lengths and Co-O-Co bond angles.

1.3. Magnetic interactions in cobalt perovskites

In order to understand the physics of cobaltites, it is necessary to know the common Co-Co magnetic interactions, i.e. the superexchange (SE) on most ionic insulators and the double-exchange (DE) interactions in materials that exhibit more conductive behavior. These two types are particularly important in cobalt oxides. Both are indirect exchange interactions between two non-neighboring magnetic (M) ions (Co in our case) that are mediated by a non-magnetic (oxygen) ion placed in between them [23, 24, 28].

1.3.1. Superexchange interaction

The first type of indirect exchange is called superexchange (SE). The idea that a possible exchange could take place mediated by an intermediate non-magnetic atom was first claimed by Kramers in 1934 [29]. Some years later, the theory was formally developed by Anderson [30]. The SE is of importance in TM oxides where the bonding orbitals are formed by the (magnetic) TM 3*d* electrons and the 2*p* valence electrons of diamagnetic oxygen. The type and strength of the magnetism that arises from SE are governed by the Goodenough-Kanamori rules [31, 32]. To understand the origin of this interaction we assume that the TM atoms are metallic (at least one unpaired electron, i.e. one half filled orbital) and the oxygen atom has a tendency to attract two electrons. Thus, in the simple case there are 4 electrons involved in the process. According to Pauli's exclusion principle (two electrons cannot have the same full set of quantum numbers) the adjacent electrons in the bonding orbitals should be antiparallel, minimizing the kinetic exchange energy. Then, the SE interaction leads to an antiferromagnetic (AFM) ground state of the metal ions [28]. On the other hand, the scenario changes when the coupling involves a filled orbital and one with a half-filled orbital. Then, the interaction will be ferromagnetic (FM). However, the SE most often occurs in AFM and insulating ferromagnets (as the $Ba_2Co_9O_{14}$ cobaltite described in Chapter 6) where the lowest energy state is found. The strength of the SE coupling depends on the magnitude of the magnetic moments on the metal atoms, the metal-oxygen (M-O) orbital overlap, and the M-O-M bond angle. Figure 1. 6 displays the two commented different scenarios for the superexchange interaction in a magnetic oxide.

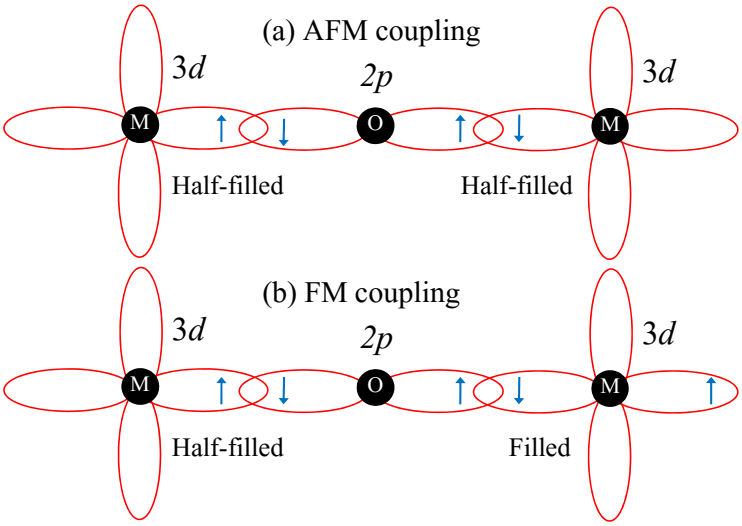

Figure 1. 6. SE interaction in a magnetic oxide showing the spin configuration for (a) an AFM ground state and (b) a FM ground state. The bonding orbitals are pictured by means of the 2*p* and 3*d* orbital charge densities and the blue arrows indicate the spin direction.

1.3.2. Double-exchange interaction

The indirect coupling of spins across a diamagnetic atom can also be FM because of the double-exchange interaction. In general, this magnetic interaction involves different valence metal ions such as the mixed-valence cobaltites $Pr_{0.50}Sr_{0.50}CoO_3$ leading metallic ferromagnetism. The double-exchange term was introduced by C. Zener in 1951 [33]. He proposed a mechanism for the hopping of an electron from one Mn to another in the doped Mn perovskites through an intermediate O atom. This should occur in two steps, by "double-exchange" because the oxygen 2*p* orbitals are fully occupied. So, the movement of an itinerant O electron to one Mn atom is followed by the transfer of a second itinerant electron from the neighboring Mn into the unoccupied oxygen orbital. The same process can be explained using Co atoms despite they tend to have different orbital occupations. Since a spin-flips is not allowed in the electron hopping process it is more energetically favorable that both metal atoms are ferromagnetically aligned. This results in the coincidence of ferromagnetism and conductive behavior in the mixed-valence cobaltites as we will see in Chapter 4.

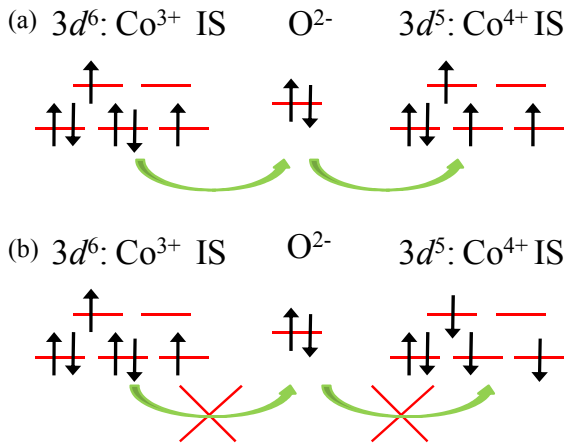

Figure 1. 7. (a) Schematic diagram of the double-exchange mechanism between Co^{3+} IS and Co^{4+} IS cations. (b) The electron mobility is blocked when the t_{2g} electrons are antiparallel.

1.4. Scope and objectives

The main objective of this thesis is to investigate the relevance and effects of spin state instabilities in cobalt oxides with spin-lattice coupling. The thesis focuses primarily on the study of cobalt oxides with electronic and spin instabilities, in cobaltites having different crystallographic structures and presenting spin-lattice coupling, thereby addressing structural, electronic, magnetic, magnetostructural and metal-insulator transitions.

This thesis memory gathers several studies based on the use of large European facilities, principally synchrotron X-ray and neutron sources. Among them, the ALBA, ESRF, SLS and Helmholtz-Zentrum Berlin synchrotrons. Besides diffraction, X-ray absorption spectroscopies as XAS and XMCD were used in the range of the soft radiation. This has been key to obtain a direct image of the electronic occupation in the valence band of Co (3*d* levels). As a complementary method, hard X-ray emission contributed to achieve conclusions on the spin state of Co in the different investigated oxides. The works based on structural and magnetic neutron diffraction were mainly performed at the ILL neutron reactor and the SINQ spallation source, and have revealed a direct influence of the spin state changes on the structural and magnetic properties of the addressed oxides. These are presented following their structural complexity: $LnCoO_3$ simple perovskites, $Ln_{1-x}A_xCoO_3$ mixed-valence simple perovskites, $LnBaCo_2O_{5.50}$ layered double-perovskites, and $Ba_2Co_9O_{14}$ a new Ba-based cobaltite. So, the manuscript is divided in five chapters, in addition to the present one. Their contents are briefly described below:

In **Chapter 2** we detail the experimental techniques used for the synthesis of the different Co compounds and their respective characterization, together with a brief description of the instruments or equipments where the measurements were carried out. The macroscopic characterization was done using commercial equipments (SQUID & PPMS). The structural characterization was mainly done by means of synchrotron x-ray powder diffraction (SXRPD) and neutron powder diffraction (NPD). On the other hand, the microscopic magnetic and electronic characterization was performed using different spectroscopic techniques such as x-ray absorption (XAS), x-ray emission (XES), and x-ray magnetic circular dichroism (XMCD).

Chapter 3 is devoted to understand the nature of the SS transition in the $LnCoO_3$ cobaltites. As we commented previously, the Co-based perovskites are a unique class of materials that can assume a wide range of different SS configurations as a function of temperature. The most thoroughly studied compound is $LaCoO_3$. However, it is not yet fully understood despite the hundreds of investigations. In this study two different members of the $LnCoO_3$ series have been investigated. The first one is $PrCoO_3$, which is considered a member of the family with moderate distortion, and the second one is $ErCoO_3$, as a highly distorted member. So, we have combined the analysis by two different techniques such as x-ray absorption spectroscopy (XAS) and neutron powder diffraction (NPD) to extend our understanding on the correlation between the electronic effects and the crystal structure evolution in the $LnCoO_3$ cobaltites.

On the other hand, the synthesis of new cobaltites with general formula $Ln_{1-x}A_xCoO_3$ yielding a Co^{3+}/Co^{4+} mixed valence, introduces remarkable new physical properties that

required to be investigated. As a continuation of recent studies in the half-doped $Pr_{0.50}Ca_{0.50}CoO_3$ cobaltite [34–36] with exceptional photoresponse properties [37], this work focused on understanding the temperature-driven magnetostructural transition in $Pr_{0.50}Sr_{0.50}CoO_3$ (**Chapter 4**). This compound presents an anomalous second magnetic transition at low temperature (T_{SI}~120K) whose origin is still nowadays a subject of debate. A complete structural study by NPD here shows that an orthorhombic-tetragonal transition is the responsible for the magnetostructural anomalies, and that they vanish by substituting Pr with other lanthanides. In addition, the spectroscopic characterization reveals no SS transition in the Co^{3+} ions and no trace of Pr^{4+} below T_{SI}, unlike the $Pr_{0.50}Ca_{0.50}CoO_3$ compound. Finally, the magnetic characterization by means of XMCD and NPD points to a leading role of the spin-lattice coupling and a spin Co reorientation in the anomalous transition. Also in this chapter the possible effects of introducing an alkali-earth (Ba) at the Sr-site and its influence on the magnetic and structural properties are investigated. This study is also accompanied by the characterization of similar cobaltites such as $Nd_{1/3}La_{1/6}Sr_{0.50}CoO_3$ and $Nd_{0.50}Sr_{0.50}CoO_3$, where the magnetostructural transition is suppressed, to better outline role of Pr ions in this transition.

In **Chapter 5**, the characterization on the layered-double perovskite $YBaCo_2O_{5.50}$, containing only Co^{3+} in different environments, is presented. The study covers the simultaneous magnetic, metal-insulator and structural transition at room temperature. In addition, the structural characterization in an extended temperature range was done by SXRPD, showing a competition between orthorhombic and monoclinic phases at low temperatures. As in other compounds, the origin of the metal-insulator transition is also here a matter of debate. One of the most popular scenarios claimed by the scientific community is a SS transition in the Co^{3+} ions with octahedral coordination. The Co^{3+} ions with pyramidal coordination would meanwhile remain unchanged. To check this hypothesis, different x-ray spectroscopies techniques have been applied as well as to other compounds of the family such as $PrBaCo_2O_{5.50}$ and $GdBaCo_2O_{5.50}$, and the results are here presented.

The last chapter (**Chapter 6**) is dedicated to a new charge-ordered Co^{2+}/Co^{3+} Ba-based cobaltite with a non perovskite structure, but with five crystallographically independent Co sites. This antiferromagnetic compound undergoes an insulator-insulator transition at T_t ~ 567 K, that arises from a SS transition, mainly ascribed to Co^{3+} ions. The analysis of the NPD and XAS data corroborate the existence of a LS to HS state transition in the Co^{3+} ions. In addition, thanks to our magnetic characterization using neutrons, we have seen that the spin-state, the super-superexchange interaction and covalence effects play a main role in the physical phenomenology displayed by this cobaltite. Finally, we include a last chapter with the principal conclusions that can be extracted from this work.

BIBLIOGRAPHY

[1] W. Kobayashi, I. Terasaki, M. Mikami, R. Funahashi, T. Nomura, and T. Katsufuji, "Universal charge transport of the Mn oxides in the high temperature limit," *J. Appl. Phys.*, vol. 95, no. 11, pp. 6825–6827, 2004.

[2] B. Raveau, "Transition metal oxides: Promising functional materials," *J. Eur. Ceram. Soc.*, vol. 25, pp. 1965–1969, 2005.

[3] A. Maignan, T. Motohashi, S. Hébert, D. Pelloquin, and B. Raveau, "Cobaltites: New materials with magnetoresistance properties," *Mater. Sci. Eng. B Solid-State Mater. Adv. Technol.*, vol. 126, pp. 296–299, 2006.

[4] E. V. Tsipis and V. V. Kharton, "Electrode materials and reaction mechanisms in solid oxide fuel cells: a brief review," *J. Solid State Electrochem.*, vol. 12, pp. 1367–1391, 2008.

[5] N. B. Ivanova, S. G. Ovchinnikov, M. M. Korshunov, I. M. Eremin, and N. V. Kazak, "Specific features of spin, charge, and orbital ordering in cobaltites," *Uspekhi Fiz. Nauk*, vol. 52, pp. 789–810, 2009.

[6] W. B. Duncan, O. Dermot, and I. W. Richard, *Functional oxides*. WILEY-VCH, 2010.

[7] D. I. Khomskii, *Transition metals compounds*. Cambridge University Press, 2014.

[8] T. Takami, *Functional Cobalt Oxides. Fundamentals, properties and applications*. Singapore: Pan Stanford Publishsing, 2014.

[9] J. G. Bednorz and K. A. Müller, "Possible High T c Superconductivity in the Ba-La-Cu-O System," *Condens. Matter*, vol. 64, pp. 189–193, 1986.

[10] M. K. Wu, J. R. Ashburn, C. J. Torng, P. H. Hor, R. L. Meng, L. Gao, Z. J. Huang, Y. Q. Wang, and C. W. Chu, "Superconductivity at 93 K in a new mixed-phase Yb-Ba-Cu-O compound system at ambient pressure," *Phys. Rev. Lett.*, vol. 58, no. 9, pp. 908–910, 1987.

[11] C. N. R. Rao and B. Raveau, *Colossal Magnetoresistance, Charge ordering, and Related properties of Manganese Oxides*. 1998.

[12] Y. Tokura, *Colossal Magnetoresistive Oxides*. New York: Science Publishers, 1999.

[13] C. Fouassier, G. Matejka, J.-M. Reau, and P. Hagenmuller, "Sur de nouveaux bronzes oxygénés de formule Na_xCoO_2 (x<1). Le système cobalt-oxygène-sodium", *J. Solid State Chem.*, vol. 6, pp. 532–537, 1973.

[14] I. Terasaki, Y. Sasago, and K. Uchinckura, "Large Thermoelectric power in $NaCo_2O_4$ single crystals", *Phys. Rev. B*, vol. 58, no. 20, pp. 4259–4262, 1998.

[15] C. Martin, A. Maignan, D. Pelloquin, N. Nguyen, and B. Raveau, "Magnetoresistance in the oxygen deficient $LnBaCo_2O_{5.4}$ (*Ln*=Eu, Gd) phases", *Appl. Phys. Lett.*, vol. 71, no. 10, p. 1421, 1997.

[16] Y. Wang, N. Rogado, R. J. Cava, and N. P. Ong, "Spin entropy as the likely source of enhanced thermopower in $Na_xCo_2O_4$.", *Nature*, vol. 423, pp. 425–428, 2003.

[17] K. Takada, H. Sakurai, and E. Takayama-muromachi, "Superconductivity in two-dimensional CoO_2 layers" *Nature*, vol. 422, pp. 53–55, 2003.

[18] C. Frontera, J. García-Muñoz, A. Llobet, and M. Aranda, "Selective spin-state switch and metal-insulator transition in $GdBaCo_2O_{5.5}$", *Phys. Rev. B*, vol. 65, no. 180405(R), pp. 3–6, 2002.

[19] A. Maignan, V. Caignaert, B. Raveau, D. Khomskii, and G. Sawatzky, "Thermoelectric power of $HoBaCo_2O_{5.5}$: Possible evidence of the spin blockade in cobaltites", *Phys. Rev. Lett.*, vol. 93, no. 2, pp. 026401–1, 2004.

[20] V. Goldsmitch, *Oxford Univ. Press*, 1958.

[21] H. D. Megaw, "Crystal Structure of Barium Titanium oxide and other double oxides of the perovskite type", *Trans. Faraday Soc.*, vol. 42, pp. A224–A231, 1946.

[22] C. A. Randall, A. S. Bhalla, T. R. Shrout, and L. E. Cross, "Classification and consequences of complex lead perovskite ferroelectrics with regard to B-site cation order", *J. Mater. Res.*, vol. 5, no. 4, pp. 829–834, 1990.

[23] J. B. Goodenough, "An interpretation of the magnetic properties of the perovskite-type mixed crystals $La_{1-x}Sr_xCoO_{3-\delta}$", *J. Phys. Chem. Solids*, vol. 6, pp. 287–297, 1958.

[24] J. B. Goodenough, A. Wold, R. J. Arnott, and N. Menyuk, "Relationship between crystal symmetry and magnetic properties of ionic compounds containing Mn^{3+}", *Phys. Rev.*, vol. 124, no. 2, pp. 373–384, 1961.

[25] H. A. Jahn and E. Teller, “Stability of Polyatomic Molecules in Degenerate Electronic States. I. Orbital Degeneracy”, *Proc. R. Soc. A Math. Phys. Eng. Sci.*, vol. 161, pp. 220–235, 1937.

[26] T. Vogt, J. a. Hriljac, N. C. Hyatt, and P. Woodward, “Pressure-Induced Intermediate-to-Low Spin State Transition in $LaCoO_3$,” *Phys. Rev*. B., vol. 67, no. 140401(R), p. 3, 2002.

[27] G. Vankó, J.-P. Rueff, A. Mattila, Z. Németh, and A. Shukla, “Temperature and pressure-induced spin-state transitions in $LaCoO_3$,” *Phys. Rev*. B., vol. 73, no. 024424, pp. 1–9, 2005.

[28] J. Störh and H. C. Siehmann, *Magnetism: from fundamentas to nanoscale dynamics*. Springer, 2006.

[29] H. Kramers, “L'interaction entre les atomes magneto-genes dans un cristal paramagnetique” *Physica*, vol. 1, no. 182, 1934.

[30] P. W. Anderson, “Antiferromagnetism. Theory of superexchange interaction,” *Phys. Rev.*, vol. 79, no. 1934, pp. 350–356, 1950.

[31] J. B. Goodenough, *J. Phys- Chem. Solids*, vol. 6, no. 287, 1958.

[32] J. Kanamori, ” *J. Phys- Chem. Solids*, vol. 10, no. 87, 1959.

[33] C. Zener, “Interaction between the d-shells in the TM. Ferromagnetic compounds of Manganese with perovskite structure,” *Phys. Rev*, vol. 82, no. 3, pp 403, 1951.

[34] A. J. Barón-González, C. Frontera, J. L. García-Muñoz, J. Blasco, and C. Ritter, “Role of A -site cations in the metal-insulator transition in $Pr_{0.5}Ca_{0.5}CoO_{3-\gamma}$ (γ~0),” *Phys. Rev. B*, vol. 81, no. 054427, pp. 1–6, 2010.

[35] J. L. García-Muñoz, C. Frontera, A. J. Barón-González, S. Valencia, J. Blasco, R. Feyerherm, E. Dudzik, R. Abrudan, and F. Radu, “Valence transition in (Pr,Ca)CoO_3 cobaltites: Charge migration at the metal-insulator transition,” *Phys. Rev. B.*, vol. 84, no. 045104, pp. 3–8, 2011.

[36] J. Herrero-Martín, J. García-Muñoz, S. Valencia, C. Frontera, J. Blasco, A. Barón-González, G. Subías, R. Abrudan, F. Radu, E. Dudzik, and R. Feyerherm, “Valence change of praseodymium in $Pr_{0.5}Ca_{0.5}CoO_3$ investigated by X-ray absorption spectroscopy,” *Phys. Rev. B*, vol. 84, no. 115131, pp. 1–6, 2011.

[37] Y. Okimoto, X. Peng, M. Tamura, T. Morita, K. Onda, T. Ishikawa, S. Koshihara, N. Todoroki, T. Kyomen, and M. Itoh, "Ultrasonic propagation of a metallic domain in $Pr_{0.5}Ca_{0.5}CoO_3$ undergoing a photoinduced insulator-metal transition," *Phys. Rev. Lett.*, vol. 103, no. 027402, pp. 1–4, 2009.

Chapter 2

Experimental techniques

2.1. Introduction

This chapter offers a brief overview of the various experimental methods and techniques used to prepare and characterize the Cobalt oxides presented in this manuscript. We also provide a brief description of the main instruments used during the experimental characterization in different large facilities. Firstly, we detail the synthesis processes of all the studied samples in different forms: polycrystalline, thin film, and single crystal. Most of the samples were prepared at the Institut de Ciència de Materials de Barcelona (ICMAB-CSIC) and some also at the Instituto de Ciencia de Materiales de Aragón (ICMA-Universidad de Zaragoza) with the collaboration of Dr. Javier Blasco. In addition to conventional X-rays, the structural analysis was carried out by means of synchrotron x-ray powder diffraction (SXRPD) and neutron powder diffraction (NPD). The experiments based on these experimental techniques were mainly performed in Grenoble: at the European Synchrotron Radiation Facility (ESRF) and at the Institute Laue-Langevin (ILL), respectively. On the other hand, nearly all the spectroscopic measurements were done on the BL29-BOREAS beamline at the ALBA Synchrotron, on the SuperXAS-ID10DA beamline at the Swiss Light Source (SLS, Villigen), and on ID26 beamline at the ESRF. Furthermore, in most cases data collection was followed by a theoretical and

quantitative analysis of the diffraction and absorption data. Details of their corresponding methodologies will be also presented in this chapter. In addition, for the study of the basic electrical and magnetic macroscopic physical properties we have used a commercial PPMS and a SQUID systems from the Low Temperature and Magnetometry Service of the ICMAB Scientific Technical Services Unit, with technical support from the Institute staff.

2.2. Samples synthesis & growth: powder, thin film & single crystal

2.2.1. Polycrystalline samples fabrication: Solid-state reaction under controlled atmosphere

Solid-state reaction is the most conventional method used to prepare perovskites-oxide materials. Thus, most of the samples studied in this thesis were prepared by means of this technique. The synthesis is produced due to the ionic diffusion between the different reactants assisted by thermal energy. So, in general it is a slow process, and high temperatures and long annealing processes are required for the solid state reaction method. Another important parameter during the heat treatments is the use of appropriate atmospheres to control the oxygen content. In particular, the properties of several cobalt oxides strongly depend on the oxygen content [1, 2]. For instance, during the annealing process an inert gas such as Argon may be used to prevent oxidation to a higher-oxidation state, and an oxygen atmosphere can be used to encourage the formation of high-oxidation states; or, conversely, a hydrogen atmosphere can be used to produce a low oxidation state [3]. Some examples are shown below:

Reaction in a reducing atmosphere

$$V_2O_5\ (V^{5+}) \xrightarrow{H_2} VO\ (V^{2+})$$

Reaction in a oxidizing atmosphere

$$LaNiO_{2.5}\ (Ni^{2+}) \xrightarrow{O_2} LaNiO_3\ (Ni^{3+})$$

The process consists on mixing the solid reactants in the required amounts (stoichiometric mixture of the precursors) to prepare a specific solid crystalline compound and then grind, press and warm up the initial mixture to high temperatures. To achieve homogenous single-phase materials, intermediate grindings and warm up rates can also be also performed before the last annealing process. The specific precursors and heating and annealing processes followed for particular compositions of the different Cobalt compounds will be detailed in the corresponding chapters where the results for the different families are presented.

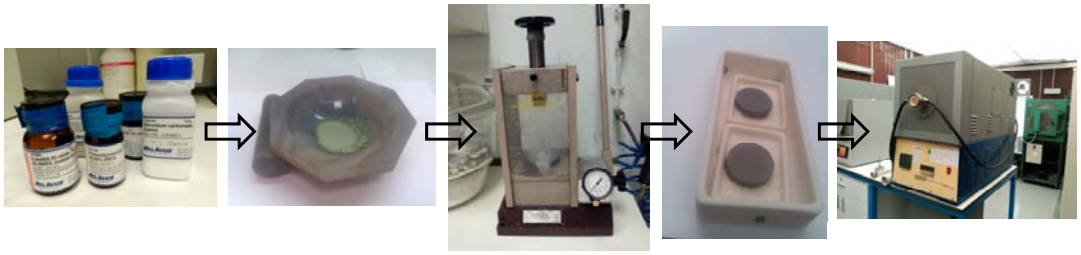

Figure 2. 1. Different sequential steps in the solid-state reaction method. The selected precursors are mixed, grinded, pressed, and heated in a tubular furnace.

2.2.2. Polycrystalline samples fabrication: Sol-gel method

Another conventional method used to synthesize cobalt oxide compounds is the sol-gel method. This method allows to enhance the reaction of the precursors and decrease the synthesis temperature. In the case of cobalt-based perovskites, the sol-gel method is particularly suitable for obtaining high-quality materials with small tolerance factors (t<<1), strong distortions in the octahedral network, or very small rare earths. Some of these materials cannot be obtained by conventional solid-state reactions. This is the case of the here presented $ErCoO_3$ and $YBaCo_2O_{5.50}$ cobaltites.

The regular procedure followed during application of the sol-gel method involves the dissolution of the precursors in an acid solution, by adding citric acid and ethylene glycol. Then, the mixture is slowly evaporated leading to a resin which is pressed and heated as it happens in the last steps of the solid-state reaction method.

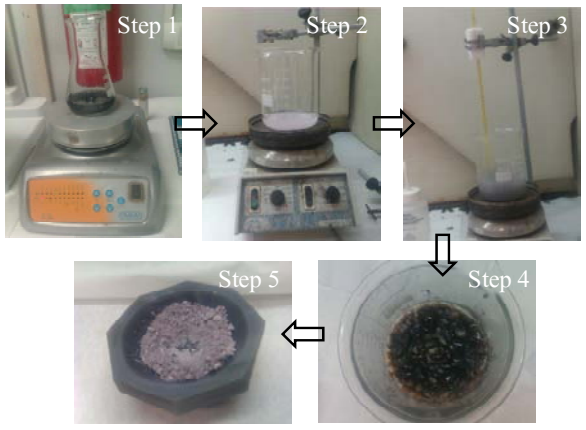

Figure 2. 2. Different steps for the synthesis of $ErCoO_3$ using the sol-gel method. Step 1: mixing of the precursors with the acid solution, Step 2: addition of the citric acid and ethylene glycol, Step 3: evaporation of the organic solution, Step 4: obtained resin, and Step 5: final product after grinding the resin.

2.2.3. Thin films fabrication: Pulsed-laser deposition

In this manuscript other forms (non polycrystalline) of cobalt oxides will be also described and investigated. For instance, this is the case of the cobaltites prepared as thin films. For their growth the technique known as Pulsed-Laser Deposition (PLD) was used, with the support from the local staff of the Thin Films Laboratory Service at the ICMAB.

In principle, PLD is an extremely simple technique which uses ultraviolet laser radiation to vaporize a target material that is deposited onto a substrate. The pulsed beam of an ultraviolet laser (usually an excimer) is focused on a ceramic target placed in a vacuum chamber. The combination of pulsed irradiation, high photon energy, and high energy density cause the ablation of the material. Then, the plasma (or laser plume) created expands rapidly along the perpendicular direction of the target, where a substrate is placed (in front the target). A schematic configuration of a PLD system is shown in Figure 2. 3. Usually, this process is carried out in ultra high vacuum or in the presence of a background gas, such as oxygen. The later is commonly used when depositing oxides to fully oxygenate the deposited films. The process of PLD can be generally divided into four stages:

(i) laser ablation of the target material and creation of plasma: this stage involves the transfer of energy from the high powered laser to a target material. The result of this interaction is a highly energetic plume of neutral atoms, ions, and electrons;
(ii) dynamics of the plasma: The energetic plume interacts with the deposition path and is directed towards the heated substrate;
(iii) deposition of the ablation material onto the substrate: in this third stage, the species in the plume stick onto the substrate;
(iv) nucleation and growth of the film on the substrate surface: in this last stage, the species in the plume diffuse and nucleate into highly ordered atomic layers.

However, the process is not as simple as it seems since a large number of variables can affect the properties of the film, such as: the laser fluence, the background gas pressure, or the substrate temperature, among others.

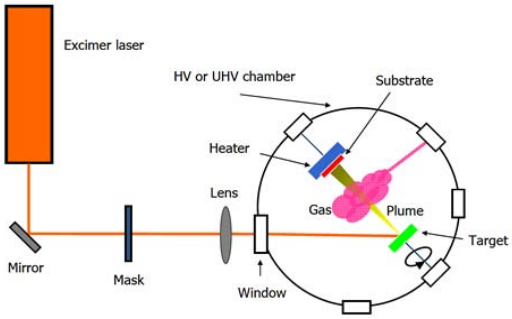

Figure 2. 3. Schematic of a PLD configuration similar to the instrument allocated at the Thin Films Laboratory Service at the Institut de Ciència de Materials de Barcelona.

2.2.4. Single crystal fabrication: Optical floating-zone furnace

Some doped cobalt perovskites single crystals (i.e. $Pr_{0.50}Sr_{0.50}CoO_{3-d}$) have been grown using an optical floating zone furnace (model: FZ-T-P1200_H-I-S-PC from Crystal System Corporation) at the new Single-crystal growth Laboratory of the ICMAB-CSIC. A schematic diagram of the optical floating-zone furnace is displayed in Figure 2. 4. Initially, we synthesized polycrystalline samples in the form of cylindrical bars [3 mm in diameter and 100 mm in length, see Figure 2. 5(a)] by solid-state reaction (also in collaboration with Dr. Javier Blasco from ICMA-CSIC). Additional details on the thermal treatment of the polycrystalline bars and other details about the growth method are given in Chapter 4. A cut piece of bar or another crystal can be used as a seed rod (lower rod) and the rest of the bar was used as a feed rod (upper rod). Both must be placed inside a quartz tube to protect the sample from air and to control the atmosphere around the crystal. When the two (vertically placed) rods are close enough to each other inside the furnace and they are exposed to an optical heating by halogen lamps [see Figure 2. 5(b)], a liquid molten zone [see Figure 2. 5(c)] is formed [4].

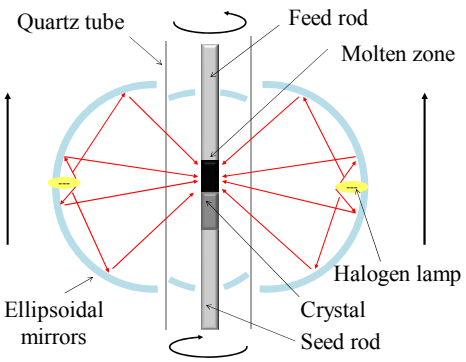

Figure 2. 4. Schematic configuration of the optical mirror furnace employed, based on ellipsoidal mirrors. The two thick black arrows indicate the crystal growth direction.

In the growing process we find two solid-liquid interphases: in the upper rod the solid polycrystalline is melted and feeds the molten zone, while the process of solidification and nucleation is produced in the lower rod. One important concern during the crystal growth is to get a uniform heating in the molten zone and to avoid local density fluctuations. For that, the sample rod is continuously rotated counterclockwise, while the seed rod is rotated clockwise. The four ellipsoidal mirrors are used to focus the light from the halogen lamps (in our furnace, their power is 400 W).

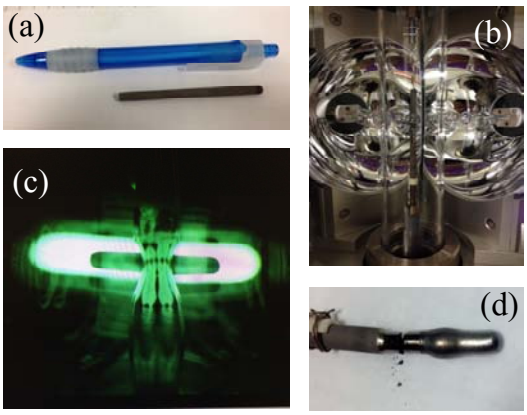

Figure 2. 5. Pictures showing the growth of PSCO single crystals: (a) polycrystalline sintered sample of PSCO used as a seed or feed rod; (b) detail of the four ellipsoidal mirrors inside the optical floating furnace that are used to focus the light from halogen lamps onto a vertically held rod sample; (c) view of the chamber with the molten zone produced during the process; and (d) the resulting single crystal of PSCO.

2.3. Magnetic and electrical characterization

The magnetic characterization of bulk samples, thin films, or single crystals studied in this work was done on a commercial Superconducting Quantum Interferometer Device (SQUID) from Quantum Design, with temperatures ranging from 1.8 K to 800 K and applied external magnetic fields up to 7 T. For ac-measurements the maximum amplitude is 15 Oe and frequencies range in an interval from 10 Hz to 10 kHz. On the other hand, the transport properties (electrical resistivity, Seebeck coefficient below room temperature) were measured by using a Physical Property Measurement System (PPMS) from Quantum Design. Both equipments belong to the Low Temperature and Magnetometry Service of the ICMAB, and the measurements were done with the support of the Service technician. Moreover, characterization measurements of the Seebeck coefficient above room temperature were also performed in a

Linseis LSR-3 commercial setup with the collaboration of Dr. Sebastian Reparaz from The Institut Català de Nanociència y Nanotecnologia (ICN2). As we know, dc-magnetic measurements determine the value of the magnetization in a sample. Generally, when a constant magnetic field is applied to a sample containing magnetic atoms, it gets magnetized. Thus, the degree of magnetization of a material in response to an steadily applied magnetic field can be measured by a magnetization curve *M(H)*.

In contrast, in ac-magnetic measurements a small ac-drive magnetic field is superimposed to the dc-field and, as a consequence, the magnetic response is a time-dependent magnetization of the sample. The ac-magnetization is given by:

$$M_{AC} = \left(\frac{dM}{dH}\right) h_{AC} \sin(\omega t) \qquad \text{(Eq. 2.1)}$$

where h_{AC} is the amplitude of the driving field, ω is the driving frequency, and $\chi = dM/dH$ is the slope of the *M(H)* curve, called magnetic susceptibility.

The SQUID is a highly sensitive instrument nowadays used for magnetic measurements providing the magnetic ac/dc-susceptibility as a function of temperature or the magnetization. This device is based on the Josephson effect via a Josephson junction in which a current flows across two weakly coupled superconductors (set of coils), separated by a very thin insulating barrier. When a sample is placed inside the SQUID and moved along the vertical axis of the superconducting coils a current-voltage is created. This is a consequence of the changes associated to the magnetic flux which is proportional to the magnetic moment of the sample. Using a sensor, the magnetic flux can be directly determined from the output voltage.

On the other hand, the PPMS is an instrument used for thermal and electrical transport measurements varying temperature and under application of magnetic fields. The measurement of transport properties as a function of temperature for thin films and bulk systems were done using the four-probe method with silver contact pads as Figure 2. 6(a) shows. The distinct procedures followed to stick the contacts on the samples are detailed in the corresponding chapter for each sample.

In order to measure the thermal transport properties we used the Thermal Transport Option (TTO) system for the PPMS. This system enables to simultaneously measure the thermal conductivity (κ) (the ability of the material to conduct heat), the Seebeck coefficient (α), the resistivity (ρ) and, as a consequence, to assess the thermoelectric figure of merit $Z=\alpha^2T/\kappa\rho$. In the case of the κ or α coefficients, the system works monitoring the temperature drop along the sample while an amount of heat passes through it, and simultaneously the electrical voltage drop that accompanies the temperature gradient. We used a special sample-

holder [see Figure 2. 6(b)] for these measurements that incorporates one heater (I^+) and two thermometer shoes [hot (V^+) and cold (V^-) probe]. The sample was mounted (sticked with an special epoxy) in a two-probe configuration between two disk-shaped copper leads. Before measuring, the sample-holder was covered by a radiation shield to minimize the radiation exchange between the sample and the environment

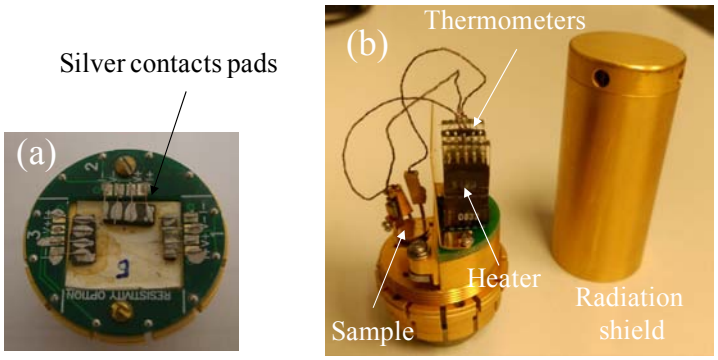

Figure 2. 6. (a) Sample-holder for resistivity measurements in a four-probe configuration; (b) sample-holder for thermal transport properties using the TTO system for the PPMS where the sample is mounted in a two-probe configuration.

2.4. Structural characterization : diffraction

The polycrystalline samples were initially characterized by the X-ray diffraction (XRD) technique using a Siemens D-5000 diffractometer [λ(Cu K_α)= 1.541840 Å]. On the other hand, the characterization of thin films and single crystals was done on a Bruker-AXS "D8 Advance" diffractometer equipped with an area detector to record the reciprocal space maps around specific reflections. Both equipments are allocated at the X-ray Diffraction Laboratory of the ICMAB-CSIC. However, the most exhaustive structural characterization was carried out by means of synchrotron X-rays and neutron diffraction in large European facilities such as the European Synchrotron Radiation Facility (ESRF) or the Institute Laue-Langevin (ILL). Other neutron and synchrotron sources used are: SINQ (Switzerland), ALBA Synchrotron Light Source (Spain), and BESSY II-Helmholtz-Zentrum Berlin (Germany).

2.4.1. X-ray diffraction

The polycrystalline powder XRD is a widely used technique to identify the crystalline structure, grain size, and internal strains of crystalline materials, i.e. those with regularly repeating atoms or ions in space, forming periodic planes. The diffraction process is the interaction of photons (incident X-ray beam considered as electromagnetic waves) with the electron cloud that surrounds each atom, producing diffracted X-rays. Although, the outgoing waves cancel one another in most directions through destructive interference, they add constructively in a few specific directions, when conditions satisfy the Bragg's law:

$$2dsin\theta = n\lambda \qquad \text{(Eq. 2.2)}$$

where d is the spacing between the lattice planes (hkl), θ is the angle of the diffracted wave with respect to the incoming one, n is the order of diffraction and λ is the wavelength of the incident X-ray beam.

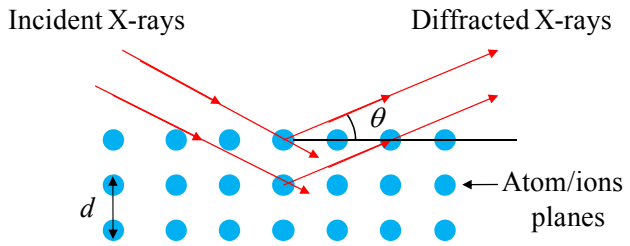

Figure 2. 7. Schematic illustration of Bragg's law in X-ray diffraction.

The analysis of the angular position and intensity of the diffracted X-rays allow us to determine the crystal structure, i.e. the unit cell parameters and atomic positions.

For a single atom the atomic form factor $f(\overrightarrow{Q})$ for X-rays is a measure of the amplitude of a wave scattered by an isolated atom and can be described as:

$$f\ (\overrightarrow{Q}) = \int \rho(\overrightarrow{r}) e^{i2\pi\vec{Q}\cdot\vec{r}} dV \qquad \text{(Eq. 2.3)}$$

where $\rho(\overrightarrow{r})$ is the electronic density and $\vec{Q}$ the scattering vector, defined as $\vec{Q} = \vec{k}_f - \vec{k}_i$, i.e.as a function of the final and initial wave vector, respectively, The scattering vector can be also defined as $2\pi/\lambda$.

In general, the atomic form factor depends on the type and characteristics of the scattering process, which in turn depends on the nature of the incident radiation, typically X-rays, electrons, or neutrons. As a general rule, for X-rays, $f(\overrightarrow{Q})$ is proportional to Z, the atomic

number, which explains the difficulty of detecting light elements like oxygen or hydrogen using X-ray diffraction.

In a real crystalline structure composed by a number of N atoms in the unit cell, the structure factor is derived from Eq. 2.3:

$$F(\overrightarrow{Q}) = \sum_{j=1}^{N} f_j(\overrightarrow{Q}) e^{i2\pi\vec{Q}\cdot\vec{r_j}} e^{-W_j} \quad \text{(Eq. 2.4)}$$

where N is the number of atoms in the unit cell, $f_j(\overrightarrow{Q})$ is the atomic form factor for the j^{th} atom in the unit cell, $\vec{r_j}$ is the position (x_j, y_j, z_j) of atom j, and W_j is the Debye-Waller factor which takes into account the thermal displacement of the atoms around their equilibrium positions.
So, the diffracted intensity can be described as:

$$I(\overrightarrow{Q}) \propto \left|F(\overrightarrow{Q})\right|^2 \quad \text{(Eq. 2.5)}$$

2.4.2. Synchrotron X-ray powder diffraction

Synchrotron radiation is just the electromagnetic field radiated by relativistic accelerated charged particles when their trajectory is bent by the use of high magnetic fields perpendicular to the horizontal orbital plane. This radiation is emitted tangentially along the orbital plane. In order to give a particular structure and/or selected polarization type to the spectral distribution of emitted intensity in a Synchrotron beamline, different special devices are used: bending magnets, undulators, or wigglers.
The main characteristics that make unique the synchrotron radiation are detailed below[5]:

(i) broad spectrum: the electromagnetic spectrum (white radiation) covers from radio-frequency to hard X-rays regions. The users can select the wavelength required for special experiments;

(ii) high flux: the synchrotron radiation is emitted in a small angular range along the tangential path of the electron trajectory. So, the number of emitted photons per unit solid angle is very high;

(iii) high brilliance: the photon beam is highly collimated due to a small divergence and small size source;

(iv) polarized beam: the radiation emitted by the electrons is linearly polarized in the orbital plane of the electrons, but it is elliptical outside the orbital plane;

(v) pulsed time structure: the pulsed length can be of the order of picoseconds or femtoseconds, and then it allows resolution of processes on the same time scale;

(vi) high stability.

The synchrotron X-ray powder diffraction is a useful technique for the structural characterization of materials due to the singular features of synchrotron radiation. The exceptional properties of the synchrotron radiation applied to powder diffraction have major advantages over the laboratory X-rays:

* high photon wavelength resolution ($\Delta\lambda/\lambda$ better than $2\cdot10^{-4}$);
* very high signal-to-noise and signal-to-background ratios;
* ultrafast data acquisition;
* tunable photon energy to use very shorts wavelengths, which allows collecting data at very high *Q* and the same time to reduce the absorption in heavy elements;
* high angular (FWHM) resolution (around 0.003º in 2θ at ID22, the old ID31 beamline at the ERSF);
* very high counting statistics in few seconds.

2.4.3. Neutron powder diffraction

Another powerful technique, is the *"neutron powder diffraction"* very useful for the characterization of most of the compounds investigated in this thesis. In most cases, diffraction is the main mechanism of interaction of neutrons with crystalline matter. Unlike X-rays, which primarily interact with the electron cloud surrounding each atom of a given material, most scattering of neutrons occurs at the atom nuclei. This fact provides complementary information not always accessible with X-rays like, for instance, precise interatomic bond distances, angles, and thermal displacements of light atoms (e.g. hydrogen and oxygen) in the presence of heavy atoms. In addition, in spite of being uncharged particles, neutrons are fermionic particles with a nonzero spin (*S*= 1/2) which interacts (dipole-dipole) with the magnetic moment of unpaired electrons, and therefore provides information about the magnetic properties of matter [5, 6].

In the case of neutrons, the structure factor (Eq. 2.4) due to the interaction with the nuclei of the atoms can be expressed as:

$$F_N(\overrightarrow{Q}) = \sum_{j=1}^{N} b_j e^{i2\pi\vec{Q}\cdot\vec{r_j}} e^{-W_j} \qquad \text{(Eq. 2.6)}$$

where b_j is the scattering length which is not proportional to *Z*, unlike the atomic form factor $f(\overrightarrow{Q})$ for X-rays. In this case the scattering length depends on the neutron-to-atomic nuclei interaction.

In addition to the *nuclear scattering*, the *magnetic scattering* must also be taken into consideration and it is described as:

$$F_M(\overrightarrow{Q}) = \sum_{j=1}^{N'} S_{k,j} f_{Mj}(\overrightarrow{Q}) e^{i2\pi\vec{Q}\cdot\vec{r_j}} e^{-W_j} \qquad \text{(Eq. 2.7)}$$

where *N'* is the number of magnetic atoms in the unit cell, $f_{Mj}(\overrightarrow{Q})$ is the magnetic form factor for the j^{th} atom in the unit cell, and $S_{k,j}$ is the Fourier component of the magnetic moment distribution. The moment distribution $m_{j,l}$ in the crystal (referred to the atom *j* in the magnetic unit cell *l*) is a periodic function that can be Fourier expanded:

$$m_{j,l} = \sum_k S_{k,j}\, e^{-i2\pi\vec{k}\cdot\overrightarrow{Rl}} \qquad \text{(Eq. 2.8)}$$

where *l* indexes the origin of a given magnetic unit cell. The Fourier coefficients verify that $S_{k,j} = S^*_{-k,j}$. $m_{j,l}$. This represents the magnetic vector distribution that gives the magnitude and direction of any magnetic moment.

On the other hand, bearing in mind the expression for the magnetic interaction operator [$\vec{D}_\perp = \vec{Q}$ x ($\vec{M}$x $\vec{Q}$)] where $\vec{M}$ is the magnetic operator and $\vec{Q}$ is the scattering vector, it can be proved that magnetic neutron scattering is only sensitive to the perpendicular direction of the magnetic moment ($M^{\perp}$) to the scattering vector [6]. So, the magnetic intensity can be determined using the general formula of Halpern and Johnson [7]:

$$I(\overrightarrow{Q}) \propto \left|F_M^{\perp}(\vec{Q})\right|^2 = \left|F_M(\overrightarrow{Q})\right|^2 - \left(e \cdot F_M(\overrightarrow{Q})\right)^2 \qquad \text{(Eq. 2.9)}$$

where, $F_M^{\perp}(\vec{Q})$ is the projection of the magnetic structure factor along the perpendicular direction, $F_M(\overrightarrow{Q})$ is the magnetic form factor, and e is the unit vector along the scattering vector $\vec{Q}$.

2.4.4. Rietveld method and agreement factors

In the present work all diffraction data (SRXPD and NPD) have been analyzed using the Rietveld method implemented in the Fullprof suite of programs [8]. This method was developed by Hugo Rietveld in 1969 and its introduction meant a significant step forward in the diffraction analysis of powdered samples. Nowadays is the most common procedure for neutron and X-rays powder diffraction data analysis when the structure is at least approximately known.

This method is based on minimizing the weighted squared difference between the observed data and the calculated pattern using an approximate structural model. The function to be minimized can be described as:

$$S_y = \sum_i w_i \left| y_i^{(o)} - y_i^{(c)} \right|^2 \quad \text{(Eq. 2.10)}$$

where $y_i^{(o)}$ and $y_i^{(c)}$ are the observed and calculated intensities at each step, and w_i is the weight for each i experimental point. This last term is taken from the experimental error margins (σ_i^2, variance of the "observation" y_i) and can be defined as $w_i = 1/\sigma_i^2$.

The calculated intensity for each position $2\theta_i$ in a diffraction pattern can be expressed as:

$$y_i^c(2\theta) = b(2\theta) + L_p(2\theta) \sum_\alpha S_\alpha \sum_k m_{k,\alpha} \left| F_{k,\alpha} \right|^2 h_\alpha (2\theta - 2\theta_{k,\alpha}) P_{k,\alpha}(2\theta) \quad \text{(Eq. 2.11)}$$

where $b(2\theta)$ is the background contribution, S_α is the scale factor for each α crystallographic phase, k is the miller's index for one specific reflection, $m_{k,\alpha}$ is the multiplicity for each k reflection, $h_\alpha(2\theta\text{-}2\theta_k)$ is the function in charge to describe the reflection's shape, $L_p(2\theta)$ contains the Lorentz and polarization correction factors, $P_{k,\alpha}$ is a factor to correct the effect of preferential orientation, absorption and extinction, and $F_{k,\alpha}$ is the structure factor [9, 10].

The main parameters used for a good refinement between the experimental and the calculated pattern in the software can be separated into two principal groups:

(i) structural parameters: scale factor, temperature factor, occupation number, and atomic position for each atom;

(ii) profile parameters: cell parameters, asymmetry, preferential orientation, background, and the full with at half maximum (FWHM).

The calculated model should refine the position, shape, and intensity for each peak from the diffraction pattern. For that, the different parameters, as detailed below, are used to refine those features:

(i) peak position: the correct position of each Bragg reflection can be refined by the cell parameters of each crystalline phase present in the specimen and the zero shift error in the goniometer;

(ii) peak intensity: the intensity of the peaks depends on the selected structural model for each crystalline phase, thus on the atomic positions;

(iii) peak shape: this can be a more complex feature for a good refinement. The complexity in a good refinement not only depends on the sample, but also on the instrumental features (radiation source, geometry, monochromator, slits sizes, and so on).

The final peak shape can be successfully refined using a specific function such as: a Gaussian function (*G*), a Lorentzian function (*L*), or a Pseudo-Voigt function (*pV*), which is the one most commonly used in the present thesis work. This function can be described as:

$$pV(x;H,\eta) = \eta L(x;H) + (1-\eta)G(x;H) \quad \text{(Eq. 2.12)}$$

where, $0 \leq \eta \leq 1$, *H* is the full width at half maximum for the Lorentzian (*L*) and Gaussian functions (*G*). *H* can be defined for each function as:

$H_G = U\tan^2\theta + V\tan\theta + W$ and $H_L = X\tan\theta + Y/\cos\theta$, where *U*, *V* and *W* are the Caglioti parameters.

The quality of the agreement between the observed and calculated profiles can be measured by a set of parameters as are:

- the profile factor:

$$R_p = 100\frac{\sum_i^n |y_i^o - y_i^c|}{\sum_i^n |y_i|} \quad \text{(Eq. 2.13)}$$

where y_i^o is the observed intensity and y_i^c in the calculated intensity;

- the weighted profile factor:

$$R_{wp} = 100\left[\frac{\sum_i^n w_i |y_i^o - y_i^c|^2}{\sum_i w_i (y_i^o)^2}\right]^{1/2} \quad \text{(Eq. 2.13)}$$

- the expected weighted factor:

$$R_{expp} = 100\left[\frac{n-p}{\sum_i w_i (y_i^o)^2}\right]^{1/2} \quad \text{(Eq. 2.15)}$$

where *n* is the number of observed points and *p* the number of refined parameters;

- the reduced chi-square:

$$\chi^2 = \left[\frac{R_{wp}}{R_{exp}}\right]^2 \quad \text{(Eq. 2.16)}$$

- the Bragg factor:

$$R_B(\%) = 100\frac{\sum_{hkl} |I_{hkl}^o - I_{hkl}^c|}{\sum_{hkl} I_{hkl}^o} \quad \text{(Eq. 2.17)}$$

2.4.5. Instrumentation: neutron & synchrotron powder diffraction

The structural and the magnetic characterization presented in this thesis using X-ray and neutron powder diffraction was performed using different instruments such as: a high-resolution synchrotron X-ray powder diffractometer (ID22, ESRF), a high-resolution neutron diffractometer (D2B, ILL), and high-intensity neutron diffractometers (D20 and D1B, ILL). among others. Here, we provide a brief description of the main instruments where most of the NPD and SRXPD experiments were carried out.

2.4.5.1. ID22 beamline (ESRF)

The SRXPD data presented in Chapter 5 were acquired in ID22 (the old ID31 beamline) at ESRF (Grenoble, France). This beamline is devoted to high-resolution X-ray powder diffraction measurements. Depending on the operating mode, the X-rays are produced by three different undulators. This makes possible to work in an extended range from 6 keV to 80 keV (wavelength from 2.07 Å to 0.15 Å) [11]. The beam is monochromatized by a double channel-cut Si (111) monochromator that is cooled with liquid nitrogen. Water-cooled slits define the size of the incident beam on the monochromator, and of the monochromatic beam transmitted to the sample. The typical spot size ranges from 0.5 to1.6 mm (horizontally) and 0.1 to 1.5 mm (vertically). In routine operation, nine detectors scan vertically to measure the diffracted intensity as a function of the 2θ angle, being each detector preceded by a Si (111) analyzer crystal. See a graphic of the diffractometer and the multianalyzer detector in Figure 2. 8 . The nine analyzer crystals are mounted on a single rotation stage, so only a single adjustment of the Bragg angle is needed when changing the wavelength routine operation. This configuration, with multiple crystals operating in parallel, increases the efficiency of detecting the diffracted radiation. This beamline works with samples contained in spinning capillaries or flat plate specimens, and different environments. In our case we also used a liquid helium-cooled cryostat for variable temperature measurements.

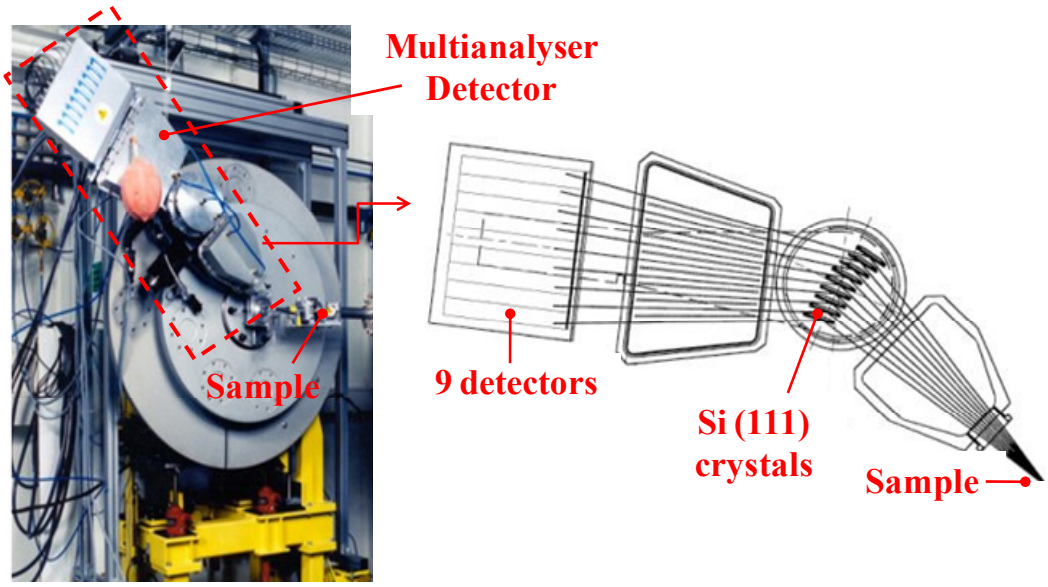

Figure 2. 8. *Left*: a picture of the diffractometer used at ID22; *right*: schematic drawing of the multianalyzer detector. From Ref. [11].

2.4.5.2. D20 and D2B instruments (ILL)

The structural and magnetic orders of most of the compounds investigated in this manuscript were characterized by means of neutron powder diffraction. Most of the experiments were performed in D20 and D2B instruments at the ILL (Grenoble, France).

The thermal neutron beam from the reactor in this neutron source is divided into two parallel beams, one for D2B, the other one for D20.

The D20 diffractometer is a very-high intensity two-axis diffractometer which is preceded by a Ge (115) monochromator with a high take-off angle up to 120°[12]. This monochromator provides a high neutron flux (from 10^7 $ns^{-1}cm^{-2}$ to 10^8 $ns^{-1}cm^{-2}$). The diffracted beams are simultaneously collected by a large ^{3}He microstrip position sensitive detector (PSD) capable to cover a scattering range of 153.6º. See the layout of D20 beamline in Figure 2. 9. This diffractometer can hold different environments such as a furnace or a cryostat, where a cylinder containing the sample powder is placed. This instrument is a useful tool for real-time experiments on very small samples thanks to the high neutron flux and detector capabilities.

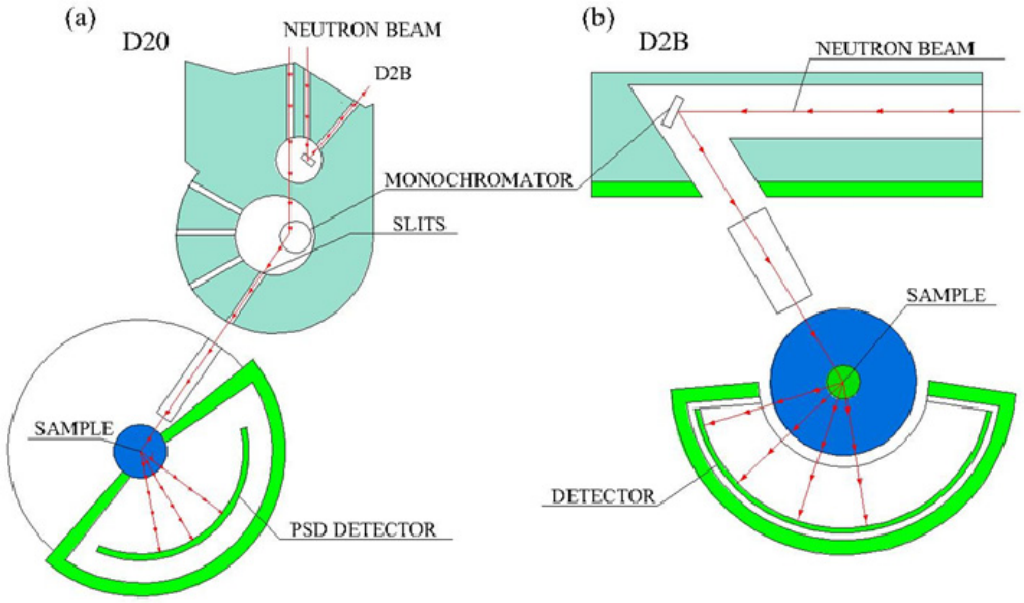

Figure 2. 9. Layout of the (a) D20 diffractometer, and (b) D2B diffractometer at the Institute Laue Langevin. Pictures have been adapted from Ref. [12, 13]

On the other hand, D2B neutron diffractometer is a very-high resolution powder diffractometer designed to achieve the ultimate resolution. This instrument was built to determine the crystal and magnetic structures of powder samples using a very high take-off angle (135º) for the monochromator, which is also formed by Ge (115) crystals. The 2D-detector is composed by a bank of 128 detectors than can be partially rotated during the data acquisition. So, the diffracted neutron counting is averaged over several detectors. The wavelength range goes from 1.051 Å to 3.152 Å. This diffractometer can hold different environments such as a pressure cell (from 2 to 4GPa), a cryomagnet, a cryofurnace (from 1.5 to 525 K), or an *orange* cryostat (from 1.5 to 300 K).

2.5. Synchrotron X-ray spectroscopies

The spectroscopic techniques used in this dissertation to study the electronic structure and the possible spin state (SS) changes of our samples range from X-ray absorption spectroscopy (XAS) to X-ray emission spectroscopy (XES), passing through X-ray magnetic circular dichroism (XMCD). In order to perform these experiments, synchrotron radiation sources are required to provide intense enough and tunable X-ray beams. In this thesis we will concentrate on the XAS measurements of 3*d* transition metals (in particular Co) where the excitation occurs

in the 2*p* states. The promoted electrons move into 3*d* orbitals. We are then talking of the $L_{2,3}$edges. Also, we have studied the O *K*-edge (1*s* $\rightarrow$ 2*p* excitations), or in the rare earths (RE) metals where the excitation takes places from 3*d* $\rightarrow$ 4*f* states ($M_{4,5}$-edges). It should be noticed that the edges are named according to the angular quantum number of the electron that is excited: *K* for l=0, *L* for *l*=1, *M* for *l*=3, and so on. On the other hand, we have looked at deexcitation channels using XES experiments, in particular 3*p* $\rightarrow$ *1s* ones (so called *Kβ* emission). In the following sections a general view about the basis of these techniques will be presented.

The different experiments were performed at various synchrotron light sources as a function of temperature. Almost all the "soft"-XAS (E < 1KeV) and XMCD experiments at the Co $L_{2,3}$ edges, Pr $M_{4,5}$ edges, and O *K*-edge were measured in the BL29-BOREAS beamline at the ALBA Synchrotron Light Facility. In addition, the "hard"-XAS (E > 3KeV) measurements at the Pr L_3 edge were done in the BL22-CLÆSS beamline of the latter facility. On the other hand, the High-Energy Resolution Fluorescence Detected (HERFD) XANES at the Co *K*-edge and XES (Co *Kβ* lines) measurements were collected in the ID26 beamline at the ESRF. Finally, complementary XES measurements at the Co *Kα* lines were acquired in the SuperXAS-X10DA beamline at the Swiss Light Synchrotron (SLS) (Villigen, Switzerland).

2.5.1. X-ray absorption spectroscopy

XAS is a powerful tool to study the local electronic and atomic structure of solids, liquids, or gases in a wide range of external conditions such as temperature, pressure, and so on. The X-ray absorption spectrum of any material is characterized by sharp increases in absorption at specific X-ray photon energies, which are characteristic for the absorbing element (i.e. XAS is chemically selective). These sudden jumps in absorption are called absorption edges, and correspond to the energy required to eject a core-electron into an excited empty state above the Fermi level E_F through the electric-dipole transition ($\Delta l = \pm 1$), thus producing a photoelectron. Then, the XAS spectrum provides us with a valuable information on the partial density of the unoccupied states in the excited levels. It can be divided in two different regions [5, 14–17]:

(i) the X-Ray Absorption Near Edge Structure (XANES): it is the spectral zone in the vicinity of the edge. The XANES region provides semiquantitative information about the oxidation state and the coordination environment of the metal atom;

(ii) the Extended X-ray Absorption Fine Structure (EXAFS): it comprehends the oscillations beyond the XANES region. These oscillations are created when the photoelectron is scattered by the nearest neighbors of the excited atom, and builds up interference patterns that contain structural information. The EXAFS region is sensitive to the radial distribution of electron density around the photo absorbing atom and is used for the quantitative determination of bond lengths and coordination numbers.

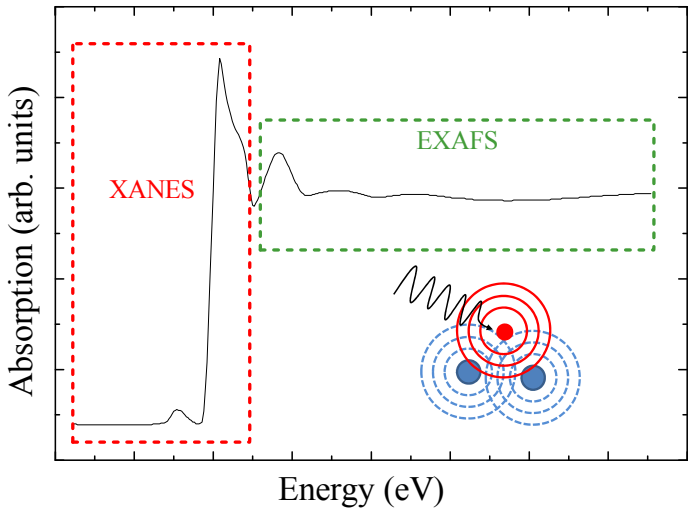

Figure 2. 10. Example of a XAS spectrum where the XANES and EXAFS regions have been distinguished. The inset shows a schematic drawing of the interference between the photoelectron wave emitted from the absorbing atom (red ball) and the back-scattered waves from the neighboring atoms (blue ball).

X-ray absorption is one of the main processes occurring when X-rays interact with matter, where the attenuation of a monochromatic X-ray beam of intensity I_0 passing through an uniform layer of material of thickness d is ruled by the Lambert-Beer Law:

$$I_1 = I_0 e^{-\mu d} \qquad \text{(Eq. 2.18)}$$

with I_1 being the transmitted beam intensity and μ the "mass-dependent absorption coefficient" usually expressed in units of cm^{-1}.

Despite, the derivation of the absorption coefficient is in principle a complicated quantum mechanical problem, a number of key approximations allow to simplify the expression. First of all the one-electron approximation should be invoked, which means that we consider only one photoelectron to be excited by each incoming photon, the other electrons are being merely spectators. Then, the absorption coefficient is proportional to the photoabsorption

cross-section [σ(E)], which is given by the Fermi's Golden which gives the probability per unit time ($\Gamma_{i,f}$) to excite an electron from the initial state $|i\rangle$ to a final state $|f\rangle$ with an energy density $\rho(E_f)$ [5, 16, 17]:

$$\sigma(E)\alpha\,\Gamma_{i,f} = \frac{2\pi}{h^2}|\langle f|H_{int}|i\rangle|^2\rho(E_f)(E - E_f - E_i) \qquad \text{(Eq. 2.19)}$$

where H_{int} denotes the interaction operator reflecting a time-dependent perturbation of the Hamiltonian of the atom.

In general, the simplest type of XAS measurements is in transmission mode. In a transmission experiment, the intensity of the X-ray beam is measured before and after the incident beam passes through the sample. The intensity of the X-ray beam is typically measured using ionization chambers or photodiode. These detectors consist of a chamber filled with inert gas or gas mixture (H_2, He or Ar). The X-ray beam goes through windows at each end of the chamber between two oppositely charged plates. The (photoelectron) current passing between the plates is proportional to the X-ray intensity. This method is normally applied for experiments involving hard X-rays (E > 3 KeV) due to the larger mean free of path photons, see Figure 2. 11(a). In the soft X-ray range (E < 1KeV), the transmission experiments are difficult because of the thickness effect or the short attenuation length (or a large lineal absorption coefficient), implying than the samples have to be extremely thin. For the same reason, soft-photons have a large absorption cross-section in air; hence the experiments have to be performed under very good vacuum conditions. In these cases, other detection modes than transmission are preferred like the total-electron yield (TEY) or fluorescence yield (FY). Both detection methods are related to the decay channels (fluorescence or Auger decay) that may fill the electronic vacancy or core-hole in the excited atom. Thus, one of the most probable channels becomes when 2*p* electrons decay filling the 1*s* core hole [Figure 2. 11(b)]. The decay of the core-hole gives rise to an avalanche of electrons, photons, and ions escaping from the surface of the sample. In the case of the photons created in the fluorescent decay excludes any surface effect. On the other hand, in the TEY method, all the electrons that emerge from the sample surface are detected, regardless of their energy. Unlike the FY, the interaction of electrons with matter is much larger than that of X-rays, which implies that most of the electrons that escape from the surface are originated close to it (the range lays from 3 to10 nm) [5].

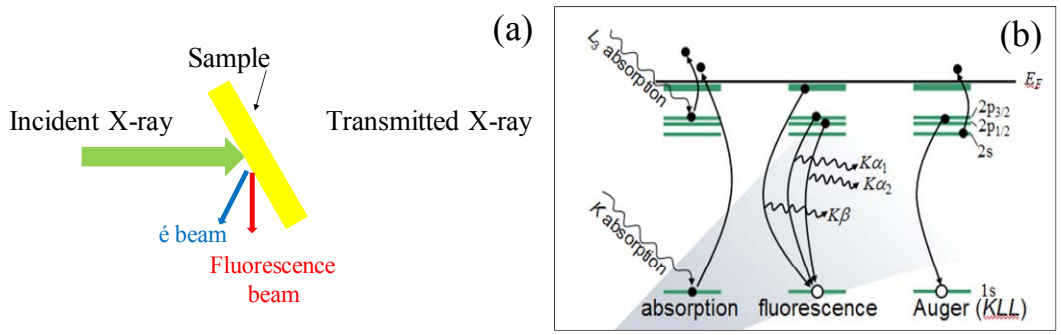

Figure 2. 11. Schematic diagram of the absorption process and possible decay channels following it.

2.5.2. X-ray magnetic circular dichroism

The basis of the X-ray magnetic circular dichroism (XMCD) spectroscopy is ascribed to the use of polarized photons in the absorption process which is proportional to the probability of electronic transitions into empty states. This allows us to measure the intensity difference between the number of spin-up and spin-down holes in a magnetic material [18, 19]. From an experimental point of view the XMCD is the difference spectrum of two X-ray absorption spectra taken in a magnetic field, one applying left circularly polarized light (positive helicity, $+\hbar$), and one with right circularly polarized light (negative helicity, $-\hbar$). The close analysis of the XMCD spectrum provides quantitative information on the magnetic properties of a ferromagnetic (or ferrimagnetic) material, such as its spin and orbital magnetic moment.

The basic principle of the XMCD can be explained with the two-step model illustrated in Figure 2.12 for 3*d* transitions metals (TM). The illustration uses the band-like model of a ferromagnetic material called the Stoner-model. The two-step model is briefly described below [19, 20]:

(i) *First step*. Creation of spin-polarized photoelectrons in the initial states thanks to the transfer of angular momentum from the incident circularly polarized X-rays: as a consequence of the spin-orbit coupling, the angular momentum is transferred to the electronic spins and the photoelectrons become spin polarized. Since the initial states L_3 ($2p_{3/2}$) and L_2 ($2p_{1/2}$) have opposite spin-orbit coupling (with $j = l + s$ and $j = l - s$, respectively) the spin polarization will be opposite at the two edges.

(ii) *Second step*. The spin-split valence shell (unoccupied final states with unequal spin-up and spin-down populations) acts as a "spin-detector" of the spin-polarized photoelectrons. Due to the magnetization of the system the spin-polarized density of states is different for spin-up and spin-down electrons.

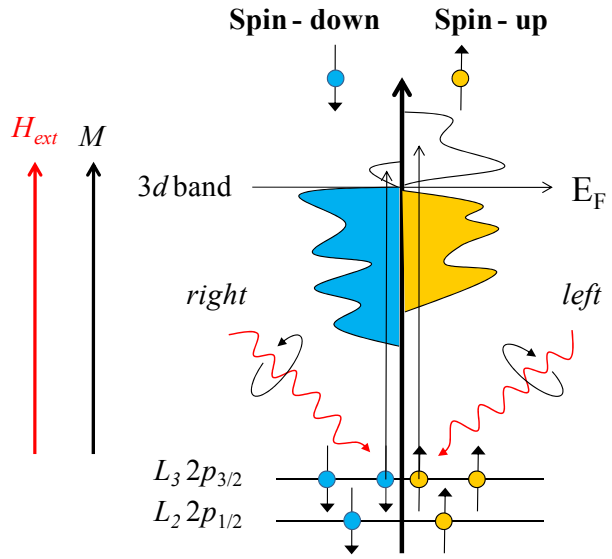

Figure 2. 12. Schematic representation of the XMCD at the $L_{2,3}$ edges for 3*d* transition metals. Filled electron states below the Fermi energy E_F are shown in color; "hole" states above the E_F are shown uncolored. The spin states occupied with the largest number of electrons are called "majority spins". In the first step, the absorption of left (right) circularly polarized light leads to spin-up (spin-down) polarization of photoelectrons via spin-orbit coupling in the core level. In the second step, *d*-valence serve as a "spin-detector" probing the larger number of unoccupied spin-up *d* states with respect to the direction of the external magnetic field H_{ext}.

By convention, the magnetization *M* of the *d* band points in the same direction of the external field H_{ext} and the occupation of the spin-down states (relative to electrons) is larger than that of the spin-up states. The spin states occupied with the largest number of electrons are called "majority spins".

According to the Fermi's Golden rule (Eq. 2.19), the transition probability for photoelectrons is then strongly spin-dependent as well, leading to a difference in absorption of left and right circularly polarized light. Then, the XMCD spectrum can be defined by [16]:

$$I\Delta_{XMCD} = I^{\uparrow\uparrow} - I^{\uparrow\downarrow} = I^{+} - I^{-} \qquad \text{(Eq. 2.20)}$$

where $I^{\uparrow\uparrow}$ ($I^{\uparrow\downarrow}$) denotes the parallel (antiparallel) orientations of the sample magnetization and the incident photon spin. I^{+} and I^{-} are the XAS spectra recorded with right and left circularly polarized X-rays, respectively. It should be noted that another common notation employing the "mass-dependent absorption coefficient" for the right and left polarized light, μ^{+} and μ^{-} can be used, respectively.

However, the convention adopted by the XMCD community is to plot the intensity of the 3*d* transition metals Fe, Co, and Ni according to the definition [19]:

$$I\Delta_{XMCD} = I^{\uparrow\downarrow} - I^{\uparrow\uparrow} = I^{-} - I^{+} \quad \text{(Eq. 2.21)}$$

2.5.2.1. Application of the Sum rules

One of the most important issues in the analysis of the XMCD spectra is the determination of quantitative values of the projected magnetic moments: the orbital moment (L_z) and the effective spin moment (S_{eff}) by applying the sum rules. These rules were originally derived by Thole *et al.* [21] and Carra *et al.* [22] in 1992 for single ions in a crystal field with a partly filled valence shell. In general the sum rules apply to one specific transition. For instance, the transitions from a 2*p* core state to 3*d* valence states as experimentally verified for the Fe and Co 3*d* metals in different reports [23–25].

For the transitions from the initial $2p_{3/2}$ and $2p_{1/2}$ into the 3*d* valence band, the orbital and the effective spin magnetic moments can be determined from the integration of $\mu^+ - \mu^-$ (XMCD spectra) and $\mu^+ + \mu^-$ (XAS spectra). According to the XMCD sum rules, the orbital (m_L) and effective spin magnetic moments (m_S^{eff}) are written as [24]:

$$m_L = -\frac{4\int_{L_3+L_2}(\mu^+ - \mu^-)dE}{3\int_{L_3+L_2}(\mu^+ + \mu^-)dE}(10 - n_{3d}) \quad \text{(Eq. 2.22)}$$

$$m_S^{eff} = -\frac{6\int_{L_3}(\mu^+ - \mu^-)dE - 4\int_{L_3+L_2}(\mu^+ - \mu^-)dE}{\int_{L_3+L_2}(\mu^+ + \mu^-)dE}(10 - n_{3d})\left(1 + \frac{7\langle T_Z\rangle}{2\langle S_Z\rangle}\right)^{-1} \quad \text{(Eq. 2.23)}$$

where $m_L \equiv -\langle L_z\rangle\mu_B/\hbar$ and $m_S \equiv -2\langle S_z\rangle\mu_B/\hbar$ are the projections of the orbital and spin magnetic moment along the X-rays propagation axis (that of the applied magnetic field), respectively, and n_{3d} is the number of occupied 3*d* states in the specific TM atom. $\langle T_z\rangle$ is the expectation value of the magnetic-dipole coupling operator. This operator represents the anisotropy of the spin density when the electronic cloud is distorted, either by the spin-orbit interaction or crystal-field effects. In general, the orbital and spin magnetic moments are given in units of μ_B/atom.

Concerning the magnetic-dipole operator, Carra *et al.* [22] claimed that T_z could be neglected in octahedral symmetry. Their calculations showed that the effect of the T_z-term is limited up to 15% of the S_z-value. In addition, later Crocombette *et al.* [26] also claimed that at room temperature the T_z values are generally very small and can be neglected. So, in our subsequent XMCD analysis this term is disregarded, and we will consider $m_S^{eff} = m_S$.

In Figure 2. 13 we display an example of $L_{2,3}$ XAS and XMCD spectra. From the XAS spectra, the $I^- - I^+$ [XMCD spectra, Figure 2. 13(b)] and $I^+ + I^-$ [XAS spectra, Figure 2. 13(c)] are determined. To apply the sum rules on the measured data, the atomic $L_{2,3}$ absorption edges jumps [the bottom dotted line in Figure 2. 13(c)] must be subtracted. In this case, we applied the following two-step function [24, 25]:

$$s = \frac{h}{3}\left[1 + \frac{2}{\pi} arctan\left(\frac{E - E_{L_3}}{\Delta E}\right)\right] + \frac{h}{6}\left[1 + \frac{2}{\pi} arctan\left(\frac{E - E_{L_2}}{\Delta E}\right)\right] \qquad \text{(Eq. 2.24)}$$

where h is the height of the $L_3(L_2)$ step, normally set to 2/3(1/3) of the average intensity at high energy end of the spectrum, and ΔE denotes the energy broadening of the edges at E_{L_3} and E_{L_2}, in this case set to 0.25 eV. We used the $2p_{3/2,1/2}$ binding energies determined by X-ray Photoelectron Spectroscopy (XPS), which here are 777.90 and 792.95 eV for the L_3 and L_3 ionization thresholds, respectively [27].

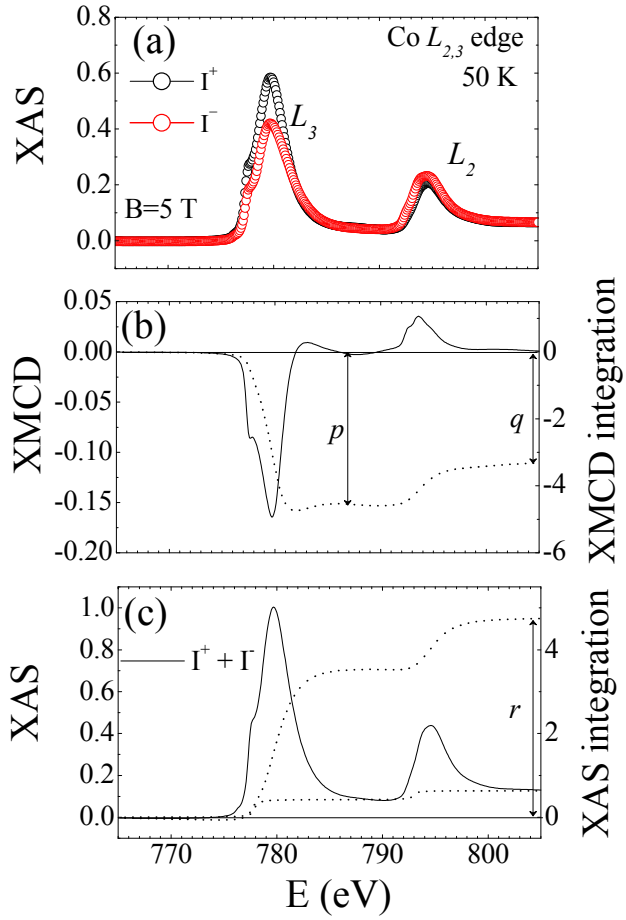

Figure 2. 13. Co $2p \rightarrow 3d$ XAS-XMCD spectra for $Pr_{0.50}Sr_{0.50}CoO_3$ measured at 50 K.

Following the notation used in Figure 2. 13, the sum rules can be also written as:

$$m_L = -\frac{4q}{3r}(10 - n_{3d}) \quad \text{(Eq. 2.25)}$$

$$m_S = -\frac{6p-4q}{3}(10 - n_{3d}) \quad \text{(Eq. 2.26)}$$

where q is the XMCD integration of the $L_{2,3}$ edges, p is the XMCD integration of the L_3 edge only, n_{3d} is the 3d electron occupation number, and r is the XAS integration at the $L_{2,3}$ edges.

It has been experimentally found that there are some limitations when using the sum rules and not always the quantitative values of $\langle S_z \rangle$ and $\langle L_z \rangle$ deduced from the XCMD experiments are correct. A detailed analysis can be found in the book written by Frank de Groot and Akio Kotani, "*Core Level Spectroscopy of Solids*" [16]. Nevertheless, we can cite that the necessary conditions for the applicability of the XMCD sum rules are: (i) L_3 and L_2 edges need to be fully separated from each other reflecting that the 2p spin-orbit coupling is larger than the Coulomb interaction in order to determine the independent integrations, (ii) an accurate knowledge of the number of 3d holes is needed, or (iii) the $\langle T_z \rangle$ operator should be known, not always the approximation that it is zero is valid.

2.5.3. X-ray emission

X-ray emission spectroscopy (XES) is a complementary technique to XAS to probe the electronic structure of atoms in the valence band. In this section we detail the main features of this technique and the procedure of data analysis that permits to quantify the effective spin state in the compounds presented along the manuscript.

The principal difference between XAS (first-order process) and XES (second-order process) is that the first one probes the density of unoccupied states in the valence band, while and the latter probes the density of occupied states, in particular the effective number of unpaired 3d electrons (the effective spin). The first step in the emission process is the same as for XAS measurements, namely the creation of an excited state through the interaction of a photon with a core-electron, and then this excited state decays to fill the core-hole via fluorescence as Figure 2. 14(a) displays. The quantity of emitted photons is measured as a function of the incident photons energy and gives rise to a fluorescence X-ray emission spectrum [see Figure 2. 14(b)]. The strongest K (i.e. for a 1s core-hole) fluorescence lines result from $2p \rightarrow 1s$ transitions ($K\alpha$ lines) while the $3p \rightarrow 1s$ ($K\beta$ lines) ones are about eight times weaker. However, the 2p orbitals are energetically and spatially isolated from the valence orbitals and so, despite the large amplitude of $K\alpha$ lines, these transitions are less sensitive to the

chemical changes and the probed atoms spin state. X. Wang *et al.* [28] reported in 1997 by theoretical and experimental comparison that the $K\beta$ spectral shape is more sensitive to electronic changes from a high-spin to a low-spin configuration than $K\alpha$ lines. Thus, the average spin of a given transition metal could be determined from the shape and position of its $K\beta$ emission lines [29].

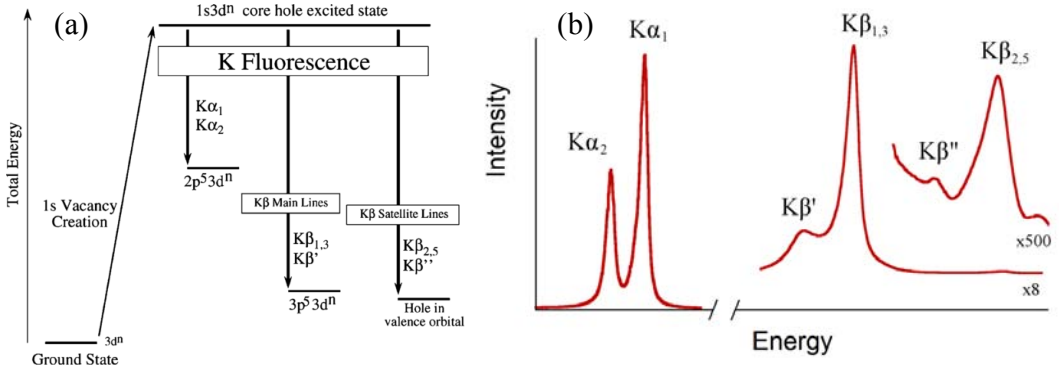

Figure 2. 14. (a) Energy diagram of the different decay channels of the *K* fluorescence emission. (b) An example of $K\alpha$ and $K\beta$ emission lines spectra measured in MnO. Pictures are extracted from Ref. [29].

For a quantitative analysis of $K\beta$ emission spectra in the different studied compounds we have employed the integral of the absolute value of the difference spectrum (IAD) method. This procedure is a useful tool to directly determine the effective spin of any compound. However, this approach presents some limitations and it is only effective when used with suitable reference samples with similar local structure where the spin state is known or the analyzed samples are measured under similar conditions (resolution, background, source size, and so on). As we will show this procedure has been tested in the determination of the spin state of different compounds such as $LaCoO_3$, $LaMn_{(1-x)}CoO_3$, and $Pr_{0.50}Ca_{0.50}CoO_3$ with excellent results. [30–32].

In Chapter 4, we also present the analysis of the $K\alpha$ lines for the determination of the SS in $Pr_{0.50}Sr_{0.50}CoO_3$ applying the so-called Van Vleck's theorem to compare with the results obtained from $K\beta$ lines. This theorem proposes that the characteristic energy splitting (or line width) in the $K\alpha_1$ emission line is directly proportional to the number of unpaired 3*d* electrons total spin in the 3*d* orbitals according to the equation [30, 33]:

$$\Delta E = J(2S + 1) \qquad \text{(Eq. 2.27)}$$

where *J* is the exchange interaction energy between the 1*s* core hole and 3*d* valence band.

Although, a good applicability for this theorem was experimentally found in some specific compounds [28, 30, 33, 34], in other cases [33, 34], it presents limitations and so it is not suitable for: (i) highly correlates oxides, (ii) high-spin TM compounds, or (iii) systems with very different atomic environment.

2.5.4. Instrumentation

As already commented, the analysis of the electronic configuration of the different materials studied in this thesis has been done by means of XAS, XMCD, and XES experiments. These were performed in the BL29-BOREAS beamline or BL22-CLÆSS beamline at the ALBA Synchrotron Light Facility, ID26 beamline at the ESRF, or the SuperXAS-X10DA beamline of the Swiss Light Source (SLS) (Villigen, Switzerland).
Here, we provide a brief description of some of these beamlines.

2.5.4.1. BL29-BOREAS beamline (ALBA)

BL29 is a soft X-ray beamline devoted to polarization-dependent spectroscopic studies of advanced materials, particularly those composed of 3*d* and 4*d* metals, and rare earths. The X-rays are produced by an elliptical undulator which provides a high flux in a wide energy range (~10^{12} photons/s at 700 eV), high energy resolution (ΔE ~ 50-100 meV) and highly polarized light. The monochromator is based on three "variable line spacing" gratings, allowing to achieve energies in the 80 eV to 4000 eV range. The typical beam spot size ranges from 100 μm-1 mm (horizontal) x 80 μm-1 mm (vertical) thanks to its vertical and horizontal refocusing mirrors system with adjustable in-situ mirror benders. These two bendable mirrors are arranged in a Kirkpatrick-Baez (KB) geometry, where the first mirror is vertically focusing and the second one is horizontally focusing [35]. In Figure 2. 15 the main optical components of the beamline downstream the optics hutch are shown.

This beamline present two end-stations:

(i) a high field vector magnet (HECTOR) for soft-XAS and XMCD or XMLD techniques;

(ii) a UHV reflectometer (MARES) for scattering and reflection approaches including resonant soft-X-ray reflectivity, resonant magnetic scattering, and GISAXS.

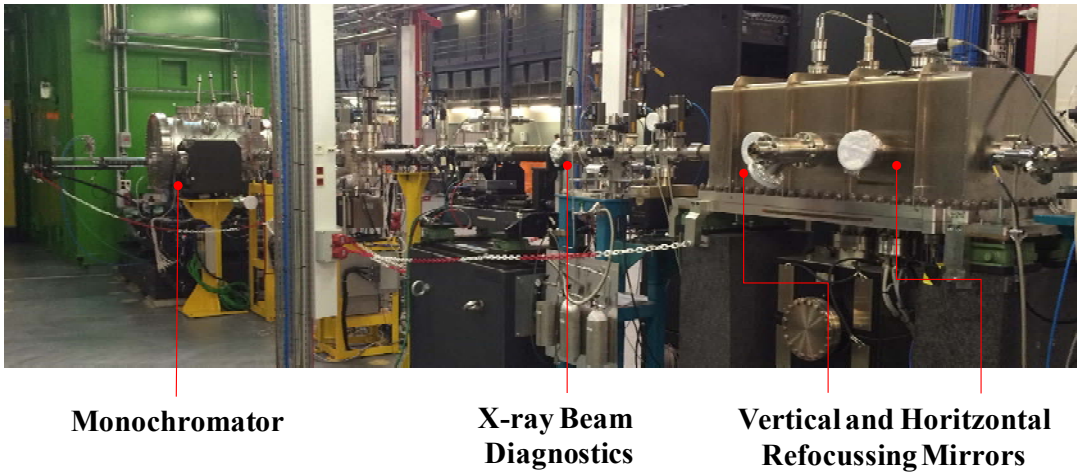

Figure 2. 15. Picture showing some of the principal optical components of BL29-BOREAS located "upstream" the end-stations.

In our case we focus on the HECTOR end-station, where all the experiments have been performed. This end-station consists of three orthogonal pairs of superconducting coils that can produce magnetic fields up to 6 T in the horizontal plane along the beam direction (2 T in any other direction). The system counts on three chambers for storage and sample preparation, all operating high-to-ultra-high vacuum conditions (UHV, $P \leq 10^{-9}$ mbar) [35] as Figure 2. 16 shows: (i) the load-lock chamber, (ii) the buffer chamber, and (iii) the preparation chamber. The first one allows to introduce/change samples at ambient pressure and to reach a good vacuum in a few minutes. The buffer chamber is a transition chamber between the load-lock and the preparation chamber where UHV conditions are mandatory. Finally, the preparation chamber presents a complete range of sample preparation tools such as: a cleaver, a scraper, evaporators for metals and organic molecules, a heating stage or even, an ion sputtering gun.

The beamline is prepared to perform experiments with variable temperatures between 2 K and 350 K using a liquid He cryostat. Samples in bulk, thin film, or powder form are accepted.

The samples in our experiments were mounted on a sample holder made of copper, gold coated, suitable for low temperature measurements [Figure 2. 16(c)]. Firstly, the bulk samples (3 or 4 per sample holder) were fixed onto Aluminum plates with Torr Seal (a strong epoxy) and coated with a graphite solution to warrant the electrical conductivity of the assembly. Then, most of the samples were in-situ cleaved or scraped to allow the study of fresh, non oxidized surfaces. During the experiments the flux and the beam exposure were controlled in order to minimize the samples degradation by photoreduction of Co ions.

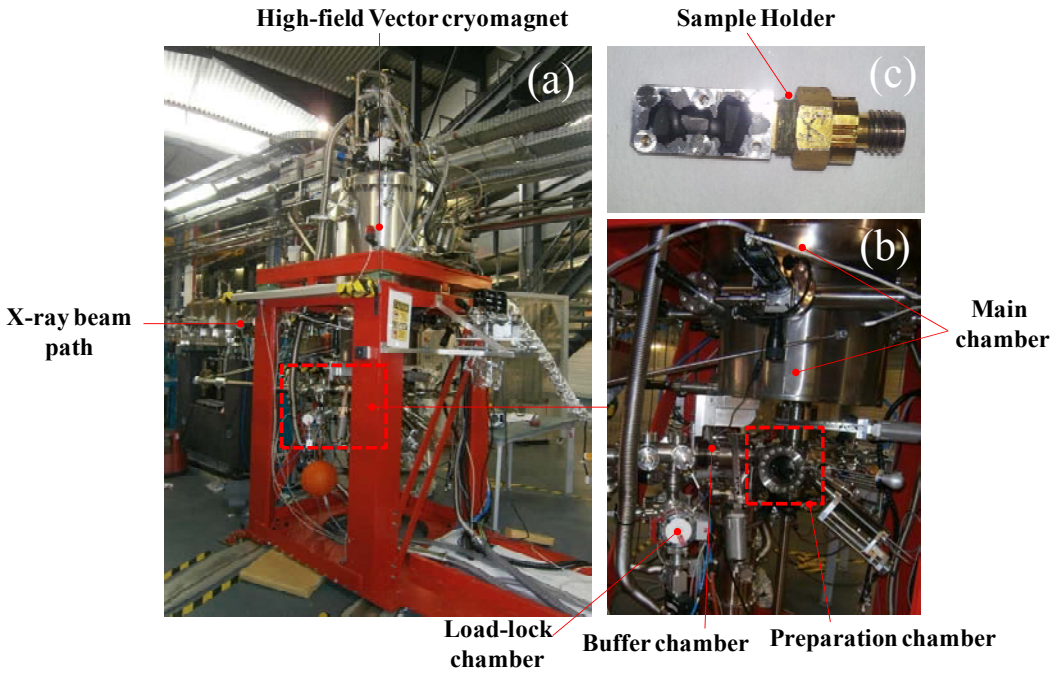

Figure 2. 16. XMCD endstation in BL29-BOREAS at the ALBA Synchrotron light source. (a) General view; (b) view of the preparation and storage chambers (load-lock, buffer, and preparation chamber); (c) Sample holder.

2.5.4.2. SuperXAS-X10DA (SLS)

SuperXAS is a dedicated beamline for time resolved X-ray absorption and X-ray emission spectroscopy. The X-rays source in this beamline is a bending magnet which provides a flux on the sample of about 10^{12} photons/s. The optics are composed by a system of two mirrors, the first one being spherical for vertical collimation and the second one a toroidal one (for vertical and horitzontal collimation). The double crystal monochromator consists of two sets of Silicon crystals, Si (111) and Si(311). The Si(111) allows to access low energies (E < 4.5 eV) and the Si (311) allows reaching E > 35 KeV. The spot size ranges from 100 x 100 μm^2 to 5 x 0.5 mm^2. The $K\alpha$ emission lines and the HERFD-XANES were acquired in the Johann-type high energy resolution X-ray emission spectrometer [see Figure 2. 17(a)]. The central components of the emission spectrometer are the Bragg crystals that spectrally analyze the fluorescence from the sample and reflects it onto the photon detector, being both in a Rowland geometry as Figure 2. 17(b) shows.

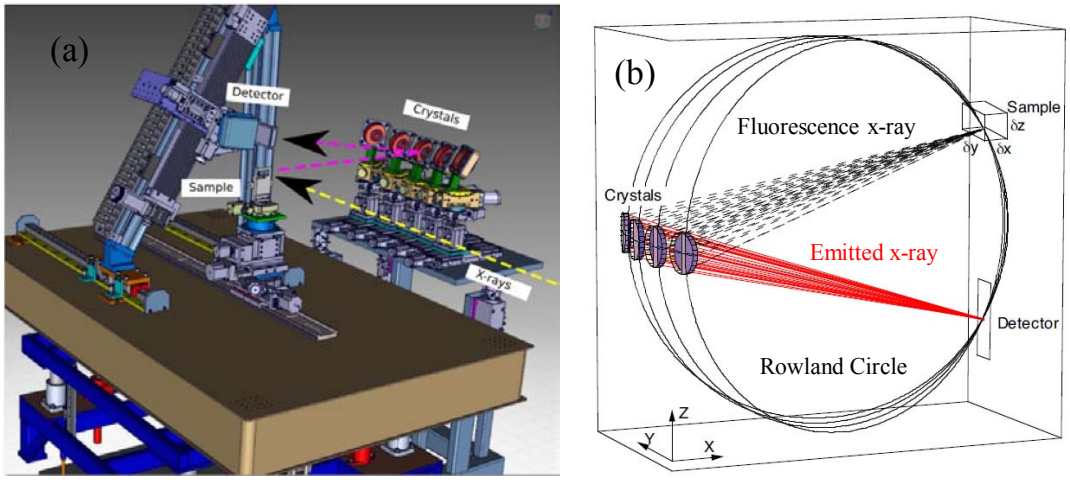

Figure 2. 17. (a) Layout of the Johann-type high energy resolution X-ray emission spectrometer from SuperXAS-X10DA extracted from Ref. [36]. (b) Example of a crystal array spectrometer with four analyzer crystals and the detector in a Rowland geometry. The Rowland circle is shown for each crystal. Figure extracted from Ref. [37].

In general, the data are recorded in normal symmetry $\theta_o = \theta_f$, but in our measurements we used an asymmetric configuration ($\theta_o \neq \theta_f$) because of technical limitations found (potential collision between the detector and the cryostat) to reach the needed angles for measuring the Co $K\beta$ emission lines. Moreover, the required detector and cryostat positions for Co $K\beta$ emission were out of range so that only the $K\alpha$ emission lines were recorded. In addition we measured HERFD-XANES spectra at the Co *K*-edge. The principal difference between both kinds of measurements is that, contrarily to HERFD-XANES, for XES measurements the crystal analyzer is not in a fixed position. Besides the Co *K*-edge, the Pr $L_{2,3}$ edges were also studied. In this case, a different set of crystal analyzers was used. For the Co measurements a Si(531) crystal was employed, while for the Pr measurements we employed a Ge(331) crystal. Figure 2. 18(a) shows a real picture of the Johann-type spectrometer in SuperXAS-X10DA beamline and an inner view of the UHV chamber were the sample holder was mounted [see Figure 2. 18(b),(c)]. A He gas bag was used to reduce the scattering and absorption of emitted X-rays by air.

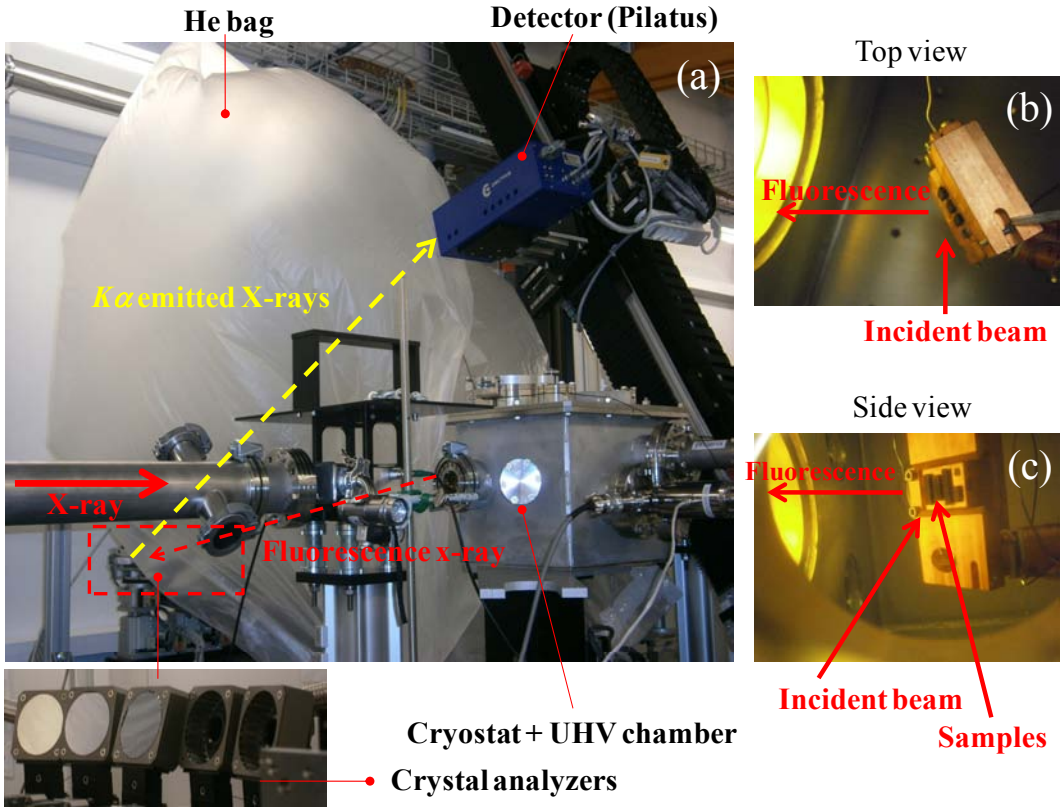

Figure 2. 18. (a) Johann-type spectrometer in SuperXAS-X10DA (SLS); (b) top and (c) side view of the UHV chamber where the sample holder was mounted with 5 samples simultaneously measured.

2.5.4.3. ID26 beamline (ESRF)

ID26 is a beamline also dedicated to the X-ray emission spectroscopy. The X-rays source in this beamline is an insertion device consisting of three mechanically independent undulators which provide a flux on the sample of about 10^{13} photons/s. The double crystal monochromator consist of two sets of Silicon crystals, Si (111) and Si(311) and it covers an energy range from 2.4 to 30 keV. The emission spectrometer uses five spherically-bent analyzer crystals with an energy resolution $\Delta E/E < 0.0001$ between 4.5 to 17 keV. A continuous He-flow cryostat can be disposed to carry out low temperature measurements

In this beamline the $K\beta$ emission lines and the HERFD-XANES spectra of $PrCoO_3$, $Pr_{0.50}Ca_{0.50}CoO_3$, $Pr_{0.50}Sr_{0.50}CoO_3$, $LnBaCo_2O_{5.50}$ (*Ln*=Pr, Gd, and Y), and $Ba_2Co_9O_{14}$ at the Co *K*-edge were collected with the support of the Dr. Sara Lafuerza. The incident energy was tuned through the Co *K*-edge by means of a pair of cryogenically cooled Si(311) monochromator crystals. A rejection of higher harmonics was achieved by three Si mirrors working under total

reflection. A metallic Co foil reference was used to calibrate the monochromator energy by setting the first inflection point of the Co *K*-edge at 7709 eV. The inelastically scattered photons were analyzed using a set of four spherically bent Ge(444) crystals that were arranged with the sample and photon detector (avalanche photodiode) in a vertical Rowland geometry (*R* = 1 m) at 90º scattering angle. The crystals were covered with masks to improve resolution. The total experimental broadening, determined as the average of the full width at half maximum of the elastic profiles, was about 0.4 eV.

2.5.5. Charge-transfer multiplet calculations

Along this thesis we will also present an analysis of the XAS spectra from a theoretical point of view. The procedure used to calculate the TM $L_{2,3}$ and the RE $M_{4,5}$ X-ray absorption spectra for the different compounds is the charge transfer multiplet (CTM) theory [16, 38]. For this, we employed the CTM4XAS program [39] by Frank de Groot and Eli Stavitski (Utrecht University), which is based on the Cowan code [40]. In this section the main aspects of the CTM approach will be prsented, but more details are given in the book on *"Core Level Spectroscopies of Solids"* written by Frank de Groot and Akio Kotani [16].

In most of the cases the description of XAS can be done using the single excitation approach. However, this theory usually fails for strongly correlated systems, such as RE systems and TM compounds. This is due to the presence of charge-transfer and intra-atomic multiplet coupling effects. In fact, the latter can be very large in TM-based compounds owing to the strong overlap of the 2*p* and 3*d* wave functions of the final states. It is for this, that the CTM theory was developed taking into account the charge-transfer and multiplet effects.

Before introducing the CTM theory, we are going to briefly describe the previous models used to describe the atomic structure: the atomic multiplet theory and the ligand-field multiplet theory.

The atomic multiplet theory is the description of the atomic structure using quantum mechanics. So, the total Hamiltonian in an atom where more than one electron is present is given by:

$$H_{atom} = \sum_N \frac{p_i^2}{2m} + \sum_N \frac{-Ze^2}{r_i} + \sum_{pairs} \frac{e^2}{r_{ij}} + \sum_N \zeta(r_i) l_i \cdot s_i \qquad \text{(Eq. 2.28)}$$

where the first term corresponds to the kinetic energy, the second one to the nuclear energy, the third one to the electron-electron interaction, and the last one to the spin-orbit coupling.

However, the atomic multiplet theory does not reproduce well enough the experimental data. Another term should be also taken into account. This is the crystal field, and the new model the ligand-field multiplet theory. This model approximates the TM to an isolated atom surrounded by a distribution of charges that should mimic the actual solid. Thus, the new Hamiltonian is now described as:

$$H_{LFM} = H_{atom} + H_{CF} \qquad \text{(Eq. 2.29)}$$

where $H_{CF} = -e\phi(r)$ and ϕ(r) is the potential that describes the surroundings.

These two models use single configurations to describe the ground state and the excited state, but for a real description in solids the effects of charge fluctuations in the initial and final states (charge transfer effects) must also be present. This is the reason why the charge transfer multiplet theory was developed. The charge transfer effects can be described by the combination of different ground state and final state configurations. In the case of TM oxides, the main charge transfer channel is the transition of a $3d^N$ configuration into a $3d^{N+1}\underline{L}$ configuration, where the ligand electron is transferred to the metal site and a ligand hole $\underline{L}$ is created.

In the case of the CTM theory, the charge transfer effects and the atomic multiplet coupling effect are taken into account for each configuration. For instance, the ground state of a $3d^N$ TM compound can be expressed by mixing $3d^N$ and $3d^{N+1}\underline{L}$ states. Then, the $2p^5 3d^{N+1}$ and $2p^5 3d^{N+2}\underline{L}$ excited states are also mixed, resulting in a more complex fine structure of the XAS spectra. A schematic diagram of the process can be seen in Figure 2. 19.

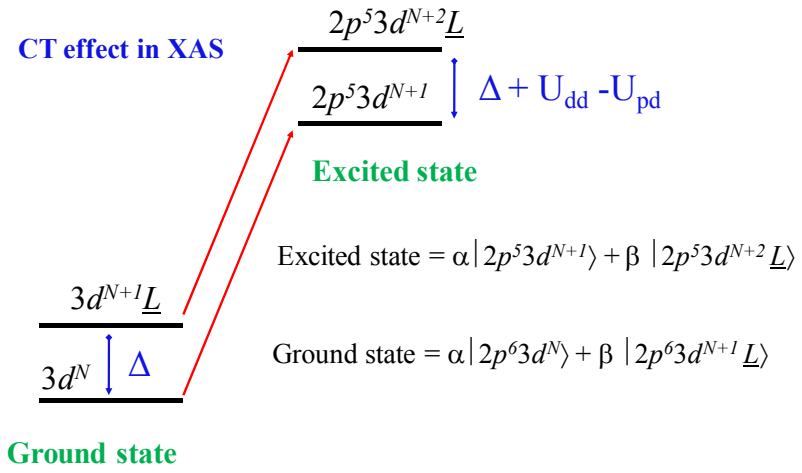

Figure 2. 19. Schematic energy diagram of the charge transfer effect for a $3d^N$ TM compound in a XAS process.

The CTM4XAS program is based on this CTM approach and allows to calculate the energies of atomic-like configurations for initial and final states. The program is capable to calculate the 1*s*, 2*p* and 3*p* XAS spectra plus the XMCD spectra for TM and RE compounds, the 1*s*, 2*s*, 3*s*, 2*p* and 3*p* XPS spectra and the 1s2*p* and 1*s*3*p* XES. Here, we define the principal parameters used in the CTM calculations in this manuscript and the value of each parameter will be given in the detailed analysis of the XAS spectra in each particular chapter. The main parameters apart from the selection of the symmetry of the system are:

(i) 10Dq: the crystal field, which measures the energy differences between the t_{2g} states and the e_g states in an octahedral (O_h) symmetry;

(ii) Δ: the charge transfer energy, which measures the energy difference between $3d^N$ and $3d^{N+1}\underline{L}$ states;

(iii) U_{dd}: the Hubbard U value, which accounts for the Coulomb repulsion energy between two 3*d* electrons;

(iv) U_{pd}: the core-hole potential, which measures the energy difference between a 3*d* electron and a 2*p* core-hole. Only the $U_{pd} - U_{dd}$ energy difference is important;

(v) F_{dd}, F_{pd} and G_{pd}: the Slater's integrals, which measures the exchange interaction between two pair of electrons.

The selection of the symmetries in the program is limited to octahedral (O_h), tetragonal (D_{4h}), four-fold symmetry (C_4) or tetrahedral (T_d), which is realized by choosing O_h symmetry with negative $10D_q$. The reason for this is that in a tetrahedral symmetry the triplet (d_{xz}, d_{xy}, d_{yz}) is higher in energy than the doublet ($d_{x^2-y^2}$ and d_{z^2}) while the opposite holds in O_h symmetry. In the ligand field model an atom with a single *d* electron in the field of negatively charged ligands (O^{2-}), it is expected that the orbitals of the atom pointing toward the ligand positions are higher in energy than the ones avoiding the ligand positions. In a O_h symmetry the doublets point directly to the ligand positions and are therefore higher in energy because of electrostatic repulsion effects. In T_d symmetry the ligands lay along the body diagonals of a cube, so that the triplet points toward the center or the edges and therefore these states are higher in energy [19].

In the case of XMCD calculations, the C_4 symmetry is chosen and an extra parameter is selected for the simulation, the Zeeman Splitting (M) with value 10 meV. For more information about other parameters used in the program see Ref. [39].

BIBLIOGRAPHY

[1] A. Maignan, C. Martin, D. Pelloquin, N. Nguyen, and B. Raveau, "Structural and Magnetic Studies of Ordered Oxygen-Deficient Perovskites *Ln*$BaCo_2O_{5+\delta}$, Closely Related to the '112' Structure," *J. Solid State Chem.*, vol. 142, pp. 247–260, 1999.

[2] A. Podlesnyak, K. Conder, E. Pomjakushina, and A. Mirmelstein, "ChemInform Abstract: Layered Cobalt Perovskites: Current Topics and Future Promises," *ChemInform*, vol. 39, no. 40, Sep. 2008.

[3] E. Lesley and A. Elaine, *Solid state chemistry□: An introduction*. New York: CRC press, 2012.

[4] S. M. Koohpayeh, D. Fort, and J. S. Abell, "The optical floating zone technique: A review of experimental procedures with special reference to oxides," *Prog. Cryst. Growth Charact. Mater.*, vol. 54, no. 3–4, pp. 121–137, 2008.

[5] J. Baruchel, J. L. Hodeau, M. S. Lehmann, J. R. Regnard, and C. Schlenker, *Neutron and synchrotron radiation for condensed matter studies. Volume I: theory, instruments and methods.*, Hercules c. EDP Sciences- Springer- Verlag, 1993.

[6] T. Chatterji, *Neutron Scatering from Magnetic materials*. Elsevier, 2007.

[7] A. . Wills, "A new protocol for the determination of magnetic structures using simulated annealing and representational analysis (SARAh)," *Phys. B Condens. Matter*, vol. 276–278, pp. 680–681, 2000.

[8] J. Rodríguez-Carvajal, "Recent advances in magnetic structure determination by neutron powder diffraction," *Phys. B Condens. Matter*, vol. 192, pp. 55–69, 1993.

[9] V. Esteve, *El método de Rietveld*. 2006, p. (Colecció ciències experimentals num.9).

[10] G. Will, *Powder Diffraction: The Rietveld Method and the Two-stage method*. Springer, 2006.

[11] "ESRF web page." [Online]. Available: http://www.esrf.eu/id22.

[12] "ILL web page." [Online]. Available: http://www.ill.eu/instruments-support/instruments-groups/instruments/d20.

[13] “ILL web page.” [Online]. Available: https://www.ill.eu/.

[14] J. E. Penner-Hahn, “X-ray Absorption Spectroscopy,” in *Comprehensive Coordination Chemistry II*, Elsevier, 1998, pp. 159–186.

[15] J. Yano and V. K. Yachandra, “X-ray absorption spectroscopy,” *Photosynth. Res.*, vol. 102, pp. 241–254, 2009.

[16] F. De Groot and A. Kotani, "*Core level spectroscopy of solids"*. 2008.

[17] F. Hippert, E. Geissler, J. L. Hodeau, E. Lelièvre-Berna, and J.-R. Regnanrd, *Neutron and X-ray spectroscopy*. Springer Sciences & Bussines, 2006.

[18] G. Schütz, W. Wagner, W. Wilhelm, P. Kienle, R. Zeller, R. Frahm, and G. Materlik, “Absorption of Circularly Polarized X-Rays in Iron,” *Phys. Rev. Lett.*, vol. 58, no. 7, pp. 737–740, 1987.

[19] J. Störh and H. C. Siehmann, *Magnetism: from fundamentas to nanoscale dynamics*. Springer, 2006.

[20] J. Stöhr, “Exploring the microscopic origin of magnetic anisotropies with X-ray magnetic circular dichroism (XMCD) spectroscopy,” *J. Magn. Magn. Mater.*, vol. 200, pp. 470–497, 1999.

[21] B. T. Thole, P. Carra, F. Sette, and G. Van Der Laan, “X-ray circular dichroism as a probe of orbital magnetization,” *Phys. Rev. Lett.*, vol. 68, no. 12, pp. 1943–1946, 1992.

[22] P. Carra, B. T. Thole, M. Altarelli, and X. D. Wang, “X-ray magnetic circular and local magnetic fields,” *Phys. Rev. Lett.*, vol. 70, no. 694, 1993.

[23] G. Y. Guo and H. Ebert, “First-principles calculation of magentic x-ray dichroism in Fe and Co multilayers,” *Phys. Rev. B*, vol. 50, no. 6, 1994.

[24] C. T. Chen, Y. U. Idzerda, H.-J. Lin, N. V. Smith, G. Meigs, E. Chaban, G. H. Ho, E. Pellegrin, and F. Sette, “Experimental confirmation fot he X-ray Magentic Circular Dicrhoism,” *Phys. Rev. Lett.*, vol. 75, no. 1, 1995.

[25] H. Elmers, G. Fecher, D. Valdaitsev, S. Nepijko, a. Gloskovskii, G. Jakob, G. Schönhense, S. Wurmehl, T. Block, C. Felser, P.-C. Hsu, W.-L. Tsai, and S. Cramm, “Element-specific magnetic moments from core-absorption magnetic circular dichroism of the doped Heusler alloy $Co_2Cr_{0.6}Fe_{0.4}Al$,” *Phys. Rev. B*, vol. 67, no.104412, 2003.

[26] J. P. Crocombette, B. T. Thole, and F. Jollet, “The importance of the magnetic dipole term in magneto-circular x-ray absorption dichroism for 3*d* transition metal compounds,” *J. Phys. Condens. Matter*, vol. 8, pp. 4095–4105, 1996.

[27] “Data base XPS.” [Online]. Available: http://srdata.nist.gov/xps/ .

[28] X. Wang, F. de Groot, and S. Cramer, “Spin-polarized x-ray emission of 3*d* transition-metal ions: A comparison via *K*β and *K*α detection,” *Phys. Rev. B*, vol. 56, no. 8, pp. 4553–4564, 1997.

[29] P. Glatzel and U. Bergmann, “High resolution 1s core hole X-ray spectroscopy in 3*d* transition metal complexes - Electronic and structural information,” *Coord. Chem. Rev.*, vol. 249, pp. 65–95, 2005.

[30] G. Vankó, T. Neisius, G. Molnár, F. Renz, S. Kárpáti, A. Shukla, and F. M. F. De Groot, “Probing the 3D spin momentum with X-ray emission spectroscopy: The case of molecular-spin transitions,” *J. Phys. Chem. B*, vol. 110, pp. 11647–11653, 2006.

[31] M. Sikora, K. Knizek, C. Kapusta, and P. Glatzel, “Evolution of charge and spin state of transition metals in the $LaMn_{(1-x)}Co_xO_3$ perovskite series,” *J. Appl. Phys.*, vol. 103, no. 07C907, 2008.

[32] J. Herrero-Martín, J. L. García-Muñoz, K. Kvashnina, E. Gallo, G. Subías, J. a. Alonso, and a. J. Barón-González, “Spin-state transition in $Pr_{0.5}Ca_{0.5}CoO_3$ analyzed by X-ray absorption and emission spectroscopies,” *Phys. Rev. B - Condens. Matter Mater. Phys.*, vol. 86, no. 125106, pp. 1–6, 2012.

[33] J. Kawai, C. Suzuki, H. Adachi, T. Konishi, and Y. Gohshi, “Charge-tranfer effect on the linewith of Fe *K*-alpha X-ray fluorescence spectra,” *Phys. Rev. B*, vol. 50, no. 16, 1994.

[34] C. Suzuki, J. Kawai, J. Tanizawa, H. Adachi, S. Kawasaki, M. Takano, and T. Mukoyama, “Local spin moment of $LaCoO_3$ probed by a core hole,” *Chem. Phys.*, vol. 241, pp. 17–27, 1999.

[35] “BL29-BOREAS beamline web page.” [Online]. Available: https://www.cells.es/en/beamlines/bl29-boreas.

[36] “SuperXAS-X10DA beamline web page.” [Online]. Available: https://www.psi.ch/sls/superxas/.

[37] Thesis, P. Glatzel, “X-Ray Fluorescence Emission Following *K* Capture and 1*s* Photoionization of Mn and Fe in Various Chemical” 2001.

[38] H. Ikeno, F. M. F. de Groot, E. Stavitski, and I. Tanaka, “Multiplet calculations of $L_{2,3}$ X-ray absorption near-edge structures for 3*d* transition-metal compounds,” *J. Phys. Condens. Matter*, vol. 21, p. 104208, 2009.

[39] E. Stavitski and F. M. F. de Groot, “The CTM4XAS program for EELS and XAS spectral shape analysis of transition metal *L* edges,” *Micron*, vol. 41, no. 7, pp. 687–694, 2010.

[40] R. D. Cowan, *The theory of Atomic structure and Spectra*, 1981st ed. Berkeley, CA: University of California, 1981.

Chapter 3

Spin-state crossover in lanthanide *Ln*CoO_3 cobaltites: $PrCoO_3$ versus $ErCoO_3$

3.1. Motivation

Transition metal oxides have been investigated in the last 50 years due to their wide range of interesting and functional physical properties that they can present such as high-temperature superconductivity in layered cuprates ($YBa_2Cu_3O_{6+\delta}$) or the colossal magnetoresistance (CMR) in $Ln_{1-x}A_xMnO_3$ (*Ln*= lanthanide and *A*= alkaline earth) manganites. Since then, a huge number of theoretical and experimental studies have been carried out to clarify the nature of strongly correlated phenomena in this type of oxides [1–4]. At the same time, the interest in other perovskite-structured oxides of 3*d* metals such as cobalt in the field of strongly correlated systems has extraordinarily increased during the last years. In cobaltites, in addition to the charge, lattice, and orbital degrees of freedom, Co ions show an unusual ability to present different spin-states. These features have led to search and find attractive new properties in cobalt oxides, including superconductivity, giant magnetoresistance, metal-insulator transitions (MIT), charge and orbital-ordering, competition of antiferromagnetic and ferromagnetic exchanges, thermoelectric response, and so on [5–7]. So, cobaltites have gained an enormous interest for practical applications as materials for solid oxide fuel cells, oxygen membranes, catalyst systems, gas sensors, thermoelectric devices, or as materials for Spintronics [8–12].

The best studied family of cobaltites is that comprising compounds with the general formula LnCoO$_3$, where Ln stands for lanthanum, yttrium, or a lanthanide. One of the reference examples in this family is the rhombohedral perovskite LaCoO$_3$ with *R-3c* (no. 167) symmetry. Still this system is not fully understood to date, remaining a controversial subject. [1, 13–23]. Despite the hundreds of investigations on LaCoO$_3$, the other members of the LnCoO$_3$ series are still poorly explored and there is no clear image of the electronic and magnetic phase diagrams of these simple cobaltites in the literature. So, owing to the lack of results in the rest of the family, mainly in the heaviest members, it is important to extend the exploratory studies done in LaCoO$_3$ to other members of the family.

In order to fill out the study of the nature of the spin-state (SS) transitions in the LnCoO$_3$ series with $Ln \neq$ La, two different members of the family have been selected with different structure from the reference compound (LaCoO$_3$). The first one is PrCoO$_3$ which is considered a member of the family with moderate distortion, and the second one is ErCoO$_3$, as a highly distorted member. In this work, we have combined the analysis of two different techniques such as X-ray absorption spectroscopy (XAS) and neutron powder diffraction (NPD) to extend our understanding of the electronic effects on the crystal structure evolution in LnCoO$_3$ cobaltites. At the end of the chapter, a general phase diagram for the properties of the LnCoO$_3$ series as a function of rare-earth ions and the progressive increasing of the structural distortion will be presented taking into consideration previous results in the literature and the conclusions obtained in this work.

3.2. Introduction

LaCoO$_3$ (LCO) presents an unusual temperature dependence of the magnetic susceptibility. A broad magnetic transition can be observed in the range T_1 ~ 50-100 K, and a second anomaly is observed in the susceptibility at around T_2 ~ 500 K. In addition, LaCoO$_3$ changes from a semiconductor behavior to a metallic state around T_{MI} ~ 500-600 concomitant with the second magnetic anomaly [24].

One of the first experiments revealing the ground electronic configuration in LCO was reported by Asai *et al.* [23] using polarized neutron scattering. Results show a nonmagnetic state (LS, $S = 0$, $t_{2g}^{\ 6}\ e_g^{\ 0}$) at low temperature and a paramagnetic state above 100 K. Hence, three different states can be indentified in LaCoO$_3$: (i) nonmagnetic dielectric, (ii) paramagnetic dielectric, and (iii) paramagnetic metal.

The two magnetic transitions previously mentioned are interpreted as possible changes in the spin state of the Co^{3+} ion. The high temperature spin-state transition (T_{SS2}) is commonly recognized as a change from a low spin state to a pure high-spin (HS, $S = 2$, $t_{2g}^{4}\, e_g^{2}$) state. This was supported by different experimental results such as resistivity measurements [25], the specific heat [26], or X-ray absorption spectroscopy (XAS) at the Co $L_{2,3}$ and O K edges measured by M. Abbate *et al*. [13]. However, the low temperature spin state transition (T_{SS1}) is still now an open question and it has been the subject of considerable debate. The first magnetic transition corresponds to an increase of the magnetic moment and since the early 1960s to the first half of the 1990s, it was interpreted as a low-spin to high-spin transition or as a mixture of LS and HS state evolving with temperature [23, 24]. A large number of experimental and theoretical investigations of $LaCoO_3$ are in favor of this picture [13, 18–22, 27–29], such as nuclear magnetic resonance (NMR), inelastic neutron scattering, X-ray photoelectron spectroscopy (XPS), XAS or Hartree-Fock calculations [21], or more recently generalized gradient approximation (GGA) + U calculations [22]. One of the studies of the electronic properties of $LaCoO_3$ reported by Yamaguchi *et al.* [30] was interpreted as a transition from a LS to a thermally excited HS state with a spin-gap energy of ~ 30 meV, much smaller than the charge gap energy (~1eV).

A discrepancy with the XAS experiments came from a weak temperature dependence of the pre-edge structure of O 1*s* edge across T_{SS1} [13]. Some initial attempts to reproduce the susceptibility above the first transition required a spin value much lower than 2. So, in contrast to the early studies on the basis of local density approximation (LDA)+U calculations, Korontin *et al*. [14] later suggested an intermediate spin (IS, $S = 1$, $t_{2g}^{5}\, e_g^{1}$) with orbital ordering as excited state for the first magnetic transition and an IS $\rightarrow$ HS transition with the orbital ordering destroyed in the metallic state. This theoretical study proposed a higher stability of the IS state than the HS due to the large effects of hybridization of the Co 3*d* and the O 2*p* orbitals. This interpretation (the LS $\rightarrow$ IS and IS $\rightarrow$ HS transitions) was applied to the results by a number of other theoretical and experimental groups, through cold-neutron elastic and inelastic scattering, electron paramagnetic resonance (EPR), infrared spectroscopy measurements, X-ray emission spectroscopy (XES) and neutron powder diffraction [15–17, 31–35]. One of the main experiments defending a LS $\rightarrow$ IS transition in the first magnetic transition was presented by Phelan *et al.* [16] in 2006. Doing inelastic cold-neutron scattering (INS) on a $LaCoO_3$ single crystal revealed two excitations at ± 0.60 meV coincident with the thermally induced magnetic transition, that were interpreted as magnetic dynamic correlations due to thermally excited intermediate S= 1 spin triplet with a dynamic orbital ordering induced by a dynamic Jahn Teller

(JT) distortion. Previously, this JT distortion was not detected in the first diffraction measurements but some phonon anomalies found in infrared spectroscopy by Yamaguchi *et al.* [34] were ascribed to a local lattice distortion. This is one of the examples where it can be seen the intense debate between the different authors, with the same author postulating even different scenarios. On the other hand, XES measurements applying temperature and pressure reported by Vankó *et al*. [35] reflect a continuous variation of the spin localized on the cobalt, which was found more compatible with a LS/IS/HS model.

However, more recently the LS $\rightarrow$ HS scenario has seemed to return after some spectroscopic studies (XAS, XPS, and EPR) and further inelastic neutron scattering (INS) measurements which support this first picture [18, 21, 28, 36]. Haverkort *et al*. [18] revealed a gradual transition to a LS:HS mixed-spin state (triply degenerate HS excited state) through the temperature dependence of XAS at the Co $L_{2,3}$ edges, producing an inhomogeneous mixed spin-state. Moreover, atomic multiplet calculations and a large orbital momentum revealed by X-ray magnetic dichroism (XMCD) measurements in the same study were used to explain magnetic susceptibility, ESR and INS data. The large orbital moment did not favored LS-IS scenarios.

The same experiments, with similar results have been interpreted in a completely different way. This is the case of the study done by Podlesnyak and co-workers [19]. They also reported an excitation at ~ 0.6 meV using inelastic neutron scattering as Phelan *et al*. did at the same time, but in contrast they suggested a LS $\rightarrow$ HS picture.

Even some groups in the line of the LS $\rightarrow$ IS state transition are now supporting the LS $\rightarrow$ HS scenario for $T_{SS1.}$ This fact contributed Radaelli *et al.* [33] and Sundaram *et al.* [29], which did not find any evidence for a Jahn-Teller (JT) distortion in either the average or the local crystal structure of $LaCoO_3$. To this respect, Maris *et al.* [37] previously analyzed single-crystal X-ray diffraction data using a monoclinic (*I2/a*) distorted structure between 20 and 300 K which was ascribed to a Jahn-Teller distortion in the crystal lattice. They reported a gradual increase of the JT distortion with temperature (reached ~ 6% at RT) which was ascribed to a thermal population of IS states. However, this monoclinic distortion has not been corroborated in the latest studies [29].

Recapitulating, in Table 3. 1 we detail a selection of the relevant studies of the spin-state scenarios in $LaCoO_3$ along the last 25 years referred to their position in front of the two competing models for the first transition at T_{SS1}. So, after this review of contradictory claims and lack of consensus for $LaCoO_3$, it is clear that further efforts are clearly necessary to properly describe the SS evolution in the $LnCoO_3$ family compounds.

Table 3. 1. Selection of some relevant studies done on $LaCoO_3$ during the last 25 years favoring one of the two main different models for the T_{SS1}.

LS → IS scenario		LS → HS scenario	
Theoretical studies			
LDA + U	Korotin *et al.,* PRB (1996)	Hartree-Fock	Zhuang *et al.,* PRB (1998)
LDA + U	Nekrasov *et al.,* PRB (2003)	GGA + U	Knizek *et al., J.Phys Cond. Matter* (2006)
GGA + U	Knizek *et al.,* PRB (2005)	GGA + U	Knizek *et al., PRB* (2009)
Experimental studies			
IR spectroscopy	Yamaguchi *et al.,* PRB (1997)	ESR	Noguchi *et al.*, PRB (2002)
NPD	Radaelli *et al.,* PRB (2002)	INS	Podlesnyak *et al.,* PRL (2006)
XRD	Maris *et al.,* PRB (2003)	XAS/XMCD	Haverkort *et al.* PRL (2006)
INS	Phelan *et al.,* PRL (2006)	PFY-XAS	Medarde *et al.* PRB (2006)
XES	Vankó *et al.,* PRB (2006)	EXAFS/NPD	Sundaram *et al.,* PRL(2009)
EELS	Klie *et al.,* PRL (2007)		

Figure 3. 1 shows the *R-3c* crystal structure together with the different spin-states that can present Co^{3+} ions and the temperature dependence of the magnetic susceptibility up to 300 K for $LaCoO_3$. In all the $LnCoO_3$ systems, the cobalt ion is surrounded by oxygen forming CoO_6 octahedra, whereas the trivalent Ln^{3+} ion is surrounded by a distorted cube-octahedron formed of 12 oxygen ions out of the 12 *Ln*-O bonds, 3 are long bonds, 6 are medium-bonds, and there are 3 short bonds.

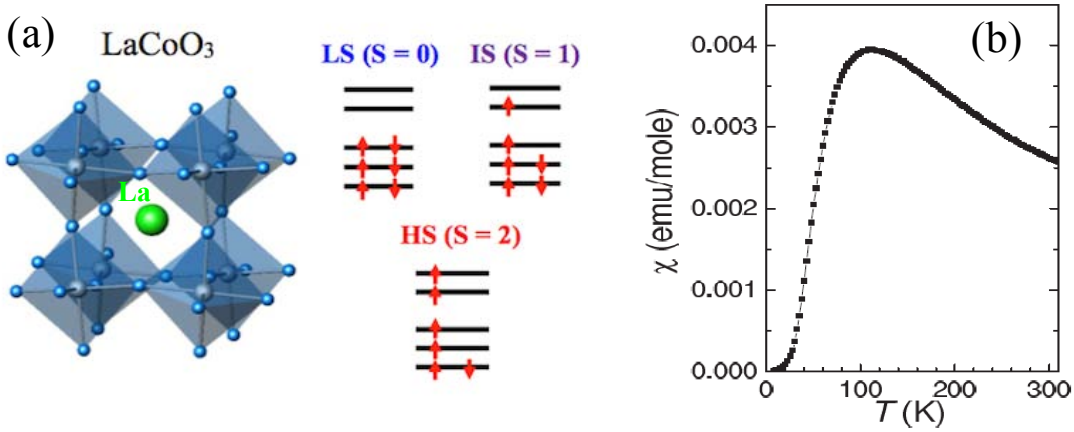

Figure 3. 1. (a) Crystal structure and spin states in $LaCoO_3$ and (b) temperature dependence of the magnetic susceptibility measured at 100 Oe in $LaCoO_3$ [38, 39].

Alternative experiments for the interpretation of the spin state as a function of temperature in LCO are high-pressure measurements. It has been observed in many metal compounds that a transition between different spin states can be stimulated by applying external pressure. A compression of the crystal volume and the Co-O bond lengths induces an increase of the crystal field splitting between t_{2g} and e_g orbitals (Δ), so the nonmagnetic state Co^{3+} ion can be stabilized [32, 35]. However, no conclusive results were obtained to unambiguously adopt a SS model in the intermediate regime of $LaCoO_3$.

3.2.1. Crystalline structure of $LaCoO_3$

From now on, we focus on the previously reported results about the crystal structure evolution in $LaCoO_3$. The dependence of the crystal structure on temperature reported by Thornton *et al*. [40] and more recently by Radaelli *et al.* [33] using neutron powder diffraction (NPD) reveals the presence of structural anomalies associated with the two separate spin-state transitions. As it is expected, a change in the spin state is accompanied by a corresponding change in the volume of the unit cell. As depicted in Figure 3. 2(a) (from numeric data extracted in Ref. [33]), the lattice parameters and the cell volume present two regions with anomalous expansion where the two broad SS transitions (SST) are expected at $T_{SS1} \sim 50$ K and $T_{SS2} \sim 450$ K (considered as the onset values for the transition) on heating. Of particular interest are also the Co-O and La-O bond lengths; see Figure 3. 2(b). The latter structural parameter surprisingly shows two inflection points coinciding with the onset of the transitions and it reaches two maxima at T ~ 150 K and T ~ 850 K where the SS transition could have been completed. The observed expansion can be ascribed to an increase of the effective ionic radius of the B site. The increase of the temperature leads to the population of higher-spin states with larger ionic radius from Co^{3+} (LS) = 0.545 Å at low temperature to Co^{3+} (IS) = 0.56 Å or Co^{3+} (HS) = 0.61 Å [41].

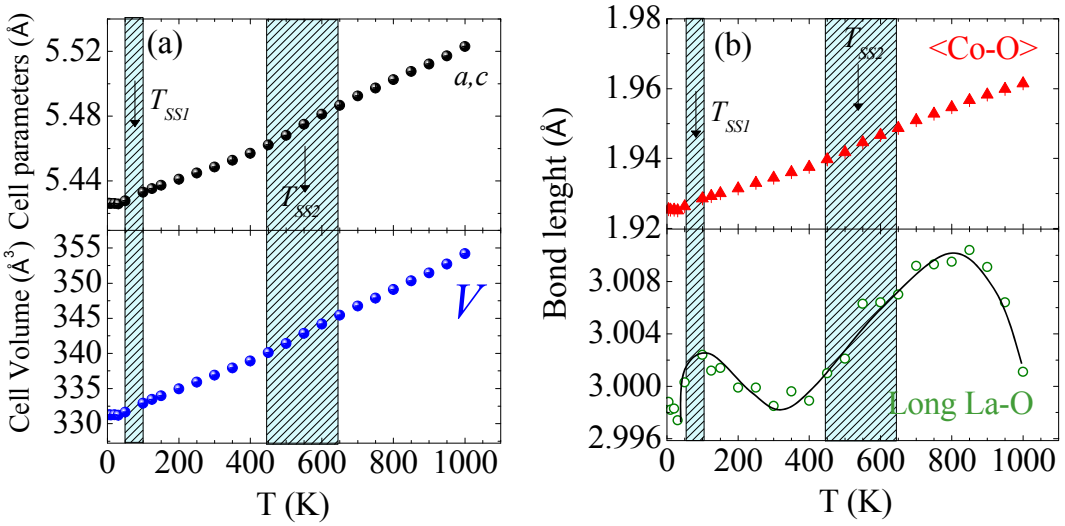

Figure 3. 2. (a) Temperature dependence of the cell parameters (top panel) and cell volume (bottom panel) in $LaCoO_3$; (b) Temperature dependence of <Co-O> and long La-O bond distances in $LaCoO_3$. The numeric data are extracted from Ref. [33].

3.2.2. Crystal structure and physical properties of *Ln*CoO_3

In order to extend the study of the evolution of the electronic configurations of Co^{3+} ions in LCO, other compositions of *Ln*CoO_3 (*Ln* = lanthanide or rare earth) have been synthesized during the last years, with the aim of exploring the influence of the chemical pressure through the substitution of La^{3+} [25, 36, 42–48]. The studies reveal that the new members of the family exhibit an orthorhombic crystal structure *Pnma* (or the equivalent group *Pbnm* obtained by exchanging crystallographic axes), unlike $LaCoO_3$.

Knížek *et al*. plotted in Ref. [42] the lattice parameters at RT as a function of the *Ln* ionic radius (see Figure 3. 3), together with the orthorhombic distortion and the Co-O-Co bond angles. It can be noted that from $YCoO_3$ to $SmCoO_3$ cell parameters obey the relation $b>c/\sqrt{2}>a$, typical for structures of so-called O-type, and for $NdCoO_3$ and $PrCoO_3$ the relation changes to $a > c/\sqrt{2} > b$ (structure called O'-type). This is a consequence of the systematic increase of the $GdFeO_3$- type orthorhombic distortion with decreasing size of the *Ln* ionic radii (see the right axis and the inset of Figure 3. 3).

However, similarly to LCO, the more distorted compounds also undergo nonmagnetic-paramagnetic and metal-insulator transitions, but the transitions are less separated from each other in temperature and are shifted to higher temperatures range. It has been observed that the onset temperatures of the transitions shift to higher temperatures when the *Ln* radius size decreases. This means that the nonmagnetic LS state becomes more stable as compared to

$LaCoO_3$. It is important to remark that in some of these systems it is difficult to directly determine the temperature of the first magnetic transition because of the magnetic contribution of the lanthanide element, which normally is stronger in front of the Co contribution and so it masks possible changes in the magnetization from Co atoms. However, Yan *et al*. [49] reported the onset temperature of the first magnetic transition in single crystals of $PrCoO_3$ and $NdCoO_3$ (200 K and 300 K, respectively), subtracting the *Ln* signal from the magnetic measurements of $LnAlO_3$.

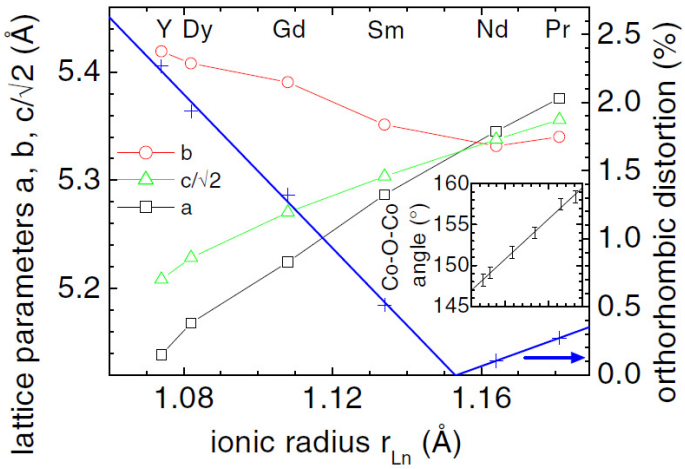

Figure 3. 3. Lattice parameters and orthorhombic distortion vs. *Ln* ionic radius for *Ln*CoO3 at room temperature. All the structures were refined using the *Pbnm* space group. The inset shows the average Co-O-Co bond angle [42].

As commented in the previous paragraph, the magnetic transitions increase in temperature with the decrease of the lanthanide ionic radii. The same effect can be concluded from Seebeck measurements and from structural X-ray powder diffraction data. Knížek *et al*. [42] reported structural anomalies on a series of $LnCoO_3$ perovskites with moderate distortion (*Ln* = Pr, Nd, Sm, Gd, Dy, Y) related to the magnetic and electric transitions. Figure 3. 4 shows the evolution of the cell parameters for these compounds and the orthorhombic distortion defined as:

$$S_{orth} = \frac{\sqrt{\Sigma(ai - \bar{a})^2}}{\bar{a}} \qquad \text{(Eq. 3.1)}$$

where a_i = *a*, *b* and $c/\sqrt{2}$ and $\bar{a}$ is the average of a_i. It is evidenced that the behavior of the orthorhombic distortion versus temperature depends on the size of the lanthanide ionic radii. For light lanthanides, where $a > c/\sqrt{2} > b$, a *maximum* appears in the orthorhombic distortion.

In contrast, for heavy lanthanides a *minimum* is observable in the orthorhombic distortion as a consequence of $b > c/\sqrt{2} > a$.

Figure 3. 5(a) displays measurements for the thermoelectrical power that confirm the occurrence of a metallic state with La down to Y. And also the MIT is shifted to higher temperatures. The study on the structural parameters with temperature allows the calculation of the *linear thermal expansion coefficient* using equation 3.2:

$$\alpha(T) = \frac{1}{l_0}\frac{l_2 - l_1}{T_2 - T_1}(K^{-1}) \qquad \text{(Eq. 3.2)}$$

where $l = (V/Z)^{1/3}$, V/Z is the cell volume per formula unit, l_0 is the value at RT, l_2 and l_1 are values at temperatures T_2 and T_1.

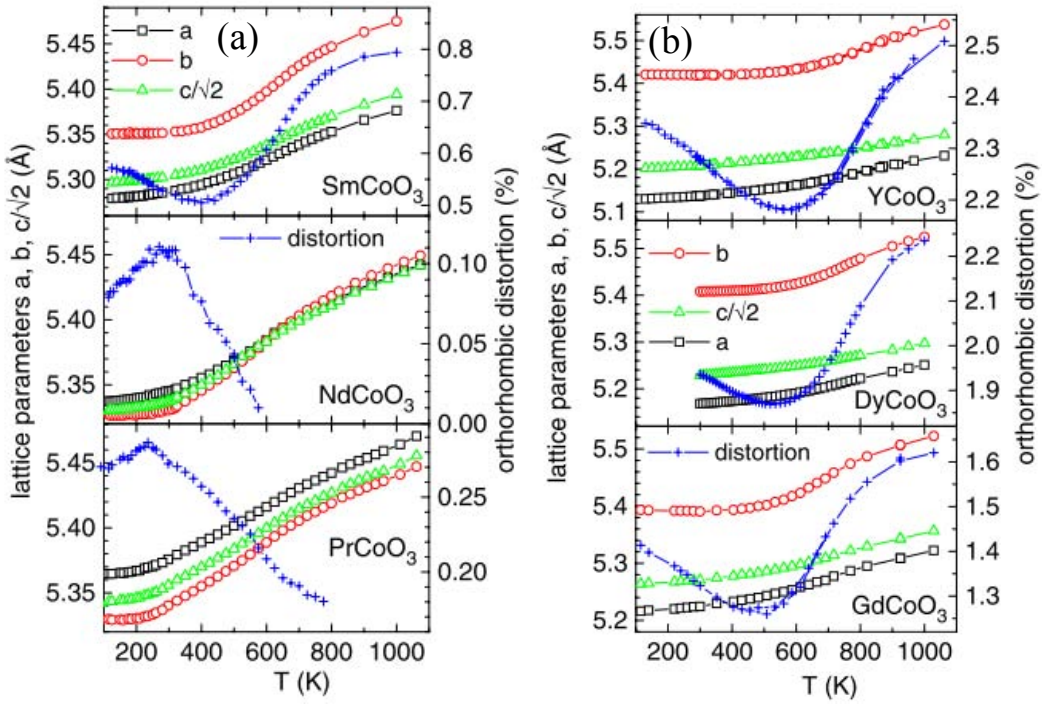

Figure 3. 4. Temperature dependence of the lattice parameters and orthorhombic distortion for different $LnCoO_3$ compounds. In the (a) panel $PrCoO_3$ and $NdCoO_3$ obey $a > c/\sqrt{2} > b$, while in (b) panel $GdCoO_3$, $DyCoO_3$, $YCoO_3$ and $SmCoO_3$ [panel (a)] obey $b > c/\sqrt{2} > a$. Figure extracted from Ref. [42].

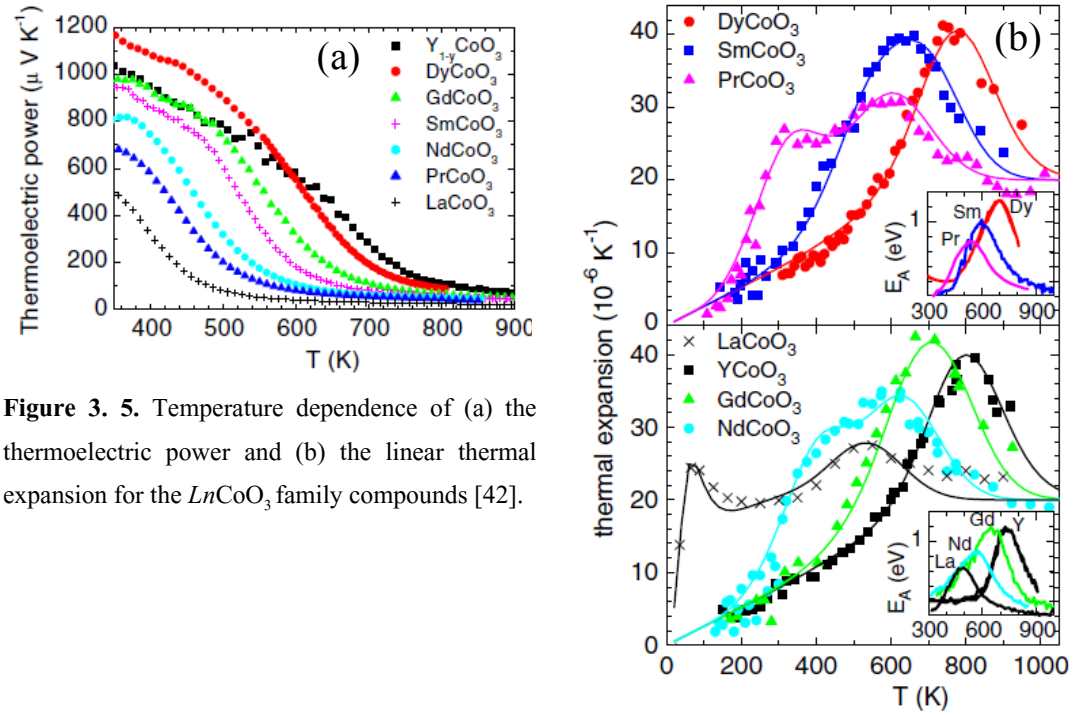

Figure 3. 5. Temperature dependence of (a) the thermoelectric power and (b) the linear thermal expansion for the $LnCoO_3$ family compounds [42].

Figure 3. 5(b) shows an initial range with a linear increase of the α expansion coefficient for all the compounds and rapidly the coefficient increases because of the thermally induced population of Co^{3+} IS or HS states. One surprising fact is that two shoulders are visible in the thermal expansion coefficient for compounds with larger *Ln*, whereas only one maximum is detected for small *Ln* compounds. This different behavior is not understood yet.

Tachibana *et al.* reported in Ref. [43] the evolution of the heat capacity of $LnCoO_3$ samples up to 1000 K. The heat capacity (C_p) measurements for a number of compounds of this family are plotted in Figure 3. 6. In this study a prominent single peak is observed close to the temperatures where the MIT is expected. In the figure, the C_p anomaly for $LaCoO_3$ is compared to that found in other $LnCoO_3$ compounds with enhanced distortion.

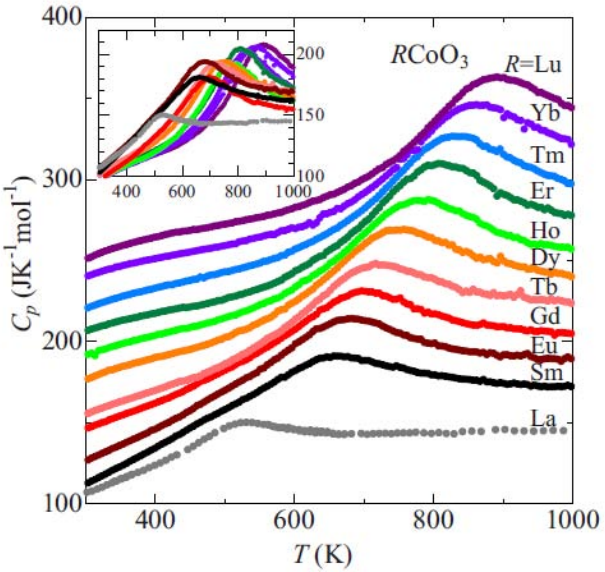

Figure 3. 6. The heat capacity of LnCoO$_3$ systems measured between 300 and 1000 K. The data have been offset by 0, 10, 20, 50, 55, 75, 95, 105, 125, 140 and 155 J·K^{-1}·mol^{-1}, respectively, for clarity. The inset shows the real data without the offset. Extracted from Ref. [43].

So, we can summarize these previous studies reported in the literature by saying that:

(i) apart from LaCoO$_3$, the existence of a high temperature metallic state has been observed in other LnCoO$_3$ cobaltites with more distorted structure;

(ii) thermally excited spin-state transitions also occur in LnCoO$_3$ cobaltites with heavier lanthanides;

(iii) the transitions are shifted to higher temperatures in the Co perovskites with smaller rare-earths;

(iv) in LnCoO$_3$ compounds with moderate distortion some works reported structural anomalies between 100 K and 1000 K directly related with changes in the electronic state of the Co^{3+} ions;

(v) the metal-insulator transition with $Ln \neq$ La is not sharp and looks rather broad in heat capacity measurements.

3.3. Sample synthesis and experimental details

Two bulk polycrystalline samples of $LnCoO_3$ have been prepared for this study, they are: $PrCoO_3$ (PCO) with a moderate distortion and $ErCoO_3$ (ECO) with a high distortion. The first one, $PrCoO_3$ was prepared by solid-state reaction of appropriate amount of Pr_6O_{11} and Co_3O_4 oxides which were first dried at 900 ºC during 18 h. Then, the precursors were mixed and pressed into pellets (d ~ 2.5 cm) and annealed during 24 h at 900 ºC in air. After the sample was gridded and pressed, the last annealings were performed at: 950 ºC during 24h, 1000 ºC during 24 h, 1000 ºC during 48 h and 1150 ºC during 48 h using slow cooling (60ºC/min).

The perovskite with a smaller *Ln* ionic radius, $ErCoO_3$ was prepared by the sol-gel method with the collaboration of J. A. Alonso from the Instituto de Ciencia de Materiales de Madrid-CSIC. In this case, a different method of preparation from $PrCoO_3$ was used because from a chemical point of view there are some difficulties in the synthesis of Cobalt perovskites with small rare earths [50]. These samples require high oxidation conditions as the size of the rare-earth cation decreases, due to the difficulties in the stabilization of the Co^{3+} ion. So, stoichiometric amounts of Er_2O_3 and $Co(NO_3)_2{\cdot}_6H_2O$ were dissolved in citric acid, by adding HNO_3 to favour the solution of rare-earth oxide. The solution was slowly evaporated leading to a resin, which was first dried at 120 ºC and then slowly decomposed at temperatures up to 600 ºC for 12 h. Finally, the obtained precursor was heated at 900 ºC under a 200 bar oxygen pressure for 12h. Then, the sample was cooled down at 5ºC/min to room temperature in order to obtain a good oxygenation.

Finally, we also disposed of a $LaCoO_3$ bulk sample prepared in 1996 by The Laboratory for Inorganic Materials from the University of Twente (Netherlands). The sample was prepared by a chemical method consisting of: (i) complexation of the metals ions in ethylenediaminetetracetic acid (EDTA) solution, (ii) evaporation of the water solvent, and (iii) thermal decomposition of the complex and formation of the perovskite phase. For more details see Ref. [51].

To check the quality of the samples X-ray diffraction and magnetic measurements have been carried out. The X-ray diffraction patterns were recorded using a Siemens D-5000 (for $PrCoO_3$) and a Brucker D8 diffractometer (40 kV, 30 mA for $ErCoO_3$) and Cu K_α radiation. We found the samples to be single phased and without impurities. Figure 3. 7(a) shows the Rietveld refinement using the FULLPROF suite of programs [52] of the diffraction pattern measured at 300 K and the crystal structure for $PrCoO_3$. The atomic positions obtained from the refined are listed in Table 3. 2. The experimental diffraction pattern for $ErCoO_3$ can be checked in Ref. [50].

A set of experiments and measurements were conducted between 5 and 1000 K. They included magnetometry, neutron powder diffraction (NPD), and X-ray absorption (XAS) and emission (XES) spectroscopies.

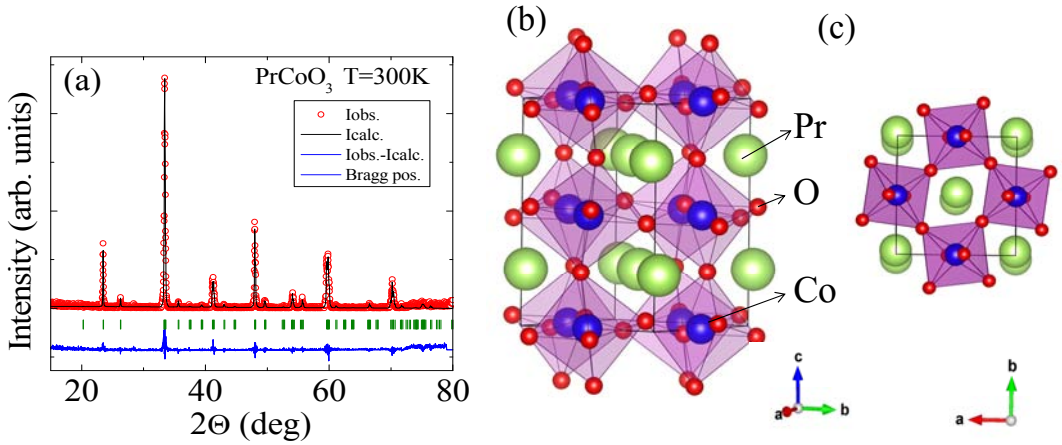

Figure 3. 7. (a) Rietveld refinement from laboratory x- ray diffraction data for $PrCoO_3$ at room temperature. The employed space group is *Pbnm* with lattice parameters a = 5.3753(4) Å, *b* = 5.3399(4) Å and *c* = 7.5745(7) Å. (b) and (c) Perspective view of the orthorhombic crystal structure of $PrCoO_3$.

Table 3. 2. Atomic positions obtained from the X-ray Rietveld refinement at room temperature for $PrCoO_3$. Agreement parameters are $\chi^2 = 4.2$ and $R_B(\%) = 19.5$.

Atom	Site	*x/a*	*y/b*	*z/c*	B_{iso} (Å^2)
Pr	*4c*	0.9966(6)	0.0306(7)	0.2500	0.56(6)
Co	*4b*	0.5000	0.0000	0.0000	0.33(2)
O1	*4c*	0.0683(8)	0.4949(7)	0.2500	0.41(5)
O2	*8d*	0.7171(8)	0.2831(6)	0.0350(5)	0.57(5)

MAGNETOMETRY: The direct current (dc) magnetization was measured using a Superconducting Quantum Interferometer Device (SQUID, Quantum Design) under 100 Oe for PCO, 10 kOe for LCO [see Figure 3. 8(a, b)] and 1000 Oe for ECO after zero-field (ZFC) and field cooling (FC) processes (see Figure 3. 22). The magnetic measurement for PCO reflects the fact that the Co magnetic contribution is weaker than the Pr contribution and then no changes from Co are observable as a function of temperature. However, at low temperature an anomaly

has been observed in the magnetic curve. As we know, in $PrCoO_3$ all the Co^{3+} ions remain in a LS state below $T_{SS1} \sim 200$ K, so no signal resulting from Co ions is expected at low temperature. This evidences a possible magnetic order from the Pr atoms around T ~ 30 K. The magnetic signal from LCO confirms the good oxygen stoichiometry of the sample.

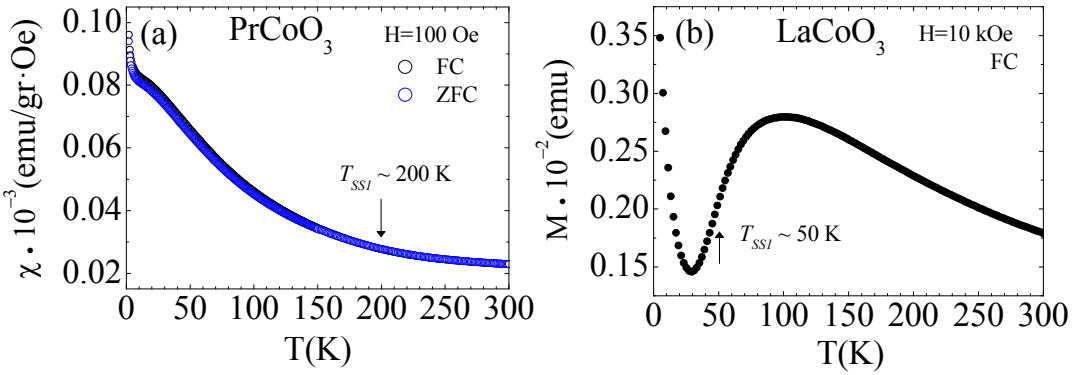

Figure 3. 8. Temperature dependence of the susceptibility measured for (a) $PrCoO_3$ at ZFC and FC at 100 Oe and (b) $LaCoO_3$ at FC at 10 kOe.

NEUTRON POWDER DIFFRACTION: NPD measurements in $ErCoO_3$ were carried out on the high-resolution D2B diffractometer of the Institute Laue-Langevin (ILL, Grenoble) at temperatures ranging from 100 K to 973 K. Above room temperature the sample was warmed in a furnace from 300 K to 973 K, while measurements at lower temperatures were performed using a CCR cryostat. Due to the relatively large absorption-cross section for neutrons of Er and Co, a narrow 5 mm sample-holder was used. NPD data were recorded at the neutron wavelength λ=1.594 Å. The high resolution NPD data at low temperature (1.5 K, 100 K, 200 K and 300 K) were also measured in the High-Resolution Powder diffractometer for Thermal neutrons (HRPT) at the SINQ spallation source (PSI, Switzerland). Acquisition of different data were carried out with a neutron wavelength of λ = 1.494 Å in the temperature range from 1.5 to 300 K using a He-cryostat.

SYNCHROTRON X-RAY ABSORPTION: Soft X-ray absorption spectroscopy (XAS) measurements at the Co $L_{2,3}$ and the O K edges for PCO and LCO were performed on the BL29-BOREAS beamline at the ALBA Synchrotron. Data were recorded by means of the surface-sensitive total electron yield (TEY) detection method. Proper bulk-pellet-sensitive measurements required in-situ scraping of the sample under ultrahigh vacuum (~10^{-9} mbar) conditions. CoO was simultaneously measured as an energy calibration reference. The nominal flux on the BL29-BOREAS beamline was on the order of 10^{12} photons/s with an energy resolution of about 100 meV.

X-ray emission spectroscopy (XES) experiments on PCO were carried out at beamline ID26 of the European Synchrotron Radiation Facility (ESRF). The incident energy ($E_{inc.}$ = 7800 eV) was tuned through the Co *K*-edge by means of a pair of cryogenically cooled Si(311) monochromator crystals and the overall resolution was 0.4 eV. A reference Co metallic foil was used to calibrate the monochromator energy. The emitted X-rays were analyzed using a set of four spherically bent Ge(444) crystals that were arranged with the sample and photon detector (avalanche photodiode) in a vertical Rowland geometry (R = 1 m) at 90º scattering angle. In addition, high-energy resolution fluorescence-detected X-ray absorption near edge structure (HERFD-XANES) spectra at the Co *K*-edge were collected at the maximum of the Co $K\beta_{1,3}$ emission line. A continuous He-flow cryostat was used to carry out low temperature measurements.

3.4. Probing the spin-state transition in $PrCoO_3$ cobaltite

As we mentioned previously, in other $LnCoO_3$ (Ln≠La) systems the magnetic and the MIT shift systematically to higher temperatures with decreasing the *Ln* ionic radius. Apart from $LaCoO_3$, a few published works focus on the properties of $PrCoO_3$ [42, 43, 46, 48–50]. This compound is the nearest member in the $LnCoO_3$ series when the size of the *Ln* = La decreases, so it presents a moderate distortion with an orthorhombic crystal structure.

In this section, the combination of the structural evolution in $PrCoO_3$ reported by different groups with the observed changes using different X-ray absorption spectroscopies, allows us to analyze and describe the spin-state transitions in this cobaltite. This study has been complemented with theoretical calculations that also indicate thermally assisted changes in the population of excited states in Co^{3+} ions.

3.4.1. Structural evidences of a spin-state transition in Co^{3+} ions

One of the first studies on the structural effects of the La^{3+} by Pr^{3+} substitution of was reported by Brinks *et al*. [53] in 1999 using laboratory X-rays. However, temperature dependent studies of the structural features using NPD were not done until 2005 by K. Knízek *et al.* [42]. In this section, we plot and discuss the structural evolution obtained through digitalized data from Ref. [42, 48].

Figure 3. 9(a) displays the temperature dependence of the cell parameters determined by neutron diffraction. We notice that the relation between lattice parameters is $a > c/\sqrt{2} > b$ as it is found in other $LnCoO_3$ members with a moderate distortion. Because of this special relation

between cell parameters and the fact that parameter *b* increases more rapidly than the other two, a *maximum* occurs in the orthorhombic distortion around T ~ 280 K. Two anomalous expansion zones are observed in the thermal evolution of the lattice parameters: at T ~ 200-300 K (Zone I) and T ~ 500-650 K (Zone II).Moreover, the changes observed in the cell parameters also coincide with the anomalous evolution found in the orthorhombic distortion which is plotted in Figure 3. 9(b). The first anomaly in the lattice evolution corresponds to a *maximum* observed in the orthorhombic distortion (Zone I), and at high temperatures there is a change in the slope of the curve coinciding with the second anomalous expansion in the lattice parameters observed in Zone II.

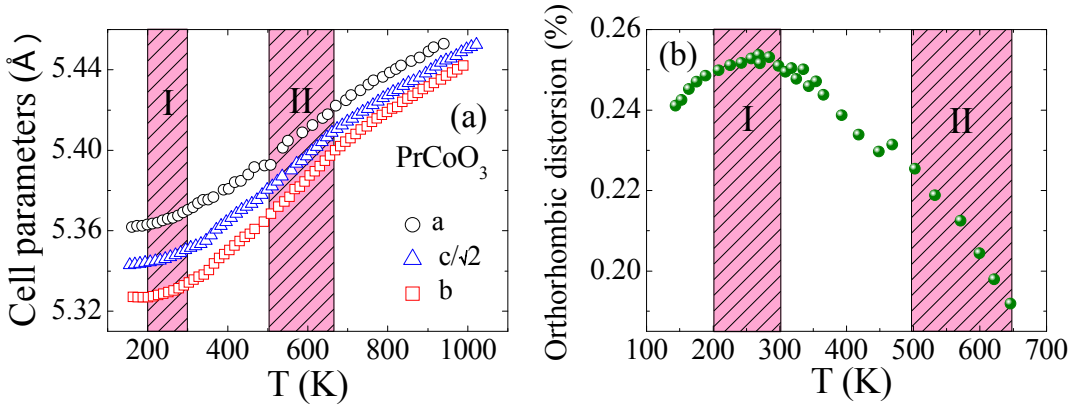

Figure 3. 9. Temperature dependence of (a) cell parameters and (b) orthorhombic distortion with respect to the pseudocubic one $\frac{\sqrt{\sum(\boldsymbol{a_i}-\bar{\boldsymbol{a}})^2}}{\bar{\boldsymbol{a}}}$ where a_i = *a*, *b*, and $c/\sqrt{2}$ and $\bar{\boldsymbol{a}}$ is the average of a_i. Data extracted from Ref. [48].

K. Knízek *et al.* in the same investigation [42, 48] plotted the evolution of the linear thermal expansion coefficient obtained applying Eq. 3.2, see Figure 3. 10. Here, the two anomalous expansion zones observed in the cell parameters can be also appreciated. Zone I corresponds to the temperature range ~200-330 K where the thermal expansion coefficient enhances, leading to the first maximum. And Zone II, corresponding to the temperature range ~ 500-650 K, agrees with the second maximum of the thermal expansion coefficient. .

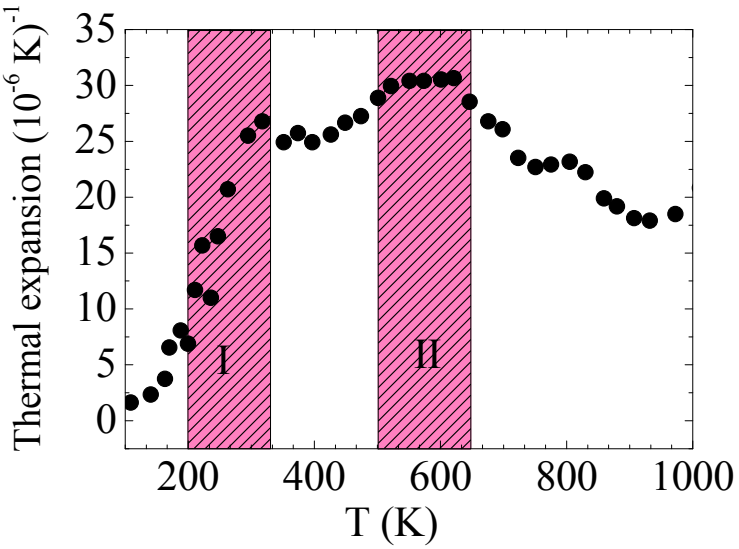

Figure 3. 10. Temperature dependence of the linear thermal expansion for $PrCoO_3$. The data is extracted from Ref. [42].

The evolution of the Co-O bond lengths and the Co-O-Co bond angles from the Rietveld refinements of the neutron diffraction data were also determined by the same authors [48]. These structural parameters are plotted in Figure 3.11.

We notice that the basal and apical Co-O bond distances are slightly different at T < 400 K, and on increasing the temperature they reach very similar values which make the CoO_6 octahedra almost regular. This can be made also visible calculating the $Co\text{-}O_c/Co\text{-}O_{ab}$ ratio which it is found to be 0.9971 at low temperature (150 K) and 1.0003 at high temperature (1000 K). The thermal evolution of the bond distances also shows three different regions that can be clearly identified by tracing a straight line (blue line) with different gradients as Figure 3.11(a) displays. For the discussion, we focus on the apical bond distance ($Co\text{-}O_c$) which suffers the largest changes at low temperature. In particular, the apical Co-O distances exhibit a slight expansion (Zone A), and above T ~ 350 K, the expansion becomes more abrupt on increasing the temperature (Zone B). This different behavior in the thermal evolution is connected with the regime where the first spin-state transition takes place. However, above ~700 K, the evolution of the Co-O bond distances changes again, decreasing the rate (Zone C). Here, again the different behavior signals the second SS transition in $PrCoO_3$.

The evolution of the Co-O-Co bond angles also shows similar areas on heating which can be correlated with the SS transitions as the Co-O bond distances: (i) (Zone A) from low temperature to ~400 K, it seems the apical $Co\text{-}O_c\text{-}Co$ angle is slightly larger than the basal

Co-O_{ab}-Co angle and it is almost constant in this temperature range, where the basal angle increases linearly with temperature; (ii) (Zone B) from ~400 K to ~700 K both Co-O-Co angles are similar and keep constant along the evolution; and (iii) (Zone C) above 700 K, it seems the basal angle suffers a slight increase that is not followed by apical angles.

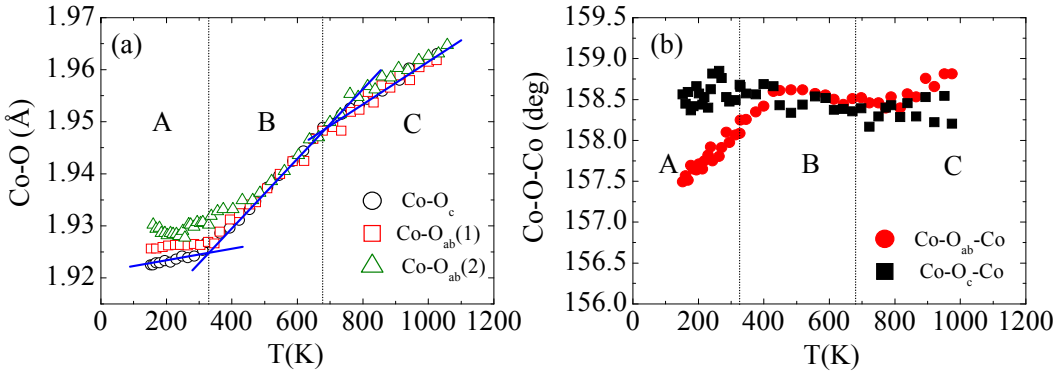

Figure 3. 11. Temperature dependence of (a) the basal Co-O_{ab} (red empty squares and green empty triangles) and apical Co-O_c (black empty circles) bond distances, and (b) the Co-O-Co bond angles. The blue lines simple are guideslines to the eye. Data extracted from Ref. [48].

Summarizing, $PrCoO_3$ undergoes two successive transitions which are observable in the evolution of some structural parameters such as the cell parameters, the orthorhombic distortion, the linear thermal expansion, the Co-O bond distances, or the Co-O-Co bond angles. The temperature intervals with an anomalous structural evolution should be associated to two successive SS transitions in $PrCoO_3$. The substitution of La^{3+} with a smaller rare ion like Pr^{3+} increases the LS state stability (the crystal field gap between the t_{2g} and e_g orbitals increases), but it becomes unstable above 50 K in $LaCoO_3$ and 200 K in $PrCoO_3$ (onset of T_{SS1}). In the latter, the SS1 seems finished around ~330 K, and the SS2 around ~ 650 K.

3.4.2. The spin-state in $PrCoO_3$ analyzed by X-ray absorption and emission spectroscopies

As it has been commented in Chapter 2, in X-ray Absorption Spectroscopy (XAS) a core electron is excited into an empty state (conduction band or continuum, depending on the incident photons energy). Thus, XAS becomes a powerful technique to probe the unoccupied states of the electronic structure. In this section, we provide a detailed and comprehensive study about the electronic configuration and the nature of the SS of Co^{3+} ions across the first spin-

state transition in $PrCoO_3$ (T_{SS1} ~ 200 K) and in $LaCoO_3$ (T_{SS1} ~ 50 K). It must be clarified that the given values of T_{SS1} and T_{SS2} always refer to the onset of the transition.

3.4.2.1. XAS and XANES investigation

First of all, we carried out XAS measurements at the Co $L_{2,3}$ and the O *K* edges between 10 K and 360 K to probe the first spin state transition. Figure 3. 12 displays the temperature dependence of the Co $L_{2,3}$ edges in a temperature range (200 K-360 K) around Zone I shown in Figures 3.9 and 3.10 corresponding to the first electronic transition (T_{SS1} ~ 200 K). One observes that these spectra closely resemble to those collected at the Co $L_{2,3}$ edges in $LaCoO_3$ [13, 18] and a clear evolution with temperature is detected. At low temperature PCO is considered to be in a LS state and this is observable at the Co L_2 edge in which we found a narrow peak at ~794 eV. This feature (noted C) is known to be the hallmark of Co^{3+} LS. Moreover, we observe above 300 K an enhancement of A feature just below the Co L_3 edge at ~ 778 eV. This feature is typical of the Co^{3+} presence in a spin-state higher than LS, namely, it confirms the presence of IS or HS excited states above 300 K. Also, a clear decrease of B feature is seen at the same time that A is changing.

The same evidences observed in the Co $L_{2,3}$ edges can be also seen at the O *K* edge X-ray absorption spectra which are also sensitive to spin-state changes in Co^{3+}. The pre-peak region between approximately 528 eV and 533 eV is an alternative way to analyze the density of empty Co 3*d* states via hybridization to the O 2*p* states. Figure 3. 13 shows the evolution of the O *K* edge spectra at different temperatures between 160 K and 360 K for $PrCoO_3$. Here, we note that the effect of increasing the temperature is mainly reflected on the D and E features. At high temperature, feature D just at 529 eV increases its intensity whereas the higher energy peak (E feature) at ~530 eV decreases. This reflects the electron promotion from t_{2g} to e_g orbitals. At low temperature Co^{3+} ions are expected to be in the LS state, this meaning a large density of 3*d* e_g empty states (a higher intensity in the E feature), while for a higher SS an enhancement of the population of t_{2g} symmetry empty states should occur.

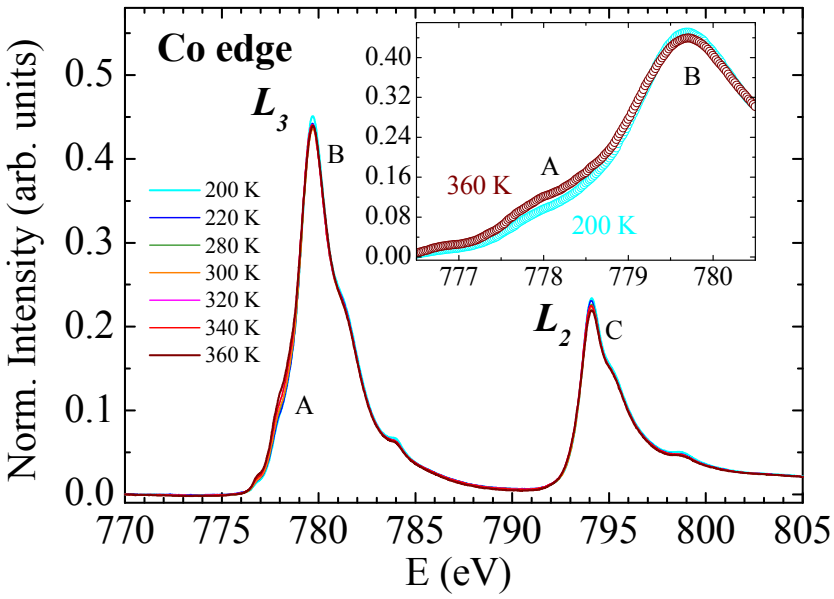

Figure 3. 12. Experimental Co $L_{2,3}$ XAS spectra as a function of temperature for $PrCoO_3$. Labels A, B and C mark features discussed in the text. The inset shows details of the L_3 edge and the evolution with temperature of label A.

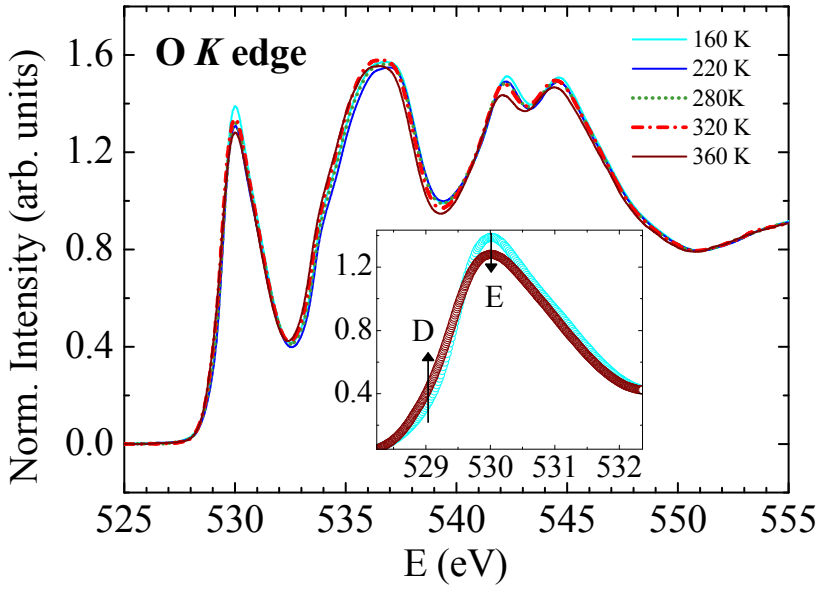

Figure 3. 13. Experimental O *K* edge XAS spectra as a function of temperature for $PrCoO_3$. The inset displays details of the pre-edge region. The arrows correspond to increasing temperatures from 160 K to 360 K. Labels D, and E mark features discussed in the text.

It should be also noted from the previous results that in $PrCoO_3$ the spin state transition is not an abrupt change like in other Co oxides. In this case, it seems that the filling of e_g unoccupied states occurs progressively with temperature. This result supports the inhomogeneous LS-HS model in $LaCoO_3$ suggested by Haverkort *et al.* [18].

Another indication of a progressive spin-state transition in PCO is the temperature evolution of the A feature intensity around E ~778 eV plotted in Figure 3. 14(a). We notice that A feature evolves without showing a marked or sharp transition, but that is relatively wide. In order to explore how far away the first magnetic transition extends above ~300 K, we have plotted in Figure 3. 14(b) the temperature dependence of the linear thermal expansion for $PrCoO_3$ from Ref. [42] in the same temperature range that XAS measurements, where it is visible the first anomalous expansion zone (Zone I: 200-330K). Figure 3.14 tell us that the first transition stems also beyond the maximum in the anomalous expansion zone. From data in Figure 14, we conclude that the zone of maximum change associated to the first SST persist up to around 330-350 K.

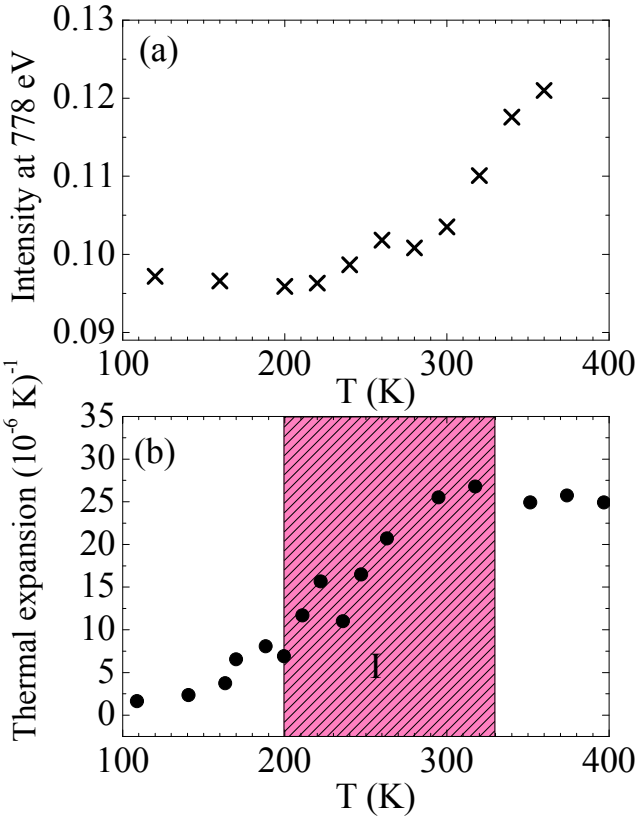

Figure 3. 14. (a) Temperature dependence of the Co L_3 edge XAS intensity for an energy of 778 eV in $PrCoO_3$. The solid line is a guide to the eye. (b) Temperature dependence of the linear thermal expansion for $PrCoO_3$ from Ref. [42].

To go further in our study, we have also measured XAS spectra at Co $L_{2,3}$ and O K edges for $LaCoO_3$ across T_{SS1}. We decided to undertake these measurements in BL29-BOREAS beamline to compare with the $PrCoO_3$ spectra measured under similar conditions. This allows us to compare both samples and detect if the changes follow or not the same trends. Figure 3. 15 displays the set of Co $L_{2,3}$ XAS spectra taken for $LaCoO_3$ at 20 K (considered as Co^{3+} in a LS state), 100 K, and 300 K. At first sight the measurements are similar to those reported by Haverkort *et al.* [18]. We observe, as they also do, that the spectral shape at 20 K is typical for compounds containing Co^{3+} in LS due to the shoulder (P feature) appearing above the Co L_3 edge at ~781 eV. As the temperature increases, we observe a clear decrease of P while the S feature increases indicating that the Co^{3+} ions change their spin-state and evolve towards a higher excited state across T_{SS1}. These results are in agreement with a progressive and inhomogeneous mixed-spin state system as Haverkort *et al.* reported earlier for the La compound.

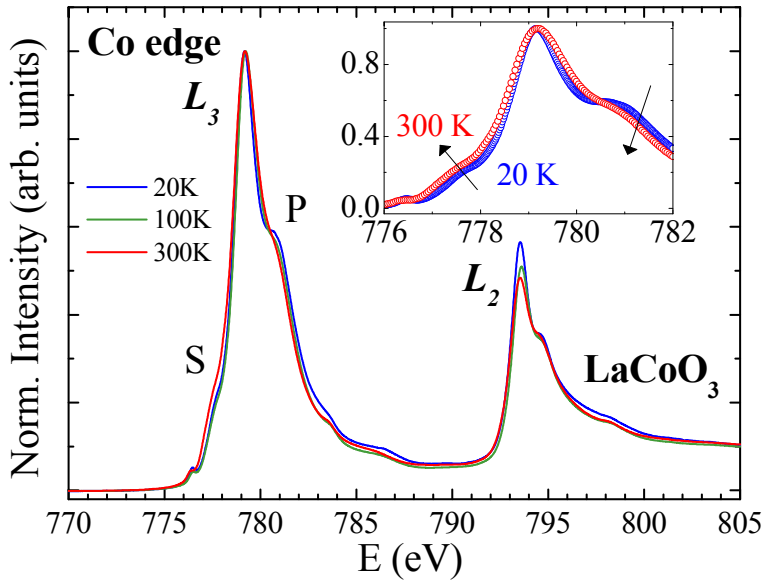

Figure 3. 15. Experimental Co $L_{2,3}$ XAS spectra as a function of temperature for $LaCoO_3$. Labels S and P denote the features discussed in the text. The inset shows details of the L_3 edge and the evolution with temperature of label S at 20 K and 300 K.

Likewise the O K edge of $LaCoO_3$ has been also measured at the same temperatures (see Figure 3. 16). The spectral shape at the pre-edge region shows similarities with the reported data by M. Abbate *et al.* in Ref. [13]. At low temperature there is a contribution at ~529.08 eV from unoccupied orbitals in e_g symmetry which it is consistent with a low-spin state. On the other hand, another component appears at ~ 528 eV at 300 K which is attributed to the

enhancement of free t_{2g} orbitals while the e_g component simultaneously decreases. This indicates that there is a transfer of electrons from t_{2g} to e_g levels when increasing the temperature and implies changes in the spin-state of Co^{3+} ions.

Thus, our study done in $PrCoO_3$ is in agreement with the observed changes across the first spin-state transition in $LaCoO_3$ and it is consistent either with an inhomogeneous mixed-spin state (LS+HS) or with a transition to an IS spin state, above T_{SS1}. Later, in this chapter we will address the problem of the best description (LS → LS+HS → HS or LS → IS → HS) to account for the observed changes in these $LnCoO_3$ systems. For that we will compare experimental and calculated XAS spectra.

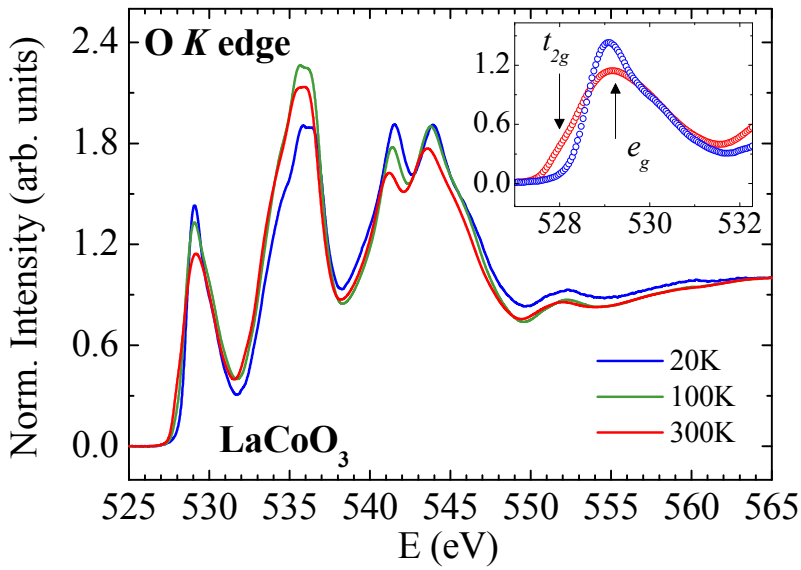

Figure 3. 16. Experimental O *K* edge XAS spectra as a function of temperature for $LaCoO_3$. The inset displays details of the pre-peak region of the LCO spectra. The arrows correspond to the orbitals with t_{2g} and e_g symmetry.

Another tool to investigate SS transitions in $PrCoO_3$ comes from the HERFD-XANES spectra at the Co *K* edge, sensitive to the occupation of the Co 3*d* states. Figure 3. 17(a) provides the measurements at the Co *K* edge for PCO at 20 K and 300 K. This hard X-ray spectroscopy probes the transition from a 1*s* core state to the empty 4*p* states, and the pre-edge region (here between 7707 eV and 7015 eV) reflects also the distribution of the t_{2g} and e_g levels.

We observe some changes in the spectral weight ascribed to the t_{2g} and e_g orbital occupation between 20 K and 300 K measured at ID26 beamline (ESRF). PCO at 20 K does not contain unpaired spins in the Co 3*d* state ($t_{2g}^6\ e_g^0$, $S = 0$), but on heating there is an increase of the spectral weight in the low energy shoulder due to the release of 3*d* states with t_{2g} symmetry.

Moreover, this SS change is also reflected by a shift of the main absorption-edge to lower energies at 300 K. As in the XAS measurements, the comparison with $LaCoO_3$ allows us to qualitatively relate similar changes in both compositions.

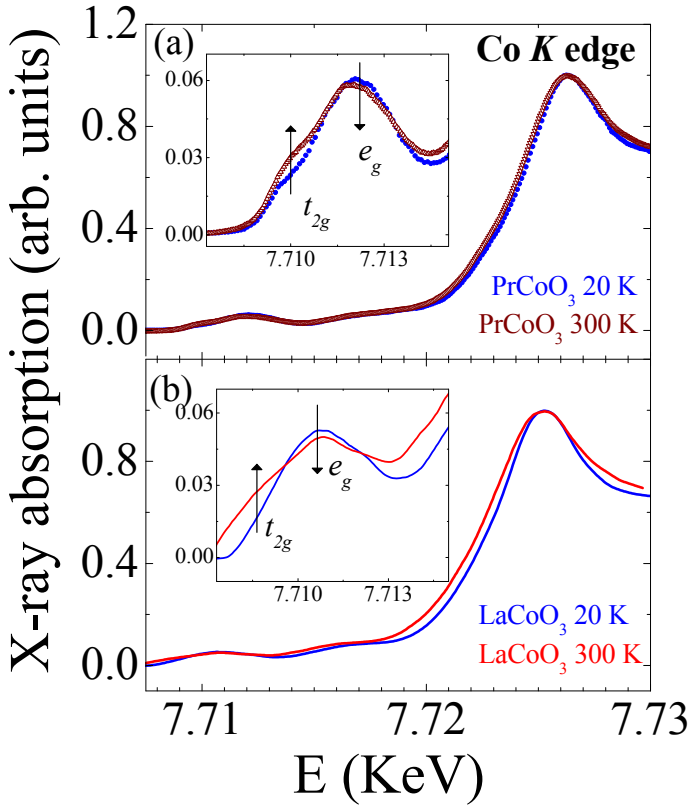

Figure 3. 17. HERFD-XANES spectra at the Co *K* edge of (a) $PrCoO_3$ at 20 K (blue filled circles) and 300 K (red empty triangles) and (b) digitalized data of $LaCoO_3$ at 20 K (blue solid line) and 300 K (red solid line) from Ref. [35]. The inset shows the pre-edge region sensitive to the occupation of the Co 3*d* states. The arrows indicate the empty states resulting from the t_{2g} and e_g states ascribed to Co^{3+} LS.

Figure 3. 17(b) displays the digitalized data extracted from Ref. [35] at 20 K and 300 K corresponding to $LaCoO_3$. We have seen in the introduction of this chapter that LCO presents the first SS transition at T_{SS1}~50-100 K and the second one at T_{SS2} ~ 500-600 K. Then, observing these data we realize that changes in the pre-peak are in the same line as those seen in our measurements in PCO. In the LCO compound the change in the spectral weight is stronger than PCO and besides, the absorption-edge is shifted (ΔE ~ 0.3 eV) to lower energies. The strong changes in LCO are consistent with the fact that the first transition is completely finished at 300 K whereas in PCO at the same temperature is almost but not totally completed. So, LCO presents a higher population of Co^{3+} in HS or IS than PCO at the same temperature. This is in

agreement with the XAS measurements reported in LCO by Haverkort *et al.* [18] in which the HS percentage as function of temperature was extracted from different fittings with different LS-HS ratios. These results reflect a LS-HS picture in an approximate 75:25 ratio at 300 K in LCO. So, this model yields and effective spin S = 0.75 x 0 + 0.25 x 2 = 0.47 at room temperature. The spin of $PrCoO_3$ will be discussed later in this chapter.

3.4.2.2. XES investigation

To get deeper into the Co^{3+} SS in $LnCoO_3$ systems, we decided also to perform Co K edge nonresonant XES measurements in $PrCoO_3$ at 20 K and 300 K in the ID26 beamline (ESRF). To the best of our knowledge this is the first XES experiment in other compound from the $LnCoO_3$ family different to $LaCoO_3$ [35]. This technique is complementary to XAS measurements providing information about the atomic electronic structure, in particular the local charge and spin-density, in this case by looking at occupied valence states. In Kβ XES a core electron (1s) is excited by an incident X-ray photon into the valence band or the continuum, followed by the decay of a 3p electron into the core hole, producing the emission if a photon (for more details see Chapter 2, Section 2.5.3). In Figure 3. 18(a) we show the Co Kβ lines of LCO at the two measured temperatures, as compared with those of $LaMn_{0.98}Co_{0.02}O_3$, which is in a perovskite structure containing only Co^{2+} in the HS state ($t_{2g}^5\ e_g^2$, S = 3/2) from Ref. [54].

The experimental spectra at 300 K present a small drop of the main line intensity and a minor displacement to higher energies is also observed. This result can be interpreted as $PrCoO_3$ at 300 K being more spin polarized than at low temperatures where Co^{3+} is in a LS state. This is in agreement with a spin-state transition as the previous absorption measurements indicated. In addition, the changes in LCO between 17 K and 300 K XES spectra (data extracted from Ref. [35]) resemble those observed in PCO, but the variations are larger than in the smaller Ln-size compound [see Figure 3. 18(b)] due to the fact that the first magnetic transition in LCO is already completed at 300 K. LCO at 300 K presents a higher number of Co^{3+} ions in a HS/IS state than PCO at the same temperature.

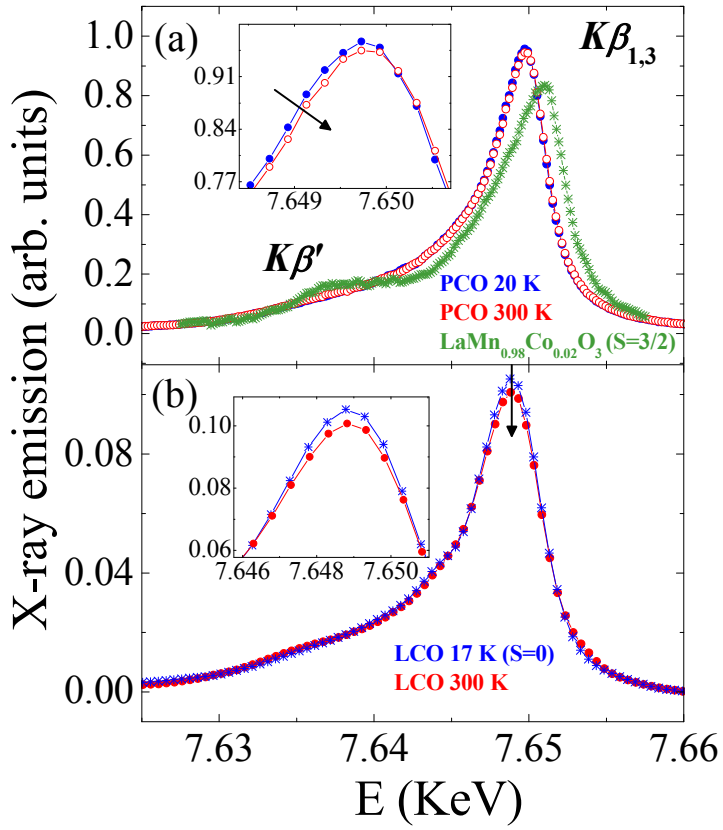

Figure 3. 18. Co *K*β emission spectra of (a) $PrCoO_3$ at 20 K and 300 K, as compared to the reference sample $LaMn_{0.98}Co_{0.02}O_3$, and (b) digitalized data of $LaCoO_3$ at 17 K and 300 K from Ref. [35]. The inset displays details of the curves.

A promising tool to directly determine the effective spin in both compounds from the *K*β emission spectra is to employ the integral of the absolute values of the difference spectra (IAD) method. This procedure is an effective approach when it is used with suitable reference samples with similar local structure in which the spin state is known.

This analysis is successful when the analyzed samples are measured under similar conditions such as resolution, source size and background. Moreover, this procedure has been used in the determination of the spin-state for different compounds [54–57], including $LaCoO_3$ where the spin-state was determined from temperature and pressure- dependence of *K*β measurements by G. Vankó *et al.* in Ref. [35].

So, we expect to quantify the spin state in $PrCoO_3$ from our measurements at the *K*β lines. In Figure 3. 19 the IAD analysis is presented for the $LnCoO_3$ systems (*Ln* = La, Pr) and compared to the results reported in Ref. [57] for $Pr_{0.50}Ca_{0.50}CoO_3$,taking only into account the model where Co^{3+} is pure IS or mixed LS:HS (1:1). In the plot we observe how the IAD values

for PCO and LCO can linearly fit the set of experimental points obtained for the reference compounds.

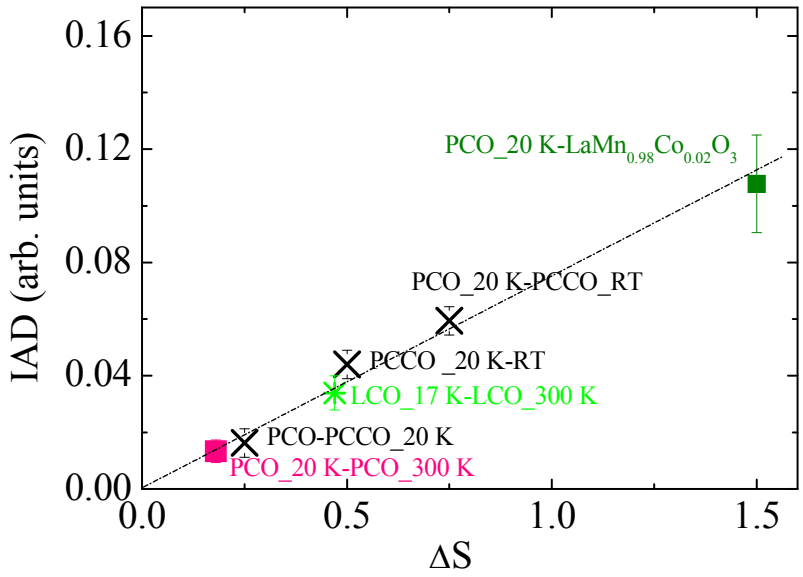

Figure 3. 19. IAD analysis of Co *K*β emission curves of $PrCoO_3$ at 20 K (S = 0) and 300 K (pink filled squares), and $LaCoO_3$ at 17 K (*S* = 0) and 300 K (green crosses). PCCO data are extracted from Ref. [57]. In this compound is considered the hypothesis of the SS of Co^{3+} ions being either pure intermediate or a mixture of low-high spin-state (1:1) (crosses). Co^{2+} ions in $LaMn_{0.98}Co_{0.02}O_3$ are considered to be in a HS state (*S* = 3/2) (green squares). The dotted-dashed line is a guide to the eye.

Then, the spin state of $PrCoO_3$ and $LaCoO_3$ at 300 K is deduced from the plot: *S* = 0.17 and *S* = 0.47, respectively. The value for LCO is in agreement with the reported value in Ref.[35] and the expected population of HS state at this temperature suggested by Haverkort *et al.* in which the LS:HS ratio is 75:25. In conclusion, the good agreement between all the results confirms the consistency of the used method.

To verify our first hypothesis, consisting on the spin state changing from LS to a mixed LS:HS configuration across the first transition, we have completed the study with charge-transfer multiplet calculations (CTM) at the Co $L_{2,3}$ edges using the CMT4XAS program which is based on the Cowan code [58] (more details about the program in Chapter 2). In Figure 3. 20, we show the experimental spectra at 300 K of PCO and the calculated spectra using the corresponding LS:HS ratio and LS:IS ratio deduced from the effective spin *S* = 0.17 (for a LS $\rightarrow$ HS scenario the ratio is 91% LS + 9% HS and for a LS $\rightarrow$ IS scenario the ratio is 82% LS + 18% IS) . The calculated vs. experimental spectra comparison reinforces the idea of an electron promotion from the LS state into the HS state. Both theoretical models are able to

reproduce features B, C and E. However, the A feature just below the Co L_3 edge gets enhanced in the LS:IS model and the D feature position shifts to lower energies by approximately 0.6 eV in comparison to the experimental spectrum. The parameters used for each calculation are listed in Table 3. 3.

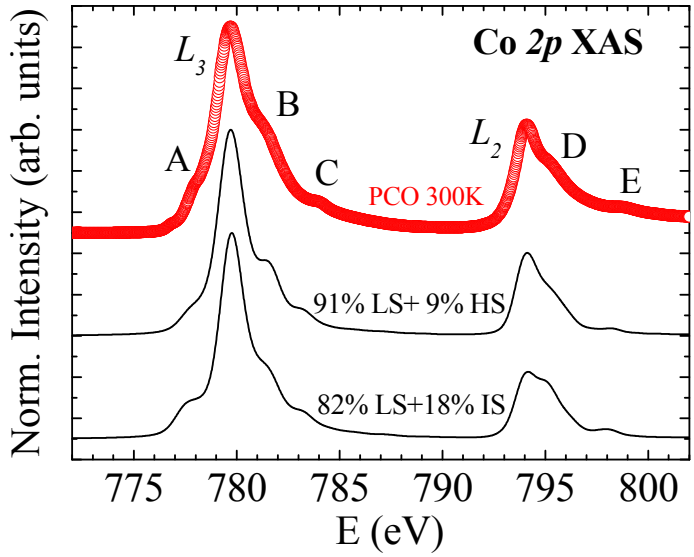

Figure 3. 20. (Top) Experimental Co $L_{2,3}$ XAS spectra of $PrCoO_3$ (red empty circles) at 300 K; (Bottom) weighted addition of CTM calculations in: (a) the LS:HS scenario or (b) the LS-IS scenario for the first magnetic transition.

Table 3. 3. Parameters from the charge-transfer multiplet calculations using CTM4XAS.

Parameter	Co^{3+} LS	Co^{3+} IS	Co^{3+} HS
Symmetry	O_h	O_h	O_h
Crystal field (*10Dq*) (eV)	+1.6	+1.3	+0.5
Charge transfer energy (Δ) (eV)	+3.0	+3.0	+3.0
U_{dd} (eV)	6.2	6.2	6.2
U_{pd} (eV)	7.5	7.5	7.5
Hopping e_g-electrons (T_{eg}) (eV)	2.0	2.0	2.0
Hopping t_{2g}-electrons (T_{t2g}) (eV)	1.0	1.0	1.0
Spin-orbit coupling (S.O)	1.0	1.0	1.0
Slater's integrals (F_{dd}, F_{pd}, G_{pd})	1.0	1.0	1.0

So, the simulations clearly show qualitatively that the spectral shape of PCO in Figure 3. 20 is dominated by mixed LS-HS states instead of LS-IS states. In addition, for better discerning between the two proposed descriptions we have also plotted the comparison between the experimental difference XAS spectrum of $LaCoO_3$ at 20 K and 100 K [curve (a)], the experimental difference spectrum for $PrCoO_3$ at 200 K and 300 K [curve (d)], and the calculated difference spectrum for each proposed model considering $\Delta S = 0.17$ (for the LCO compound) and $\Delta S = 0.06$ (for the PCO compound). We decided to compare the difference spectrum for LCO at 20 K and 100 K (and not at 300 K) because at this intermediate temperature the first SS has progressed a similar grade and the number of excited states is probably the same as in PCO at 300 K, where we determined from XES data that the effective spin is 0.17. The difference spectra between the LS model and (91:8) LS-HS model [curve (b)] on one hand, and the LS model and (82:18) LS-IS model [curve (c)] on the other hand are compared to the experimental LCO curve. Despite, PCO at 200 K is dominated by Co^{3+} LS ions, this temperature is considered as the onset of the first transition $T_{SS1} \sim 200$ K, at this point the transition probably being started and $S \neq 0$. Then, we extrapolated the effective spin at this temperature ($S = 0.11$) where the corresponding LS:HS ratio is turn up to be 94.5 % Co^{3+} LS + 5.5 % Co^{3+} HS. The difference between this LS:HS ratio model at 200 K and the (91:8) one at 300 K ($S = 0.17$) is plotted in curve (e).

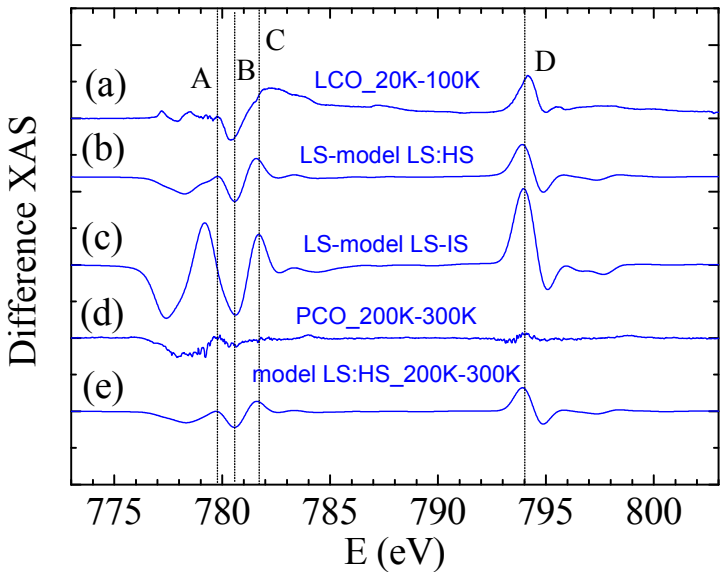

Figure 3. 21. Difference XAS spectra between (a) the experimental XAS for $LaCoO_3$ at 20 K and 100 K, (b) the calculated spectra considering Co^{3+} LS and mixed LS:HS states (91:9), (c) the calculated spectra considering Co^{3+} LS and mixed LS:IS states (82:18), (d) the experimental XAS for $PrCoO_3$ at 200 K and 300 K and (e) the calculated spectra considering Co^{3+} LS and mixed LS:HS states (94.5:5.5).

From the analysis of the intensity and position of the different features appearing in the different XAS curves we have realized that: (i) the position and magnitude of the A feature around 779.8 eV in the experimental LCO spectrum agree better with curve (b), which corresponds to the mixed LS:HS scenario than with curve (c) (LS-IS scenario); (ii) the magnitude of the D feature (~ 794 eV) which appears in curve (b) also fits better the experimental data than curve (c). For the PCO compound, similar characteristics are observed. The comparison between the experimental and calculated differences allows us to conclude that a mixed LS:HS description is justifiable by the inspection of the peak position and magnitude of the different features.

So, after this deep analysis of the spin-state transition in these two systems by means of X-ray absorption and emission spectroscopies, we can interpret the first electronic transition in La-and Pr-based perovskites as a low-spin to high-spin transition where there is a partial crossover up to an approximately 90% + 10% LS+HS mixed states. Therefore our results are consistent with the LS $\rightarrow$ LS+HS $\rightarrow$ HS scenario against others involving Co^{3+} ions in an IS state.

3.5. The spin-state transition at high temperature in the highly distorted $ErCoO_3$ cobaltite

In this section a comprehensive structural study of the distorted $ErCoO_3$ cobaltite is presented with the aim of investigating the nature of the spin state transitions in $LnCoO_3$ cobaltites when the *Ln* ionic radius strongly decreases, in contrast to the light lanthanides. In particular, $ErCoO_3$ perovskite is the most distorted specimen of the series studied up to now in a very wide temperature range. In this work we present evidences of structural anomalies produced by SS excitations up to 1000 K, on the basis of neutron powder diffraction (NPD) data profiting from the sensitivity of this technique to the oxygen atoms displacement. The observed changes are analyzed in the light of a progressive SS transition from Co^{3+} ions in LS (t_{2g}^6, $S = 0$) to excited magnetic states at high temperature. The study of the highly distorted $ErCoO_3$ is of interest for comparison with the $LnCoO_3$ systems with slight or moderate distortions (such as La or Pr) and here NPD was combined with magnetometry data.

.

3.5.1. Magnetic characterization and the magnetic ordering at low temperature in $ErCoO_3$

Figure 3. 22(a) shows the inverse susceptibility up to 50 K measured under field cooling conditions at 1000 Oe, and the inset shows the susceptibility measured in the whole temperature range below 300 K. Similarly to other *Ln*CoO_3 compounds, the magnetic contribution of the lanthanide element is strong in front of the Co contribution and then it masks possible anomalies in the Co magnetization of $ErCoO_3$. We had no access to $ErAlO_3$ in order to subtract the Erbium signal. However, we can observe a marked change in the slope of the inverse susceptibility indicating a possible magnetic ordering at very low temperature (T<10K).

Figure 3. 22(b) displays the magnetic field dependence of the magnetization measured at 2 K and 10 K. Here, we notice the M-H curve at 10 K, indicative of a paramagnetic material, while the curve at 2 K evidences a possible magnetic polarization coming from the order of Erbium atoms at this low temperature. This possible magnetic order was also revealed by high-resolution neutron diffraction data obtained at the HRPT beamline in the Swiss Spallation Neutron Source (SINQ).

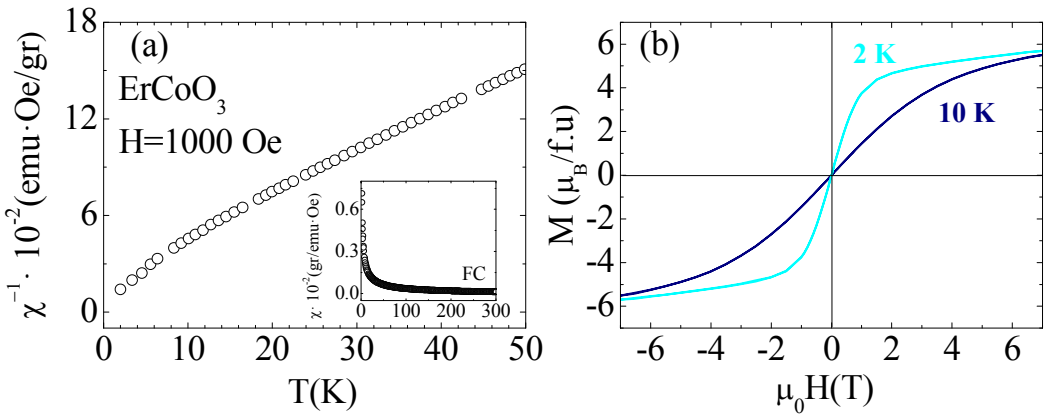

Figure 3. 22. (a) Temperature dependence (from 2 K to 50 K) of the inverse susceptibility measured under field cooling (FC) conditions at 1000 Oe. The inset shows the non inverted susceptibility. (b) Magnetic field dependence of the magnetization measured at 2 K and 10 K for $ErCoO_3$.

In Figure 3. 23 we plot the neutron diffraction patterns data measured at at 1.5 K and 100 K in HRPT instrument (SINQ spallation source) using a wavelength of λ = 1.494 Å. The comparison between the two patterns allows us to confirm the appearance of new magnetic peaks in the low angular range [they are marked by an asterisk (*)] at 1.5 K. We attribute the growth of new peaks at very low temperature to the ordering of Erbium moments and not to the Co moments.

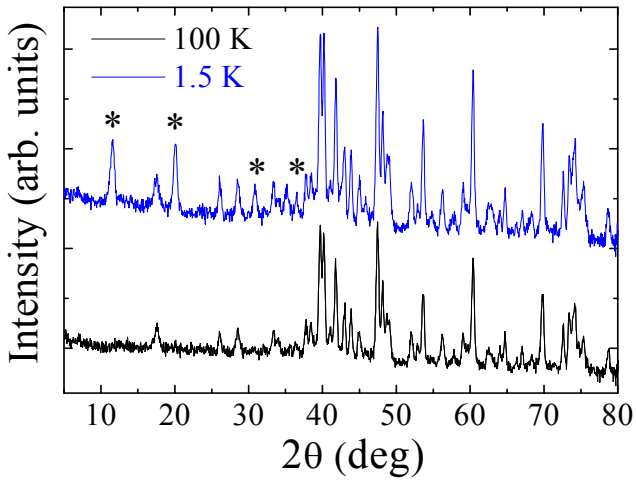

Figure 3. 23. Neutron powder diffraction patterns measured at HRPT beamline in SINQ (PSI) at 100 K and 1.5 K. The (*) peaks reflect the new magnetic peaks appearing due to Er moments ordering.

3.5.2. Structural effects of the spin-state transition up to 1000 K

Additional, diffractions patterns for $ErCoO_3$ have been collected between 100 K and 1000 K on the high resolution D2B diffractometer of the Institute Laue-Langevin (ILL). The data were recorded at the neutron wavelength of λ= 1.594 Å and were analyzed with the Rietveld method using the FULLPROF suite of programs [52]. Rietveld refinements have been successfully refined using a single phase with a space group *Pbnm* (no. 62) and cell parameters $a \approx \sqrt{2}a_0$, $b \approx \sqrt{2}a_0$, $c \approx 2\ a_0$ (where a_0 is the ideal cubic parameter). The refined NPD data at 300 K (upper panel) and at 600 K (lower panel) are shown in Figure 3. 24 and Figure 3. 25 display the projections of the distorted crystal structure. The structural parameters obtained from refinements at different temperatures together with the agreement factors are listed in Table 3. 4.

The thermal evolution of the cell parameters (left panel) and the cell volume (right panel) obtained from the refinements are plotted in Figure 3. 26. We can appreciate that the relation between lattice parameters is $b > c/\sqrt{2} > a$ as expected for other similar perovskites with small size rare-earths. This kind of structures is called O type. In this case the relation between the lattice parameters differs from that light rare-earths where $a > c/\sqrt{2} > b$. We observe that the three lattice parameters expand with temperature, but beyond $T_{SS} \sim 575$ K they enlarge more rapidly The origin of this anomalous expansion is attributed to an increase of the Co^{3+} ion size. It is worth mentioning that the diamagnetic Co^{3+} ion presents an ionic radius size r(LS) = 0.545 Å, whereas in excited states it can reach r(IS) = 0.56 Å or r(HS) = 0.61 Å.

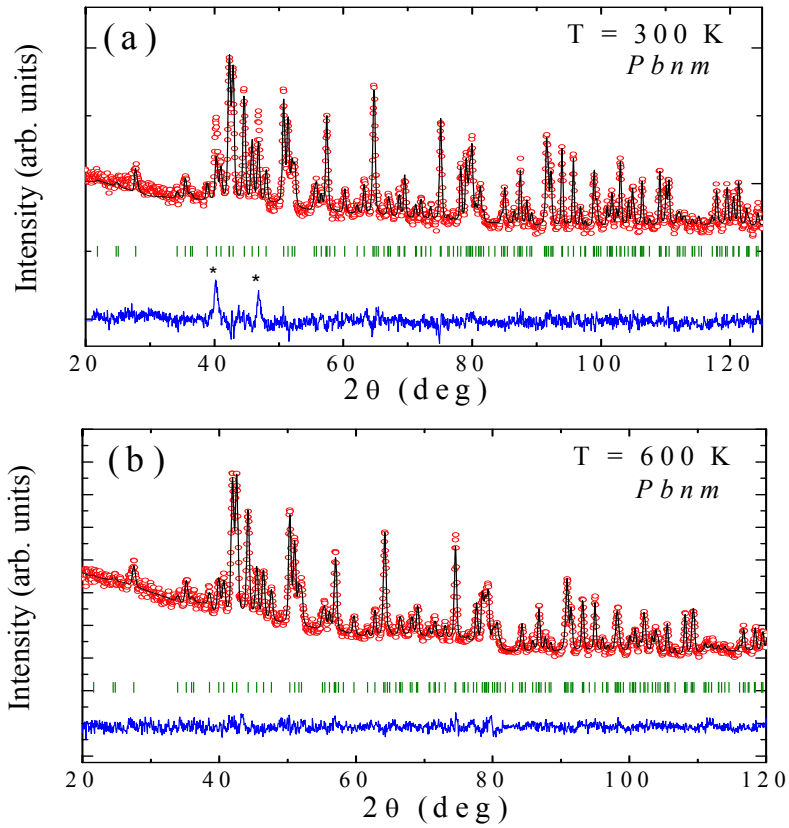

Figure 3. 24. Rietveld refinements (black line) of neutron diffraction patterns (red circles, experimental points; bottom blue line, difference; green lines, Bragg reflections) for $ErCoO_3$ at selected temperatures: (a) 300 K and (b) 600 K. (*) Signal from the vanadium container used at RT.

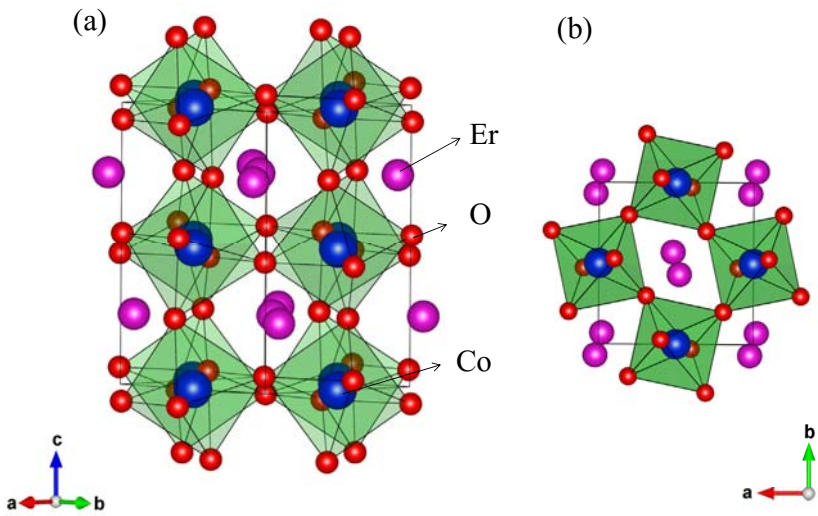

Figure 3. 25. Projections of the orthorhombic crystal structure at 300 K for $ErCoO_3$ obtained from the Rietveld refinement.

The anomalies found in the cell parameters are also observable in the temperature evolution of the cell volume (it expands by around 2%) at T_{SS} when the occupation of excited magnetic states is activated, see Figure 3. 26(b). In the same graph, the red solid line fits the Eq.3.3, which represents the normal thermal evolution below T_{SS}:

$$V_0 = V_1 + V_2\,\Theta\coth(\Theta/T) \qquad \text{(Eq. 3.3)}$$

Table 3. 4. Structural parameters of $ErCoO_3$ as a function of temperature. The space is *Pbnm* (S.G. 62).

T(K)	100 K	300 K	600 K	1000 K
a (Å)	2.1087(2)	5.1158(3)	5.1472(7)	5.2014(4)
b (Å)	5.4114(2)	5.4133(3)	5.4379(9)	5.5230(4)
c (Å)	7.3331(4)	7.3439(4)	7.3815(4)	7.4406(6)
Atomic coordinates: Er 4*c* (*x*, *y*, 1/4), Co *4b* (1/2, 0, 0), O1 *4c* (*x*, *y*, 1/4), O2 *8d* (*x, y, z*)				
Er (*x*)	0.97902(6)	0.9834(7)	0.9810(6)	0.9794(9)
Er (*y*)	0.0709(5)	0.0708(6)	0.0682(5)	0.0721(7)
Er, B_{iso} (Å^2)	1.33(6)	0.85(6)	1.08(6)	1.44(8)
Co, B_{iso} (Å^2)	0.78(3)	0.66(2)	0.91(2)	1.20(3)
O1 (*x*)	0.0971(7)	0.0976(8)	0.0959(7)	0.0983(9)
O1 (*y*)	0.4721(7)	0.4655(8)	0.4733(6)	0.4750(9)
O1, B_{iso} (Å^2)	1.68(8)	0.948(8)	1.28(5)	2.18(9)
O2 (*x*)	0.6942(6)	0.6881(6)	0.6926(5)	0.6963(8)
O2 (*y*)	0.2995(6)	0.3061(7)	0.301085)	0.3045(8)
O2 (*z*)	0.0488(4)	0.0491(4)	0.0475(3)	0.0491(5)
O2, B_{iso} (Å^2)	1.51(6)	0.79(6)	1.30(5)	1.94(8)
Agreement factors:				
χ^2 (%)	1.52	2.03	1.14	1.49
R_B (%)	13.2	8.45	6.36	10.5

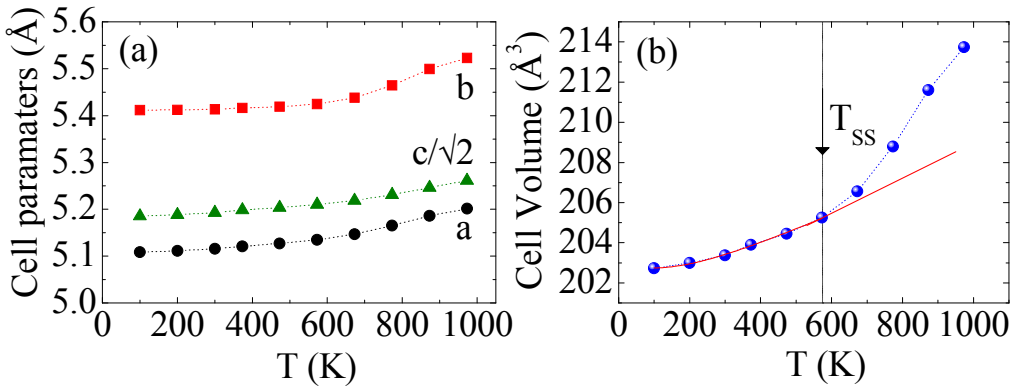

Figure 3. 26. Temperature dependence of (a) the lattice parameters and (b) the cell volume for $ErCoO_3$. The solid line, fitting the equation $V_0 = V_1 + V_2\,\Theta\coth(\Theta/T)$, is a guide to the eye.

The linear thermal expansion coefficients (α) of all three lattice parameters deduced from equation 3.4 are displayed in Figure 3. 27:

$$\alpha(T) = \frac{1}{C_0}\frac{C_2 - C_1}{T_2 - T_1}(K^{-1}) \qquad \text{(Eq. 3.4)}$$

where $C = a$, b or c , C_0 is the value at RT, l_2 and l_1 are values at temperatures T_2 and T_1.

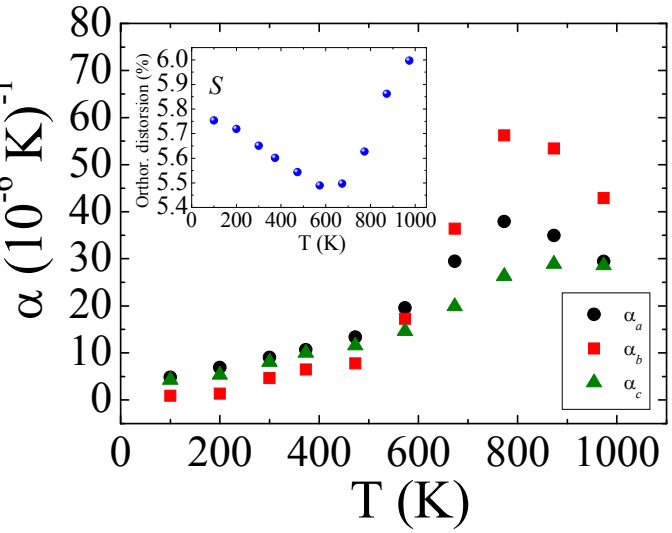

Figure 3. 27. Temperature dependence for the linear thermal expansion along the three cell parameters: α_a (black circles), α_b (red squares), α_c (green triangles). The inset shows the temperature dependence of the orthorhombic strain (*S*).

The thermal expansion shows an initial linear regime between 100 K and 500 K and above 550 K the three coefficients rapidly enhance until above 800 K where all coefficients

start to decrease. In contrast to larger *Ln*-based compounds where two shoulders are visible in the thermal expansion coefficient curve such as $LaCoO_3$ or $PrCoO_3$, here we only detect one maximum. This maximum is considered as the highest excitation ratio of IS or HS Co^{3+} ions. Morever, we must observe in the same figure that coefficient α_b undergoes a large variation as compared to coefficients α_a or α_c. This evidences that the increase of *b* cell parameter is more pronounced in comparison with *a* or $c/\sqrt{2}$. The inset of the same Figure 3. 27 displays an atypical evolution of the orthorhombic distortion defined as $S = 2(b-a)/(a-b)$. We have seen that *S* decreases on heating and beyond T_{SS} a *minimum* is reached. Above this temperature, *S* enhances until 973 K where it seems that *S* continues to increase. This behavior points out that the SS transition is not yet finished at that temperature value in $ErCoO_3$. The same behavior has been also observed in compounds with small rare-earths such as $YCoO_3$, $DyCoO_3$, $GdCoO_3$ or $SmCoO_3$, in contrast to the light *Ln* in which *S* presents a pronounced maximum at T_{SS} [42, 48].

The Co-O bond length evolution up to 1000 K in the equatorial plane (<Co-O_{ab}>) and apical axis (Co-O_c) for $ErCoO_3$ are plotted in Figure 3. 28(a). The temperature dependence of the average <Co-O-Co> bond angle is also plotted in Figure 3. 28(b). At 100 K, the average Co-O distance in the *ab* plane is 1.9 % longer than Co-O distance along the *c* axis, whereas at T_{SS} the difference between the <Co-O_{ab}> and Co-O_c distances reaches a minimum value of 1.5 % and at high temperature the mentioned difference between them is 2.1 % (see Table 3. 5). So, the Co-O bonds do not show a monotonous evolution, although no sign of any static Jahn-Teller distortion of CoO_6 octahedra is observed. However, both distances expand at $T_{SS,}$ but the equatorial bonds present a higher sloping curve above T_{SS} than the apical bonds. That evolution of the Co-O bonds can be also monitored through the thermal evolution of the $d_{Co\text{-}Oab}/d_{Co\text{-}Oc}$ ratio [see Figure 3. 28(b), right axis] which reaches a minimum value at T_{SS} as a result of the SS changes in the Co^{3+} ion.

On the other hand, the evolution of the average <Co-O-Co> bond angle is plotted in Figure 3. 28 (b) (left axis). As expected, we notice this value is notably smaller in $ErCoO_3$ as compared to other much bigger $LnCoO_3$ perovskites (it makes about 148.5º in the maximum point). <Co-O-Co> expands from 147.7º to 148.5º on warming up, but coinciding with T_{SS} we observe a drop of the bond angle. We have thus detected a qualitative change in the evolution of the structural distortion from a SS transition produced by the activation of populated excited states. It is also worth noticing that the different evolution above 600 K in Figure 3. 28(b) holds at least up to 1000 K, our highest temperature reached.

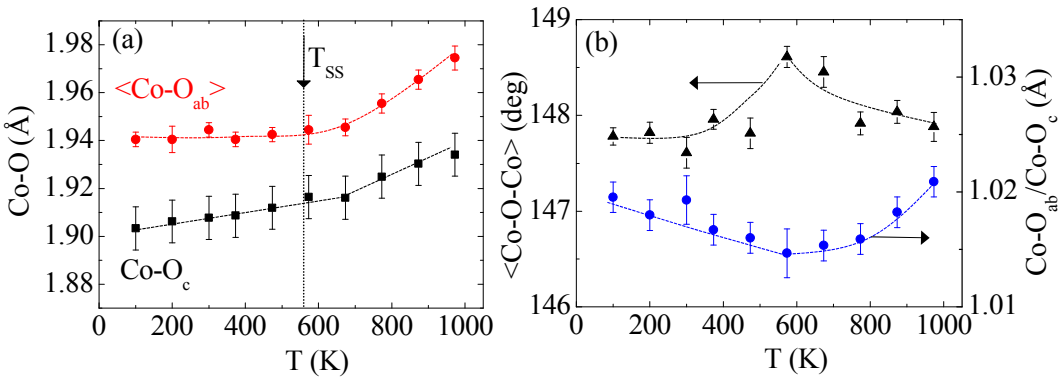

Figure 3. 28. Temperature evolution of (a) the average Co-O_c (black squares) and Co-O_{ab} (red circles) bond lengths in the CoO_6 octahedra; (b) the average Co-O-Co bond angle (black triangles, left axis) and Co-O_{ab}/Co-O_c ratio (blue circles, right axis). The dotted lines are eye-guides.

Table 3. 5. The CoO_6 octahedra distortion and the Co-O-Co bond angles obtained from refinements at different temperatures for $ErCoO_3$.

	100 K	300 K	600 K	1000 K
Co-O average (Å)	1.928(6)	1.932(4)	1.932(3)	1.961(6)
Co-O-Co average (deg)	147.8(9)	147.6(6)	148.6(5)	147.9(2)
Co-O_c(Å) x 2	1.903(1)	1.907(1)	1.918(2)	1.934(6)
Co-O_{ab}(Å) x 2	1.939(3)	1.954(3)	1.936(4)	2.001(5)
Co-O_{ab}(Å) x 2	1.942(3)	1.944(3)	1.943(4)	1.948(5)
Co-O_c-Co (deg)	147.5(5)	147.5(6)	148.6(5)	147.7(2)
Co-O_{ab}-Co (deg)	148.3(5)	147.8(5)	148.6(5)	148.2(5)

The CoO_6 octahedra distortion and the Co-O-Co bond angles obtained from refinements at different temperatures are listed in Table 3. 5. Figure 3. 29 shows a comparison of the distortion in the perovskite structure between $PrCoO_3$ and $ErCoO_3$ at the same temperature.

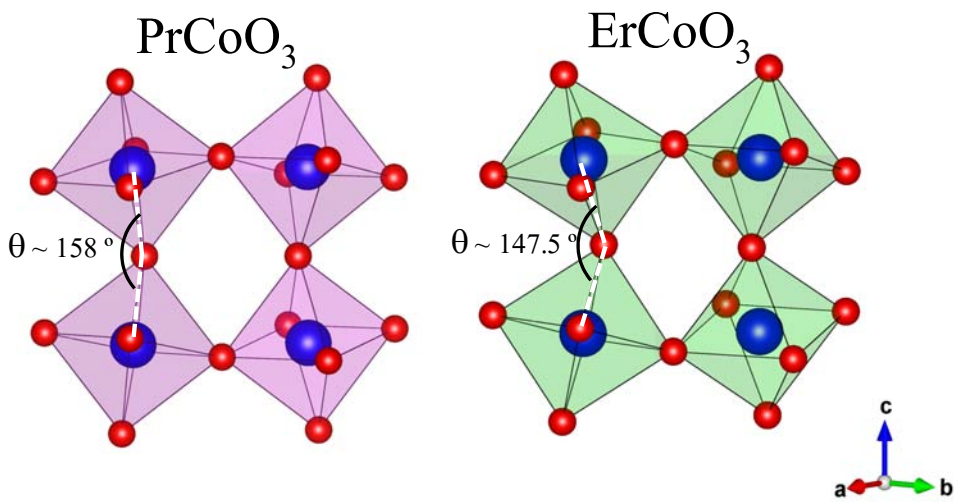

Figure 3. 29. Perspective view of CoO_6 octahedra in $PrCoO_3$ and $ErCoO_3$, where different structural distortion is shown. At the same temperature (300 K) the average Co-O-Co bond angle is much more bent for $ErCoO_3$, with smaller lanthanide.

Let us now compare the previous results with complementary data reported for the $LnCoO_3$ compounds $LaCoO_3$, $PrCoO_3$ and $YCoO_3$. In the case of $LaCoO_3$ the structural data are extracted from Ref. [33], and for $PrCoO_3$ and $YCoO_3$ from Ref. [48] and [47], respectively.
Using the available structural information for the four compounds, next we can compare the temperature evolution of the tilting octahedra. In Figure 3. 30 we plot the thermal evolution of the average <Co-O-Co> bond angle [θ(T)] for the perovskites with small ($LaCoO_3$), moderate ($PrCoO_3$), large ($YCoO_3$), and very large ($ErCoO_3$) distortion up to practically 1000 K. Both of them, the less distorted (La and Pr), show two separately SS transitions (SS1 and SS2). On the other hand, the most distorted compounds (Y and Er) exhibit their first SS transition by around 600 K, close to the SS2 transition for the light lanthanides. The typical slope of the θ(T) curve in a perovskite should present a positive sign. We observe a common behavior in these cobaltites: the SS changes above ~500-600 K bring about an enhanced tilt of the octahedra. The Co-O-Co distortion increases due to the electronic excitations (θ decreases) at the SST in $YCoO_3$ and $ErCoO_3$. And the same effect is visible in $LaCoO_3$ and $PrCoO_3$. In addition, we see that the slope of θ(T) becomes again positive after the second transition in the two bigger compounds (Pr and La). But not below 900 K in the smaller specimens, for which the metallic state requires higher temperatures than for La or Pr. Finally, we recall that the creation of oxygen vacancies is likely in $LaCoO_3$ above ~850 K [33].

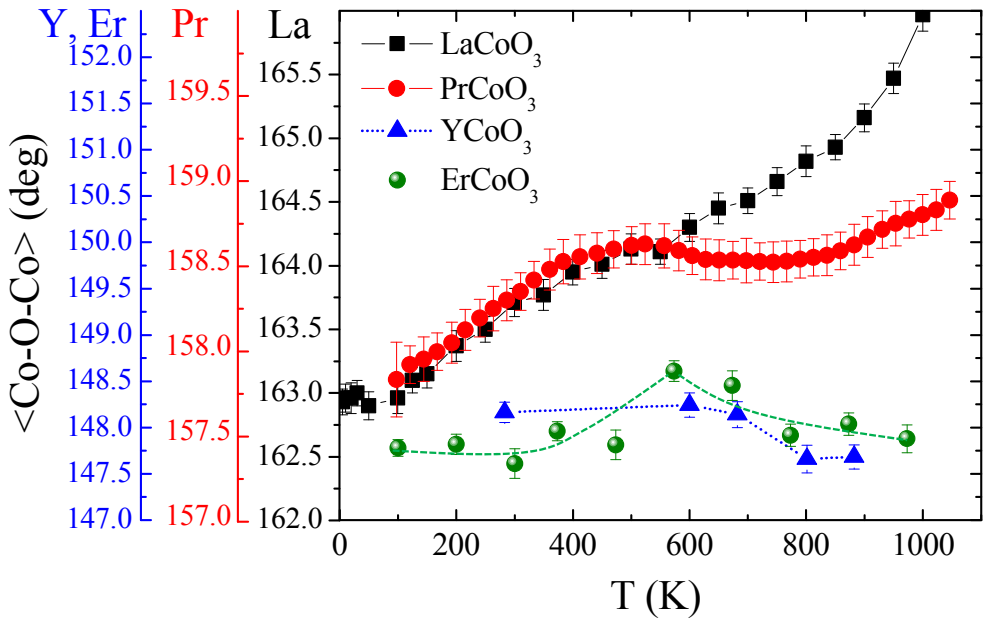

Figure 3. 30. Thermal evolution of the average <Co-O-Co> bond angle for $LaCoO_3$, $PrCoO_3$, $YCoO_3$ and $ErCoO_3$. Data are digitalized for $LaCoO_3$, $PrCoO_3$, $YCoO_3$ from Refs. [33, 47, 48], respectively.

3.6. Evolution of the spin-state crossover in the *Ln*CoO_3 series

The main purpose of this section is to extrapolate the Pr and Er results to the description of the evolution of the spin state crossover in the *Ln*CoO_3 series. It has been commented that in this family the temperature of the SST increases indicating that the low-spin state of Co^{3+} ions is more stable when the ionic radius $<r_A>$ is reduced. During the last years several compounds of the *Ln*CoO_3 series have been synthesized and some of their physical properties have been studied by different authors [42, 47, 48, 50, 53]. Taking advantage of these preliminary studies together with our characterization done in $ErCoO_3$, we can propose a general phase diagram to puzzle the evolution of the SSTs along this series.

Next we will describe the features or physical properties used to identify the onset and width of the SSTs of the different compounds. The first SS transition (T_{SS1}) can be monitored by: (i) magnetic measurements, (ii) the orthorhombic distortion, and (iii) the coefficient of the thermal expansion calculated from the evolution of the cell parameters. In the case of $LaCoO_3$ the two magnetic transitions appear well separated, unlike the most distorted *Ln*CoO_3 samples.

(a) The onset of SS1 transition has been determined from the $T_{ONSET}(\chi)$ seen in the magnetic susceptibility of $LaCoO_3$ [36], $PrCoO_3$ [49], $NdCoO_3$ [49], $GdCoO_3$ [45], $YCoO_3$ [47] and $LuCoO_3$ [44].

(b) Moreover, the maxima of the susceptibility (T_{MAX}) can be taken as the middle point of the transition also plotted in the phase diagram for $LaCoO_3$.

(c) Another physical property that allows us to identified T_{SS1} is the orthorhombic distortion with respect to the pseudocubic lattice as it as defined in Eq. (3.1) and which is plotted in Figure 3.4. One has to notice that only for the heavy rare earths the relation cell parameters is $b > c/\sqrt{2} > a$. In this case, the difference increase between a and b with temperature producing a pronounced *minimum* in the orthorhombic distortion. In contrast, for light rare earths the relation changes to $a>c/\sqrt{2}>b$, being b the parameter changing most, increasing temperature b approaches to a producing a *maximum* that signals the SST. These anomalies in the cell parameters are related with the increase of the Co-O bonds lengths due to the excitations to e_g levels in the Co^{3+} ions. Apart from our measurements we have considered the orthorhombic distortion evolution for several $LnCoO_3$ compounds reported in Ref. [42]. Moreover, the evolution of the cell for $ErCoO_3$ and $LuCoO_3$ were extracted from our neutron data and Ref. [44], respectively.

On the other hand, the second SS transition (T_{SS2}) can be distinguished by different anomalies in measurements like: (i) the resistivity, (ii) the thermoelectric power, (iii) the heat capacity, and also (iv) the thermal expansion coefficient. The reason is that this high-transition-temperature produces an insulator to metal transition (MIT).

(d) The MIT temperatures have been determined from the prominent peak in the $d\ln\rho/d(T^{-1})$ for $LnCoO_3$ (Ln = La to Gd, and Y) [25]. For these compounds the center and width [$W(\rho)$] of the SS2 has been estimated from the full width at high maximum (FWHM) of the peak of $d\ln\rho/d(T^{-1})$ or the energy activation (E_A). We consider the maximum of the peak as the central point of the transition [$T_{MI}(\rho)$]. Notice that above these temperatures ($T>T_{MI}$) the compounds present metallic behavior. However, in most of the cases the spin excitations persist also in the metallic regime. For this reason, the end of the transition is not T_{MI} (we have defined as $T^*=T_{MI}+W/2$), but it has to be extracted from the width of the peaks in the heat capacity [$W(C_p)$] and $d\ln\rho/d(T^{-1})$ (black crosses in Figure 3.32) .

(e) Additionally, we have used the gradient of the Seebeck curve to define $T_{MI}(S)$ for $LnCoO_3$ (Ln = La to Y) [42].

(f) Moreover, the phase diagram has been completed using heat capacity data for other small lanthanides (*Ln* = Ho to Lu) reported in Ref. [43] [$T_{MI}(C_p)$].

(g) The last measurements used to complete the phase diagram were also extracted from Ref.[42] where the authors plotted the linear thermal expansion $\alpha(T)$ for the cobaltites with *Ln*=La, Pr, Nd, Sm, Gd, Dy, and Y as Figure 3.5 (Section 3.2) displays. In the $\alpha(T)$ curve two maxima are visible for $LaCoO_3$, $PrCoO_3$, and $NdCoO_3$ which are signaling T_{SS1} and T_{SS2}, respectively. However, for the intermediate-size and heavy lanthanides only one maximum is visible. It is of interest to note that in $PrCoO_3$, for example, the two maxima in $\alpha(T)$ start overlap. Then, the total width of the two peaks is almost twice the width of the single peak in $YCoO_3$ or $ErCoO_3$. For clarity, we will call SS2 to the only transition at high-temperature in the distorted cobaltites. In such a way, we are associating SS2 to the transition going a metallic state. In order to define the end of the SS1 transition we have taken the first maximum in $\alpha(T)$ for $LaCoO_3$, $PrCoO_3$, $NdCoO_3$, and $SmCoO_3$. For the smaller cobaltites this feature is not visible in $\alpha(T)$. Therefore, in Figure 3.31 and Figure3.32 we have simply drawn the virtual straight line extrapolated from the four biggest compounds.

In Table 3. 6 we gave gathered all temperatures values extracted as described in the precedence paragraph using the information of the table in Figure 3.31 we plot the experimental points (T_{ONSET}, T_{SS1} and T_{SS2}) for SS1 and SS2 transitions extracted from the different physical measurements detailed above. In addition to these points in Figure 3.32 we have added the estimated widths for the transitions inferred as explained above in points (d) and (f).

Finally, observing the phase diagram of the Figure 3.32 we must underline the following conclusions:

(1) not only there is a systematic shift to higher transition temperatures by reducing $<r_A>$, but interestingly the separation between the two SSTs dramatically is reduced for cobaltites smaller than $PrCoO_3$.

(2) there are three distinguishable electronic phases in compounds based on *Ln* ions larger than $SmCoO_3$: phase 1 (PH1, lowest SS), phase 2 (PH2, intermediate spin [LS:HS/IS state]), and phase 3 (PH3, metallic phase with the highest SS).

(3) for the cobaltites smaller than $SmCoO_3$, only PH1 and PH3 are thermodynamically stable. Thus, PH2 becomes metastable.

(4) The boundary region between PH1 and PH2 (yellow zone) is narrower than the boundary region between PH2 and PH3 (blue zone) for the largest compounds.

(5) In the systems smaller than $SmCoO_3$ there is a tendency of virtual boundary regions to overlap (green zone).

The difference in temperature between the end of PH1 [$T_{ONSET}(\chi)$] and the metallic high temperature phase is approximately independent of $<r_A>$ or it shows a hard variation with $<r_A>$. In all cases the metallic state is preceded of a temperature interval with remarkable electronic fluctuations. Figure 3.31 suggests that PH2 transforms into a thermodynamically unstable phase for small $<r_A>$ ionic sizes. As a consequence, by distorting the perovskite structure we force the system to notable enlarge the electronically unstable region which precedes the metallic regime. Figure 3.32 seems to suggest that the dynamic properties and magnetic fluctuations in the metallic state of light and heavy specimens could significantly differ.

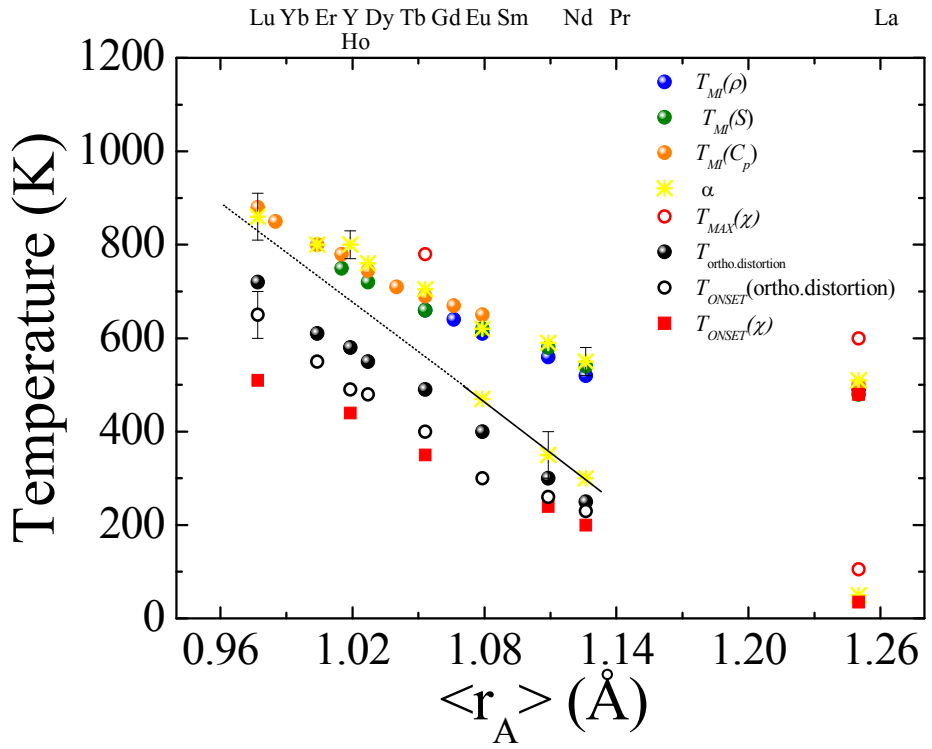

Figure 3. 31. Proposed phase diagram for $LnCoO_3$ as a function of the ionic radius $<r_A>$. Red solid squares are the T_{SS1} onset (T^{O}_{SS1}) values from magnetic susceptibility [36, 44, 45, 47, 49]. T_{MAX} (red open circles) is the maximum of the magnetic susceptibility associated to T_{SS1} and T_{SS2}, respectively. Black open circles and black solid circles are the T_{ONSET} and T_{SS1} values extracted from anomalies in the orthorhombic distortion [42]. Solid circles (blue, green and orange) represent the MIT temperatures from resistivity [25], thermoelectric power [42] and heat capacity [43]. Yellow crosses represent T_{SS1} and T_{SS2} from thermal expansion coefficient. See explanation in the text.

Table 3. 6. Transition temperatures T_{SS1} and T_{SS2} from different physical measurements for $LnCoO_3$ series. W is considered as the thermal amplitude of transitions as extracted from resistivity and heat capacity measurements, respectively.

$LnCoO_3$	$<r_A>$ (Å)	$T_{.ortho.\ distortion}$ (K)	$T_{ONSET}(\chi)$ (K)		$T_{MAX}(\chi)$ (K)		$T_{MI}(S)$ (K)	$T_{MI}(\rho)$ (K)	$W(\rho)$ (K)	$T_{MI}(C_p)$ (K)	$W(C_p)$ (K)	α (K)	
			T^O_{SS1}	T^O_{SS2}	T_{SS1}	T_{SS2}						T_{SS1}	T_{SS2}
$LaCoO_3$	1.25	-	35	480	50.2	550	480	490	210	500	270	50	510
$PrCoO_3$	1.126	230	200	-	-	-	540	520	230	-	-	300	550
$NdCoO_3$	1.109	300	300	-	-	-	580	560	240	-	-	350	590
$SmCoO_3$	1.079	400	-	-	-	-	620	610	230	650	350	-	620
$EuCoO_3$	1.066	-	-	-	-	-	-	640	230	670	330	-	-
$GdCoO_3$	1.053	490	350	-	-	-	660	660	220	690	340	-	705
$TbCoO_3$	1.04	-	-	-	-	-	-	-		710	330	-	-
$DyCoO_3$	1.027	550	-	-	-	-	720	-		745	360	-	760
$HoCoO_3$	1.015	-	-	-	-	-	750	-		780	370	-	-
$YCoO_3$	1.019	580	440	-		-	-	-		-	-	-	800
$ErCoO_3$	1.004	610	-	-	-	-	-	-		800	380	-	800
$YbCoO_3$	0.985	-	-	-	-	-	-	-		850	380	-	-
$LuCoO_3$	0.977	720	510	-		-	-	-		880	380	-	860

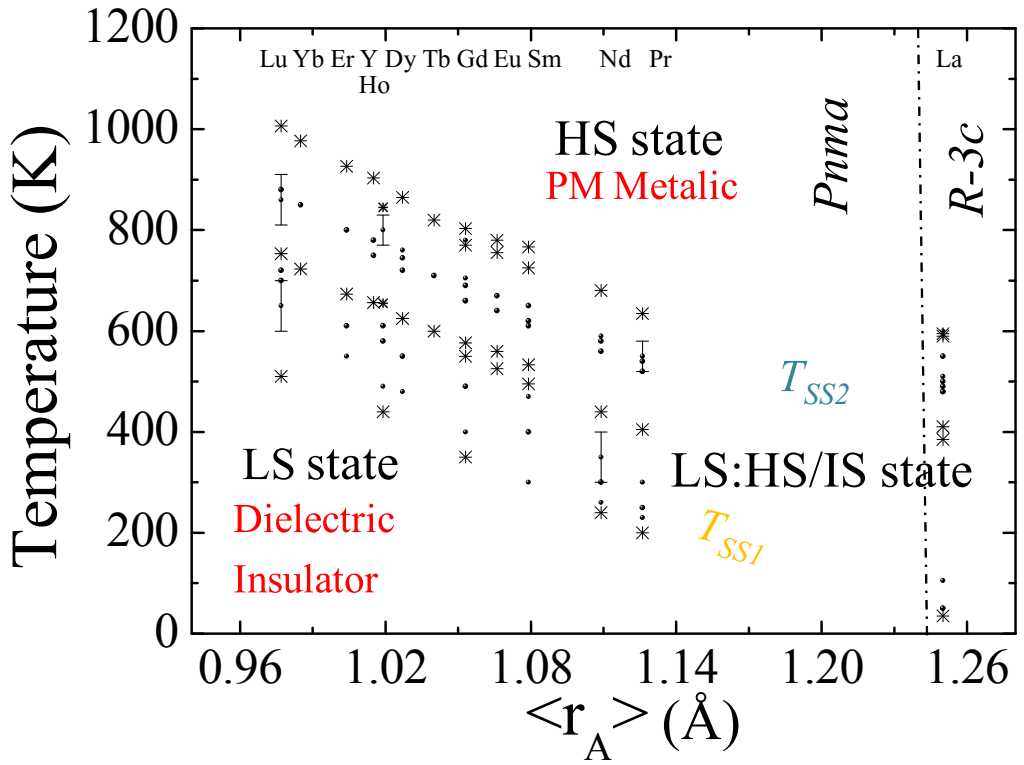

Figure 3. 32. Proposed phase diagram for $LnCoO_3$ as a function of the ionic radius $<r_A>$.The boundary region between the PH1 and PH2 (PH2 and PH3) is colored yellow (blue). The estimated virtually overlapped region between the two boundaries is shown in green. The black circles indicate T_{SS1} and T_{SS2}. and black crosses the T_{ONSET} and T^* of each transitions from the physical measurements detailed and referred in the text.

3.7. Summary and conclusions

Along this chapter we have investigated the nature of the spin-state transition in the $LnCoO_3$ (*Ln*: lanthanide) cobaltites as a function of temperature and *Ln* size. Combining our results on several particular compositions with the physical properties characterization previously reported for different $LnCoO_3$ compounds, we have proposed a general phase diagram for the family, focused on the width of boundary regions between the different electronic phases and their evolution with the distortion of the structure.

The investigation done in $PrCoO_3$ (moderate distortion) by means of XAS techniques is to our knowledge the first one reported in a $LnCoO_3$ compound different to $LaCoO_3$ with *Pnma* structure. The spectroscopic analysis was focused on the first Co SST, whereas the analysis of the second SS crossover was based on structural data. Changes in the absorption spectra demonstrate the activation of the SS crossover above T~200 K. The observed changes progressively evolve with temperature (without abrupt variations). We have also used XES measurements to gain information on the effective Co spin-state in $PrCoO_3$ at room temperature. The determination of the effective spin from emission experiments has latter been used for the determination of the possible electronic configuration. For that, we have carried out CTM calculations in order to reproduce the Co *2p* XAS spectra for $PrCoO_3$ at room temperature. The combined experimental results from XAS, XES, and CTM calculations establish that the model that better reproduces the Co XAS spectra in PH2 (between T_{SS1} and T_{SS2}) is an inhomogeneous mixed spin-state system (LS $\rightarrow$ LS+HS). This model works clearly better than the IS based model for Co^{3+} ions between the two transitions.

The analysis of the structural evolution up to 1000 K in the highly distorted $ErCoO_3$ using neutron power diffraction was used to monitor the electronic phenomena associated with the spin-state changes of Co^{3+} ions. The evolution of some structural parameters such as the lattice, cell volume, Co-O distances, or Co-O-Co bond angles reflect a broad SS crossover from LS to excited states that begins at T_{SS} ~ 575 K. In this distorted cobaltite the Co-O bond lengths isotropically increase from *Tss* due to an expansion of the CoO_6 octahedra by an electronic origin states, without signs of Jahn-Teller distortion. In addition, an atypical augmentation of the orthorhombic strain gives direct evidences of the electronic changes in the octahedra. In contrast with typical thermally assisted decrease of the structural distortion, we have described an anomalous increase of the Co-O-Co distortion produced by the increase of the SS.

.

BIBLIOGRAPHY

[1] P. M. Raccah and J. B. Goodenough, "First-Order Localized-Electron → Collective-Electron Transition in $LaCoO_3$," *Phys. Rev.*, vol. 155, no. 1965, p. 932, 1967.

[2] M. A Senaris-Rodriguez and J. B. Goodenough, "Magnetic and Transport Properties of the System," *Journal of Solid State Chemistry*, vol. 118. pp. 323–336, 1995.

[3] C. Martin, A. Maignan, D. Pelloquin, N. Nguyen, and B. Raveau, "Magnetoresistance in the oxygen deficient $LnBaCo_2O_{5.4}$ (*Ln*=Eu, Gd) phases," *Appl. Phys. Lett.*, vol. 71, no. 10, p. 1421, 1997.

[4] I. Troyanchuk, N. Kasper, D. Khalyavin, H. Szymczak, R. Szymczak, and M. Baran, "Phase Transitions in the $Gd_{0.5}Ba_{0.5}CoO_3$ Perovskite," *Phys. Rev. Lett.*, vol. 80, no. 15, pp. 3380–3383, 1998.

[5] A. Podlesnyak, K. Conder, E. Pomjakushina, and A. Mirmelstein, "Layered Cobalt Perovskites: Current Topics and Future Promises," *ChemInform*, vol. 39, no. 40, Sep. 2008.

[6] B. Raveau and M. Motin Seikh, *Cobalt oxides. From Crystal Chemistry to Physics*. WILEY-VCH, 2012.

[7] N. B. Ivanova, S. G. Ovchinnikov, M. M. Korshunov, I. M. Eremin, and N. V. Kazak, "Specific features of spin, charge, and orbital ordering in cobaltites," *Uspekhi Fiz. Nauk*, vol. 52, pp. 789–810, 2009.

[8] Y. Takeda, H. Ueno, N. Imanishi, N. Sammes, and M. B. Phillipps, "$Gd_{1-x}Sr_xCoO_3$ for electrode of solid oxide fuel cells," *Solid State Ionics*, vol. 2738, no. 96, 1996.

[9] Y. Teraoka, "Oxygen permeation through perovskite-type oxides," *Chem. Lett.*, vol. 11, pp. 1743–1746, 1985.

[10] Y. Teraoka, "Mixed ionic-electronic conductivity of $La_{1-x}Sr_xCo_{1-y}Fe_yO_{3-\delta}$ perovskite type-oxide," *Mater. Res. Bull.*, vol. 23, pp. 51–58, 1988.

[11] C. R. Michel, A. S. Gago, H. Guzman, E. R. López-Mena, and D. Lardizabal, "Electrical properties of the perovskite $Y_{0.90}Sr_{0.1}CoO_{3-\delta}$ prepared by a solution method," *Mater. Res. Bull.*, vol. 39, pp. 2295–2302, 2004.

[12] J. Moon, Y. Masuda, W. Seo, and K. Koumoto, "Ca-doped $HoCoO_3$ as *p*-type oxide thermoelectric material," *Mat. Lett*, vol. 48 pp. 225–229, 2001.

[13] M. Abbate, J. C. Fuggle, a. Fujimori, L. H. Tjeng, C. T. Chen, R. Potze, G. a. Sawatzky, H. Eisaki, and S. Uchida, "Electronic structure and spin-state transition of $LaCoO_3$," *Phys. Rev. B*, vol. 47, no. 24, pp. 16124–16130, 1993.

[14] M. Korotin, S. Ezhov, I. Solovyev, V. Anisimov, D. Khomskii, and G. Sawatzky, "Intermediate-spin state and properties of $LaCoO_3$," *Phys. Rev. B*, vol. 54, no. 8, pp. 5309–5316, 1996.

[15] K. Knížek, P. Novák, and Z. Jirák, "Spin state of $LaCoO_3$: Dependence on CoO_6 octahedra geometry," *Phys. Rev. B*, vol. 71, no. 054420, pp. 1–6, 2005.

[16] D. Phelan, D. Louca, S. Rosenkranz, S. H. Lee, Y. Qiu, P. J. Chupas, R. Osborn, H. Zheng, J. F. Mitchell, J. R. D. Copley, J. L. Sarrao, and Y. Moritomo, "Nanomagnetic droplets and implications to orbital ordering in $La_{1-x}Sr_xCoO_3$," *Phys. Rev. Lett.*, vol. 96, no. 027201, pp. 6–9, 2006.

[17] M. J. R. Hoch, S. Nellutla, J. Van Tol, E. S. Choi, J. Lu, H. Zheng, and J. F. Mitchell, "Diamagnetic to paramagnetic transition in $LaCoO_3$," *Phys. Rev. B,* vol. 79, no. 214421, pp. 1–7, 2009.

[18] M. W. Haverkort, Z. Hu, J. C. Cezar, T. Burnus, H. Hartmann, M. Reuther, C. Zobel, T. Lorenz, a. Tanaka, N. B. Brookes, H. H. Hsieh, H. J. Lin, C. T. Chen, and L. H. Tjeng, "Spin state transition in $LaCoO_3$ studied using soft X-ray absorption spectroscopy and magnetic circular dichroism," *Phys. Rev. Lett.*, vol. 97, no.176405, pp. 38–41, 2006.

[19] A. Podlesnyak, S. Streule, J. Mesot, M. Medarde, E. Pomjakushina, K. Conder, A. Tanaka, M. W. Haverkort, and D. I. Khomskii, "Spin-state transition in $LaCoO_3$: Direct neutron spectroscopic evidence of excited magnetic states," *Phys. Rev. Lett.*, vol. 97, no. 247208. December, pp. 1–4, 2006.

[20] R. F. Klie, J. C. Zheng, Y. Zhu, M. Varela, J. Wu, and C. Leighton, "Direct measurement of the low-temperature spin-state transition in $LaCoO_3$," *Phys. Rev. Lett.*, vol. 99, no. 047203, pp. 1–4, 2007.

[21] M. Zhuang, W. Zhang, and N. Ming, "Competition of various spin states of $LaCoO_3$," *Phys. Rev. B*, vol. 57, no. 17, pp. 10705–10709, 1998.

[22] K. Knížek, Z. Jirák, J. Hejtmánek, and P. Novák, "Character of the excited state of the Co^{3+} ion in $LaCoO_3$," *J. Phys. Condens. Matter*, vol. 18, pp. 3285–3297, 2006.

[23] K. Asai, P. Gehring, H. Chou, and G. Shirane, "Temperature-induced magnetism in $LaCoO_3$" *Phys. Rev. B* ,vol. 40, no. 16, pp. 982–985, 1989.

[24] M. A. Señarıs-Rodrıguez and J. B. Goodenough, "$LaCoO_3$ Revisited," *Journal of Solid State Chemistry*, vol. 116. pp. 224–231, 1995.

[25] S. Yamaguchi, Y. Okimoto, and Y. Tokura, "Bandwidth dependence of insulator-metal transitions in perovskite cobalt oxides," *Phys. Rev. B*, vol. 54, no. 16, pp.R11022–R11025, 1996.

[26] S. Stølen, F. Grønvold, H. Brinks, T. Atake, and H. Mori, "Energetics of the spin transition in $LaCoO_3$," *Phys. Rev. B*, vol. 55, no. 21, pp. 14103–14106, 1997.

[27] J. B. Goodenough, "An interpretation of the magnetic properties of the perovskite-type mixed crystals $La_{1-x}Sr_xCoO_{3-\lambda}$," *J. Phys. Chem. Solids*, vol. 6, pp. 287–297, 1958.

[28] S. Noguchi, S. Kawamata, K. Okuda, H. Nojiri, and M. Motokawa, "Evidence for the excited triplet of Co^{3+} in $LaCoO_3$," *Phys. Rev. B*, vol. 66, no. 094404, pp. 1–5, 2002.

[29] N. Sundaram, Y. Jiang, I. E. Anderson, D. P. Belanger, C. H. Booth, F. Bridges, J. F. Mitchell, T. Proffen, and H. Zheng, "Local Structure of $La_{1-x}Sr_xCoO_3$ Determined from EXAFS ans Neutron Pair Distribution Function Studies," *Phys. Rev. Lett.*, vol. 102, no. 026401, 2009.

[30] S. Yamaguchi, Y. Okimoto, H. Taniguchi, and Y. Tokura, "Spin-state transition and high-spin polarons in $LaCoO_3$," *Phys. Rev. B*, vol. 53, no. 6, pp. 2926–2929, 1996.

[31] I. A. Nekrasov, S. V. Streltsov, M. A. Korotin, and V. I. Anisimov, "The influence of the rare earth ions radii on the Low Spin to Intermediate Spin state transition in lanthanide cobaltite perovskites: $LaCoO_3$ vs. $HoCoO_3$," *Phys. Rev. B* , vol. 63, no. 235113, 2003.

[32] T. Vogt, J. A. Hriljac, N. C. Hyatt, and P. Woodward, "Pressure-Induced Intermediate-to-Low Spin State Transition in $LaCoO_3$," *Phys. Rev. B*, vol. 67, no. 140401(R), p. 3, 2002.

[33] P. G. Radaelli and S.-W. Cheong, "Structural phenomena associated with the spin-state transition in $LaCoO_3$," *Phys. Rev. B*, vol. 66, no. 094408, p. 33, 2002.

[34] S. Yamaguchi, Y. Okimoto, and Y. Tokura, "Local lattice distortion during the spin-state transition in $LaCoO_3$," *Phys. Rev. B*, vol. 55, no. 14, pp. R8666–R8669, 1997.

[35] G. Vankó, J.-P. Rueff, A. Mattila, Z. Németh, and A. Shukla, "Temperature and pressure-induced spin-state transitions in $LaCoO_3$," *Phys. Rev. B* , vol. 73, no. 024424, pp. 1–9, 2005.

[36] M. Medarde, C. Dallera, M. Grioni, J. Voigt, a. Podlesnyak, E. Pomjakushina, K. Conder, T. Neisius, O. Tjernberg, and S. N. Barilo, "Low-temperature spin-state transition in $LaCoO_3$ investigated using resonant X-ray absorption at the Co *K* edge," *Phys. Rev. B - Condens. Matter Mater. Phys.*, vol. 73, pp. 1–10, 2006.

[37] G. Maris, Y. Ren, V. Volotchaev, C. Zobel, T. Lorenz, and T. T. M. Palstra, "Evidence for orbital ordering in $LaCoO_3$," *Phys. Rev. B* , vol. 67, no., 224423, pp. 1–5, 2003.

[38] "image $LaCoO_3$." [Online]. http://vlab-nu.jp/en/e_research/131028_$LaCoO_3$.html.

[39] N. O. Golosova, D. P. Kozlenko, a. I. Kolesnikov, V. Y. Kazimirov, M. B. Smirnov, Z. Jirák, and B. N. Savenko, "Evolution of the phonon density of states of $LaCoO_3$ over the spin state transition," *Phys. Rev. B*, vol. 83, no. 214305, pp. 1–6, 2011.

[40] G. Thornton, G. Thornton, B. C. Tofield, B. C. Tofield, a W. Hewat, and a W. Hewat, "A Neutron Diffraction study of $LaCoO_3$ in the Temperature Range 4.2 K < T 2148 K," *J. Solid State Chem.*, vol. 307, pp. 301–307, 1986.

[41] B. Y. R. D. Shannon, M. H, N. H. Baur, O. H. Gibbs, M. Eu, and V. Cu, "Revised Effective Ionic Radii and Systematic Studies of Interatomie Distances in Halides and Chaleogenides " *Acta Cryst.* 1976.

[42] K. Knížek, Z. Jirák, J. Hejtmánek, M. Veverka, M. Maryško, G. Maris, and T. T. M. Palstra, "Structural anomalies associated with the electronic and spin transitions in *Ln*CoO_3," *Eur. Phys. J. B*, vol. 47, pp. 213–220, 2005.

[43] M. Tachibana, T. Yoshida, H. Kawaji, T. Atake, and E. Takayama-Muromachi, "Evolution of electronic states in $RCoO_3$ (R=rare earth): Heat capacity measurements," *Phys. Rev. B*, vol. 77, no. 094402, pp. 1–5, 2008.

[44] G. Demazeu, M. Pouchard, and P. Hagenmuller, "Sur de Nouveaux Compo & de la Perovskite," *J. Solid State Chem.*, vol. 9, pp. 202–209, 1974.

[45] Y. S. Orlov, L. a. Solovyov, V. a. Dudnikov, a. S. Fedorov, a. a. Kuzubov, N. V. Kazak, V. N. Voronov, S. N. Vereshchagin, N. N. Shishkina, N. S. Perov, K. V. Lamonova, R. Y. Babkin, Y. G. Pashkevich, a. G. Anshits, and S. G. Ovchinnikov, "Structural properties and high-temperature spin and electronic transitions in $GdCoO_3$: Experiment and theory," *Phys. Rev. B - Condens. Matter Mater. Phys.*, vol. 88, 2013.

[46] J. Yu, D. Phelan, and D. Louca, "Spin-state transitions in $PrCoO_3$ investigated by neutron scattering," *Phys. Rev. B*, vol. 84, no. 132410, pp. 1–4, 2011.

[47] K. Knížek, Z. Jirák, J. Hejtmánek, M. Veverka, M. Maryško, B. Hauback, and H. Fjellvåg, "Structure and physical properties of $YCoO_3$ at temperatures up to 1000K," *Phys. Rev. B*, vol. 73, no. 2027, pp. 1–6, 2006.

[48] K. Knížek, J. Hejtmánek, Z. Jirák, P. Tomeš, P. Henry, and G. André, "Neutron diffraction and heat capacity studies of $PrCoO_3$ and $NdCoO_3$," *Phys. Rev. B,* vol. 79, no. 134103, pp. 1–7, 2009.

[49] J. Q. Yan, J. S. Zhou, and J. B. Goodenough, "Bond-length fluctuations and the spin-state transition in $LnCoO_3$ (Ln=La, Pr, and Nd)," *Phys. Rev. B,* vol. 69, no.134409, pp. 1–6, 2004.

[50] J. A. Alonso, M. J. Martínez-Lope, C. de la Calle, and V. Pomjakushin, "Preparation and structural study from neutron diffraction data of $RCoO_3$ (R=Pr, Tb, Dy, Ho, Er, Tm, Yb, Lu) perovskites," *J. Mater. Chem.*, vol. 16, pp. 1555–1560, 2006.

[51] R. H. E. Van Doorn, H. Kruidhof, A. Nijmeijer, L. Winnubst, and A. J. Bruggraaf, "Preparation of $La_{0.30}Sr_{0.70}CoO_{3-\delta}$ perovskite by thermal decomposition of metal- EDTA complexes," *J. Mater. Chem.*, vol. 8, pp. 2109–2112, 1998.

[52] J. Rodríguez-Carvajal, "Recent advances in magnetic structure determination by neutron powder diffraction," *Phys. B Condens. Matter*, vol. 192, pp. 55–69, 1993.

[53] H. W. Brinks, H. Fjellvag, A. Kjekshys, and B. C. Hauback, "Structure and Magnetism of $Pr_{1-x}Sr_xCoO_3$," *Journal of Solid State Chemistry*, vol. 147. pp. 464–477, 1999.

[54] M. Sikora, K. Knizek, C. Kapusta, and P. Glatzel, "Evolution of charge and spin state of transition metals in the $LaMn_{(1-x)}Co_xO_3$ perovskite series," *J. Appl. Phys.*, vol. 103, no. 07C907, 2008.

[55] G. Vankó, T. Neisius, G. Molnár, F. Renz, S. Kárpáti, A. Shukla, and F. M. F. De Groot, "Probing the 3D spin momentum with X-ray emission spectroscopy: The case of molecular-spin transitions," *J. Phys. Chem. B*, vol. 110, pp. 11647–11653, 2006.

[56] J. Herrero-Martín, A. Mirone, J. Fernández-Rodríguez, P. Glatzel, J. García, J. Blasco, and J. Geck, "Hard x-ray probe to study doping-dependent electron redistribution and strong covalency in $La_{1-x}Sr_{1+x}MnO_4$," *Phys. Rev. B ,* vol. 82, no. 075112, pp. 1–8, 2010.

[57] J. Herrero-Martín, J. L. García-Muñoz, K. Kvashnina, E. Gallo, G. Subías, J. a. Alonso, and a. J. Barón-González, "Spin-state transition in $Pr_{0.5}Ca_{0.5}CoO_3$ analyzed by x-ray absorption and emission spectroscopies," *Phys. Rev. B*, vol. 86, no. 125106, pp. 1–6, 2012.

[58] R. D. Cowan, *The theory of Atomic structure and Spectra*, 1981st ed. Berkeley, CA: University of California, 1981.

Chapter 4

Magnetostructural effects and spin-lattice coupling in $Pr_{0.50}Sr_{0.50}CoO_3$

4.1. Motivation

Co oxides present a rich variety of interesting physical properties such as non-conventional magnetic and electronic phase transitions, largely determined by the electronic filling of the Co 3*d* valence band. A good example of simple cobalt oxides with spin-charge-lattice coupling that are gaining an interest for future applications in the field of Spintronics are the half-doped $Pr_{0.50}A_{0.50}CoO_3$ (A = Ca, Sr) perovskites. These two families of compounds interestingly exhibit very distinct structural, electrical, and magnetic properties whose interpretation has been largely controversial during many years and it continues to inspire numerous investigations.

Moreover, after the observation of exceptional photoresponse properties in $Pr_{0.50}Ca_{0.50}CoO_3$ (PCCO), where spin-state (SS) changes are responsible for the generation of metallic domains after photoirradiation in the non-conducting state, cobalt oxides are attracting much more attention in the field of strongly correlated electron systems. Such discovery triggered us to a new perspective on the study of PCCO, focused on understanding the challenging magnetic behavior and the origin of the striking spin-lattice coupling in $Pr_{0.50}Sr_{0.50}CoO_3$ (PSCO).

In this chapter the structural, magnetic and electronic characterization of this last synthesized Pr-based cobaltite is presented. This has been possible by combining neutron diffraction and different synchrotron X-ray techniques. One of the main points in this chapter is the detailed structural analysis. The crystal and magnetic structure of PSCO has long been a matter of debate and it requires further investigations. So, the different mechanisms proposed for the double ferromagnetic transition in recent literature have been checked. Also, the investigation has been extended to similar compounds in polycrystalline, thin film, or single crystal forms where the anomalous magnetic transition may be suppressed or remain unchanged, depending on the type/degree of perovskite distortion.

4.2. Introduction

4.2.1. $Ln_{1-x}A_xCoO_3$ systems

Since the investigations made in $LaCoO_3$ and other rare-earth cobaltites, the scientific community synthesized new hole-doped compounds with general formula $Ln_{1-x}A_xCoO_3$ (A = Ca, Sr, Ba). The substitution of the trivalent rare-earth by divalent alkaline earths lead to a mixed valence Co^{3+}/Co^{4+} similarly to the case of manganites. This substitution at the A-site may considerably alter the physical properties of these cobaltites, leading to the appearance of: new magnetic transitions, high-temperature ferromagnetism, colossal magnetoresistance (MR), charge ordering, or magnetoelectronic phase separation [1–3]. One of the most investigated systems is $La_{1-x}Sr_xCoO_3$, whereas there are only a few studies on $La_{1-x}Ca_xCoO_3$ and $La_{1-x}Ba_xCoO_3$. As in the manganese-based systems, if the Strontium ions are substituted by lanthanide ions, a ferromagnetic (FM) and metallic phase appears. However, the maximum Curie temperature is observed around a concentration $x \sim 0.5$ ($Ln_{0.50}Sr_{0.50}CoO_3$) instead of x~0.33 like in manganites ($Ln_{0.67}Sr_{0.33}MnO_3$) [4]. It is believed that the responsible for the ferromagnetism in cobaltites is a magnetic interaction of the double-exchange type between Co^{3+} and Co^{4+} ions [5–7]. Moreover, upon doping with Sr ions, the structural distortion also changes.

One example is the $La_{1-x}Sr_xCoO_3$ compound. As we know, the $LnCoO_3$ compounds present an orthorhombic structure (*Pnma,* No. 62) except $LaCoO_3$, which has a rhombohedral structure (*R-3c*, No.148). So, $La_{1-x}Sr_xCoO_3$ presents a rhombohedral structure in the $0 \leq x \leq 0.5$ range. When the Sr doping gets beyond $x \sim 0.5$ the crystal symmetry evolves to cubic (*Pm3m*, No. 221) [8, 9]. .

Many studies have contributed to set up the complex magnetic phase diagram of $La_{1-x}Sr_xCoO_3$ with increasing Sr content, but the most detailed work about the evolution of its

properties was reported by M. A. Señaris and J. B. Goodenough in 1995 [10]. Figure 4.1 shows the *T*-*x* phase diagram of $La_{1-x}Sr_xCoO_3$ ($0 \leq x \leq 0.5$).

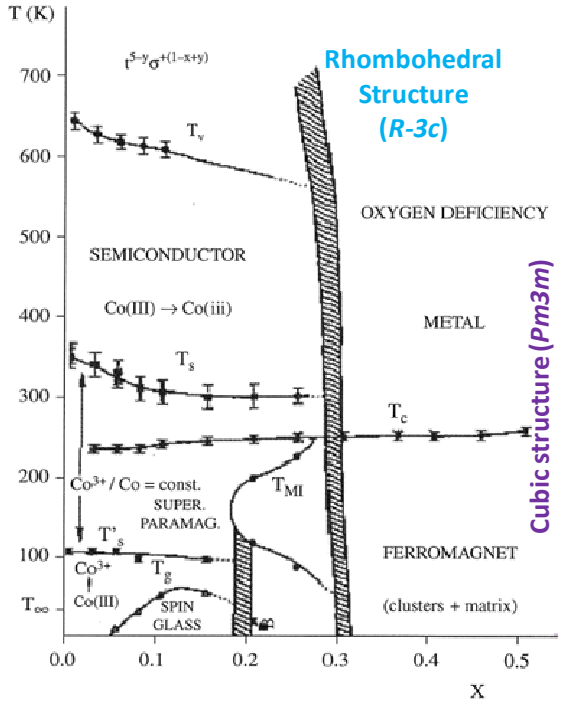

Figure 4. 1. *T*-*x* phase diagram of $La_{1-x}Sr_xCoO_3$.
Reproduced from Ref. [10]

Main characteristic upon Sr^{2+} doping:

(i) $0 < x < 0.1$: superparamagnetic clusters at T_C ~230 K;

(ii) $0.1 \leq x \leq 0.18$: spin-glass clusters at $T_g < T_C$;

(iii) $0.18 < x \leq 0.25$: coupling between ferromagnetic clusters below a metal-insulator transition at $T_{MI} < T_C$ ~240 K;

(iv) $x > 0.2$-25: long-range ferromagnetic order and metallic clusters;

(v) $x = 0.5$: cluster glass freezing and PM to FM transition at $T_C \sim 250$ K

A first inspection to the electronic configuration in the doped compound suggests that the Co^{4+} and Co^{3+} ions are in the LS and IS, respectively. However, the spin state in the doped $La_{1-x}Sr_xCoO_3$ is still an unresolved issue as in the undoped cobaltite. Calorimetric studies reported by Tsubouchi et *al*. [11] suggest that the SS gradually changes as *x* increases in the paramagnetic-insulating phase ($0 < x \leq 0.18$). The stabilization of Co^{3+} ions in the intermediate-spin (IS) with Sr doping was attributed to Jahn-Teller distortions (JT) as in the $LaCoO_3$ system. This hypothesis is supported by several experiments such as, the pair density function (PDF), neutron diffraction [12], elastic and inelastic neutron scattering [13], and X-ray powder diffraction [14]. These experimental results also agree in the presence of a JT distortion for concentrations $x \geq 0.18$. However, later Sundaram et *al.* [15] determined the local structure of $La_{1-x}Sr_xCoO_3$ using X-ray Absorption Fine Structure (EXAFS) and neutron PDF analysis, and their results indicated that the Jahn-Teller effect in the Co-O bonds for concentrations $x \leq 0.35$

is modest. So, the IS scenario in the Co^{3+} ions could be ruled out, leaving the high-spin (HS) scenario as the dominant one as proposed for the simple perovskite $LaCoO_3$.

4.2.2. Half-doped $Pr_{0.50}A_{0.50}CoO_3$ cobaltites (A = Ca, Sr)

$Pr_{0.50}Ca_{0.50}CoO_3$

Similarly to the half-doped manganite perovskites, half-doped $Ln_{0.50}A_{0.50}CoO_3$ cobaltites (50:50 Co^{3+}:Co^{4+}) have been widely studied. One of these interesting perovskites is $Pr_{0.50}Ca_{0.50}CoO_3$. This compound has been the first strongly correlated oxide to show the capability to generate metallic domains after photoirradiation in the insulating phase as reported recently by Okimoto *et al.* [16]. The investigation of this oxide started in 2002 when Tsubouchi and collaborators [17] reported the first evidences of a spin-state transition by neutron diffraction as a mechanism driving the metal-insulator transition (MIT).

The magnetic and electric characterization shows a paramagnetic and metallic behavior at T > T_{MI} . Several works have reported the existence of an abrupt increase of the resistivity and anomalies in the heat capacity around T_{MI} < 80 K, usually described as a MIT. These features can be seen in the measurements plotted in Figure 4. 2.

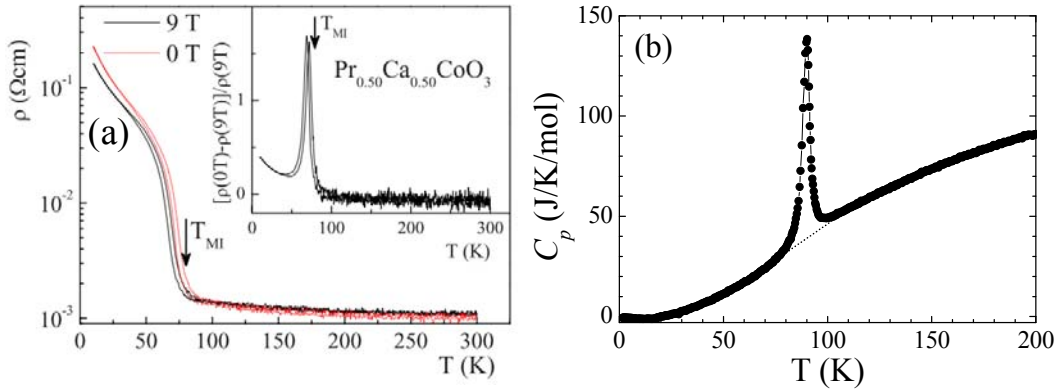

Figure 4. 2. (a) Four-probe resistivity of PCCO at 0 T and under an applied field of 9 T. The inset shows the magnetoresistance vs. T [18]. (b) Heat capacity curve measured at 0 T (digitalized from Ref. [17])

A previous structural study of our group reveals an orthorhombic *Pnma* phase with lattice parameters $a \sim c \sim a_p$ x $\sqrt{2}$; b ~$2a_p$ and a remarkable contraction of the cell volume (~2%) across the MIT [17–19]. However, this contraction is not due to changes in the size of the octahedra (this means no variations in the Co-O bond distances across MIT). In turn, it has been related to a (Pr,Ca)-O bond shortening (~ 0.04 Å) as it shows Figure 4. 3 . In addition, this

contraction is accompanied by a strong bending of the Co-O-Co bond angles in the insulating phase (by around 3 degrees).

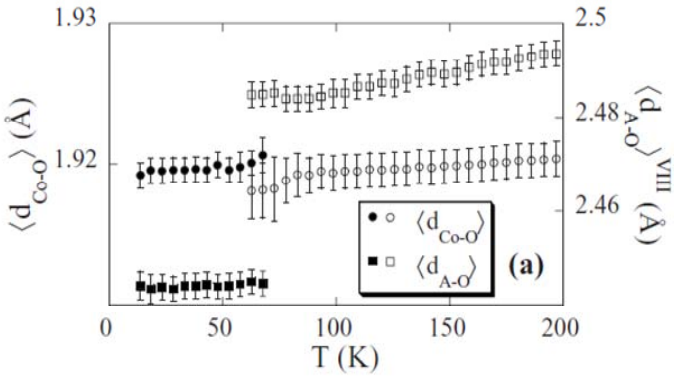

Figure 4. 3. Evolution with temperature of the average Co-O bond distances (left axis) and (Pr, Ca)-O bond distances (right axis). Data extracted from Ref. [18] and the A. J. Barón- Gonzalez PhD thesis work.

Given these the structural results, A. J. Barón- Gonzalez et *al.* proposed the hybridization of Pr *4f* levels with O *2p* orbitals and a partial charge transfer from *A* to *B* sites in the perovskite ($Pr^{3+}/Co^{4+} \rightarrow Pr^{4+}/Co^{3+}$). This hypothesis was checked by Jose Luis García-Muñoz [20] and Javier Herrero-Martín [21] using X-ray Absorption Spectroscopies (XAS) and different simulations. Figure 4. 4(a) shows the experimental spectra at the Pr L_3 ($2p_{3/2} \rightarrow 5d$) edge where we observe some intensity changes in the features at 5967 eV ($4f^2$ state) and 5978 eV ($4f^1$ state). On cooling, the peak related to Pr^{3+} ($4f^2$ state) decreases at the same time that the peak related to the Pr^{4+} ($4f^1$ state) increases. These results revealed an enhancement of the Pr oxidation ($Pr^{3+} \rightarrow Pr^{4+}$) across the MIT. Moreover, these measurements agreed with the XAS results obtained at the Pr $M_{4,5}$ ($3d \rightarrow 4f$) edges plotted in Figure 4. 4(b). In this case, the following was observed due to the conversion of Pr^{3+} into Pr^{4+} between 300 and 10 K: (i) the spectra slightly displace toward higher energies in the insulating phase, (ii) changes in the energy position and intensity of spectral features C, D and E, and (iii) appearance of features B and F, characteristics of Pr^{4+} compounds at $T < T_{MI}$. So, after the inspection of both absorption spectra and the confirmation by some simulations using reference compounds (Pr_2O_3 and $BaPrO_3$), a partial oxidation of the Pr^{3+} into Pr^{4+} was proposed, estimating the presence of about 15% of Pr^{4+} ions in the insulating phase.

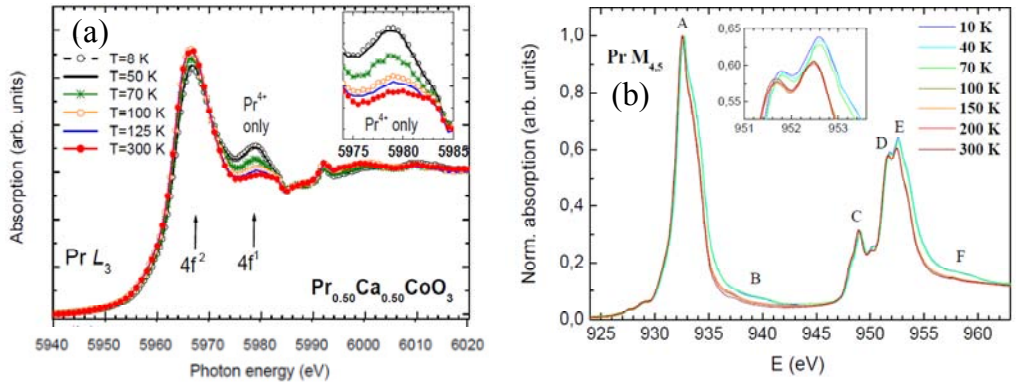

Figure 4. 4. (a) Temperature dependence of the Pr L_3-edge XAS [20]. (b) Experimental soft X-ray absorption at the Pr $M_{4,5}$ edges in $Pr_{0.50}Ca_{0.50}CoO_3$. A, B, C, D, E, F are labels for spectroscopic features [21]. The insets show details at the Pr L_3 and M_5 edges.

In addition, the valence shift in Pr ions is expected to be accompanied by a Pr → Co charge transfer because of the necessity of charge neutrality. The experimental Co L_3 XAS spectra evidence changes in the Co valence as the Pr valence shifts [20]. In Figure 4. 5(a) we see the temperature dependence of the experimental Co L_3 edge XAS spectra where a intensity decrease in the shoulder at ~780.7 eV across MIT is evident. The comparison with reference compounds as $SrCoO_3$ (Co^{4+}) and $AgCoO_3$ (Co^{3+}) allows us to determine that the spectra contain a larger contribution of Co^{4+} (in addition to Co^{3+}) at $T > T_{MI}$ than at $T < T_{MI}$. The evolution of the estimated Co and Pr valence changes from the experimental spectra are also observed in Figure 4. 5(b).

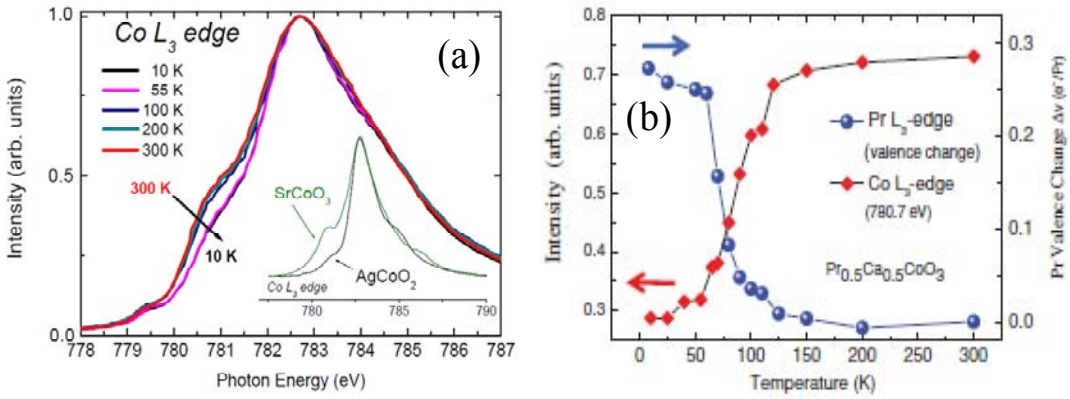

Figure 4. 5. (a) Temperature dependence of the Co L_3 edge spectra across the transition in PCCO. The experimental spectra of $SrCoO_3$ (Co^{4+}) and $AgCoO_2$ (Co^{3+}) at RT are plotted as reference samples. (b) Evolution of the estimated Co and Pr valence transfer deduced from the Co L_3 and Pr L_3edges data, respectively. All data are extracted from Ref. [20].

So, was concluded that the Co^{3+} ions get stabilized in a LS state by an electron transfer from the Pr ions in the insulating phase following the relation:

$$\frac{1}{2}Pr^{3+} + Co^{3.5} \rightarrow \frac{1}{2}Pr^{3+2\delta} + Co^{3.5-\delta}, \text{ with } 2\delta \sim 0.16 \text{ electrons in PCCO.}$$

Despite the fact there is barely any change in the volume of CoO_6 octahedra with temperature the investigation of the electronic configuration reveals Co SS variations across the MIT [22]. Soft XAS spectra at the Co $L_{2,3}$ and O *K*-edges evidenced a spin-crossover in $Pr_{0.50}Ca_{0.50}CoO_3$. In the same study, using charge transfer multiplet (CTM) calculations the authors proposed a mixed LS:HS (25:25) state for trivalent Co ions and a LS (S = 1/2, $t_{2g}^{5}\, e_g^{0}$) state for Co^{4+} ions with an effective spin S = 0.75 in the metallic phase (at 300 K). In contrast, the model proposed for the insulating phase was an inhomogeneous mixed LS:HS (58:42) state for Co^{3+} ions, with Co^{4+} remaining in a LS state (effective spin S = 0.25 at 10 K).

To conclude, the mechanism which drives the metal-insulator transition in $Pr_{0.50}Ca_{0.50}CoO_3$ is a charge transfer from Pr to Co ions accompanied by a SS transition in Co^{3+} ions due to the strong contraction of selected Pr-O bonds.

$Pr_{0.50}Sr_{0.50}CoO_3$

The first attempt to characterize structurally and magnetically this Sr-based cobaltite was reported by H. W. Brinks *et al*. in 1999. [23] In this work the synthesis of $Pr_{1-x}Sr_xCoO_3$ gave rise to compounds with oxygen vacancies and less contain of Co^{4+} ions than expected. The magnetic characterization showed that the Sr substitution for Pr in $PrCoO_3$ leads to the appearance of ferromagnetic phases for $x > 0.2$ and it was also seen that T_C increases with the Sr content. For concentrations close to x = 0.5 (50:50 Co^{3+}/Co^{4+}), the Curie temperature occurs at T~235 K, and a monoclinic symmetry ($P2_{1/n}$) was determined from neutron powder diffraction. However, later K. Yoshii *et al*. [24] synthesized better quality samples and the magnetic measurements showed a ferromagnetic order below T_C ~233 K and a further unexpected transition at ~ 100 K. More complete magnetic report of $Pr_{0.50}Sr_{0.50}CoO_3$ (PSCO) was done by R. Mahendiran *et al.* in 2003 [25]. As in the other studies reported, an unusual feature in the magnetization curve at T_A ~ 120 K was observed. This anomaly was manifested as a step-like behavior in M(T), where the magnetization decreases or increases depending on the magnitude of the applied field. In addition, the temperature dependence of the coercive field (H_C) showed a maximum around T_A, suggesting changes in the magnetocrystalline anisotropy axis of this system (see Figure 4. 6).

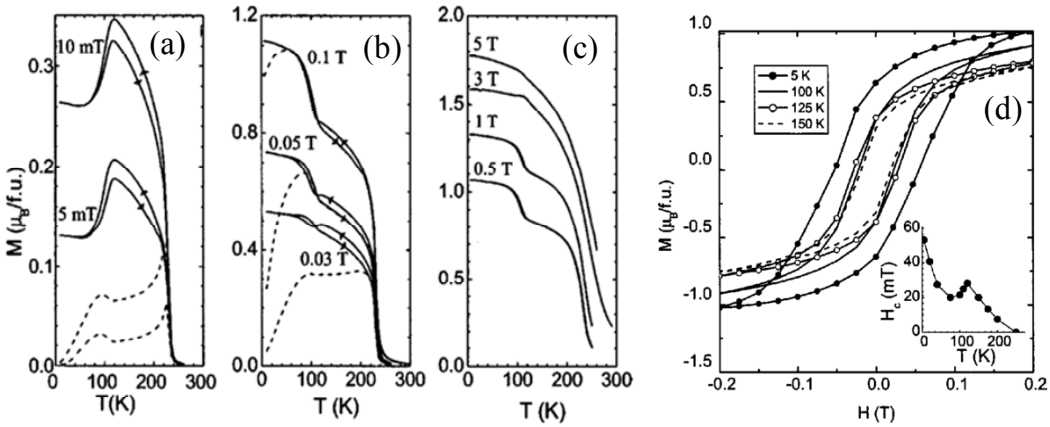

Figure 4. 6. (a), (b) and (c) Temperature dependence of the dc magnetization of $Pr_{0.50}Sr_{0.50}CoO_3$ measured under different magnetic fields. (d) M(H) curves measured at selected temperatures. The inset shows the evolution of the coercive field. From Ref. [25].

The anomalous magnetic transition in this Pr-based ferromagnetic metallic cobaltite has been a controversial subject in the last years and different hypothetical pictures have been proposed to explain it: (i) an antiferromagnetic order at low temperature, (ii) a structural phase separation, (iii) an ordering of the Pr moments, (iv) an orbital ordering in the e_g orbitals of Co^{3+} IS ions, (v) a hybridization between Pr 4*f* and O 2*p* orbitals, or (vi) a SS transition in Co^{3+} ions. Apart from the magnetic discussion, the evolution of the crystal structure in PSCO also remains unclear until now. The crystal structure at room temperature is an open question and different space groups (orthorhombic and monoclinic) such as: *$P2_1/n$, $P2_1/a$, Imma, I2/a, or $P2_1/m$* [26, 27] have been proposed by different authors. However, A. M. Balagurov *et al.* [28] reported the first structural transition at low temperatures concomitant with the anomalous magnetic transition, using neutron diffraction and synchrotron radiation. The study reveal successive structural transitions from cubic (*Pm3m*) to rhombohedral (*R-3c* ~ 800 K), passing through an orthorhombic symmetry (*Imma*, ~ 300 K) and, then to triclinic (*P-1*) at 120 K. In the same report different spaces groups were checked for the low temperature phase, like the tetragonal *I4/mcm* or the monoclinic *$P2_1/c$*. The first one was tested because it was consistent with the low temperature phase in $Pr_{0.50}Sr_{0.50}Co_{0.50}Fe_{0.50}O_3$ [29], but neither of them provides good reliability factors (R_B and χ^2). At the same time Leighton *et al.* [27] provided a magnetic study in $Pr_{1-x}Sr_xCoO_3$ for concentrations $0.0 < x < 0.70$ looking for a better understanding of the double-ferromagnetic phase. The results allowed them to reproduce a phase diagram in which for low x the system was considered as a spin/cluster glass (SGS) like the similar perovskites $La_{1-x}Sr_xCoO_3$ and it was clear that the T_A was more prevalent for x close to 0.5. The

study also reported that the magnetic transition can be suppressed when the Pr ions are substituted by other lanthanides such as La in the $(La_{1-y}Sr_y)_{0.50}CoO_3$ series. In Figure 4. **7** it is shown the evolution of T_A in $Pr_{1-x}Sr_xCoO_3$ and $(La_{1-y}Sr_y)_{0.50}CoO_3$ series from the same report [27]. The structural study done by Leighton *et al*. using high resolution X-rays and NPD revealed a monoclinic phase (*I2/a*, No. 15) at all temperatures from 300 K to 3.5 K. The changes in the crystal structure showed a coupled structural/magnetocrystalline anisotropy transition where the Pr-O bond lengths change across T_A. So, they defended an active participation of the Pr ions in the second magnetic transition because of the hybridization between Pr 4*f* orbitals and O 2*p* orbitals and suggested changes in the magnetocrystalline anisotropy (MCA) coupled to the evolution of the easy axis of the magnetization.

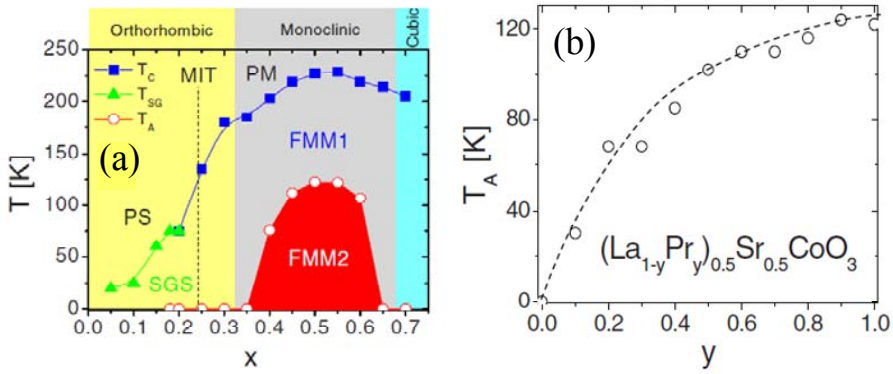

Figure 4. 7. (a) *x* vs *T* phase diagram of the $Pr_{1-x}Sr_xCoO_3$ series where the different crystal and magnetic symmetries are detailed; (b) temperature dependence of T_A in the $(La_{1-y}Pr_y)_{0.50}Sr_{0.50}CoO_3$ series.

On the other hand, part of the scientific community did not approve the symmetry proposed by Leighton *et al.* and other structural studies at low temperatures were reported. So, Balagurov *et al.* [30] followed their earlier investigation in Ref. [28] to propose a coexistence of phases (*Imma* + *I-1*) at low temperatures. They saw the Pr-O bond lengths changes and also observed a reorientation of the magnetic moment direction across T_A where the magnetic moment in the basal plane transforms into two components: one in the basal plane and the other along the long axis. In addition, different experiments revealed a similar conclusion: (i) Uchida *et al.* [31], using Lorentz microscopy images reported magnetic domains with magnetic moments rotating from the [110] to [100] direction at low temperatures; (ii) using conventional magnetometry on single crystals, Hirahara *et al.* [32] also observed a [100] easy axis after cooling. Then, based on the literature it is clear that the low temperature phase and the mechanism for the double magnetic transition is still a controversial issue and this justifies similar exploratory studies across the magnetostructural transition (MS) in this work.

4.2.3. Half-doped $Ln_{0.50}Sr_{0.50}CoO_3$ cobaltites

As it was mentioned in Section 4.2.2, the unexpected magnetic transition at T_A ~ 120 K disappears when the praseodymium is substituted by other lanthanides. A study on similar half doped cobaltites $Ln_{0.50}Sr_{0.50}CoO_3$ (*Ln* = La, Nd, Sm, Eu) shows that all are ferromagnetic and metallic down to 4.2 K [33]. However, the second magnetic transition is absent for these compounds. One interesting member is $Nd_{0.50}Sr_{0.50}CoO_3$ (NSCO) which seems to adopt an orthorhombic (*Pnma*) cell as reported by K. Yoshii *et al.* [33]. This compound is also metallic and presents a PM to FM transition at T_C ~ 228 K as well as a drop in the magnetization curve at low temperature, (see Figure 4. 8). However, unlike PSCO, this anomaly in the Nd-based cobaltite has been ascribed to an AFM alignment between the Nd(4*f*) and Co(3*d*) moments [33–35].

Observing that Pr ions play an important role in the magnetic properties at low temperature in PSCO, we decided to synthesize a similar cobaltite without the presence of Pr ions but with identical average ionic radius at the *A* site (1.24 Å, IX-coordination) as in PSCO. This new compound is $La_{1/6}Nd_{1/3}Sr_{0.50}CoO_3$, which does not contains Pr ions but it also shows a metallic behavior. Although this cobaltite shows a Curie temperature close to that observed in PSCO, we have seen no anomalies in the magnetization at low temperatures. The magnetization curve is also plotted in Figure 4. 8. The crystal structure of this compound will be analyzed in Section 4.10 after the inspection of neutron powder diffraction data.

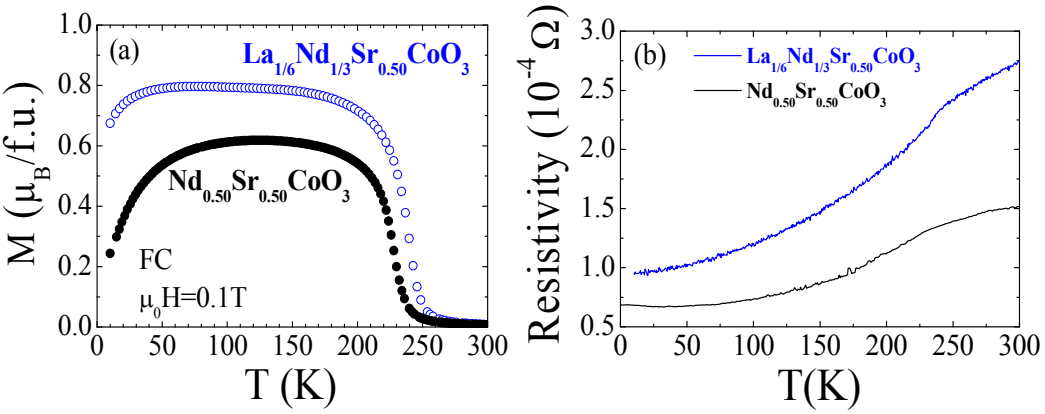

Figure 4. 8. (a) Temperature dependence of the magnetization for $Nd_{0.50}Sr_{0.50}CoO_3$ (black circles) and $La_{1/6}Nd_{1/3}Sr_{0.50}CoO_3$ (blue circles) measured on heating under 0.1 T. (b) Resistivity as a function of temperature measured without applied magnetic field for both compounds.

4.3. Sample synthesis and experimental details

Polycrystalline PSCO powder was prepared by solid-state reaction under a oxygen atmosphere. High- purity Co_3O_4 and Pr_6O_{11} oxides were first dried at 1100 ºC for 15h. $SrCO_3$ was heated at 850 ºC during 12h, then up to 950 ºC during 15h to decompose calcium carbonate. The precursors were mixed up in a stoichiometric amount. The mixture was pressed into pellets and heated under an oxygen atmosphere at 1000 ºC for 12h, with a slow cooling (60 ºC/h). After gridding and pressing, the last two annealings were performed at 1100 ºC (for 12h) and 1170 ºC (for 24h) under O_2, making a slow cooling too.

We have also prepared PSCO in thin film form. Taking profit of the ceramic pellets for the target, thin PSCO films (70 nm) were grown on (100)-oriented $LaAlO_3$ (LAO) single-crystal substrates (3 x 5 x 1 mm^3) by RHEED assisted Pulsed Laser Deposition (PLD) technique by using a KrF excimer laser at energies of 65 mJ and a fluence of 1.4 J/cm^2. Different growth and annealing conditions were tested. Finally, strained epitaxial PSCO (010) film was grown at 700 ºC under 0.40 mbar O_2 partial pressure. An annealing process was done at 500 ºC for 1 hour under 400 mbar O_2 pressure, followed by a slow cooling from 500 ºC to room temperature (RT).

In this chapter the comparison between PCCO and PSCO in some measurements was also required. Although polycrystalline PCCO samples were previously synthesized, the preparation method is also detailed below. PCCO samples were also prepared by solid-state reaction, but under air. Stoichiometric fractions of high-purity Pr_6O_{11}, Co_3O_4 and $CaCO_3$ were mixed up and the first treatment was done at 900 ºC to decompose calcium carbonate. Then, the mixture was pressed into pellets and heated to 1160 ºC under O_2 atmosphere. After several intermediate-stage sintering, it was necessary to treat PCCO twice under high oxygen pressure in order to get optimal oxygenation: (i) the first one at 900 ºC with p_{O2} = 200 bars during 14h, and (ii) the second at 475 ºC with p_{O2} = 150 bars during 6h.

In this chapter, a new family of mixed half-doped cobaltites $Pr_{0.50}(Sr_{1-x}Ba_X)_{0.50}CoO_3$ in which the Sr^{2+} ion is substituted by a bigger alkaline-earth ion such as Ba^{2+} were prepared for x= 0.025, 0.05 and 0.1 compositions. The $Pr_{0.50}(Sr_{1-x}Ba_X)_{0.50}CoO_3$ series was prepared by sol-gel method with the collaboration of Dr. Javier Blasco from the Instituto de Ciencia de Materiales de Aragón (ICMA-CSIC). Stoichiometric amounts of Pr_6O_{11}, Co-metal, $SrCoO_3$ and $BaCoO_3$. were used. The mixture was dissolved in a solution of HNO_3 1M, by adding citric acid and ethylene glycol (the proportion was 3 g for the reactives, 7 g for the citric acid and 3.5 ml for the ethylene glycol). Then, this pink solution was slowly evaporated leading to a brown resin which was first dried at 650 ºC for 6h. Finally, the obtained precursor was pressed into pellets

and heated under O_2 atmosphere at 1175 ºC for 24h. After gridding and pressing, the last annealing was performed at 1200 ºC for 24h under O_2. The final product was heated again at 800 ºC for 16h under the same atmosphere.

X-RAY DIFFRACTION: Polycrystalline samples quality and (θ-2θ) diffraction patterns on thin films were checked by X-ray diffraction (XRD) technique using a Siemens D-5000 diffractometer (λ(Cu K_α)= 1.54 Å). They were found to be single phased and free from impurities. The Bruker-AXS "D8 Advance" equipped with an area detector was used to image reciprocal space maps recorded around the (103), (003) and (200) LAO reflections to check the presence of twined domains in the film (unsuccessful) as well as complementary measurements of lattice mismatch.

ATOMIC FORCE MICROSCOPY: The surface quality of the film was imaged by means of the Atomic Force Microscopy (AFM) technique using a Scanning Probe Microscopy (SPM, "Agilent 5100") system operating in dynamic mode at 174 kHz. Different size scan images, 5 x 5 μm, 1 x 1 μm and 0.5 x 0.5 μm were acquired with the intention to get information about surface roughness and presence of defects at different resolution scales.

ELECTROMETRY: Electrical-transport (using the four-probe method) and the magnetic response to both dc and ac magnetic fields were measured using a Superconducting Quantum Interferometer Device (SQUID) and Physical Properties Measurement System (PPMS) from Quantum Design under different magnetic fields in the temperature range 5 K < T < 300K. The transport measurements for the thin films were made through metal-silver contacts grown on top of the surface film using a physical mask. The Ag was fixed onto the film doing a thermal treatment at 450º C for 1 hour under O_2 atmosphere. Contacts were done with an ultrasonic wire bonder (4526 Kuliche & Soffa). In Figure 4. 9 it is shown the process previous to the transport measurements.

Figure 4. 9. Visual process before the transport measurements in thin films. The first step is to growth metal-silver contacts using a physical mask on the top. Then, it is evaporated by 500 nm of silver and a thermal treatment is needed to fix the Ag. Finally, the Aluminum (25 μm) contacts are fixed to the sample through ultrasonic wire bonding.

MAGNETOMETRY: The dc and ac magnetic measurements for PSCO system in bulk form are plotted in Figure 4. 10 together with the resistivity curve. As we can observe from both magnetic measurements the Curie temperature is 230 K, and we found singular magnetic changes around ~120 K (from now on T_{SI}) as previously reported in literature. In the dc curves the anomaly is manifested as a downward step in low fields ($\mu_o H < 0.03$ T), but it is transformed into an upward step for $\mu_o H \geq 0.04$ T (FC). On the other hand, in the ac susceptibility the low transition temperature produces a sharp peak at 92 K, preceded by a local minimum found at 120 K. The resistivity curve shows the metallicity of PSCO down to the lowest temperature, and a change of slope at $T_C = 230$ K.

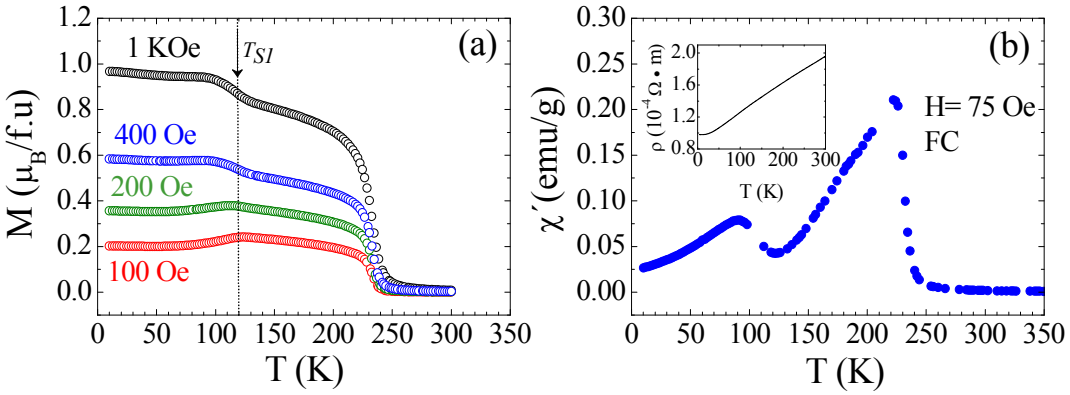

Figure 4. 10. (a) Temperature dependence of the dc magnetization (FC) measured at 100, 200, 400 and 1000 Oe for PSCO. (b) ac susceptibility (H =10 Oe, f =13 Hz) measured in PSCO using a dc field of 75 Oe (FC). The inset shows the resistivity curve.

The field dependence of the magnetization at different temperatures is plotted in Figure 4. 11(a) where it is visible the PM phase at 300 K and the FM phase below T_C. At 5 K, the magnetic saturation reaches a maximum value close to 2 μ_B/f.u. ($M_S = 1.96$ μ_B/f.u.) and for T_{SI} < T= 150 K we found $M_S = 1.77$ μ_B/f.u. The temperature dependence of the coercive field is shown in Figure 4. 11(b) where we found a maximum just across T_{SI} and which suggests changes in the magnetocrystalline anisotropy as it has been reported earlier [25, 27]. The magnetic measurements demonstrate the good quality and oxygenation of our sample because of the correct transitions temperature.

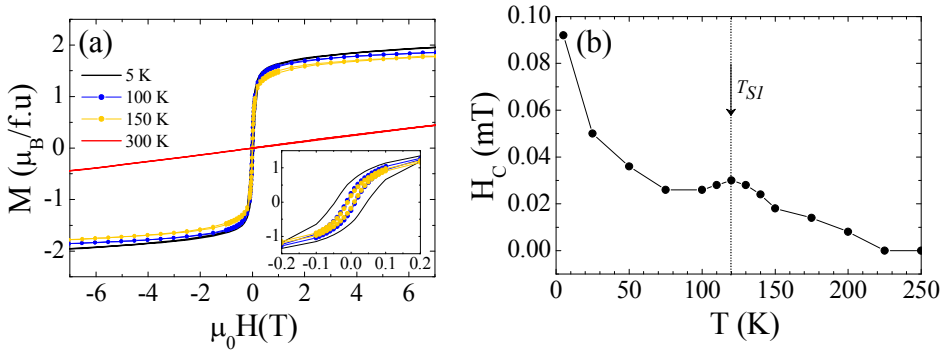

Figure 4. 11. (a) Magnetization versus field measured under zero-field cooled and (b) temperature dependence of the coercive field where a maximum just across T_{S1} is observed.

NEUTRON DIFFRACTION: For the structural characterization of the PSCO and $Nd_{1/3}La_{1/6}Sr_{0.50}CoO_3$ (NLSCO) bulk systems, we carried out neutron diffraction experiments on the D20 diffractometer of Institute Laue-Langevin (ILL, Grenoble). This two-axis high-intensity diffractometer uses a high take-off angle of 118° for the Ge(115) monochromator, and a radial oscillating collimator precedes the large microstrip PSD detector, which covers an angular range of 150°. In this range high resolution data as a function of temperature was obtained warming the sample in a cryofurnace from 15 K up to 443 K. In ramp mode the temperature shift for individual scans was smaller than 5 K. Using an He cryostat additional NPD patterns were also recorded at fixed selected temperatures. The data were collected at the neutron wavelength λ=1.87 Å. On the other hand, $Nd_{0.50}Sr_{0.50}CoO_3$ neutron patterns were collected at D2B (λ=1.5940 Å) at selected temperatures. The structural characterization of the $Pr_{0.50}(Sr_{1-x}Ba_X)_{0.50}CoO_3$ series was done on the D1B high resolution two-axis powder diffractometer at the ILL. The samples were shaped into cylindrical bars of 5 mm in diameter and 50 mm in length and the data were recorded at the neutron wavelength λ=2.52 Å. A cryomagnet able to apply magnetic fields up to 5 T was used to cool down the sample down to 10 K. All the structural data were analyzed with the Rietveld method using the FULLPROF suite of programs [36].

SURFACE DIFFRACTION: In addition, the structure of the PSCO film was studied at the surface diffraction beamline BM25B at the ESRF (Grenoble), using a one dimensional detector (NaI scintillator). The sample was mounted in a cryogenically adapted UHV baby chamber coupled to a six-circle diffractometer. The incident beam energy was set to 15.0 keV.

SYNCHROTRON X-RAY ABSORPTION: Soft X-ray absorption spectroscopy (XAS) measurements at the Pr $M_{4,5}$, O K and Co $L_{2,3}$ edges were collected at BL29-BOREAS beamline in the ALBA Synchrotron Light Facility and at ID08 beamline in the ESRF. The

X-ray Magnetic Circular Dichroism (XMCD) measurements were also recorded at BL29-BOREAS beamline at different temperatures (from 50 K to 300 K) using alternatively left and right circularly polarized X-rays produced by an APPLE II undulator. A superconducting split-coil setup allowed generating the required magnetic fields up to 5 T. Data were recorded by means of surface-sensitive total electron yield and total fluorescence yield. Proper bulk pellets sensitive measurements required in-situ cleaving of the samples under ultrahigh-vacuum ($\sim 10^{-9}$ mbar) conditions. CoO was simultaneously measured as an energy calibration reference. Nominal flux at BL29-BOREAS beamline was of the order of 10^{12} photons/s with an energy resolution of about 50 meV. Flux and time exposure were selectively reduced in some cases in order to minimize Co ions photoreduction. Additional Pr L_3-edge XAS measurements were recorded in transmission at BL22-CLÆSS beamline in the ALBA Synchrotron Light Facility. The measurements were carried out on pellets made of fine powders of the material homogeneously mixed up with cellulose. The thickness of the pellets was optimized for transmission measurements to get an edge step close to one. The energy calibration was simultaneously done by measuring a Cr foil (Cr K edge, 5989 eV). A Si stripe was selected on the white beam mirror to remove higher order harmonics. The incident beam was defocused and the spot size was 1.0 x 0.7 mm^2 (H x V). A Si (111) double crystal monochromator was used to get ~ 1 eV energy resolution at 6 keV with 10^{12} photons/s approximately

X-ray emission spectroscopy (XES) ($K\beta$ lines) was carried out at beamline ID26 of the European Synchrotron Radiation Facility (ESRF). The incident energy was tuned through the Co *K*-edge (the incident energy was 7800 eV) by means of a pair of cryogenically cooled Si(311) monochromator crystals, being the overall resolution about 0.4 eV. A reference Co metallic foil was used to calibrate the monochromator energy. The emitted X-rays were analyzed using a set of four spherically bent Ge(444) crystals that were arranged with the sample and photon detector (avalanche photodiode) in a vertical Rowland geometry (R = 1 m) at 90º scattering angle. On the other hand, X-ray Kα emission spectra and high-energy resolution fluorescence detection (HERFD-XANES) spectra at the Co *K* edge were acquired at the SuperXAS-X10DA beamline of the Swiss Light Synchrotron (SLS, Villigen). A Si (111) monochromator was used, and the overall resolution was about 1 eV. The monochromator energy was calibrated with a metallic Co metallic foil. The emitted X-rays were analyzed using the Johan-type high energy resolution X-ray emission spectrometer which is a five-crystal spectrometer relying on a Si (531) crystal analyzer. The total flux on the samples was 10^{12} photons/s. A He-flow cryostat was also here used to cool down the samples. .

4.4. Suppression of the magnetostructural transition in epitaxial PSCO thin film

The need to shed more light on the origin of the magnetostructural transition at T_{SI} and the importance of the Pr ions for this transition, led us to consider parallel studies in PSCO thin films. As it has been commented in Section 4.3, thin films were grown on (100)-LAO by PLD and the magnetic and the detailed structural studies will be presented in this section. The resistivity and the magnetic susceptibility as a function of temperature are displayed in Figure 4. 12 and it is compared to the ceramic sample measured under the same magnetic field (100 Oe). As we can observe both specimens are ferromagnetic below T_C ~230 K (ceramic) and ~ 225 K (film). Despite the Curie temperature is similar and both are metallic in the whole temperature range, their behavior at low temperature are quite different. Meanwhile, the ceramic sample shows a step-like behavior in the magnetization around 120 K, the thin film on (100)-LAO does not show any reduction of the FM moment. So, this is another example where the second magnetic transition can be suppressed like it happens in other similar compounds ($Nd_{0.50}Sr_{0.50}CoO_3$ or $La_{1/6}Nd_{1/3}Sr_{0.50}CoO_3$) as we have explained in Section 4.2.3.

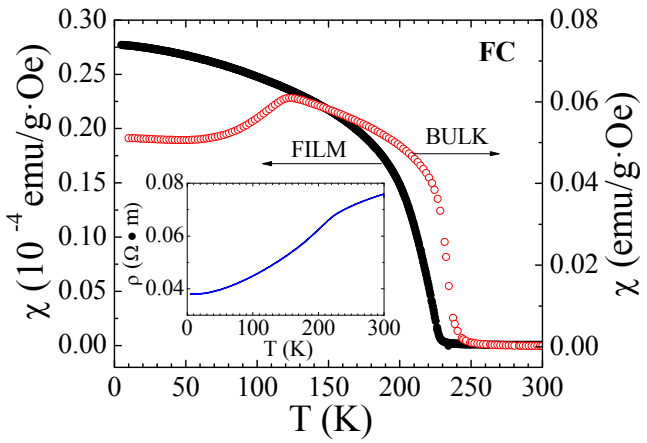

Figure 4. 12. Magnetic susceptibility of the PSCO film (left axis) grown on (100)-LAO and the PSCO ceramic sample (right axis). Field-cooled curves measured on heating under 100 Oe. The inset shows the metallic zero-field resistivity as a function of temperature in the thin film.

To clarify the possible relation between the magnetic and the structural properties of the sample (as in the ceramic system), we have analyzed the thin film by means of X-ray diffraction (XRD) and synchrotron diffraction. The θ-2θ XRD pattern in Figure 4. 13(a) reveal that the peaks from the LAO substrate are more intense than the thin film reflections. However, the inset shows the position and intensity of the (040) reflection becoming from the PSCO-film.

From the 2θ position we can confirm an epitaxial growth of the PSCO film, with the out-of-plane lattice parameter close to that of the long PSCO bulk lattice value, c_{PSCO} = 7.71 Å (bulk value 7.60 Å from Ref. [27]). So, this means the film grows with the *c*-axis perpendicular to the substrate surface.

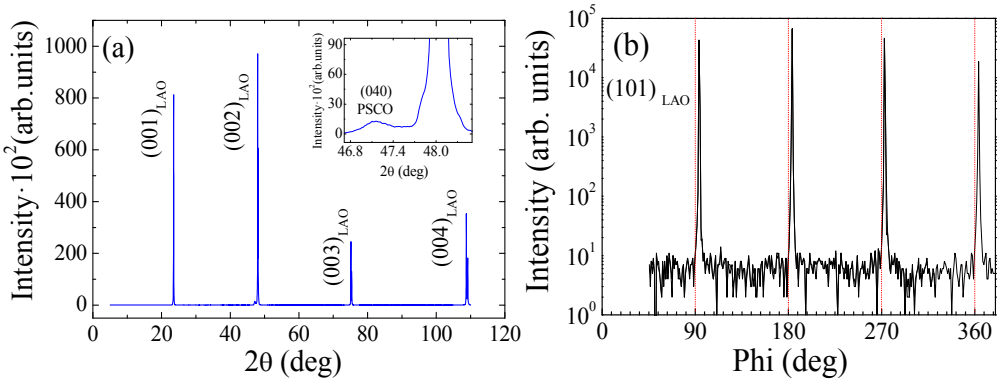

Figure 4. 13. (a) X-ray diffraction pattern for $Pr_{0.50}Sr_{0.50}CoO_3$ on LAO. The inset focus on the (002) LAO reflection in order to appreciate the reflection (040) corresponding to the cobaltite PSCO. The main reflections are indexed in the LAO basis while the film reflections are indexed according to the crystal cell setting of the PSCO perovskite defined by the (a_{PSCO}, b_{PSCO}, c_{PSCO}) unit cell ($\sqrt{a_0}$ x $\sqrt{a_0}$ x $2a_0$). (b) Phi scan through the (101)-LAO reflection.

The out-of- plane and the in-plane parameters were also extracted from reciprocal space maps. We measured the (103), (200) and (003) diffraction peaks (referred to the LAO substrate) as it is shown in Figure 4. 14.

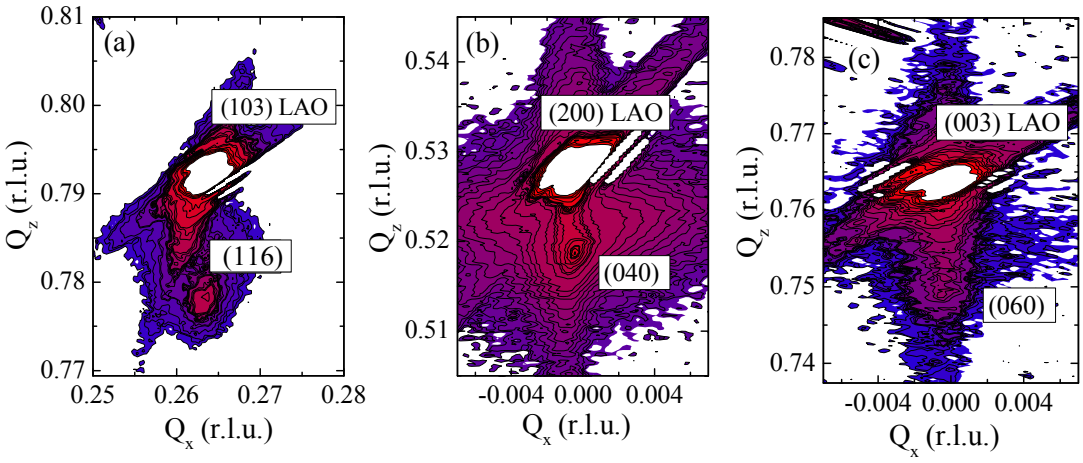

Figure 4. 14. Reciprocal space maps of the (a) (103) reflection (b) (200) reflection and (c) (003) LAO reflection for $Pr_{0.50}Sr_{0.50}CoO_3$ film grown on (100)-LAO. LAO and film reflections are indexed in their respective a_{LAO} and (a_{PSCO}, b_{PSCO}, c_{PSCO}) basis.

Results show that PSCO film grows with their in-plane lattice parameters identical and rotated 45º respect to the LAO(100) substrate [a_{PSCO} = b_{PSCO}= $\sqrt{2}$* a_{LAO} = 5.35 Å (bulk orthorhombic values 5.39 and 5.43 Å from Ref. [27])] and confirm that the longest cell axis of PSCO is perpendicular to the substrate. Thus, the mismatch of the LAO substrate induces an in-plain compressive strain into the PSCO film with respect to the bulk (-1.1 %); and a tensile strain (+1.3 %) along the out-of-plane direction. In addition, the azimutal (phi) scans demonstrate a four-fold symmetry because the (101)- LAO reflections are separated by 90º as it is plotted in Figure 4. 13(b).

The aim of using synchrotron X-ray diffraction is that this technique allows us to more easily make a deeper analysis of the structure and determine the possible symmetry of the thin film. Then, some selected scans at RT were collected at the surface diffraction beamline BM25B (ESRF, Grenoble). Some scans are plotted in Figure 4. 15, where the selected (*h*,*k*,*l*) reflections in the basis of the PSCO cell are labeled by letters: a = (-1, 1, 2), b = (0, 1, 3), c = (1, 1, 4), d = (-1, 1, 3), and e = (0, 1, 6). Bearing in mind that the symmetry of the bulk system at RT has been discussed in the literature [28–30] and it is most likely orthorhombic, then we wanted to discern between the more likely *Pnma* or *Imma* symmetries. The "a", "b" and "c" type reflections (h+k+l=2n) in Figure 4. 15(a) are compatible with both space groups. However, the "d" and "e" type reflections (h+k+l=2n+1), permitted by *Pnma* and forbidden by *Imma*, are absent in the scans shown in Figure 4. 15(b) and (c). Thus, the *Pnma* symmetry is excluded and the *Imma* space group is confirmed in the PSCO film.

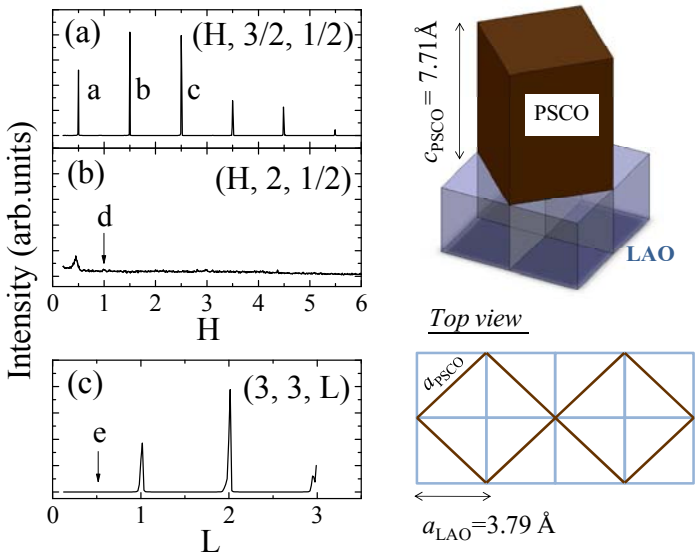

Figure 4. 15. Selected synchrotron X-ray diffraction scans (λ=1.87 Å) at RT from PSCO epitaxial film (see explanation in the text). Indexation in the figure corresponds to LAO cell. The sketch at the right side of the figure illustrates the orientation of the film on top of LAO.

In the ceramic sample several authors proposed a structural transition from orthorhombic to monoclinic symmetry (*Imma* to *I2/a*), concomitant with the second magnetic transition [27]. However, the low temperature phase is still unclear. Here, in the thin film we have not detected anomalies at low temperatures in the magnetization or the crystal symmetry by synchrotron X-ray surface diffraction. Then, we can conclude that the second transition at T_{S1} has been suppressed in the epitaxial PSCO film on (101)-LAO and this evidences the importance of the lattice degrees of freedom for the singular changes detected in the ceramic sample.

4.5. Stability of the electronic configuration in Pr/Co ions

Two of the proposed mechanisms for the low temperature magnetostructural transition in $Pr_{0.50}Sr_{0.50}CoO_3$ are (i) the hybridization between Pr 4*f* orbitals and O 2*p* orbitals, and (ii) a spin-state transition in the Co ions such as reported in $Pr_{0.50}Ca_{0.50}CoO_3$ or other (Pr, *Ln*)$_{1-x}Ca_xCoO_3$ cobaltites at the MIT. Moreover, our initial analysis of the crystal structure reveals a strong contraction of the average Pr-O bond length (<Pr-O>^{VIII}) at T_{S1}, which reinforces the idea of a large hybridization between the Pr and O ions. Later in this chapter, a complete description of the successive structural transitions and their correct symmetries will be given. Considering this scenario, similar spectroscopic studies done in PCCO are now justified in PSCO across the coupled structural/magnetocrystalline anisotropy transition. In order to check the electronic configuration in the Pr ions and some possible SS crossover in the Co ions, we have recorded out soft XAS spectra at the Pr $M_{4,5}$, Co $L_{2,3}$ and O *K* edges in the ID08 (ESRF) and BL29-BOREAS (ALBA Synchrotron) beamlines, and XANES at the Pr L_3 edge in the BL22-CLAESS beamline (ALBA) with hard X-ray photons.

4.5.1. XAS at the Pr $M_{4,5}$ and Pr L_3 edges

Figure 4. 16 shows the experimental X-ray absorption spectra of PSCO at the Pr $M_{4,5}$ edges recorded at different temperatures between 10 K and 340 K. For comparison, we have also plotted the corresponding spectra of PCCO at RT and 10 K already shown Figure 4. 4(b) and that of $PrCoO_3$ (PCO) at 300 K as a Pr^{3+} reference compound. There is hardly any change in the PSCO spectra in the whole thermal range studied, which comprehends T_C and T_{S1}. Moreover, the PCCO spectrum at 300 K shows remarkable similarities to them. We only find some dissimilarities in the $M_{4,5}$ branching ratio, i.e. $I(M_5)/ [I(M_4) + I(M_5)]$, where *I* is the measured absorption intensity. These are probably due to small differences in the spin-orbit splitting [37].

We find $M_{4,5}$ branching ratio values of 0.582 and 0.589 for PCCO at 10 K and 300 K, respectively. Meanwhile, this parameter is within 0.600 and 0.598 for PSCO at all temperatures between 10 K and 340 K. As a reference, we also experimentally find 0.646 for PCO at 300 K. The general trend of the $M_{4,5}$ branching ratio in lanthanides is directly proportional to the 4*f* orbitals occupation due to a progressively less prominent M_4 edge [38], which is in qualitative agreement to the values we found.

Although the Pr ions at room temperature in PCCO are in the expected trivalent state, the appearance of Pr^{4+} at $T<T_{MI}$ has been demonstrated by different groups using diverse experimental techniques such as XAS and heat capacity measurements [20, 39] . The process of intersite charge transfer between Pr and Co ions is reflected, among others, on the X-ray absorption spectra of Pr and Co atoms at different edges. At the Pr $M_{4,5}$, a clear signature of Pr^{4+} is the enhancement and shift to higher energies of C and D spectral features. The absorption cross section at E and F features enlarges too. This evolution is absent in PSCO which, in combination to the commented spectral similarity to PCCO at 300 K, suggests that there is no trace of tetravalent Pr ions in PSCO at low temperatures.

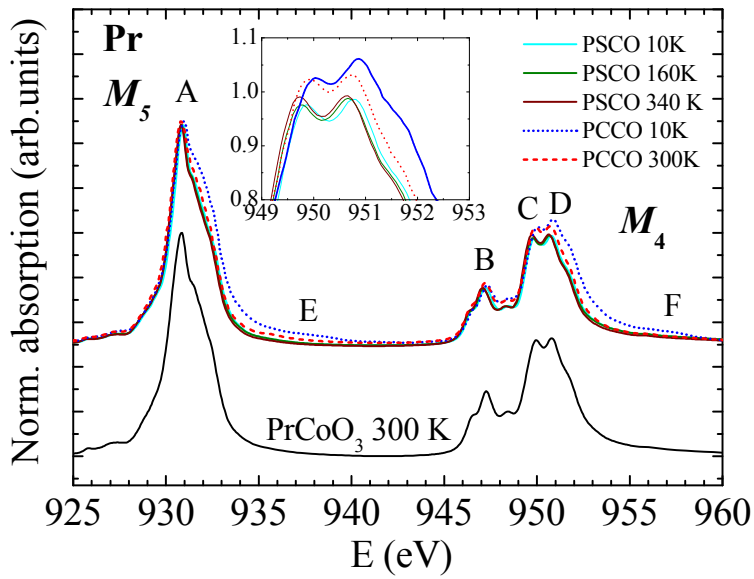

Figure 4. 16. Experimental Pr $M_{4,5}$ XAS spectra of PSCO as a function of temperature, as compared to PCCO at 10 K (blue dotted) and 300 K (red dashed). Black line shows the experimental spectra of $PrCoO_3$ at 300 K as reference sample. A, B, C, D, E, and F are labels for spectroscopic features. The inset shows a detail of the Pr M_4 edge.

In order to compare with the experimental data we have also carried out charge-transfer multiplet (CTM) calculations of the experimental X-ray absorption spectra plotted in

Figure 4. 16 using the CTM4XAS program which is based on the Cowan code [40] (more details about the program in Chapter 2). These calculations allow us to explore the effects of a hypothetical Pr^{4+} content in these cobaltites.

In Figure 4. 17 we show the calculated spectra at the Pr $M_{4,5}$ absorption edges for a Pr^{4+}-based oxide with pseudocubic perovskite structure and a pure Pr^{3+}-based one. We note here that we have included a significant charge transfer component in the Pr^{4+}-cobaltite calculation trying to simulate the experimental spectrum of PCCO [41]. We have therefore decided to label it as Pr^{4+}_CT. In this case the initial and final state of the 3*d* XAS process can be respectively described as a mixture of $4f^{1}$ and $4f^{2}\underline{L}$, and a mixture of the $3d^{9}4f^{2}$ and $3d^{9}4f^{3}\underline{L}$ configurations, respectively, where $\underline{L}$ stands for a hole in the valence band. A pure Pr^{4+}-based compound calculation is also shown for comparison [Figure 4. 17 (c)]**.** The parameter values used for every calculation are listed in Table 4. 1.

Table 4. 1. Parameters from the charge-transfer multiplet calculations using CTM4XAS. The simulation for Pr^{4+}_CT was done with command mode. The other two were done with the easy-to-use graphical user interface (GUI).

Parameter	Pr^{3+}	Pr^{4+}	Pr^{4+}_CT
Charge transfer energy (Δ) (eV)	0.0	0.0	+1.0
Slater's integral F_{dd} (eV)	0.9	0.95	Default
Slater's integral F_{pd} (eV)	1.0	1.0	Default
Slater's integral G_{pd} (eV)	1.0	1.0	Default
Spin-orbit coupling (S.O)	-	0.95	Default
Hopping e_g-electrons (T_{eg}) (eV)	-	-	0.8
Hopping t_{2g}-electrons (T_{t2g}) (eV)	-	-	0.8

As empirically shown in a recent work [21], the Pr $M_{4,5}$ (and Pr L_3) experimental XAS spectra of PCCO at $T<T_{MI}$ can be reproduced as the weighted addition of the two latter components in a variable Pr^{3+} : Pr^{4+}CT ratio, which is directly proportional to the temperature. In Figure 4. 17(d) we show the simulations for the PCCO spectra at 10 and 300 K following this method, using the values derived in Ref. [21] (85:15 Pr^{3+}:Pr^{4+}). The comparison to the low temperature experimental spectra for PCCO and PSCO [Figure 4. 17(e)] reinforces the idea of an absence of tetravalent Pr ions in the latter compound.

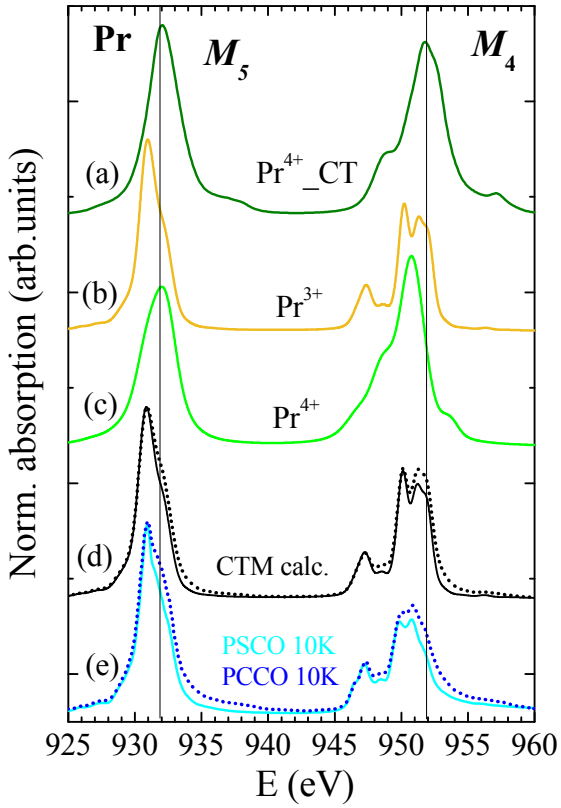

Figure 4. 17. Top to bottom: (a-c) calculated Pr $M_{4,5}$ XAS spectrum of a Co-based perovskite only containing Pr^{4+}CT (charge transfer allowed) (green), Pr^{3+} (no charge transfer) (yellow), and Pr^{4+} (no charge transfer) (light green); (d) comparison of a Pr^{3+}-based cobaltite multiplet calculation (solid line) to the 85:15 weighted addition of Pr^{3+} and Pr^{4+}CT calculated spectra (dotted black); (e) experimental $Pr_{0.50}Sr_{0.50}CoO_3$ (solid blue) and $Pr_{0.50}Ca_{0.50}CoO_3$ (dotted blue) measured at 10K. Spectra are vertically shifted for clarity.

To complete this analysis we have also performed XAS at the Pr L_3 in the BL22-CLAESS beamline (ALBA Synchrotron). The experimental data is plotted in Figure 4. 18. The experimental spectrum confirms our conclusions obtained from the soft X-ray regime on the stability of Pr oxidation state because of the similarities between the spectra measured at 300 K and 80 K. Let us note that the appearance of Pr^{4+} in PCCO leads to a noticeable enhancement of B feature at T_{MI} (as it can be seen in the inset). Regardless of temperature, the absorption cross section at ~ 5980 eV shows a local maximum due to multiple scattering of the photoelectron from ionized Pr atoms with the surrounding atomic environment, i.e. it has a structural origin. Nevertheless, its enhancement at $T<T_{MI}$ responds to the Pr^{4+} formation as it has been reported in Ref. [20] . This thermally modulated spectral evolution does not occur in PSCO, in agreement with the absence of Pr^{4+} derived from the analysis of XAS spectra shown in Figure 4. 16, 4.17.

To gain insight on the Pr L_3 edge results, we have also carried out X-ray absorption simulations based on the self-consistent real space multiple scattering approach [42] using FEFF8.2 program. The simulations were performed employing the crystallographic *Imma* structure (as later will be described) of PSCO at $T > T_{SI}$ [28–30] and the parameters employed were: (i) a Dirac-Hara + Hedin – Lundqvist for the exchange model and (ii) a cluster of radius 7.5 Å around Pr atoms. The theoretical spectrum obtained is plotted at the bottom of Figure 4. 18, and it is in a good agreement with the experimental spectra.

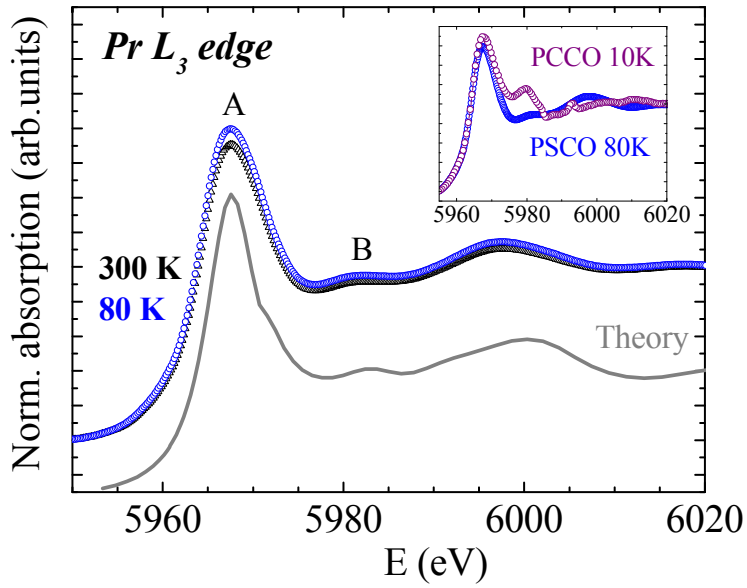

Figure 4. 18. Experimental Pr L_3 XAS spectra of PSCO at room temperature (open triangles) and at 80 K (open circles). The solid grey line corresponds to the calculated spectrum. The inset shows a comparison between PCCO and PSCO in their low temperature phases.

4.5.2. XAS at the Co $L_{2,3}$ and O *K* edges

Another possibility to explain the magnetostructural transition could be a SS transition in the Co^{3+} ions. This physical phenomenon is very common in cobalt oxides such as $LnCoO_3$, $Pr_{0.50}Ca_{0.50}CoO_3$, or $LnBaCo_2O_{5.50}$ systems. XAS is a technique sensitive to the electronic filling details of the valence orbitals, and to profit this we have carried out XAS at the Co $L_{2,3}$ edges in the BL29-BOREAS beamline. Figure 4. 19 shows the evolution of Co $L_{2,3}$ XAS spectra of PSCO as a function of temperature, between 3 K and 290 K. Changes are minimal in the whole thermal range studied. In other words, there are no relevant variations in the occupation of Co 3*d* states. In view of this and the results presented in Section 4.2.4. we cannot relate the

mechanism driving the anomalous transition taking place at T_{S1} in $Pr_{0.50}Sr_{0.50}CoO_3$ to neither a Pr to Co charge transfer nor Co spin state changes.

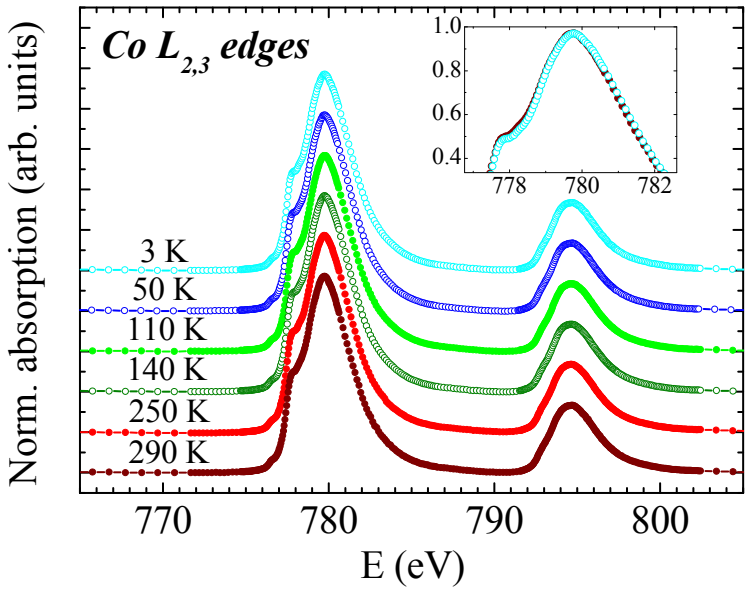

Figure 4. 19. Experimental Co $L_{2,3}$ XAS spectra as a function of temperature for $Pr_{0.50}Sr_{0.50}CoO_3$. The inset shows a detail of the 290 K (red solid circles) and 3 K (blue open circles) curves. Spectra are vertically shifted for clarity.

An alternative way to analyze the density of empty Co 3*d* states via hybridization to the O 2*p* states is by studying the pre-peak region (between 524 eV and 531 eV) in the O *K* edge XAS spectra. Figure 4. 20 displays the temperature-dependent O *K* spectra for PSCO also measured in the BL29-BOREAS beamline. We have also plotted the spectrum of $PrCoO_3$ at 10 K containing only Co^{3+} in a LS state (t_{2g}^6, S=0) as we have seen in Chapter 3. We note the absence of changes with temperature in PSCO, similarly as in Co $L_{2,3}$ edge spectra, thus a SS crossover is not expected. In addition, the comparison to reference PCO is a strong indication of the existence of a large density of 3*d* t_{2g} empty states in Co ions for $Pr_{0.50}Sr_{0.50}CoO_3$. The temperature dependent spectral weight ratio of empty t_{2g} and e_g states is characteristic of PCCO and similar Pr-Ca cobaltites [22, 43]. This allows us to remark that the electronic configuration of Co ions in PSCO is very different to that in PCCO at $T < T_{MI}$. In $Pr_{0.50}Ca_{0.50}CoO_3$, the insulating phase presents a coexistence of Co^{3+} ($3d\ t_{2g}^6\ e_g^0$, $S = 0$) and Co^{4+} ($3d\ t_{2g}^5\ e_g^0$, $S = 1/2$) ions, both in a LS state. This involves a scarcity of empty 3*d* states with t_{2g} symmetry in PCCO and helps to understand the large amplitude of PSCO O *K* pre-peak features at ~ 526 eV. Thus, this indicates the appearance of excited HS ($3d\ t_{2g}^4\ e_g^2$, $S = 2$) or IS ($3d\ t_{2g}^5\ e_g^1$, $S = 1$) Co^{3+} states in PSCO, either pure or mixed with a small LS state contribution.

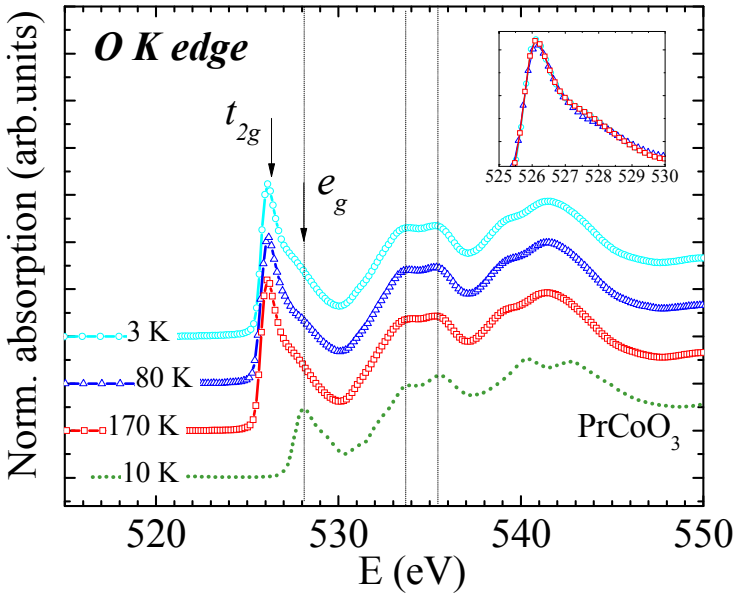

Figure 4. 20. Experimental O *K* XAS of $Pr_{0.50}Sr_{0.50}CoO_3$ at different temperatures. The experimental spectrum of $PrCoO_3$ (green dotted line) serves as a reference. The inset displays a detail of the pre-edge region of PSCO spectra.

4.6. Successive structural phase transitions in $Pr_{0.50}Sr_{0.50}CoO_3$

One of the issues to understand the unexpected properties in this half-doped cobaltite, it is to determine the crystal structure evolution and its structural properties, particularly across T_{S1}. For that reason, we have undertaken an exhaustive structural analysis on its evolution from 450 K to low temperature. In this work, we have used high-resolution neutron diffraction (from D20, λ = 1.87 Å, ILL) and X-ray powder diffraction (from ID22, λ = 0.40 Å, ESRF). However, the results presented here are from neutron diffraction (X-rays data will be not discussed). Neutrons are more precise for the location of light atoms (such as oxygen) in the presence of heavy atoms, allowing to determine with great accuracy the Co-O and Pr-O bond distances.

In Figure 4. 21 the T-2θ diagram the neutron-diffracted intensities in two different angular ranges is plotted. In panel (a) we can observe a first structural transition from *Structure 1* to *Structure 2* at T_{S1} ~ 120 K and also the disappearance the FM order at T_C ~230 K.

Furthermore, in panel (b) the temperature range is expanded and it is possible to observe separately the occurrence of three different crystal structures. The transition temperature to the high temperature phase was determined as T_{S2} ~ 314 K. Above this value (and up to 800K) the crystal structure adopts *Pm-3m* cubic symmetry [28].

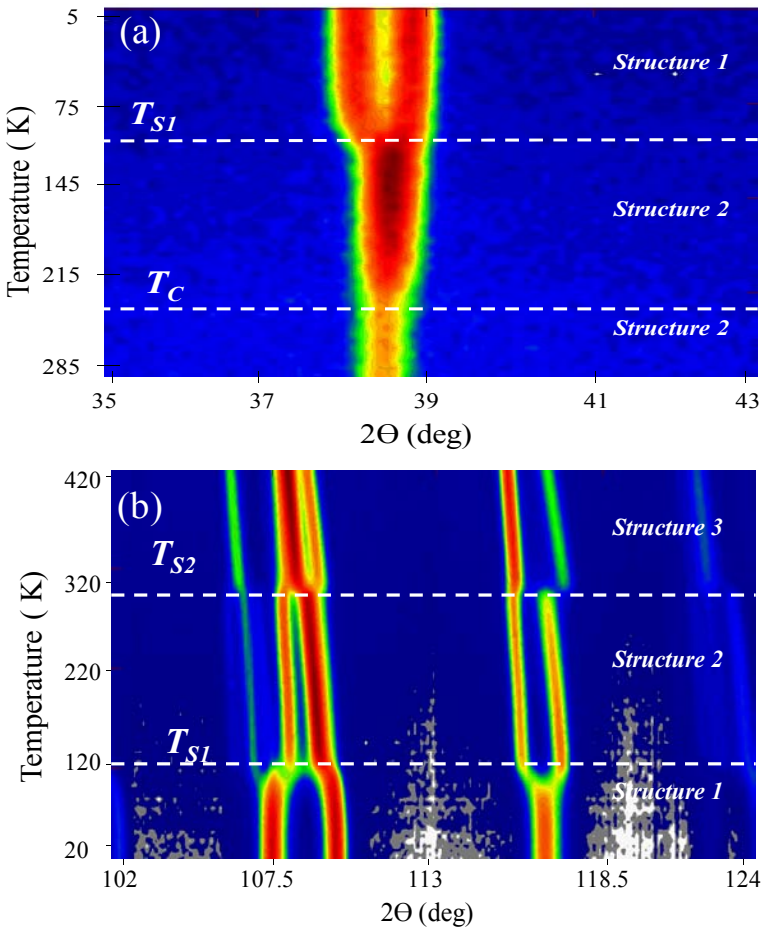

Figure 4. 21. Neutron diffraction intensities for characteristic reflections of the successive crystal structures as a function of temperature. (a) Selected angular region where the PM phase transforming into the FM phase and additional changes occur at T_{S1}. (b) Selected angular region comprehending the three successive structural phases.

The patterns collected between 450K and 330 K can be refined using a rhombohedral phase with space group symmetry *R-3c* (No. 167). On cooling, in the 314 K > T > 319 K temperature range PSCO transforms into an orthorhombic phase with space group symmetry *Imma* (No. 74). We have determined that symmetry as the correct one at RT, discarding a series of monoclinic groups proposed by different authors ($P2_1/m$, *I2/a*, $P2_1/a$).

In addition, as we will show in this chapter we have also unambiguously determined the real symmetry of PSCO emerging below the magnetostructural transition. We will show that below 120 K, the perovskite adopts the tetragonal I*4/mcm* space group (No. 140).

In Figure 4. 22, we show the evolution of some reflections measured by powder neutron diffraction within the $85^{o} < 2\theta < 90^{o}$ interval at three selected temperatures where the structural phase is different. The solid line corresponds to the calculated Rietveld refinement profile, which as we can see is in good agreement with the experimental data (red circles).

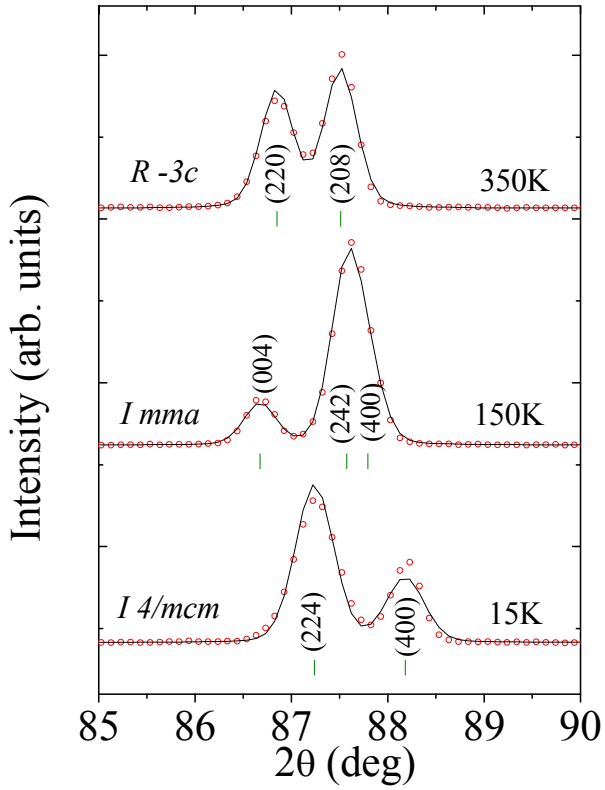

Figure 4. 22. Selected angular region of the Rietveld refinement (solid line) of neutron patterns measured at the indicated temperatures for each structural phase. Diffraction patterns have been shifted up for clarity and are indexed according to $\sqrt{2}a_0$ x $2a_0$ x $\sqrt{2}a_0$ at 150 K and $\sqrt{2}a_0$ x $\sqrt{2}a_0$ x $2a_0$ at 15 K.

Table 4. 2 summarizes the refined lattice parameters, atomic positions, isotropic thermal factors, FM moment, and reliability factors of the Rietveld refinement for each crystal structure at 350 K (rhombohedral *R-3c*) , 150 K (orthorhombic *Imma*), and 15 K (tetragonal *I4/mcm*). Moreover, in Figure 4. 23 (a-d) the complete diffraction patterns for PSCO at selected temperatures (400, 300, 150 and 15 K) are plotted.

A detailed description of each structural phase will be presented in the next sections.

Table 4. 2. Crystal structures of PSCO and reliability factors found by Rietveld refinements of neutron data at selected temperatures.

$Pr_{0.50}Sr_{0.50}CoO_3$	400 K	300 K	150 K	15 K
Space group	*R -3c* (No. 167)	*I mma* (No. 74)	*I mma* (No. 74)	*I 4/mcm* (No.140)
a (Å)	5.4270(1)	5.3894(8)	5.3773(8)	5.3585(1)
b (Å)	5.4270(1)	7.61358(1)	7.5963(1)	5.3585(1)
c (Å)	13.1813(4)	5.43707(8)	5.4325(7)	7.7093(1)
Vol ($Å^3$)	336.207(2)	223.097(6)	221.906(5)	221.367(9)
Pr/Sr	6*a*	4*e*	4*e*	4*b*
x	0	0	0	0
y	0	0.25	0.25	0.5
z	0.25	0.0001(7)	-0.0005(4)	0.25
B ($Å^2$)	1.268(7)	1.129(5)	1.036(5)	0.790(6)
Co	6*b*	4*b*	4*b*	4*c*
x	0	0	0	0
y	0	0	0	0
z	0	0.5	0.5	0
B ($Å^2$)	0.718(5)	0.4778(9)	0.162(3)	0.459(2)
O1	18*e*	4*e*	4*e*	4*a*
x	0.466(2)	0	0	0
y	0	0.25	0.25	0
z	0.25	0.4582(7)	0.4540(6)	0.25
B ($Å^2$)	1.641(5)	1.164(6)	1.077(4)	1.190(1)
O2		8*g*	8*g*	8*h*
x	-	0.25	0.25	0.2849(3)
y	-	0.0231(4)	0.0233(2)	0.7849 (3)
z	-	0.75	0.75	0
β	-	1.531(3)	1.085(4)	1.028(6)
Ordered FM moment (μ_B/Co)	-	-	1.47(3)	1.76(9)*
χ^2	2.06	1.08	1.63	2.38
R_B (%)	2.89	3.15	2.47	2.39
R_{mag} (%)	-	-	6.17	7.2

* The magnetic structure will be discussed in Section 4.8.

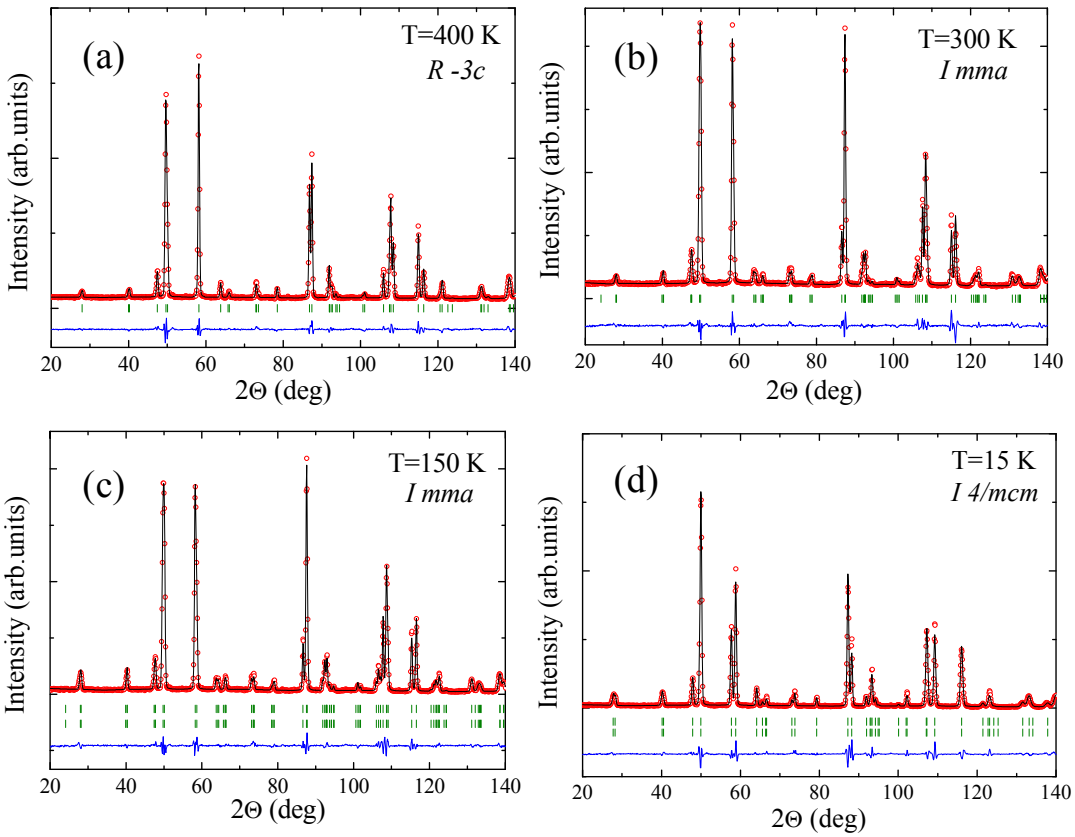

Figure 4. 23. Rietveld refinement (black line) of neutron diffraction patterns (red circles, experimental points; bottom blue line, difference) for $Pr_{0.50}Sr_{0.50}CoO_3$ at selected temperatures: (a) 400 K, rhombohedral *R-3c* structure; (b) 300 K, orthorhombic *Imma* paramagnetic phase; (c) 150 K, orthorhombic *Imma* ferromagnetic phase (second row of Bragg positions is the magnetic phase); (d) 15 K, tetragonal *I4/mcm* phase.

4.6.1. The high-temperature Rhombohedral phase

In agreement with the reported data by Balagurov *et al.* [28], we refined the structure from the highest temperature recorded at 450 K to 330 K as a single rhombohedral phase (*R-3c*, No. 167). In this phase, the cell parameters are a = 5.3965 Å, α = 60.37 º and the atomic positions Pr/Sr at (¼, ¼, ¼), Co at (0, 0, 0), and O at (x+¼, -x+¼, ¼) with x = 0.466 (2). In Table 4. 2 the structural parameters are detailed for 400 K and Figure 4. 23(a) shows the Rietveld refinement at same temperature. In Figure 4. 24(c) it is shown the projected view of the *R-3c* crystal structure.

4.6.2. The room-temperature Orthorhombic phase

On cooling below T_{S2} = 314 K, neutron diffraction data are well described using the *Imma* (No.74) space group with the standard $\sqrt{2}a_0$ x $2a_0$ x $\sqrt{2}a_0$ cell (where a_0 refers to the cubic cell). In this phase the atomic positions are allocated for Pr/Sr at (0, ¼, z), Co at (0, 0, ½), and two nonequivalent oxygen atoms O1 at (0, ¼, *z*) and O2 at (¼, *y* + ½, ¾).

At RT we find that the rhombohedral-orthorhombic transition is already completed, and it is a single-phased *Imma*. See Table 4. 2 for the atomic parameters and Figure 4. 23(b) for the Rietveld refinement of neutron diffraction pattern.

In this same structural phase we observe the apparition of some FM peaks in the diffraction pattern below T_C = 230 K. Our refinements reproduce the experimental data at 150 K considering an *Imma* FM phase, where the FM Co moments are aligned along the *x* axis [see Figure 4. 23(c) for the Rietveld refinement]. At this temperature, the magnetic moment reaches a value of 1.5 μ_B/Co, which is compatible with a mixture of Co^{3+} ions in the IS (LS) configuration coexisting with Co^{4+} ions in LS (IS) state. However, we should remind that a pure Co^{3+} in LS should be ruled out from XAS measurements presented in Section 4.5. In the next sections the determination of the magnetic structure above and below T_{S1} and the SS in the Co ions will be deeply analyzed and discussed. In Figure 4. 24(b) it is shown the projected view of the *Imma* crystal structure.

4.6.3. The low-temperature Tetragonal phase

Below T_{S1} neutron diffraction can be well refined using a single tetragonal phase, *I4/mcm* (No. 140) space group with the standard $\sqrt{2}a_0$ x $\sqrt{2}a_0$ x $2a_0$ cell. In this phase the atomic positions are allocated for Pr/Sr at (0, ½, ¼), Co at (0, 0, 0), and the oxygen atoms O1 at (0, 0, ¼) and O2 at (*x*, *x* + ½, 0). Thus, in the tetragonal phase only one free atomic coordinate is involved, while in the orthorhombic phase we find 3 refinable coordinates.

In the first attempts to solve the crystal structure at low temperature, we checked the monoclinic *I2/a* (No. 15) space group, proposed by Leighton *et al.* in Ref. [27], which is a maximal subgroup of *Imma.* Despite the fact that refinements fit data very well, we confirmed that the refined solution approaches the tetragonal phase (for instance, we observed that the Co-O1-Co bond angle was very close to 180º).

On the other hand, in our exhaustive structural analysis we have also tested different space subgroups of *Imma* like *I2/m*, $P2_1/n$, *Cmmm*, *Fmmm* with a standard $2a_0$ x $2a_0$ x $2a_0$ cell, but no positive results were obtained for PSCO. Recapitulating, the experimental neutron profile is perfectly reproduced using the *I2/a* symmetry, but we realized that the solution

converged to a higher symmetry (*I4/mcm*), with a smaller number of free coordinates [44]. Interestingly, the low temperature symmetry is not a subgroup of the *Imma* group but the latter is subgroup of the tetragonal structure.

In Table 4. 2 the structural parameters are detailed for 15 K and Figure 4. 23(d) shows the Rietveld refinement at this temperature. In Figure 4. 24(a) it is shown the projected view of the *I4/mcm* crystal structure.

In this low temperature phase, the neutron diffraction patterns do not show any pure AFM reflection. We proved that any order of Pr moments would give rise to new magnetic reflections not observed in the neutron pattern. The contribution of Pr moments to the magnetization anomalies was unambiguously discarded.

The refined ferromagnetic moment reaches a value of $1.8\mu_B$/Co at 15 K. Nevertheless, the question of the magnetic order evolution requires an specific discussion that will be presented in Section 4.8.

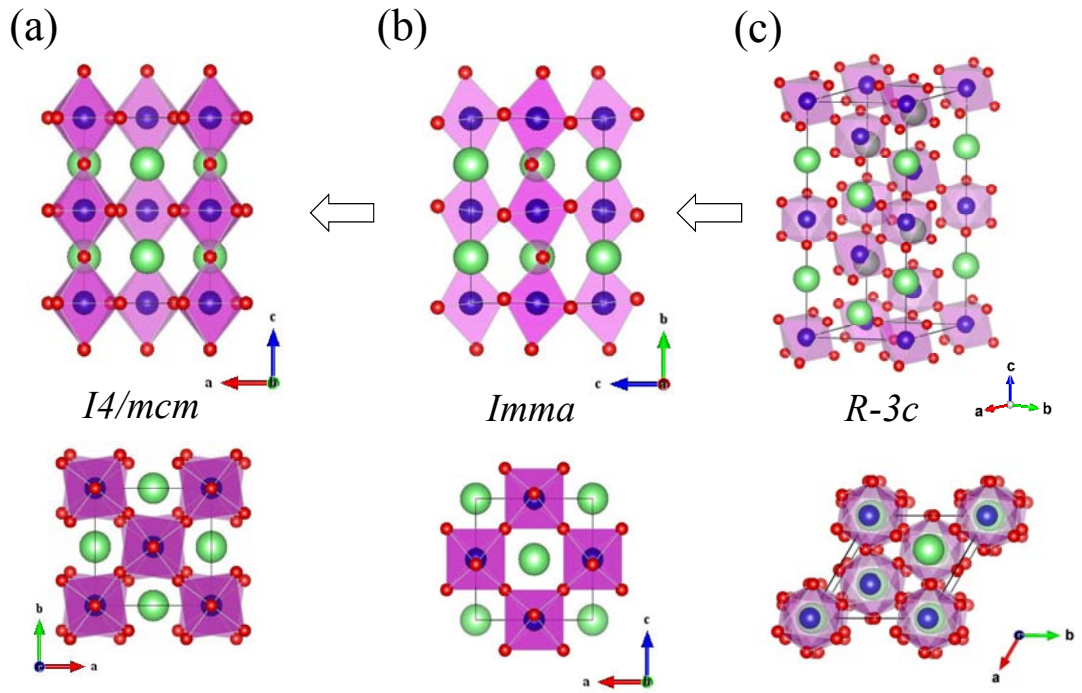

Figure 4. 24. Projections of (a) the tetragonal *I4/mcm* crystal structure refined at 15 K, (b) The orthorhombic *Imma* structure refined at 300 K and (c) the rhombohedral *R-3c* structure of PSCO at 400 K. The green balls are Pr /Sr atoms; the blue balls are Co atoms and the red balls are O atoms.

4.6.4. The structural changes across the successive phases

As we have reported in the previous section, the successive crystal symmetries found in PSCO differ from those in similar $Ln_{0.50}Sr_{0.50}CoO_3$ perovskites (where it is commonly found a *Pnma* symmetry). We have determined for PSCO that decreasing the temperature successive phase transformations are taking place from the ideal cubic perovskite: *Pm-3m* ⟶ *R-3c* ⟶ *Imma* ⟶ *I4/mcm.* In Figure 4. 24 it is shown the evolution of the crystal across the successive phase transformations. We observe remarkable changes in the rotational configuration of the octahedra between the three successive phases. In the *R-3c* ⟶ *Imma* transition the rotation around the vertical pseudocubic axis has been suppressed. However, in the *Imma* ⟶ *I4/mcm* transformation the tilting around the vertical axis is activated in antiphase for successive octahedra along *c* (apical direction). At the same time the orthorhombic tilting of the octahedra in antiphase along *a* and *b* axis pseudocubic axis is suppressed in the tetragonal phase ($a^0a^0a^0 \rightarrow a^-a^-a^- \rightarrow a^-a^-a^0 \rightarrow a^0a^0a^-$)

The temperature dependence of the analysis of the neutron diffraction patterns allows us to further discuss the structural changes across T_{S1} and T_{S2}.

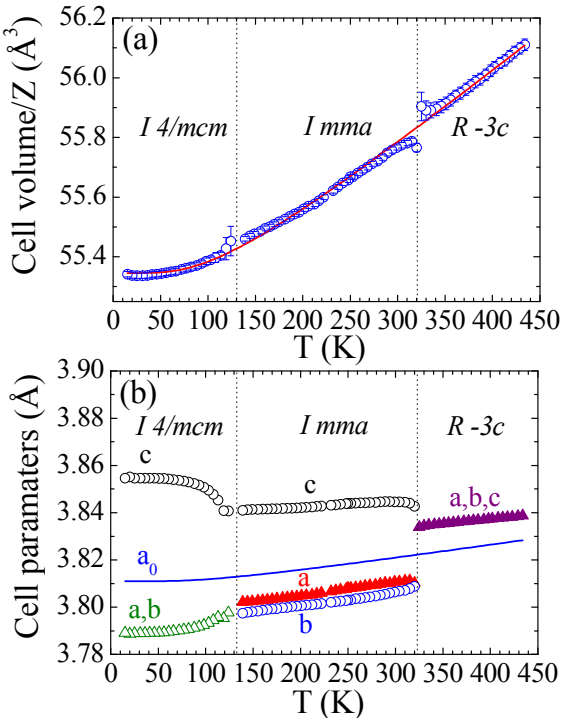

Figure 4. 25. (a) Evolution of the cell volume (per formula unit, Z) up to 450 K. The solid line, fitting the equation $V_0 = V_1 + V_2\,\Theta\coth(\Theta/T)$ is a guide to the eye. (b) Evolution of the reduced lattice parameters with temperature. Solid line shows the reference parameter a_0 obtained from the reduced volume ($a_0 = V_0^{1/3}$).

The evolution of the cell volume and the cell parameters up to 450 K are plotted in Figure 4. 25(a,b). A contraction of the cell volume is detected on cooling, but the volume change in the *Imma* ⟶ *I4/mcm* phase transition is very small (0.1 %) compared to the 2% volume contraction in PCCO at *Pnma* ⟶ *Pnma* transition when enters the insulating phase [see Figure 4. 27(a)]. For a better monitoring of the cell volume we have also fitted the experimental values to the following equation [solid line in Figure 4. 25(a)]:

$$V_0 = V_1 + V_2\,\Theta\coth(\Theta/T) \qquad \text{(Eq. 4.1)}$$

where Θ temperature accounts for the saturation effects in the thermal contractions as T approaches 0 K [45]. Then, the determination of V_0 volume per formula unit allows us to obtain the evolution of the reduced parameter a_0 with temperature ($a_0 = V_0^{1/3}$), which is plotted in Figure 4. 25(b). The temperature dependence of the lattice parameters shows a discontinuous phase transitions due to the abrupt changes across the two structural changes from *R-3c* ⟶ *Imma* and from *Imma* ⟶ *I4/mcm* transitions.

Apart from getting a different rotational system as it was mentioned before, we have also observed a deformation of the regular octahedra across the magnetostructural transition at T_{S1}, through the evolution of the Co-O bond distances and the Co-O-Co bond angles, see Table 4. 3.

In the orthorhombic phase we observe that the CoO_6 octahedra remains close to regular (d_{apical}/d_{basal}=1.917Å/1.922Å and $<d_{Co-O}>$=1.919 Å at RT). On the other hand, when entering in the tetragonal phase we see a stretching deformation of the CoO_6 octahedra at T_{S1} (d_{apical}/d_{basal}=1.927Å/1.913Å and $<d_{Co-O}>$=1.92 Å at 15 K). The evolution of the basal and apical Co-O bond lengths for PSCO is depicted in Figure 4. 26(b). In the *Imma* ⟶ *I4/mcm* transition it is shown that the apical Co-O1 bond enlarges on cooling (around +0.62 %) while the basal Co-O2 bond suffers a contraction which is around -0.32 %.

Concerning the evolution of the bond angles, a similar behavior has been observed. In the orthorhombic phase the bond-angle distortion in the basal plane Co-O2-Co (θ2) is slightly larger than the bond-angle along the apical oxygen Co-O1-Co (θ1) (Co-O2-Co = 169.4º *vs* Co-O1-Co=166.4º at RT). But in the tetragonal phase there is an enlargement of the Co-O1-Co bond angle (+8.3 %) and a shortening of the Co-O2-Co bond angle (-3.2 %) as we can see from Figure 4. 26(a). The comparison between the longest cell parameter in the orthorhombic phase (b = 7.596 Å at 150 K) and the tetragonal phase (c = 7.709 Å at 15 K) shows there is an expansion (+1.5 %) along this direction which is produced by: (i) a stretching deformation in the octahedra and (ii) a straightening of the θ1 angle (there is an increase of around 15º in the tetragonal phase). See Figure 4. 24 (a,b).

Table 4. 3. Evolution of main interatomic distances and bonding angles in the successive phases of $Pr_{0.50}Sr_{0.50}CoO_3$.

$Pr_{0.50}Sr_{0.50}CoO_3$	**400 K** *R -3c*	**300 K** *I mma*	**150 K** *I mma*	**15 K** *I 4/mcm*	Relative Variation (15K-150K)
d_{Co-O1} (Å) *x2*	1.922(13)	1.917(3)	1.915(4)	1.927(3)	0.6%
d_{Co-O2} (Å) *x4*	1.922(13)	1.922(4)	1.919(2)	1.913(6)	-0.3%
$< d_{Co-O} >$ (Å)	1.922(13)	1.919(4)	1.918(3)	1.920(5)	0.1%
Co-O1-Co (deg)	168.92(8)	166.38(16)	165.00(15)	180.00(4)	8.3%
Co-O2-Co (deg)	168.92(8)	169.50(6)	169.41(2)	164.11(2)	-3.2%
<Co-O-Co> (deg)	168.92(8)	168.46(11)	167.94(9)	169.41(3)	0.9%
R-O1 (Å)	2.899(16)	2.946(4)	2.963(15)	2.679(5)	-10.6%
R-O1 (Å)	2.528(16)	2.491(4)	2.469(15)	2.679(5)	7.8%
R-O1 (Å) *x2*	2.705(13)	2.704(3)	2.700(3)	2.679(5)	-0.8%
<R-O1> (Å)	2.709(15)	2.711(4)	2.711(11)	2.679(5)	-1.2%
R-O2 (Å) *x2*	2.528(16)	2.579(16)	2.571(14)	2.524(14)	-1.9%
R-O2 (Å) *x2*	2.899(16)	2.828(18)	2.822(13)	2.524(14)	-11.8%
R-O2 (Å) *x2*	2.705(13)	2.828(18)	2.822(13)	2.894(13)	2.5%
R-O2 (Å) *x2*	2.705(13)	2.579(16)	2.571(14)	2.894(13)	11.2%
<R-O2> (Å)	2.709(15)	2.702(17)	2.697(14)	2.709(13)	0.4%

To get deeper in our analysis it is also interesting to compare some structural parameters to the PCCO compound. Although we observe an elongation along the tetragonal axis in the *Imma* ⟶ *I4/mcm* transition, the inner volume of the CoO_6 octahedra (<Co-O>) is hardly modified as the inset in Figure 4. 27 (b) shows. This evolution in the octahedra is comparable to that observed in PCCO across the MIT when the SS crossover occurs.

Because of the almost inexistent changes in the volume of the octahedra, the volume reduction observed in both samples [see Figure 4. 27(a)] should be attributed to changes in the *R*-O bond lengths [*R* = (Pr, *A*) with *A* = Sr or Ca] that modify the tilting configuration.

Figure 4. 27(b) displays the evolution of <*R*-O> bond distances of the first eight nearest-neighbor oxygen atoms around the *R* site [it consists in four apical *R*-O1 and four basal *R*-O2 bonds] for the two half-doped cobaltites.

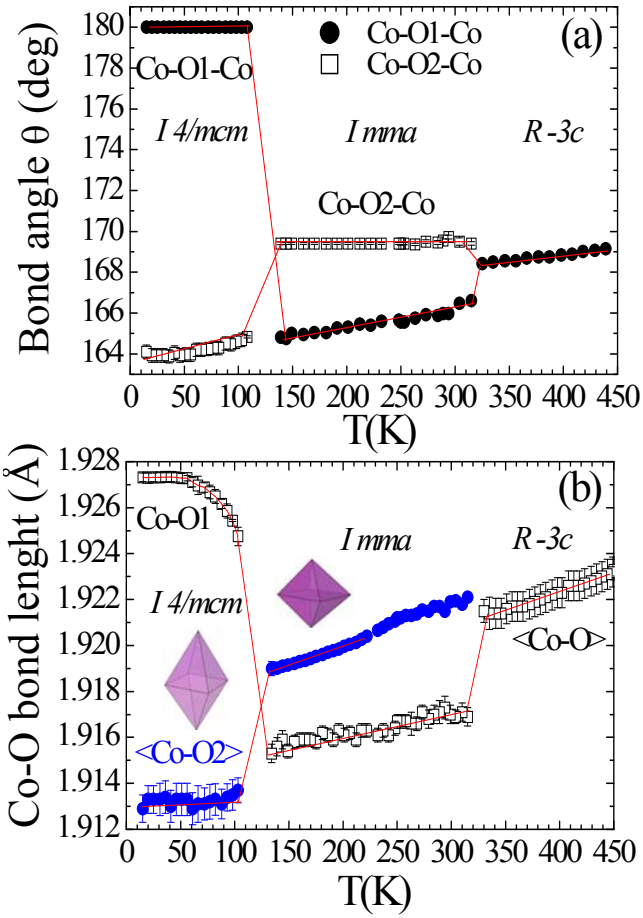

Figure 4. 26. (a) Evolution with temperature of the Co-O-Co bond angles. (b) Evolution of the average Co-O1 and Co-O2 bond lengths in the CoO_6 octahedra across the structural phase transitions.

As we can see in Figure 4. 27(b), PSCO undergoes larger bond contraction at T_{SI} (~ -4 %) than PCCO at T_{MI} (see also Table 4. 3), where a Pr^{3+} to Pr^{4+} valence shift takes place. So, this finding in PSCO could suggest an active participation of Pr ions in the magnetostructural transition. despite the fact that there is any Pr^{3+} to Pr^{4+} oxidation process. Apart from the XAS results; the Pr oxidation state has been also verified by the analysis of the Brown's bond valence model [46, 47]. The most common expression for the variation of length d_{ij} of a bond with valence v_{ij} is:

$$v_{ij} = e^{(R_0 - d_{ij})/b} \qquad \text{(Eq. 4.2)}$$

Where R_0 (Pr^{3+}) = 2.138 extracted from Ref. [46] and b is an universal constant equal to 0.37.

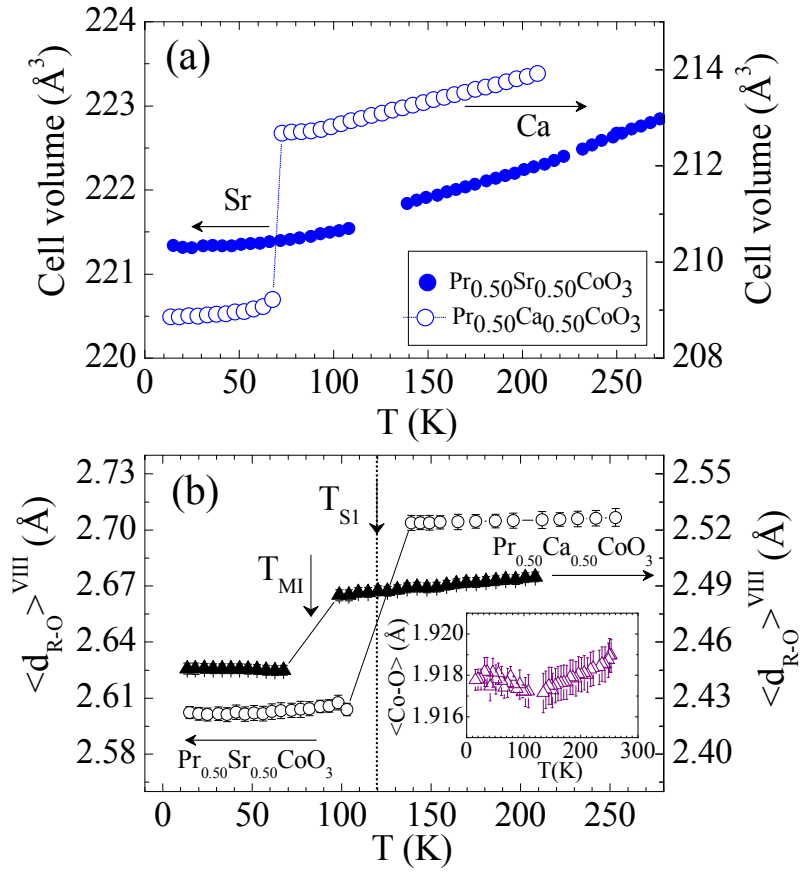

Figure 4. 27. Comparative evolution of (a) the cell volume and (b) the average (Pr,A)-O bond distance (VIII-shell, A: Ca or Sr) of $Pr_{0.50}Sr_{0.50}CoO_3$ (left axis) and $Pr_{0.50}Ca_{0.50}CoO_3$ (right axis).The inset in panel (b) depicts the average Co-O distance in PSCO.

The experimental values for the Pr-O bond distances and the bond valence are listed in Table 4. 4 The experimental Pr-O1/O2 are determined using the reference value $d(\text{Sr-O})^{\text{VIII}}$ = 2.66 Å for the Sr- O distance extracted from Ref. [48]. So, the resulting valence associated with the Pr-O bonds in the VIII shell changes from +2.12 at 150 K up to +2.92 at 15 K.

Table 4. 4. Calculated Pr valence using the valence bond method once the experimental Pr-O bond distance is determined.

$Pr_{0.50}Sr_{0.50}CoO_3$	400 K	149 K	15 K
$V_{Pr\text{-}O1}$	0.067	0.047	0.220
$V_{Pr\text{-}O1}$	0.498	0.685	0.220
$V_{Pr\text{-}O1}$ *x2*	0.192	0.197	0.220
$< v_{Pr\text{-}O1} >$	0.237±0.25	0.281±0.24	0.220
$V_{Pr\text{-}O2}$ *x2*	0.498	0.395	0.509
$V_{Pr\text{-}O2}$ *x2*	0.1917	0.101	0.509
$< v_{Pr\text{-}O2} >$	0.345±0.23	0.248±0.15	0.509±0.05
$< v_{Pr\text{-}O} >$	0.291	0.264	0.366
V_R	2.33	2.12	2.92

In Figure 4. 28 the temperature evolution of all individual *R*-O bond length [considering the twelve nearest neighbor oxygens around Pr (8+4)] are plotted for the three different phases. We observe in the orthorhombic phase 3 inequivalent Pr-O1 with values: 2.96 Å, 2.70 Å (x 2) and 2.47 Å as Leighton *et al.* reported in Ref. [27] and the shortest eight Pr-O2 distances. However, in the tetragonal phase there is only one Pr-O1 distances, unlike the report presented by Leighton which showed the tendency to equalize the inequivalent Pr-O1 distances in the low temperature phase, and also eight Pr-O2 distances. Thus, in the tetragonal phase there are only 3 different Pr-O distances in front the 5 distances that presents the orthorhombic phase.

To get further insight we have also determined the evolution of the average distances $<R\text{-O}>^{VIII}$, considering only the first coordination sphere. The data are plotted in Figure 4. 29, and we only focus on the *Imma* $\longrightarrow$ *I4/mcm* transition. This figure clearly evidences that the largest changes in $<R\text{-O}>^{VIII}$ are attributed to the oxygen in the basal plane of the octahedra ($R\text{-O2}>^{VIII}$) during the magnetostructural transition. The variation of the *R*-O2 bond distances comparing both sides of the transition is around $\Delta d \sim 6.5$ %.

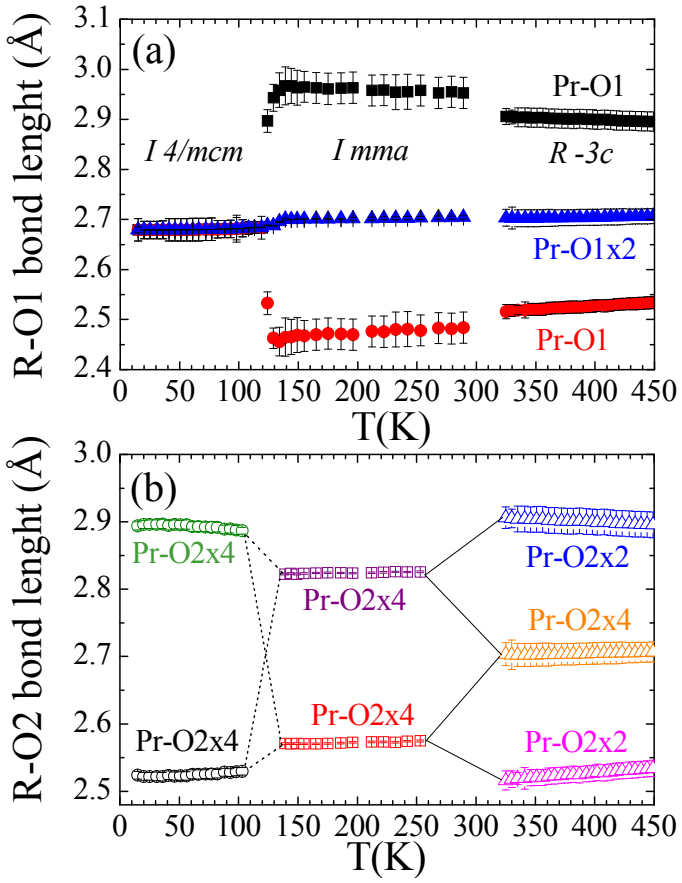

Figure 4. 28. Evolution of (a) the *R*-O1 and (b) *R*-O2 bond lengths in $Pr_{0.50}Sr_{0.50}CoO_3$ in the rhombohedral, orthorhombic and tetragonal phases and across the structural transitions.

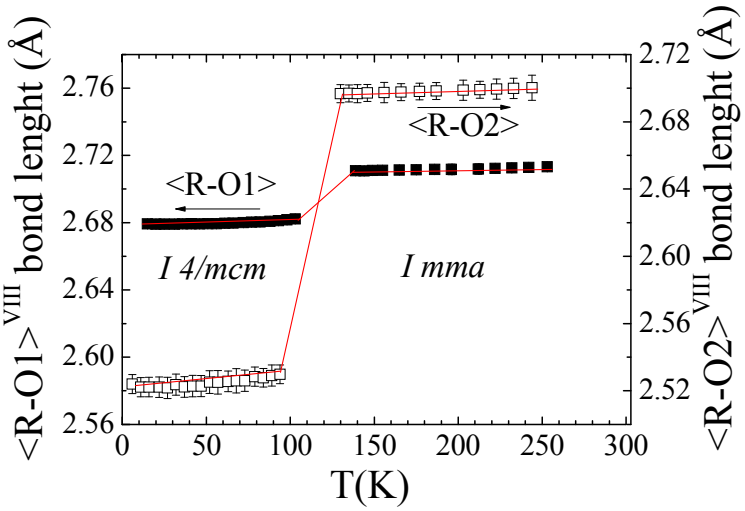

Figure 4. 29. Evolution with temperature of the average (Pr,Sr)-O1/O2 bond distances (VIII-coordination) across T_{SI} in PSCO. The solid lines are guides to the eye.

4.7. The spin-lattice coupling across the magnetostructural transition studied by XMCD

The presumption of magnetocrystalline changes at the origin of the magnetization anomalies at ~120 K led us to explore the presence of unquenched orbital moment contribution to the magnetization. A possible interplay between orbital and spin components requires additional characterization efforts. For this reason, we have performed temperature dependent X-ray Magnetic Circular Dichroism (XMCD) measurements at the Co $L_{2,3}$ edges. The theoretical grounds of XMCD were settled more than two decades ago and this is a now well established technique [49–53]. One of the most attractive features of XMCD is the possibility to determine the element specific spin and orbital magnetic moments via sum rules.

We have carried out the XMCD measurements at two different magnetic fields (0.1 T and 5 T) at BL29-BOREAS beamline (ALBA Synchrotron) by total electron yield (TEY). In Figure 4. 30(a) we show the X-ray absorption spectra (XAS) collected at the Co $L_{2,3}$ edges for left (I^-) and right (I^+) circularly polarized X-rays at 50 K, under a large applied magnetic field of 5 T parallel to photons helicity. For this field value we guarantee that the Co magnetization is fully saturated. The XMCD signal is determined from the difference of I^- and I^+ as shown in Figure 4. 30(b). We observe a large negative peak at the Co L_3 in the XMCD spectrum which is typical for a ferromagnetically ordered (FM) system like PSCO at T < T_C. In contrast, we also see that the Co L_2 dichroic signal is far smaller than the L_3 edge one, which suggests a relatively large orbital moment contribution to the total Co magnetic moment. The same can be deduced observing the XMCD integration signal where the q value is considerably large in front the p value (see Chapter 2 for the definitions of p and q numbers). In addition, the temperature dependence of the XMCD spectra between 40 K and room temperature under an applied magnetic field of 0.1 T is plotted in Figure 4. 30(c). In this case, we see that the dichroic signal is larger when the temperature decrease and it becomes zero for temperatures close to T_C when the FM order vanishes.

Orbital and spin moments

According to the XMCD sum rules (see equations 2.25 and 2.26 from Chapter 2) we can directly extract the orbital (m_L) and the spin effective (m_S^{eff}) moments, which are the projection of the $\langle \mathbf{L} \rangle$ and $\langle \mathbf{S}^{\text{eff}} \rangle$ operators along the X-rays propagation axis (in this case along the z axis which is the direction of the applied magnetic field). $\langle \mathbf{S}^{\text{eff}} \rangle$ is defined as $\langle \mathbf{S}^{\text{eff}} \rangle = \langle \mathbf{S} \rangle + \langle \mathbf{T} \rangle / 2$, tends to $\langle \mathbf{S} \rangle$ the spin operator and $\langle \mathbf{T} \rangle$ the intra-atomic spin dipole operator which can be negligible

for octahedral metallic systems characterized by reduced exchange fields [54]. For this reason, it will be discarded it in our analysis and we will assume $m_S^{eff} \sim m_S$ from now on.

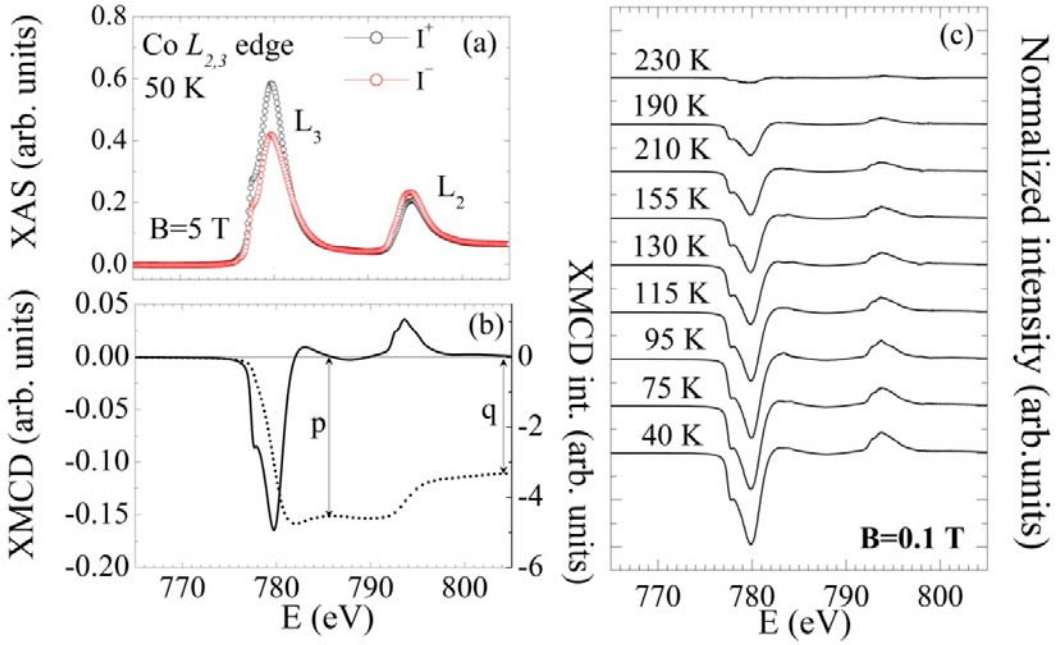

Figure 4. 30. (a) Co $L_{2,3}$ X-ray absorption spectra with positive (I^+, open black circles) and negative (I^-, open red circles) helicity in $Pr_{0.50}Sr_{0.50}CoO_3$ at 50 K and 5 T applied field. (b) XMCD signal (solid black line, left axis) and the corresponding XMCD integration applied in sum-rules calculations (dotted line, right axis). (c) Temperature dependence of the Co $L_{2,3}$ XMCD signal at 0.1 T. The spectra have been vertically shifted for clarity.

The application of the sum rules to the XMCD spectra at 50 K in the high field case (5 T) yields m_S = 0.297(6) μ_B/3*d* hole and m_L = 0.095(2) μ_B/ 3*d* hole, from which we derive m_L/m_S = 0.32. Let us mention that the most common values in cobaltites with different oxidation states range from m_L/m_S =0.2 to 0.6 [55, 56]. At this point, we can compare the magnetization results obtained with XMCD at saturation with neutrons data, assuming a nominal average number of Co 3*d* holes $\langle n_h \rangle$ = 4.5 for this system. Using this value for the data measured at 5 T and 50 K, the spin and orbital sum rules yield m_S = 1.34 μ_B and m_L = 0.43 μ_B in average per Co ion, with a net magnetic moment of 1.77 μ_B/Co ion. This value is in excellent agreement with the magnitude of the ordered FM moment found by neutron diffraction at 15 K without applying any external field [m=1.76(9) μ_B/Co ion, see Table 4.2]. By matching this value to the net magnetic moment $m_S + m_L$ obtained from XMCD, we extract $\langle n_h \rangle$ = 4.48. So, we got confident about the taken average number of Co 3*d* holes and we may consider the occupation

of Co 3d orbitals to be somewhat larger than 10-$\langle n_h \rangle$ = 5.52 electrons. We must note that one of the most important errors when applying the sum rules comes from the estimation of the number of holes, as we commented in Section 2.5.2.1.

Now, we will focus on the results obtained under an applied field of 0.1 T. In Figure 4. 31(b) we have plotted the temperature evolution of the PSCO magnetization measured under this magnetic field value on warming. As we have commented in Section 4.3, the characteristic feature in the M(T) at this field value is a positive-step. The sign crossover of the magnetization amplitude (H_{cr}) can be determined by inspection of the temperature dependence of the coercive field in the inset of Figure 4. 31. As we see the local maximum of ~30 mT at T_{S1} corresponds to H_{cr}. The temperature dependence of m_S and m_L obtained by applying the spin and orbital sum rules to the XMCD spectra at 0.1 T is plotted in Figure 4. 31(a).
From the analysis we can extract the following conclusions:

(i) the spin moment projection m_S along the axis of the external magnetic field follows the same step-like behavior shown by the magnetization at the same applied field;
(ii) the projected orbital moment m_L is sizeable (around 1/3 of the spin component);
(iii) m_L mimics the evolution of the bulk magnetization and m_S, presenting a positive step.

So, the similar evolution between m_L and m_S strongly suggests the presence of a spin-orbit coupling in the system similar to the behavior found in other compounds such as $Nd_2Fe_{14}B$ and ε-Fe_2O_3 [57, 58]. As we know, the spin-orbit interaction is given by [59]:

$$H_{SO} = \xi_{nl}(r) S \cdot L \qquad \text{(Eq. 4.3)}$$

where ξ_{nl} is the spin-orbit coupling constant

Thus, this coupling promotes a parallel alignment of both kinds of magnetic moments at both sides of the MS transition namely: (i) the FM phase with *Imma* symmetry (**FM2**) and (iii) the FM phase with *I4/mcm* symmetry (**FM1**). Finally, it should be noted that the evolution of the net magnetic moment $m_L + m_S$, is consistent with the bulk magnetization measured at 0.1 T, as expected.

Bearing in mind the results presented in the previous sections, now it is the turn to comment the evolution of m_S and m_L across T_{S1} shown in Figure 4. 31(a). One of the main conclusions is that the changes in both magnetic moments are not related with a SS transition in the Co ions as pointes out in Section 4.5 by XAS studies at the Co $L_{2,3}$ and O *K* edges. An alternative scenario also proposed by different authors [31, 32] might be a change in the magnetic easy-axis direction when the system adopts the tetragonal *I4/mcm* phase. The

symmetry changes at the MS transition in the absence of an external field can easily provoke the reorientation of the orbital moment, and as a consequence, the rotation of the ordered Co spins across T_{SI} owing to the spin-orbit coupling. To confirm this, a detailed magnetic characterization using neutron diffraction is required as is presented in the next section.

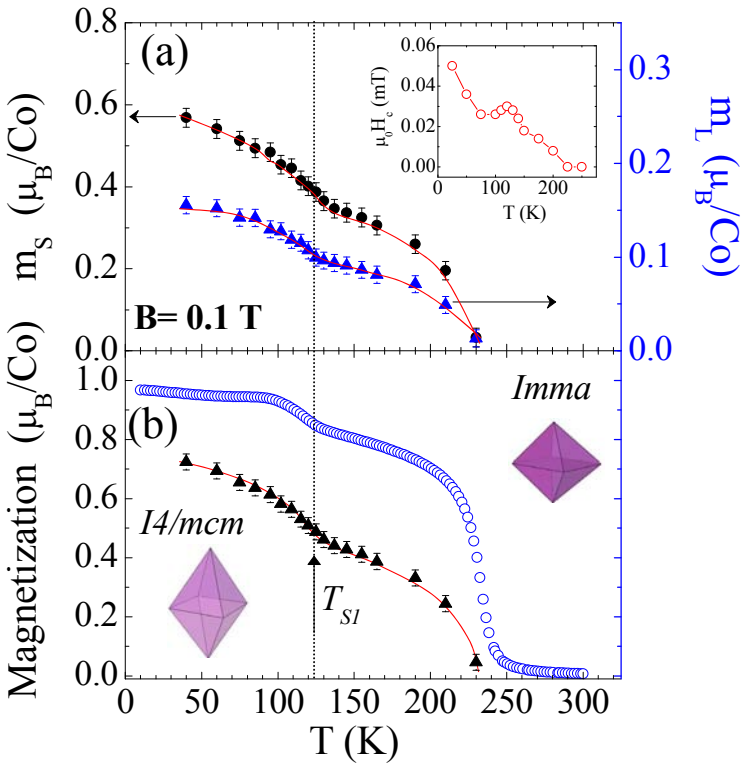

Figure 4. 31. (a) Temperature dependence of the spin magnetic moment m_S (solid black circles) and the orbital magnetic moment m_L (solid blue triangles) derived from XMCD spectra of PSCO at 0.1 T. *Inset*: coercive field ($\mu_0 H_C$) vs T. (b) Temperature dependence of m_L+m_S (solid black triangles), and dc magnetization (open blue circles) measured at 0.1 T. The solid red line is an eye-guide. The shape of CoO_6 octahedra in each structural phase is schematically represented.

Electronic models

Concerning the electronic configuration of Co ions in PSCO, we can propose possible models compatible with the presented XAS and XMCD results. We have built three different models based on the average $S = 0.75$ value, a plausible value taking into account the m_S here found by XMCD at 5T and the effective spin $S = 0.75$ in the metallic phase for PCCO. In principle, half of the Co atoms should be in the Co^{4+} LS (S =1/2, $t_{2g}^{5}\ e_g^{0}$) configuration, as to what reported in PCCO [22].

:

However, Co^{4+} could be partial excited into an IS state following the studies by Guillou *et al.* [43] and J. M. Chen *et al.* [60] on $(Pr_{0.7}Sm_{0.3})_{0.7}Ca_{0.3}CoO_3$. Thus, it is interesting to consider up to three different scenarios taking into account that PSCO cannot be dominated by a LS state [61]: the *first model* contemplates all Co^{3+} in an IS (S=1, $t_{2g}^{5}\ e_g^{1}$) state; the *second model* assumes an equilibrated mixture of LS:HS(25:25) Co^{3+} ions and Co^{4+} remaining in LS; and finally the *third model* requires one fifth of all Co^{4+} ions in the IS state, and the convenient ratio of Co^{3+} LS and HS (30:20) to fulfill S=0.75.

A further discussion to outline the spin state of co ions in $Pr_{0.50}Sr_{0.50}CoO_3$ will be given in Section 4.9, complementing XAS and XMCD results with other experimental spectroscopic measurements and theoretical calculations.

4.8. Determination of the magnetic structures across the magnetostructural transition

As we have commented in Section 4.6.2, below T_C = 230 K we observe changes in the neutron diffraction profile because of emerging FM peaks in the PM *Imma* phase. The intensity augmentation of some Bragg reflections is clearly observed if we compare patterns at 300 K and 140 K in the range up to 90º (where the FM intensities are still present) as Figure 4. 32 shows. The principal magnetic reflections are indicated in the basis of $\sqrt{2}a_0$ x $2a_0$ x $\sqrt{2}a_0$ unit cell.

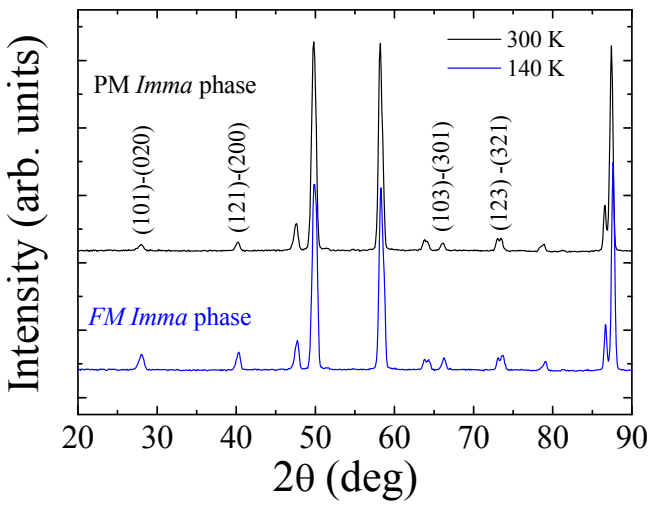

Figure 4. 32. Selected angular region of neutron powder diffraction pattern measured at 300 K (PM *Imma* phase) and 140 K (FM *Imma* phase) in D20 (λ=1.87 Å). Profiles have been shifted up for clarity and are indexed according to $\sqrt{2}a_0$ x $2a_0$ x $\sqrt{2}a_0$. The indexed peaks correspond to the most important magnetic peaks.

Since the two FM phases at both sides of the magnetostructural transition are not identical, we shall distinguish:

(i) the FM phase with *Imma* symmetry (**FM2**) at $T_C > T > T_{S1}$;

(ii) the FM phase with *I4/mcm* symmetry (**FM1**) at $T < T_{S1}$.

In both FM phases the propagation vector of the magnetic structure is $k = 0$, so the magnetic unit cell coincides with the chemical cell.

From Rietveld refinements using the correct Magnetic Space Groups (MSGs) the thermal evolution of the FM magnetic moment at the Co ion for $Pr_{0.50}Sr_{0.50}CoO_3$ has been extracted. Figure 4. 33 shows its evolution from 300 K to 15 K, the FM moment taking a value of 1.87(5) μ_B/Co at low temperature. The selection of the correct MSGs will be discussed latter.

We observe that the ordered FM moment enhances as the temperature decreases and just across the MS, the magnitude of the moment suffers a slight reduction induced by the natural disorder during the *Imma* $\rightarrow$ *I4/mcm* transition (between 98 K $\leq$ T $\leq$ 134 K we found the coexistence phase, yellow zone).

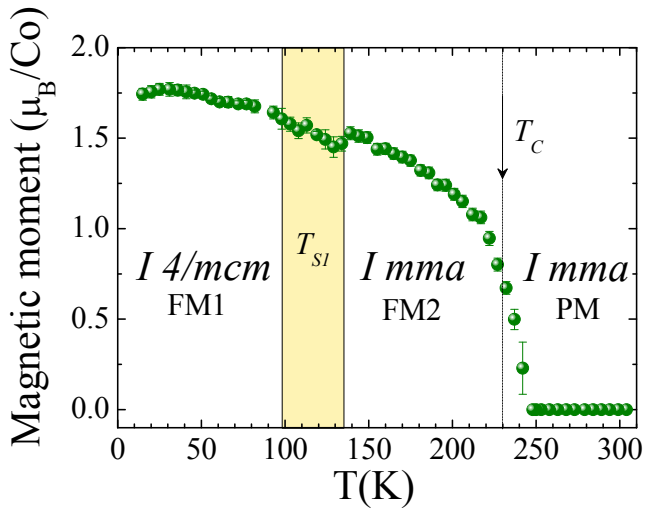

Figure 4. 33. Temperature dependence of the magnetic moment across the *Imma* to *I4/mcm* transition obtained from Rietveld refinements of the neutron diffraction pattern.

From now on, the orientation of the magnetic moments will be detailed separately for each FM phase. However, before going deeper into the problem, it should be noted that the magnetic symmetry is correlated with the structural symmetry. One of the main difficulties of the problem in the Rietveld refinements is the cross-correlation between magnetic and structural parameters. So, both the atomic positions (i.e. of the oxygen atoms) and the magnetic parameters (i.e. symmetry) contribute to the experimental intensity of many reflections. Thus,

it is important firstly to solve the crystal symmetry (which is already done) and secondly, to determine the magnetic symmetry taking into consideration possible space groups compatible with the crystal symmetry.

On the other hand, another point to avoid possible confusions in the analysis of the magnetic structures is to define the FM models in the same unit cell settings. As we have seen, the standard settings *Imma* and *I4/mcm* groups correspond to different orientations of the perovskite cell: $\sqrt{}a_0$ x $2a_0$ x $\sqrt{}a_0$ and $\sqrt{}a_0$ x $\sqrt{}a_0$ x $2a_0$, respectively. For that reason and to gain clarity, from now on, for the discussion of the FM orientations $F_{x,\,y,\,z}$ are referred or defined in the unit cell setting of the tetragonal phase, where the coordinate z refers to the longest axis $2a_0$, So, this means that in the F_z model all the spins are pointing parallel to the longest axis, which is *c* axis in the *I4/mcm* and *b* axis in the *Imma* phase.

However, the indexation of the different Bragg reflections presented along this section will be done in the basis of the standard setting of the corresponding phase (*Imma* or *I4/mcm*).

4.8.1. Ferromagnetism in the *Imma* phase (FM2)

In this section we will present the details of the magnetic structure and the orientation of the magnetic moments in the FM2 phase.

Because of the small orthorhombic distortion of PSCO in the *Imma* phase, we found not easy to determine the exact orientation of the ferromagnetic Co moments. The magnetic structure in the orthorhombic phase has been resolved from a NPD pattern acquired at 140 K in the D20 diffractometer. We have tried refinements using different moment orientations (F_x, F_y, F_z) (they are described in Table 4. 5, corresponding to the *Imma* setting) to reproduce the experimental profile and we found the best fitting for F_x model [*Im'm'a* (#74.558)] for which the agreement factors are (in the range up to 90º): R_B = 3.38 %, R_f = 2.74 %, R_{Mag} = 4.89 %, χ^2 = 1.58 %. The ferromagnetic moment obtained from neutron data at 140 K was m_x = 1.49(4) μ_B/Co. The Rietveld refinement at 140 K (**FM2** *Imma*) using F_x model is plotted in Figure 4. 34 below 80º. In the inset a close view of the refined most important magnetic reflections [(103), (301), (123) and (321)] between 62º and 75º is shown.

Table 4. 5. Some possible collinear magnetic space groups (BNS notation) compatible with the *Imma* symmetry and *k*=(0,0,0). Coordinates using the *Imma* setting.

Magnetic Space Group	Coordinates for Co /moment	Magnetic structure (example)
Im'm'a (#74.558)	(0,0,1/2 | 0, m_y, m_z) (0,1/2,1/2 | 0, -m_y, m_z) (1/2,1/2,0 | 0, m_y, m_z) (1/2,0,0 | 0, -m_y, m_z)	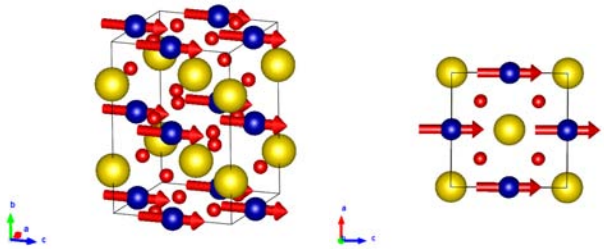
Imm'a' (#74.559)	(0,0,1/2 | m_x,0, 0) (0,1/2,1/2 | m_x,0, 0) (1/2,1/2,0 | m_x,0, 0) (1/2,0,0 | m_x,0, 0)	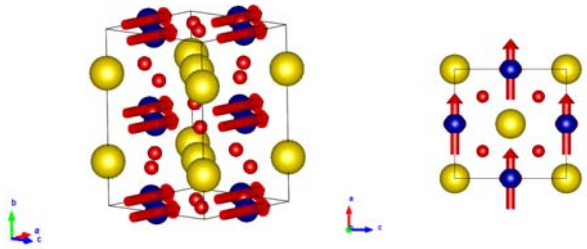
Imm'a' (#74.559)	(0,0,1/2 | 0, m_y, m_z) (0,1/2,1/2 | 0, m_y,-m_z) (1/2,1/2,0 | 0, m_y, m_z) (1/2,0,0 | 0, m_y,-m_z)	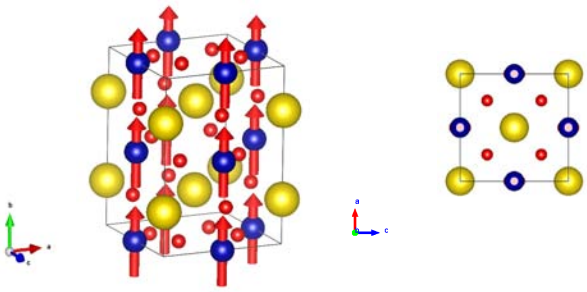

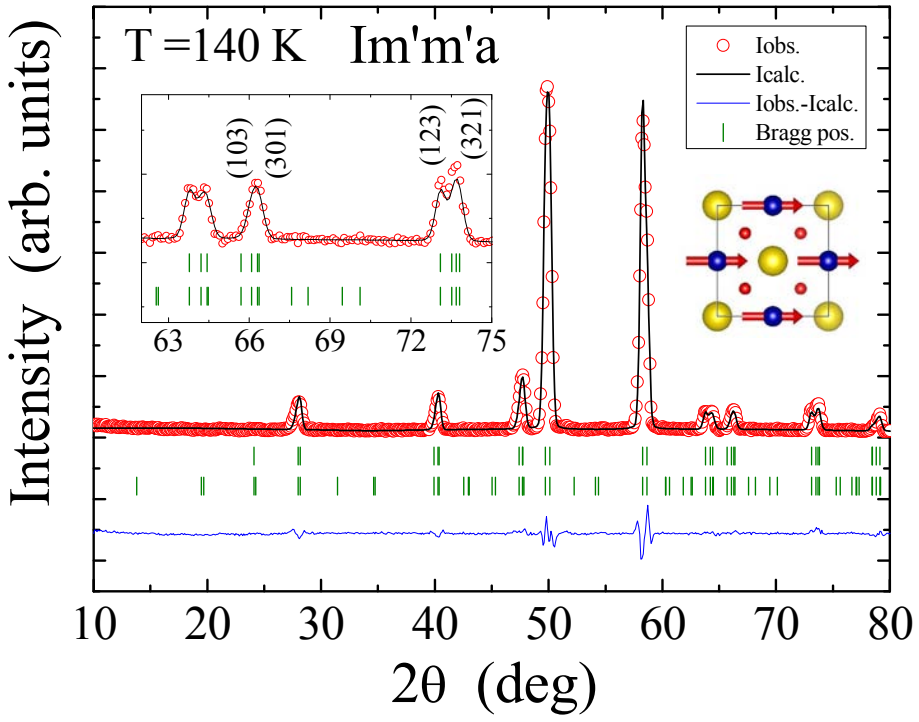

Figure 4. 34. Rietveld refinement (solid line) of neutrons patterns measured in D20 at 140 K (FM2 phase) for the orthorhombic structure *Imma*. Diffraction patterns are indexed according $\sqrt{2}a_0$ x $2a_0$ x $\sqrt{2}a_0$. The inset shows indexed magnetic peaks. Also a schematic view of the magnetic structure is plotted: the yellow balls are Pr/Sr atoms; the blue balls are Co atoms and the red balls are O atoms.

To notice is that the refinements testing F_y and F_z orientations are subtly worst resolving the intensities and profile of some peaks. The goodness factors obtained yields: R_B = 3.14 %, R_f = 2.90 %, R_{Mag} = 7.41 %, χ^2 = 1.37 % for F_y and R_B = 3.27 %, R_f = 2.97 %, R_{Mag} = 6.77 %, χ^2 = 1.37 % for F_z. We proved by simulations that the magnetic intensities using these two orientations produce an excess of intensity at (103) reflection as Figure 4. 35 (c, d) shows (for F_y or F_z models), in contrast to the F_x model [see Figure 4. 35 (a)] in which the (103) peak is negligible compared to (301) reflection. Moreover, the different relative distribution of the magnetic intensity at (123) and (321) is better reproduced with F_x ordering than the other two orientations as it is shown in Figure 4. 35 (d, e, f,) (in these graphics the moment magnitude is exaggerated to better observe the effect). So, we can conclude that the magnetic structure in $Pr_{0.50}Sr_{0.50}CoO_3$ is well reproduced with [100] FM domains above T_{SI}, discarding [010] and [001] magnetic domains in this FM2 phase [orientations here are referred to ($\sqrt{2}a_o$, $\sqrt{2}a_o$, $2a_o$) cell].

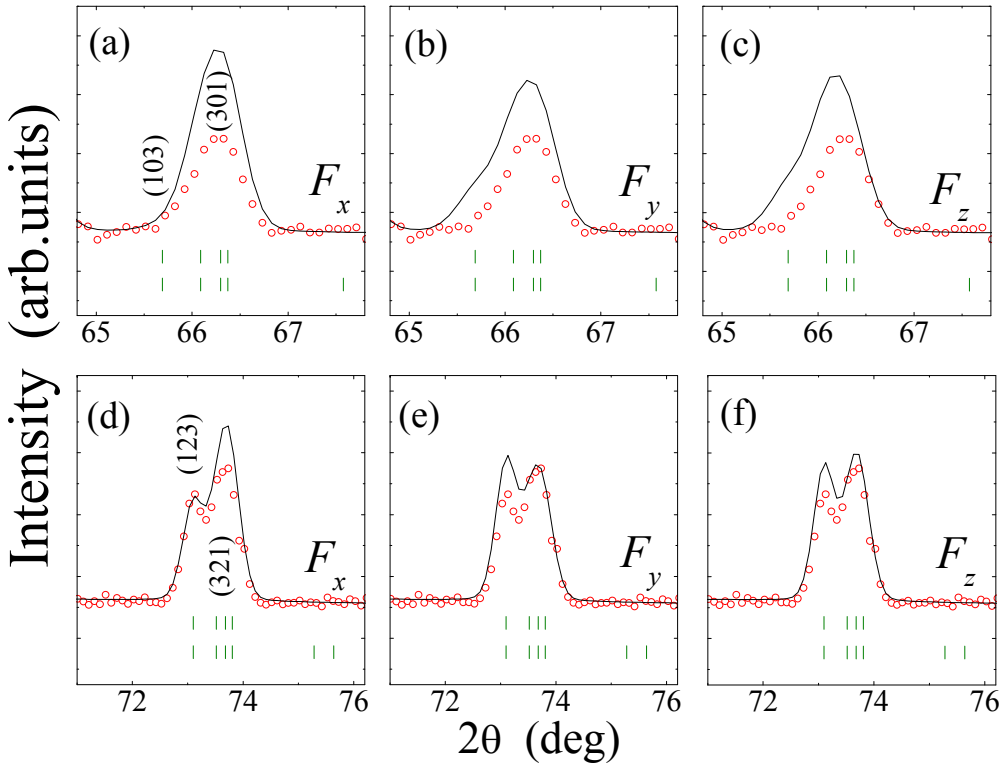

Figure 4. 35. Simulation of some selected magnetic peaks (solid line) of neutrons patterns (red open circles) measured at 140 K: (a), (b) and (c) correspond to (103) and (301) peaks and (d), (e) and (f) correspond to (123) and (321) ones. In the calculations the size of the FM moment was exaggerated.

4.8.2. Cobalt spin reorientation in the *I4/mcm* phase (FM1)

The thermal evolution of the integrated intensity of some selected magnetic reflections have been investigated owing to its intensity decrease observed in NPD patterns just when the FM1 phase takes place. In Figure 4. 36 is plotted the thermal evolution of the integrated intensity for some magnetic reflections (101)-(020) and (121)-(200) allocated at 2θ ~ 28º and 2θ ~ 40º, respectively (D20 data). First, we observe the onset of the FM2 order at T_C ~230 K, as expected from the magnetic measurements earlier discussed in Section 4.3. Second, from the integrated intensity of these peaks, we observe a reduction of their magnitude across the magnetostructural transition which reminds the step-like behavior observed in the M(T) measured at low fields. Different hypothetical scenarios could explain this reduction coinciding with the tetragonal phase: (i) a decrease of the spin state across the MS transition which implies an spin-state transition, (ii) a modified magnetic order in the low temperature phase without producing new magnetic peaks, or (iii) emerging covalence effects leading to a Co → O magnetic transfer as it has been reported in other cobaltites [62].

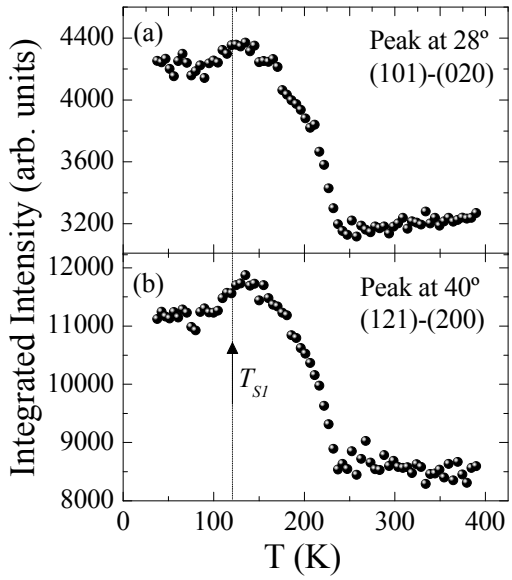

Figure 4. 36. Thermal variation of the integrated intensities of selected magnetic reflections (a) (101)-(020) and (b) (121)-(200). The peaks are indexed according to the $\sqrt{2}a_0$ x $2a_0$ x $\sqrt{2}a_0$.

The first hypothesis can be discarded because of the results obtained by means of X-ray absorption spectroscopy presented in Section 4.5.2. No spin state transition is seen for PSCO. The two last hypothesis have been investigated as detailed next.

I. The problem of the FM1 magnetic order.

In order to solve the problem of the FM1 magnetic order (the key to understand the anomaly in the magnetization of PSCO) we have explored a variety of possibilities. Using as starting point the tetragonal *I4/mcm* crystal symmetry determined by us, and the k=(0,0,0) magnetic propagation vector of the FM1 phase, with the collaboration of J.L. García Muñoz, a series of symmetry compatible magnetic groups were checked against our neutron data. Using the Bilbao Crystallographic Server [63] we have considered possible collinear and non-collinear magnetic space groups (MSG) compatible with the *I4/mcm* symmetry. Some of them are described in Table 4.6 and are compatible with k=(0,0,0). The magnetic coordinates in the table correspond to the *I4/mcm* setting. As shown, collinear and non-collinear subgroups were considered: *Iba'm'* (BNS 72.544), *Fm'm'm* (BNS 69.524), *C2'/m'* (BNS 12.62), *I4/mc'm'* (BNS 140.547), among others. All of them compatible with a net ferromagnetic. The magnetic subgroups (MSG, also called Shubnikov group) are referred to the Belov-Neronova-Smirnova (BNS) notation. The accompanying magnetic structures are examples compatible with each MSG.

Table 4.6. Some possible collinear and non-collinear structures and magnetic space groups (BNS notation) compatible with the *I4/mcm* symmetry and k=(0,0,0). Coordinates using the *I4/mcm* setting.

Magnetic Space Group	**Coordinates for Co /moment**	**Magnetic structure (example)**
Iba'm' (#72.544)	(0,0,0 | m_x,m_y,0) (0,0,1/2 | m_x,-m_y,0) (1/2,1/2,1/2 | m_x,m_y,0) (1/2,1/2,0 | m_x,-m_y,0)	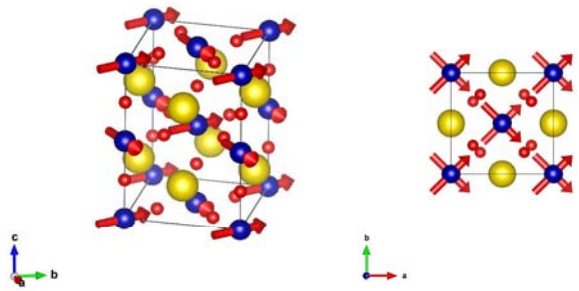
Fm'm'm (#69.524)	(0,0,0 | m_x,m_y,0) (0,0,1/2 | -m_y,-m_x,0) (1/2,1/2,1/2 | m_x,m_y,0) (1/2,1/2,1/2|-m_y,-m_x,0)	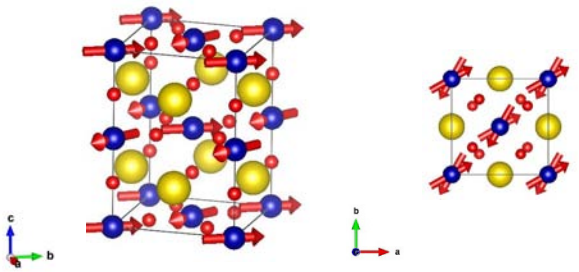
C2'/m' (#12.62)	(0,0,0 | m_x,m_y,0) (0,0,1/2 | m_x,m_y,0) (1/2,1/2,1/2 | m_x,m_y,0) (1/2,1/2,0 | m_x,m_y,0)	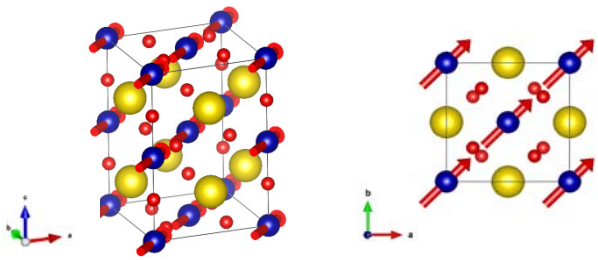
I4/mc'm' (#140.547)	(0,0,0 | 0,0,m_z) (0,0,1/2 | 0,0,m_z) (1/2,1/2,1/2 | 0,0,m_z) (1/2,1/2,0 | 0,0,m_z)	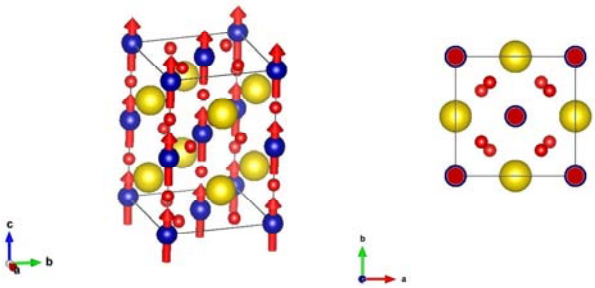

II. Discerning between out-of-plane or in-plane ordering.

From the proposed compatible MSGs, we can distinguish models in which the orientation of the FM moments could be: (i) out-of-plane, which involves F_z order, or (ii) in-plane, which involves F_x, F_y, F_{xy} models. Since now on, all the in-plane models will be called "*models perpendicular to z"* ($F_{\perp z}$). Owing to the tetragonal symmetry at low temperature, the magnetic reflections generated, using FM order along the *x* or *y* directions (F_x or F_y models) or a lineal combination of both *(*F_{xy} model), are equivalents. We have not found any difference in the refinements and reliability factors using these models.

We have tried refinements to reproduce the experimental profile at 15 K using two different moment orientations: the first one by considering Co magnetic moments in-plane models ($F_{\perp z}$ models with *Iba'm'*, F*m'mm*, *C2'/m'* magnetic symmetries) and the second one Co moments out-of-plane (F_z model, like in *I4/mc'm'* magnetic symmetry). The Rietveld refinements at 15 K using F_z and $F_{\perp z}$ models in a selected angular region are plotted in Figure 4. 37. As we can see the set of magnetic reflections (002)-(110)-(1-10) are well reproduced using the $F_{\perp z}$ models [panel (a)] while the F_z model [panel (b)] produces an excess of intensity at (110)-(1-10) reflections in front the lack of intensity at (002) reflection. Also the goodness factors from refinements show the good fitting for $F_{\perp z}$ model: R_B = 6.59 %, R_f = 4.07 %, R_{Mag} = 7.34 %, χ^2 = 1.95 % for $F_{\perp z}$ and R_B = 7.80 %, R_f = 5.98 %, R_{Mag} = 7.34 %, χ^2 = 2.78 % for F_z. So, we can conclude that the magnetic structure in $Pr_{0.50}Sr_{0.50}CoO_3$ at low temperature (FM1) is well reproduced with in-plane FM ordering, and the out-of-plane FM ordering ([001] magnetic domains) can be ruled out.

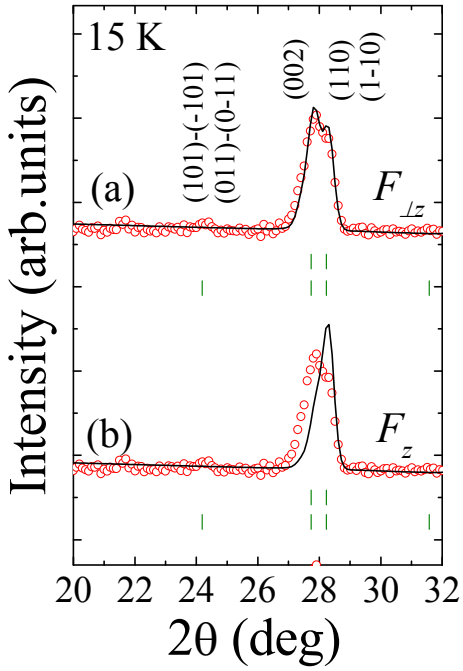

Figure 4. 37. Selected angular region of the Rietveld refinement (solid line) of neutron pattern measured at 15 K using different orientations for the Co magnetic moment: (a) FM model with in-plane magnetic moment ($F_{\perp z}$ model) and (b) FM model with the out-of-plane magnetic moment (F_z model). The reflections are indexed according the $\sqrt{2}a_0$ x $\sqrt{2}a_0$ x $2a_0$ cell (*I4/mcm* setting).

III. Concluding on the FM1 magnetic order.

Collinear and non-collinear models using magnetic symmetries *Iba'm'* and *C2'/m'* were found to reproduce the 15 K neutron pattern. The different attempts to check these two compatible magnetic symmetries, with collinear and non-collinear FM ordering, show that the refinements plainly converge to collinear descriptions. The refinements using non-collinear magnetic structures converges to solutions in which the angle between the magnetic moments is around θ=8º or less which we consider very close to the collinear solutions.

Recapitulating, the acceptable magnetic solutions found to give account of the FM1 phase are well described by the *C2'/m'* (BNS 12.62) MSG (see Table 4.6). The magnetic components can be seen in the table. All Co moments present the same orientation (m_x, m_y, 0). In agreement with the tetragonal symmetry of the structure, any rotation of the identical moments in the *a*-*b* plane around the tetragonal *c*-axis can reproduce the neutron profile at 15 K. Namely, any in-plane FM ordering (being examples F_x, F_y, F_{xy} models) is compatible with neutron data. However, as we have commented in the introduction, the literature [31, 32] suggests a Co spin reorientation at low temperature. Specifically, not well resolved

magnetization measurements across T_{S1} on a PSCO single crystal by Hirahara *et al.* [32] and observations made by Lorentz Transmission Electron Microscopy (TEM) by Uchida *et al.* [31], suggest a rotation by 45º of the magnetic easy-axis. This is shown in the Lorentz TEM images at 140 K and 80 K shown in Figure 4. 38 that we reproduce from Ref. [31]. They are compatible with a 45º rotation of the magnetization.

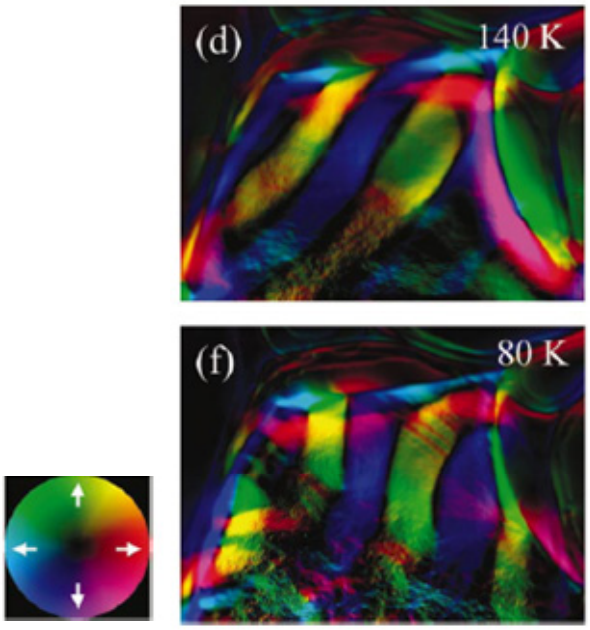

Figure 4. 38. Lorentz images upon zero-field cooling: magnetization distribution proposed from the Transport Intensity Equation calculations in Ref. [31], across T_{S1}=120K in PSCO.

But, having in mind that we have determined F_x ordering above T_{S1}, the two possibilities below T_{S1} would be F_{xz} and F_{xy} models. Hence, combining our neutron results and the available information we are led to conclude that the FM1 magnetic order breaks the structural tetragonal symmetry, to give the monoclinic *C2'/m'* magnetic symmetry, with cobalts having equal m_x and m_y components [$m_x = m_y$ = 1.32(3) μ_B/Co at 15 K]. Resulting in Co moments pointing along the diagonal [110] direction within the *xy* plane. The Rietveld refinement up to 80 º at 15 K (FM1 *I4/mcm*) using this F_{xy} model (*C2'/m'* with $m_x = m_y$) is plotted in Figure 4. 39. The refined total FM ordered moment is 1.87(4) μ_B/Co and the goodness factors obtained yields: R_B = 4.81 %, R_f = 3.16 %, R_{Mag} = 8.55 %, χ^2 = 1.59 %.

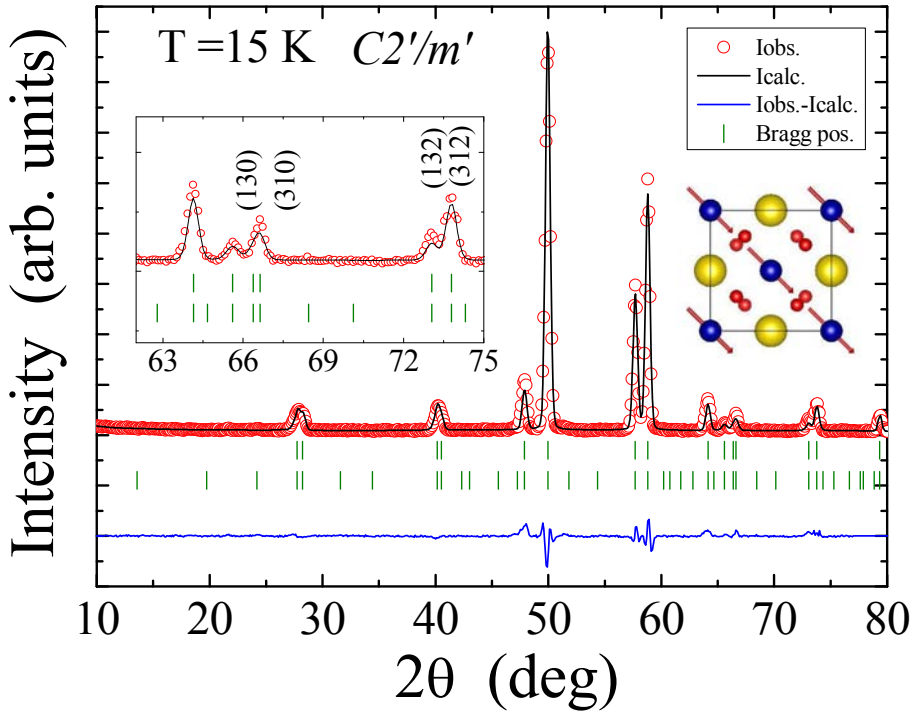

Figure 4. 39. Rietveld refinement (solid line) of neutrons patterns measured in D20 at 15 K (FM1 phase) for the tetragonal *I4/mcm* structure using the monoclinic C2'/m' magentic symmetry with $m_x=m_y$ (F_{xy}). The inset shows relevant magnetic peaks. Also an schematic view of the magnetic structure is plotted: the yellow balls are Pr/Sr atoms; the blue balls are Co atoms and the red balls are O atoms.

4.9. Determination of the spin-state in $Pr_{0.50}Sr_{0.50}CoO_3$

4.9.1. *K*β and *K*α X-ray emission lines

With the aim to determine the spin-state in $Pr_{0.50}Sr_{0.50}CoO_3$, we have performed Co 1*s*3*p* (or Co *K*β main) non-resonant X-ray Emission Spectroscopy (XES) measured in the ID26 (ESRF, Grenoble) and SuperXAS-X10DA (SLS, Villingen) beamlines. In this spectroscopic technique a Co 1*s* core electron is excited by an incident X-ray photon into the continuum, and the core hole is recombined with a Co 3*p* decaying electron, therefore emitting an X-ray photon. In 3*d* transition metals (TM), the *K*β main emission lines reflect the electronic configuration of the valence band (via their energy position and intensity) due to the 3*p*-3*d* exchange interaction. So, this technique is complementary to X-ray absorption (XAS) measurements at the TM $L_{2,3}$ edges since it also provides information about the local charge and the effective number of unpaired 3*d* electrons.

Figure 4. 40 shows the Co *K*β main emission lines measured in $Pr_{0.50}Sr_{0.50}CoO_3$ at 20 K, 150 K, and 300 K, as compared to those of the two compounds used as references: $PrCoO_3$ at 20 K (t_{2g}^6, $S = 0$), and PCCO at 20 K ($S = 0.25$) and 300 K ($S = 0.75$). In addition, we also plotted the $LaMn_{0.98}Co_{0.02}O_3$ spectrum because of its interesting characteristics; it presents a perovskite structure similar to that of PCCO and PSCO, containing Co^{2+} in a HS state ($t_{2g}^5\ e_g^2$, $S = 3/2$) from Ref. [64].

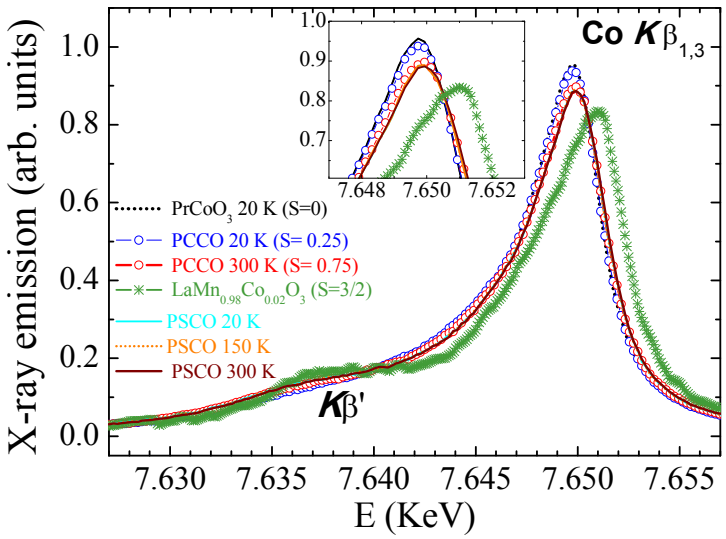

Figure 4. 40. Co *K*β emission spectra of $Pr_{0.50}Sr_{0.50}CoO_3$ at 20 K ($T < T_{SI}$) , 150 K and 300 K ($T > T_{SI}$) , as compared to some references samples: $PrCoO_3$ and $LaMn_{0.98}Co_{0.02}O_3$ at 20 K, and $Pr_{0.50}Ca_{0.50}CoO_3$ at 20 K and 300 K. The inset displays details of the curves.

At first inspection, we do not see variations in the experimental $K\beta_{1,3}$ and $K\beta'$ XES spectra of PSCO across T_{SI}. This is indicative of a nearly constant oxidation and spin-state of Co in this compound in the analyzed temperature range. This assumption is already proposed in Section 4.5.2 as based on XAS measurements at the Co $L_{2,3}$ edges that allowed to discard a spin-state transition in PSCO. The comparison of the Co $K\beta_{1,3}$ spectral shape between PSCO and PCCO at 20 K allows us to determine that both samples have a different electronic configuration of the Co ions. Whereas PCCO is considered to be a mixed Co^{3+} LS:Co^{4+} LS in an approximate 58:42 ratio ($S = 0.21$) in the insulating phase at 10 K as it has been reported by J. Herrero-Martín *et al.* [22], PSCO presents a lower intensity of the Co $K\beta_{1,3}$ main line and at the same time a slight increase of the satellite ($K\beta'$) intensity which points to a larger spin polarization. This is in good agreement with the previous O *K* edge XAS measurements presented in Section 4.5.2, where a large density of empty Co 3*d* states with t_{2g} symmetry has been observed. This result points out to a small contribution of Co^{3+} ions in the low-spin

configuration for $Pr_{0.50}Sr_{0.50}CoO_3$ at T < T_{S1}. On the other hand, the small difference between PSCO and PCCO spectra at 300 K indicates a slightly more excited electronic configuration in the metallic phase for the first one. As we know from XES data in Ref. [22], PCCO is well explained as a mixed Co^{3+} LS:HS (1:1) and Co^{4+} LS mixture, yielding an effective spin S = 0.75 ($S_{PCCO,RT}$ = 0.75). Thus, we can hypothesize that PSCO may have around S ~1 at 300 K, remaining constant or with little variations over the studied range.

To assess the effective spin from the Co $K\beta$ main emission lines in $Pr_{0.50}Sr_{0.50}CoO_3$ we employ the integral of the absolute values of the difference spectra (IAD) method as we have done for the $LnCoO_3$ cobaltites in Chapter 3. This analysis method is an effective approach when used with suitable reference samples, namely samples with a similar local structure to the investigated compound, and known spin state. The IAD procedure has been tested in the determination of the spin state of different compounds yielding excellent results [22, 64–66].
In Figure 4. 41 we summarize the results of the IAD analysis for $Pr_{0.50}Sr_{0.50}CoO_3$, together with the set of experimental points obtained by the comparison of the XES spectra of PSCO with those of PCCO and $PrCoO_3$ reference samples, and also by contrasting PSCO spectra at different temperatures. We can observe a nearly perfect linear correlation between the IAD values and the effective spin derived for all compounds. So, our initial consideration of S = 1 for PSCO (S_{PSCO} =1) at 300 K is pretty consistent in front the IAD method.

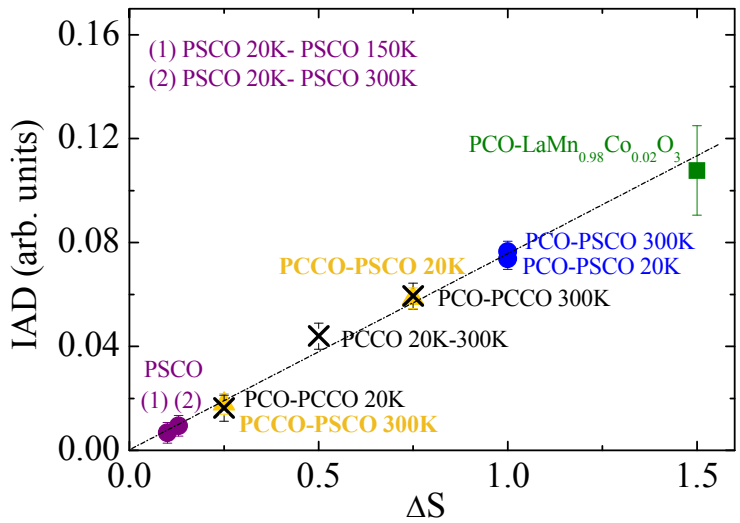

Figure 4. 41. IAD analysis of Co $K\beta$ XES spectra of $Pr_{0.50}Sr_{0.50}CoO_3$ at 150 K and 300 K as compared to 20 K data, which are taken as a reference (purple solid circles). For PSCO at RT we assume S = 1. For PCCO we consider the SS model described in Ref. [22] . For $PrCoO_3$ at 20 K we assume all Co^{3+} LS ions (blue solid circles), while the divalent Co in $LaMn_{0.98}Co_{0.02}O_3$ (HS, green solid squares). The dotted-dashed line is a guide to the eye reflecting the empirical IAD/ΔS linear relation derived.

However, from the IAD values for the XES difference spectra of PSCO at 20 K, 150 K, and 300 K [experimental points (1) and (2) in Figure 4. 41], we deduce that at intermediate and low temperatures (20 K, 150 K) $S_{PSCO} < 1$. Assuming $S_{PSCO} = 1$ at 300 K, then we obtain $S_{PSCO} = 0.85$ at 20 K, and 0.87 at 150 K. This small evolution in the effective spin between low and room temperatures are rather ascribed to a thermal activation of electron mobility than to a real SS transition bearing in mind the earlier reported XAS measurements, and also considering that S_{PSCO} is nearly constant across T_{S1}.

To get deeper into the determination of the SS in $Pr_{0.50}Sr_{0.50}CoO_3$, we have complemented the experimental Co $K\beta$ emission lines analysis with the study of the Co $K\alpha$ main X-ray emission lines. The $K\alpha$ spectra arise from the $2p \rightarrow 1s$ deexcitation channels that follows the absorption of an X-ray photon by a 1*s* core electron.

As reported by several theoretical and experimental works, the most intense Co $K\alpha_1$ full width at half maximum (FWHM) is directly proportional to the number of unpaired 3*d* electrons and thus, it can serve as an indicator of the spin state [67–70]. This is known as the Van Vleck's theorem. However, due to the different exchange interaction energies of either the 2*p* (for $K\alpha$ emission spectroscopy) or 3*p* ($K\beta$) core-hole with the 3*d* electrons in the final state, $K\alpha$ spectroscopy offers a more limited sensitivity to the electronic configuration at the valence band.

Figure 4. 42(a) presents the Co $K\alpha$ experimental spectra for PSCO at 90, 150 K, and room temperature (RT), as compared to PCCO at 10 K, 90 K, and RT. We have seen minor changes in the $K\alpha_1$ intensities for PSCO across T_{SI}. Nevertheless, the comparison to the PCCO compound shows a smaller $K\alpha_1$ intensity suggesting a higher spin state as the $K\beta$ lines do. In contrast, we notice a thermal evolution of the $K\alpha_1$ spectra across T_{MI} for the PCCO compound: the intensity decreases as the temperature increases. This can be interpreted as a variation of the average spin-state in Co ions across the MIT, although these changes are rather small as compared to those observed in the $K\beta$ lines.

In order to extract a quantitative value of the effective spin from the $K\alpha$ spectra, we have applied the Van Vleck's theorem. This theorem proposes that the characteristic energy splitting (or linewidth) in the $K\alpha$ emission lines is proportional to the total spin *S* in the 3*d* orbitals according to the Eq. 2.27.

It has been experimentally observed that the linewidth $K\alpha$ is broader for compounds in a high-spin state and narrower for low-spin states [70]. It should be noted that this approach is not always valid, like for example, in HS transition metal compounds, or when comparing systems with very different atomic environments [70]. In our case we applied this method to the study

of PCCO and PSCO for several temperatures to contrast with the information on S extracted from $K\beta$ spectroscopy. The similar orthorhombic crystal structure of these two cobaltites justifies the choice.

Figure 4. 42(b) displays the obtained correlation between S and the FWHM of the $K\alpha_1$ line. For the PSCO compound we have got $S = 0.86$ K at 20 K and $S = 0.87$ at 150 K from the $K\beta$ measurements. On the other hand, no Co $K\beta$ measurements were recorder in the 150 K < T < 300 K range, and we have thus assumed a monotonic linear increase of S_{PSCO} with temperature. This would reflect a progressive increase of the electron population in the 3d e_g levels with temperature similarly to as reported in close systems such as $LaCoO_3$ [55, 65]. So, using this assumption we have found $S = 0.88$ at 170 K and $S = 0.98$ at 280 K.

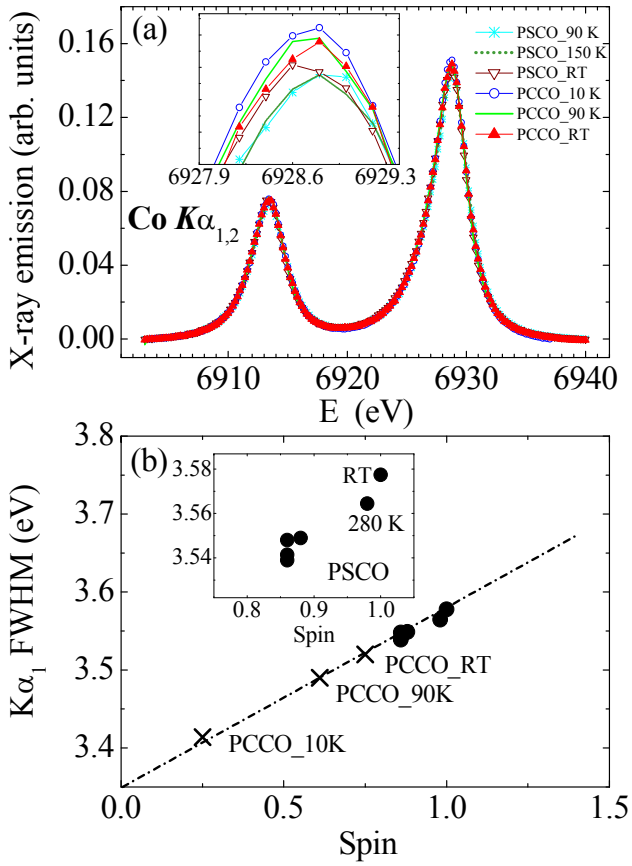

Figure 4. 42. (a) Co $K\alpha$ emission spectra of $Pr_{0.50}Sr_{0.50}CoO_3$ at 90 K (T < T_{SI}), 150 K, and 295 K (T > T_{SI}), as compared to $Pr_{0.50}Ca_{0.50}CoO_3$ at 10 K, 90 K, and 295 K. (b) Measured $K\alpha_1$ FWHM plotted against the net Co 3d spin in $Pr_{0.50}Sr_{0.50}CoO_3$ at different temperatures (black solid circles) and $Pr_{0.50}Ca_{0.50}CoO_3$ at 10 K, 90 K, and 295 K for an IS or LS:HS(1:1) model. The inset zooms in the experimental points for PSCO, for measurements (yielding $S = 0.86$) at 90 K, 101 K, 130 K, and 170 K ($S = 0.88$).

Looking at Figure 4. 42(b), it is clear that the $K\alpha_1$ linewidth follows a linear relation with the spin-state and that the $K\alpha$ results are consistent with the data reported by the XAS and the $K\beta$ measurements.

4.9.2. XAS at Co *K* and Co $L_{2,3}$ edges

The subtle electronic changes that take place in the valence band of PSCO as a function of temperature do also leave their fingerprint in the Co *K* HERFD-XANES spectra, which are a direct measure of the density of empty Co states with *p* symmetry beyond the Fermi level. Figure 4. 43 displays the HERFD XAS curves at 10 K, 170 K, and 295 K, as compared to that of $PrCoO_3$ at 20 K, containing only Co^{3+} in the LS state. The inset shows the pre-edge region, from 7.704 eV to 7.715 eV, which reflects the distribution of empty 3*d* t_{2g} and e_g levels thanks to the hybridization with the O 2*p* states (dipole-allowed transition).

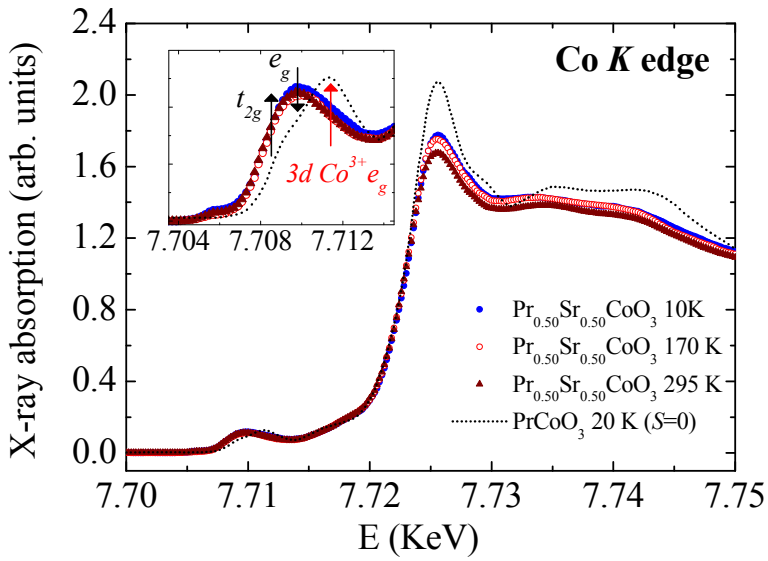

Figure 4. 43. HERFD-XANES spectra at the Co *K* edge of $Pr_{0.50}Sr_{0.50}CoO_3$ at 10 K (blue solid circles), 170 K (red open circles), and 295 K (red solid triangles), as compared to $PrCoO_3$ at 10 K (dotted line). The inset shows the pre-edge region, sensitive to the occupation of the Co 3*d* states. Black arrows indicate the tendency of occupation the t_{2g} and e_g states vs. temperature attributed the mixture of Co^{3+} and Co^{4+} ions in PSCO, and the red arrow signals the presence of e_g empty states solely ascribed to Co^{3+} LS in PCO.

Qualitatively speaking, we observe slight variations in the spectral weight ascribed to the t_{2g} and e_g orbitals between 10 K and 295 K. The density of empty e_g states decreases on

warming parallel to the enhancement of the feature reflecting the density of empty t_{2g} states (at about 1.5 eV lower energy). As earlier commented, this $t_{2g} \rightarrow e_g$ electron transfer is not considered as an actual spin state transition of the Co ions but rather as a gradual increase of the excited electron population due to the thermal excitations. For a real spin-state transition to occur larger changes would be needed. In any case, the observed temperature evolution is much smaller than that seen in the Ca-based compound. In addition, the comparison to $PrCoO_3$ precludes the presence of pure non-magnetic Co^{3+} ions at low temperature.

To go further in the investigation of the spin-state in $Pr_{0.50}Sr_{0.50}CoO_3$ we have also carried out Charge-Transfer Multiplet calculations (CTM) to simulate the experimental Co X-ray absorption spectra of PCCO and PSCO presented in Ref. [22] and in Section 4.5.2, respectively. Like in earlier Section 3.4.2.2., for the theoretical calculations we have used the CTM4XAS program which is based on the Cowan code [40]. According to the effective Co spin (S = 1) for PSCO at 300 K as extracted from Kβ emission lines analysis, we have considered different possible scenarios. So, Co^{3+} could appear in a mixed LS/HS configuration, while Co^{4+}, often eager to remain in a LS state due to its larger crystal field splitting, might be partially excited into the IS state similarly to as reported by Guillou *et al.* [43] and J. M. Chen *et al.* [60] for $(Pr_{0.7}Sm_{0.3})_{0.7}Ca_{0.3}CoO_3$. More precisely:

(i) *model 1* considers a similar electronic configuration as PCCO, i.e. a mixed LS:HS (12.5:37.5) state for Co^{3+} and all Co^{4+} in a LS state (S = 1/2);

(ii) (ii) *model 2* is similar to the first one but considering all Co^{4+} in an IS state (S = 3/2), thus yielding a 37.5:12.5 LS:HS state ratio for Co^{3+} ions;

(iii) (iii) *model 3* is based on a mixed LS:HS (17.5:32.5) state for Co^{3+} and a mixed LS:IS (40:10) state for Co^{4+};

(iv) (iv) *model 4* takes into account a mixed IS:HS (25:25) state for Co^{3+} and all Co^{4+} in LS state so as to fulfill S_{PSCO} = 1 (as in the all other three models).

The comparison of the experimental Co $L_{2,3}$ XAS spectra of PSCO and PCCO at RT to the weighted combination of CTM calculated spectra that allow to create the four proposed models is summarized in Figure 4. 44. The parameters value employed for every calculation are reported in Table 4. 7.

Due to the similar electronic and lattice structure of PSCO and PCCO their experimental XAS spectra only present minor differences. These are:

(i) the amplitude of the *A* feature just below the Co L_3 edge around 776.5 eV, which is larger for PCCO;

(ii) the width of the XAS curve at the Co L_3 edge and the sharpness of the *B* feature, respectively larger and more marked for PSCO;

(iii) the *C* feature which is a fingerprint of PCCO spectra at the Co L_2 edge.

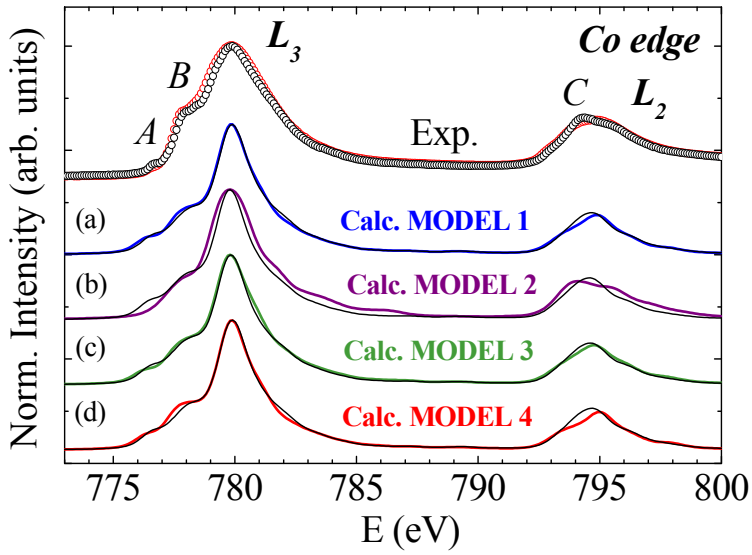

Figure 4. 44. (Top) Experimental Co $L_{2,3}$ XAS spectra of PSCO (red circles) and PCCO (black circles) at RT; (a-d) weighted addition of CTM calculations for PSCO: (a) *Model 1*, 12.5:37.5:50 of Co^{3+}LS:Co^{3+}HS:Co^{4+}LS (blue line); (b) *Model 2*, 37.5:12.5:50 of Co^{3+}LS:Co^{3+}HS:Co^{4+}IS (yellow line); (c) *Model 3*, 17.5:32.5:40:10 of Co^{3+}LS:Co^{3+}HS:Co^{4+}LS:Co^{4+} IS (green line); and (d) M*odel 4*, 25:25:50 of Co^{3+}IS:Co^{3+}HS:Co^{4+}LS (red line) as compared to calculated PCCO (black solid line).

Table 4. 7. Parameters employed for the charge-transfer multiplet calculations with CTM4XAS.

Parameter	Co^{3+} LS	Co^{3+} IS	Co^{3+} HS	Co^{4+} LS	Co^{4+} IS
Symmetry	O_h	O_h	O_h	O_h	O_h
Crystal field (*10Dq*) (eV)	+1.8	+1.3	+0.9	+2.4	+1.8
Charge transfer energy (Δ) (eV)	+3.0	+3.0	+3.0	-3.5	-3.5
U_{dd} (eV)	6.2	6.2	6.2	5.2	6.5
U_{pd} (eV)	7.5	7.5	7.5	7.5	7.5
Hopping e_g electrons (T_{eg}) (eV)	2.0	2.0	2.0	2.0	2.0
Hopping t_{2g} electrons (T_{t2g}) (eV)	1.0	1.0	1.0	1.0	1.0
Spin-orbit coupling (S.O)	1.0	1.0	1.0	1.0	1.0
Slater's integrals (F_{dd}, F_{pd}, G_{pd})	1.0	1.0	1.0	1.0	1.0
L. and G. Broadening	0.25;0.35	0.25;0.35	0.25;0.35	0.25;0.35	0.25;0.35

We decided to compare the calculated spectra of PCCO and PSCO to try to reproduce these experimental feature differences. We note from the calculated spectra for octahedrally coordinated Co^{4+} ions that the *A* feature can only be reproduced if the tetravalent ions remain in a LS state. So, qualitatively speaking this suggests a larger presence of Co^{4+} LS in PCCO than in PSCO and points out to possible mixing of different spin states for Co^{4+} in the Sr-based cobaltite. From Figure 4. 44 we can see that the *model 1* does not adequately reproduce the experimental characteristics reported in (i) and (ii). However, this model reproduces the shape at the L_2 edge [i.e. it fulfills (iii)], thus becoming a plausible scenario for PSCO. The large population of Co^{3+} LS in *model 2*, not expected from the experimental XAS, on top of the metallic behavior of PSCO, makes us to rule it out. On the other hand, *model 3* reproduces the experimental amplitude of *A* feature thanks to the mixed Co^{4+} LS:IS state. In addition, experimental observations (ii) and (iii) are finely reproduced. Finally, model 4, considering the existence of Co^{3+} in an IS state, overestimates the amplitude of *B* feature, while *A* feature is not properly reproduced. As a result, the number of feasible scenarios for the discussion on the SS of PSCO is reduced to *model 1* and *model 3*, with a certain preference for the latter.

For better discerning between these two electronic configuration models in Figure 4. 45 we have plotted the comparison between the difference spectrum of experimental PSCO and PCCO XAS curves, as compared to the calculated difference spectrum for each of the four proposed models for PSCO and the model refined for PCCO in Ref. [22] at room temperature. There are some similarities between the difference experimental and calculated spectra but a close analysis of the difference curves reveals that: (a) the position of the *D* feature at 776.6 eV in the experimental difference spectrum agrees better with *models 1*, *3*, and *4*; (b) the *E* feature appears in all the calculated difference spectra; (c) *model 2* does not fit the position and magnitude of *F* (~779.9 eV) and *G* (~794.3 eV) features, respectively. This leads us to definitely dismiss *models 2* and *4*, as also concluded from Figure 4. 44. Recalling our previous considerations on the *A* feature (Figure 4.43) which is a hallmark of Co^{4+} LS, we propose that the electronic configuration for $Pr_{0.50}Sr_{0.50}CoO_3$ involves a mixture of LS:HS states in Co^{3+} ions and also a mixed LS:IS state in Co^{4+} ions, in contrast to the $Pr_{0.50}Ca_{0.50}CoO_3$ cobaltite, i.e. *model 3* would be favored with respect to *model 1*.

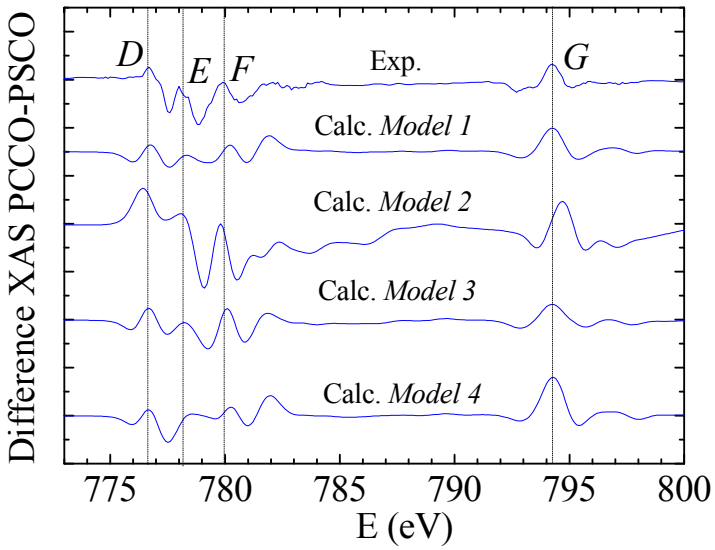

Figure 4. 45. Difference XAS between: (Top) the experimental PCCO and experimental PSCO; (Bottom) the CTM calculation PCCO and PSCO for the different proposed models.

We can use the calculated XAS considered in *model 1* and *model 3* to calculate the corresponding XMCD spectra. The comparison with the experimental one is presented in Figure 4.46. The agreement is not fully satisfactory in any of the two models, but the calculated spectrum using *model 3* is somewhat better than that with *model 1*. This is evident if we focus on the width of the main negative peak at the Co L_3 edge and the two main features at the Co L_2 edge.

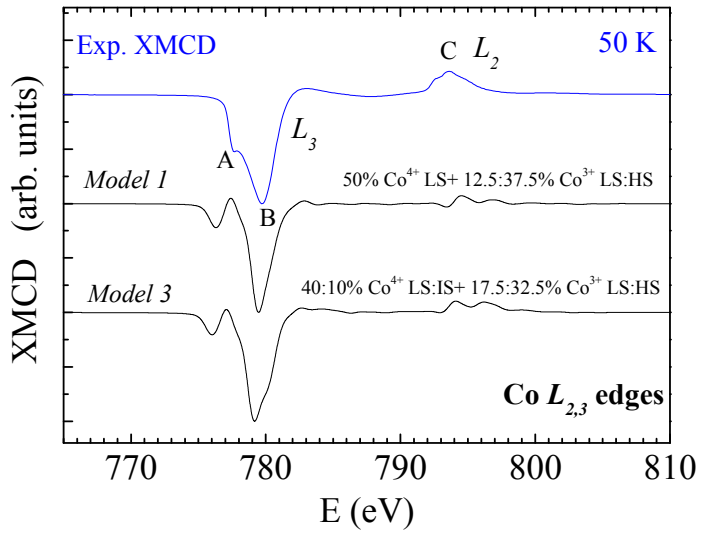

Figure 4. 46. (From top to bottom). Experimental XMCD spectrum of PSCO at 50 K under an applied magnetic field of 5 T (solid blue line) and weighted addition of CTM calculations to build *model 1* and *model 3* (solid black lines).

4.10. Structural and magnetic evolution in $Ln_{0.50}Sr_{0.50}CoO_3$: $Nd_{1/3}La_{1/6}Sr_{0.50}CoO_3$ and $Nd_{0.50}Sr_{0.50}CoO_3$

With the purpose of understanding better the $Ln_{0.50}Sr_{0.50}CoO_3$ family and the real participation of the Pr ions in the magnetostructural evolution of PSCO, we present next a structural investigation of two close cobaltites: $Nd_{0.50}Sr_{0.50}CoO_3$ (NSCO) and $Nd_{1/3}La_{1/6}Sr_{0.50}CoO_3$ (NLSCO). The composition of the latter was selected estimating an average ionic radius of *A* cations almost identical to PSCO. Although, these compounds present similar electrical and magnetic properties to PSCO (they are metallic and ferromagnetic), the second magnetic transition al low temperature is absent in both compounds without Pr (see Section 4.2.3 for the magnetic and electrical properties).

4.10.1. Two successive crystal structures in $Nd_{1/3}La_{1/6}Sr_{0.50}CoO_3$

As in the PSCO compound, we have performed high-resolution neutron powder diffraction as a function of temperature at D20 beamline (ILL, Grenoble) using a wavelength of λ = 1.87 Å. We have collected data from 540 K to 10 K and the thermal evolution of the neutron-diffracted intensities plotted in Figure 4. 47 shows similarities with the thermal evolution recorded in the same angular range for PSCO [see Figure 4. 21 (b)] where the *R-3c* $\rightarrow$ *Imma* transition takes place at T_{S2}. However, for $Nd_{1/3}La_{1/6}Sr_{0.50}CoO_3$ we have seen only two successive structures and not three as it occurs in PSCO. The diffraction data collected between 540 K and 250 K are well refined by a rhombohedral paramagnetic phase with *R-3c* (No. 167) symmetry, but below T_C ~ 240 K it appears a ferromagnetic order, producing new peaks in the neutron diffraction profile. On the other hand, the patterns collected below T_{S2} can be well described using an orthorhombic and ferromagnetic phase with *Imma* (No. 74) space group (S.G). So, the equivalent structural transition in PSCO shifts to lower temperatures here, indicating that the rhombohedral phase is stable down to lower temperatures (T_{S2} ~115 K). The remarkable fact is that the orthorhombic to tetragonal transition is not observable at low temperature in $Nd_{1/3}La_{1/6}Sr_{0.50}CoO_3$, unlike $Pr_{0.50}Sr_{0.50}CoO_3$ cobaltite. In Figure 4. 48 is plotted the Rietveld refinements of NPD at 300 K (PM rhombohedral phase) and 80 K (FM orthorhombic phase). In the last temperature we found a phase coexistence between the *Imma* (84%) and *R3-c* (6%) phase. The structural details obtained from the refinements together with the agreement factors are listed in Table 4. 8.

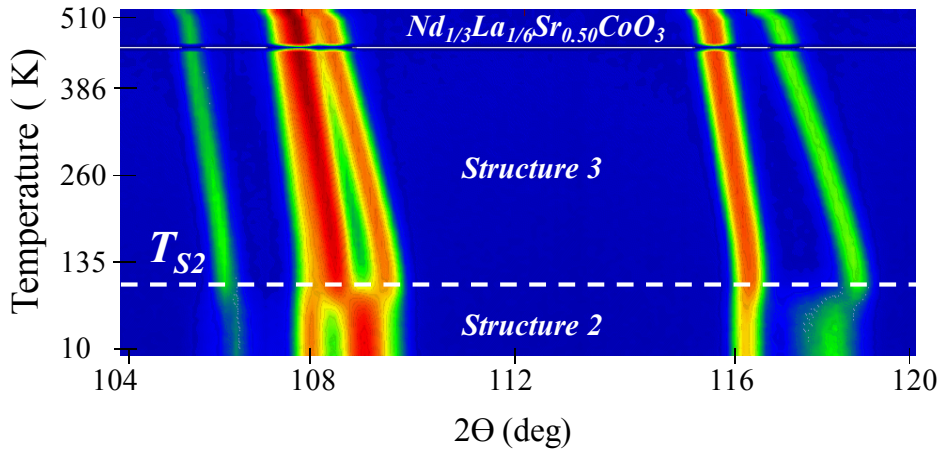

Figure 4. 47. Neutron diffraction intensities for characteristics reflections of the two successive crystal structures as a function of temperature for $Nd_{1/3}La_{1/6}Sr_{0.50}CoO_3$ measured at D20 beamline.

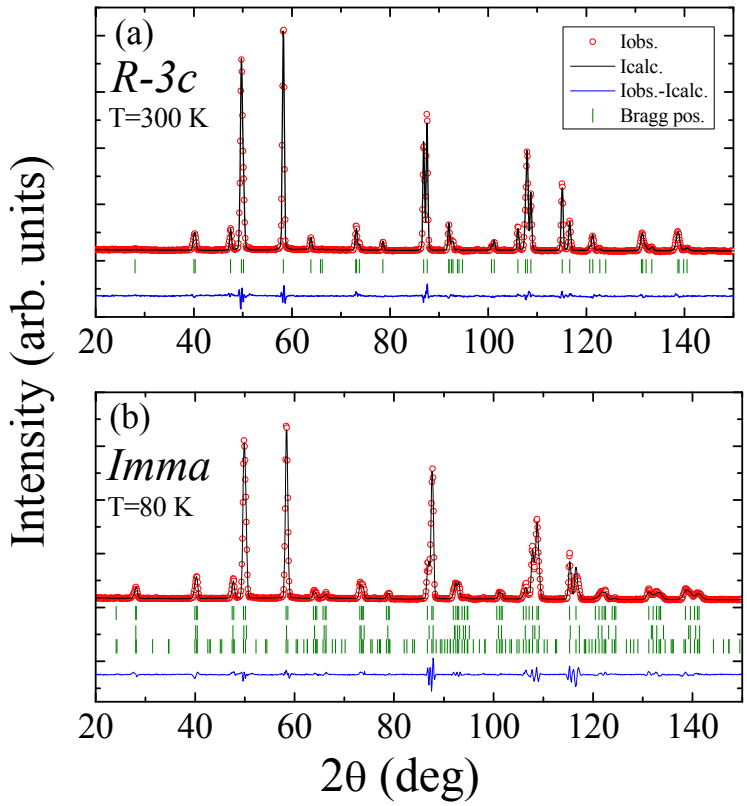

Figure 4. 48. Rietveld refinements of neutron pattern from D2B for $Nd_{1/3}La_{1/6}Sr_{0.50}CoO_3$ measured at (a) 300 K using a rhombohedral *R-3c* paramagnetic phase and (b) at 80 K showing coexistence of phases between the orthorhombic *Imma* FM phase and the rhombohedral *R-3c* phase (the third row of Bragg positions is the magnetic phase).

As it was done in the PSCO cobaltite, the magnetic structure has been resolved for $Nd_{1/3}La_{1/6}Sr_{0.50}CoO_3$. In the first attempt, we decided to refine the NPD data using [100] FM magnetic domains (F_x model, referred to the tetragonal setting in PSCO) as moment orientation in the orthorhombic phase. We found a good result in which the agreement factors were: R_B = 4.3 %, R_f = 5.97 %, R_{Mag} = 13.8 %, χ^2 = 3.15 %. However, we detected (and it is not related to the residual *R-3c* phase) a different relative distribution of the magnetic intensity at (123) and (321) unlike the PSCO compound that it was not well reproduced using the F_x model. Taking into consideration the simulations previously done for PSCO (see Figure 4. 35), we found the F_y model to reproduce better the experimental profile. Figure 4. 49 shows the Rietveld refinement using [010] FM domains and as we can see the peak intensity and the shape are well resolved. Moreover, we obtained better values for the agreement factors: R_B = 3.58 %, R_f= 5.14 %, R_{Mag} = 9.43 %, χ^2 = 1.93 %.

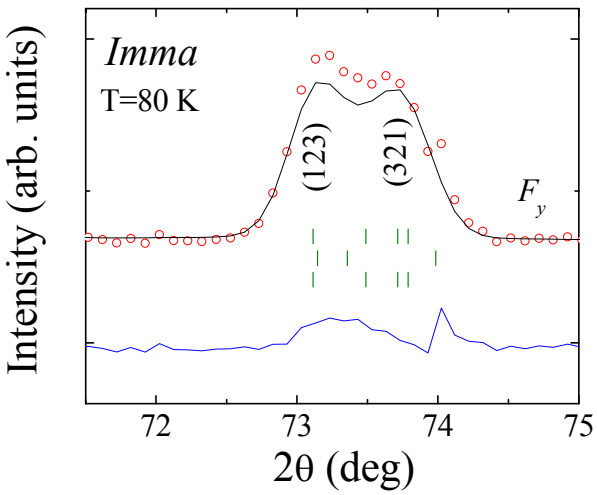

Figure 4. 49. Selected angular region of the Rietveld refinement (solid line) of neutron pattern measured at 80 K using the F_y model to reproduce the peak intensity of (123) and (321) magnetic reflection.

Table 4. 8 . Crystal structures of $Nd_{1/3}La_{1/6}Sr_{0.50}CoO_3$ and reliability factors found by Rietveld refinements of Neutron Data at selected temperatures.

$Nd_{1/3}La_{1/6}Sr_{0.50}CoO_3$	300 K	80 K
Space group	*R -3c* (No. 167)	*I mma* (No. 74)
a (Å)	5.4245(1)	5.3725(7)
b (Å)	5.4245(1)	7.6025(2)
c (Å)	13.1628(4)	5.4278(2)
Vol ($Å^3$)	335.425(2)	221.697(2)
Nd/La/Sr	6*a*	4*e*
x	0	0
y	0	0.25
z	0.25	0.0004(6)
B *(Å^2)*	1.219(6)	0.791(5)
Co	6*b*	4*b*
x	0	0
y	0	0
z	0	0.5
B *(Å^2)*	0.724(5)	0.149(9)
O1	18*e*	4*e*
x	0.465(3)	0
y	0	0.25
z	0.25	0.4591(5)
B *(Å^2)*	1.567(5)	1.562(7)
O2		8*g*
x	-	0.25
y	-	0.0243(3)
z	-	0.75
β	-	1.231(2)
Ordered FM moment (μ_B/Co)	-	1.93 (5)
χ^2	2.76	1.67
R_B (%)	3.32	3.58
R_{mag} (%)	-	9.43

The ionic radius of La (r_A= 1.22 Å, IX-coordination), Pr (r_A= 1.18 Å, IX-coordination), and Nd (r_A= 1.16 Å, IX-coordination) produce an average distortion in NLSCO very similar to PSCO. θ1, θ2 and ⟨θ⟩ found for NLSCO at 80 K are 164.8º, 169.4º and 167.9º, respectively. Very similar to the values for PSCO at 140 K: 164.8º, 169.4º and 167.9º. Both with the *Imma* structure. Given the similar tilting in both perovskites, although NLSCO is slightly less distorted, we consider that the higher stability of the *R-3c* phase in NLSCO is favored by the higher variance of the ionic sizes at the *A*-site. As a consequence of this temperature shift the tetragonal phase probably would need (virtual) negative temperature to emerge.

Concerning the magnetic behavior, we observed in the temperature dependence of the integrated intensity of some selected magnetic peaks [(020) and (101) at 2θ ~ 28.5º, indexed according to $\sqrt{a_0}$ x $2a_0$ x $\sqrt{a_0}$ cell] that at low temperature (~ 60 K) there is an increase of the FM intensity (see Figure 4. 50). This enhancement at very low temperature indicates the partial polarization of Nd moments. For that reason we studied the Co ordering at 80 K, where Nd moments are still unpolarized.

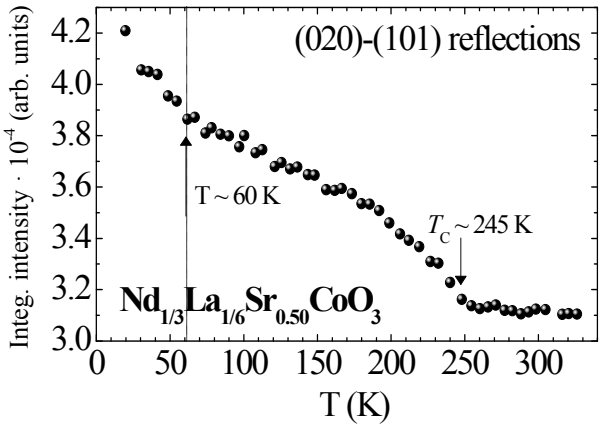

Figure 4. 50. Temperature dependence of the integrated intensity at 2θ ~ 28º for neutron powder diffraction measured at D20 for $Nd_{1/3}La_{1/6}Sr_{0.50}CoO_3$.

4.10.2. Suppression of the magnetostructural transition in $Nd_{0.50}Sr_{0.50}CoO_3$

$Nd_{0.50}Sr_{0.50}CoO_3$ is also a composition very close to PSCO. In the previous reports from the literature, it is always assumed that this half-doped cobaltite adopts an orthorhombic *Pnma* (No. 62) S.G [33, 34]. We have collected high-resolution neutron powder diffraction at some selected temperatures (5, 100, 200, 250 and 300 K) at D2B beamline (λ= 1.594 Å). Moreover, the thermal evolution of the neutron-diffracted intensities collected on D20 (λ= 1.594 Å) from

high to low temperature is plotted in Figure 4.51. As NLSCO, it shows one structural transition instead of the two of PSCO. However, the structural transition corresponding to T_{S2} does not shift to lower temperatures as NLSCO. The transition temperature takes place at 340 K which is slightly higher to T_{S2} ~ 314 K reported in PSCO. The Rietveld refinements at high temperature reveal a rhombohedral *R-3c* phase, but on cooling below 340 K we have detected an orthorhombic phase. In contrast to the earlier reported interpretations, our data is very well reproduced using an *Imma* phase. Firstly, we have tested a *Pnma* symmetry whose refinement gives a good solution and good reliability factors, but after a carefully inspection we have realized that many reflections are indexed when they are absent in the pattern diffraction. These type of reflections ($h + k + l$ = 2n+1 or $h + l$ = 2n+1) are permitted by *Pnma* symmetry and forbidden by *Imma* symmetry. Figure 4. 52 (at 250 K we find the sample in the paramagnetic phase) shows in panel (a) some examples of extra indexed peaks without intensity (they are marked with an asterisk *) permitted by *Pnma* symmetry but forbidden by the *Imma* S.G., see panel (b).

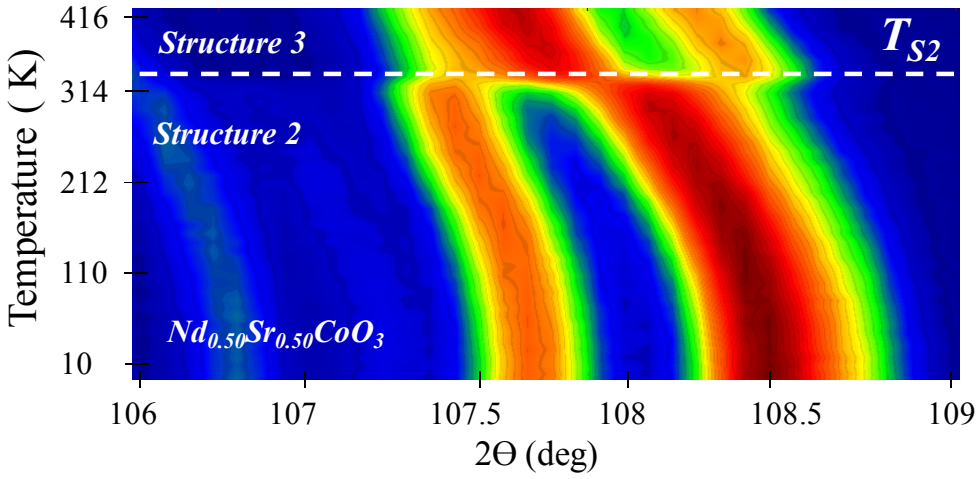

Figure 4. 51. Neutron diffraction intensities for characteristic reflections of the two successive crystal structures as a function of temperature for $Nd_{0.50}Sr_{0.50}CoO_3$, measured at D20 beamline.

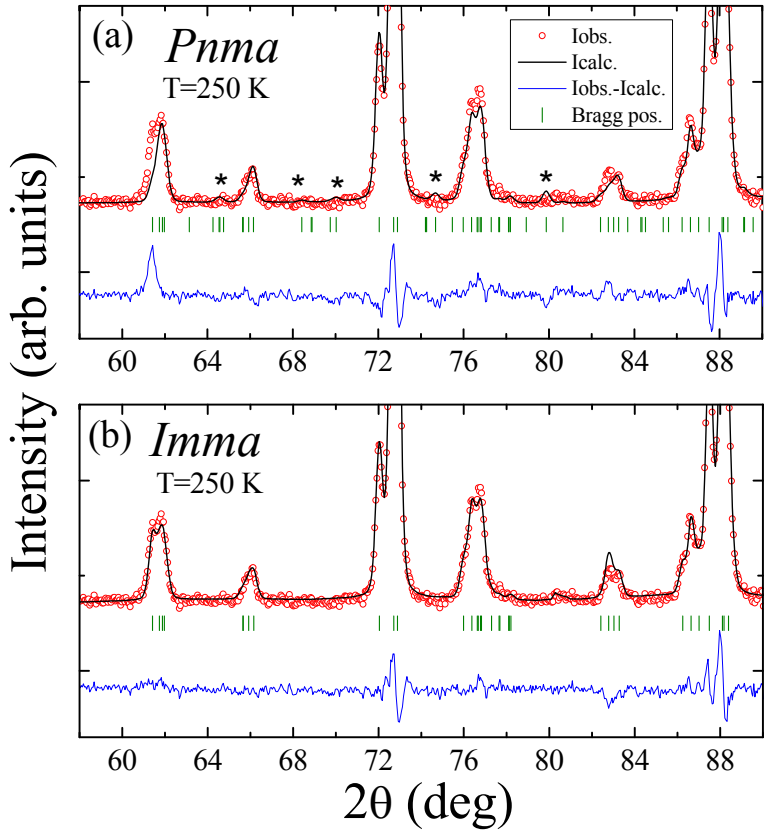

Figure 4. 52. Rietveld refinements of neutron pattern from D2B measured at 250 K for $Nd_{0.50}Sr_{0.50}CoO_3$ using (a) an orthorhombic *Pnma* phase and (b) an orthorhombic *Imma* phase. (*) indicates selected type reflections ($h + k + l$ = 2n+1 or $h + l$ = 2n+1). Diffractions patterns are indexed according to $\sqrt{}a_o$ x $2a_o$ x $\sqrt{}a_o$.

The refined *Imma* structure of NSCO is shown in Table 4.9. The transition temperatures are shifted (respect PSCO) in the opposite direction to NLSCO. The *R-3c* → *Imma* transition is increased (T_{S2} ~ 340 K for Nd and 314 K for Pr). According to the bigger distortion T_C slightly decreases (228 K versus 230 K). Finally, to be underlined is that the same *Imma* symmetry of PSCO persists here at low temperature without being substituted by the tetragonal symmetry. Unexpectedly, the MS transition is absent in $Nd_{0.50}Sr_{0.50}CoO_3$.

.

Table 4. 9. Structure at 250 K refined using SG *Imma* for $Nd_{0.50}Sr_{0.50}CoO_3$. Lattice parameters are a = 5.3686(9), b = 7.5848(1), c = 5.4234(8), V = 220.840 (6). The agreement factors are χ^2 = 2.27, R_B=3.31%

Atom	Whychoff Position	*x/a*	*y/b*	*z/c*	β_{iso}
Nd	*4e*	0.0000	0.2500	0.0018(2)	0.259(2)
Sr	*4e*	0.0000	0.2500	0.0018(2)	0.259(2)
Co	*4b*	0.0000	0.0000	0.5000	0.176(4)
O1	*4e*	0.0000	0.2500(7)	0.5498(3)	0.969(3)
O2	*8g*	0.2500	0.0253(1)	0.2500	0.966(3)

4.11. Probing the magnetostructural transition in half-doped $Pr_{0.50}(Sr_{1-x}Ba_x)_{0.50}CoO_3$

We have previously commented that the MS transition does not appear in $Nd_{0.50}Sr_{0.50}CoO_3$ or smaller cells compounds and it vanishes when the larger La replaces Pr as in $(La_{1-y}Pr_y)_{0.50}CoO_3$. Next we will discuss the new family of mixed half-doped cobaltites $Pr_{0.50}(Sr_{1-x}Ba_x)_{0.50}CoO_3$ (PSBCO) in which the Sr^{2+} ion is substituted by a bigger alkaline-earth ion such as Ba^{2+} (preserving a 50% of composition in the *A*-site). We have prepared the x= 0.025, 0.5 and 0.1 compositions and have observed the MS transition in these bigger cells. The magnetic and the electric characterization reveal that all compositions are FM metallic (Figure 4. 53 and Figure 4. 54). The transition temperatures (T_C and T_{SI}) are shifted to smaller temperatures when the Ba content is bigger. Moreover, the characteristic step-like behavior in the magnetization depending on the applied magnetic field can be seen in Figure 4.52 (a,b) for PSBCO cobaltites. The size of the step seems to increase with the Ba content in this new perovskite.

In Figure 4. 53 the PM-FM transition occurs at 236 K, 231 K and 225 K and the MS transition at 108 K, 116 K and 90 K for $Pr_{0.50}Sr_{0.475}Ba_{0.025}CoO_3$ (PSBCO_2.5%) , $Pr_{0.50}Sr_{0.45}Ba_{0.05}CoO_3$ (PSBCO_5%) and $Pr_{0.50}Sr_{0.40}Ba_{0.10}CoO_3$ (PSBCO_10%), respectively. The hysteresis loops curves were measured at 10 K, 150 K and 300 K for all compositions (not shown here). In Table 4. 10 the transition temperature, the magnetic saturation, the coercive field at 10 K and the step-like jump ΔM extracted from the magnetization curves are listed.

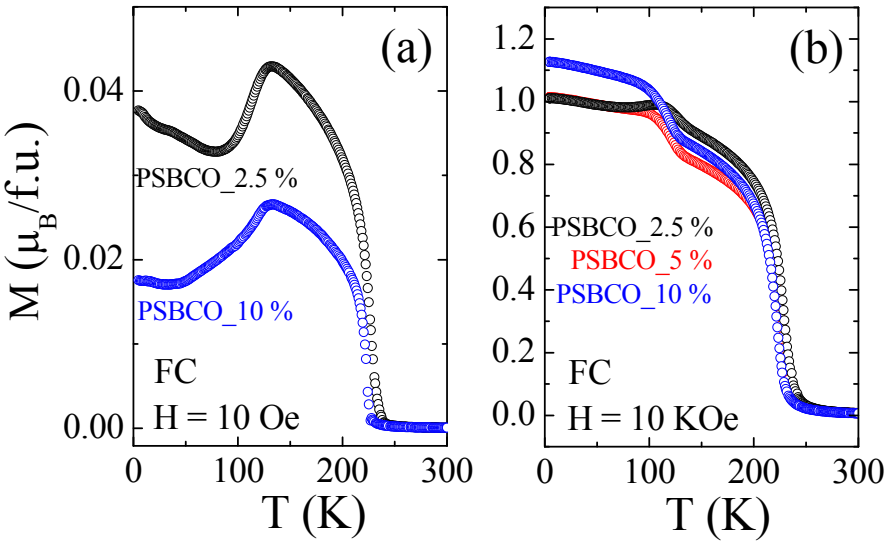

Figure 4. 53. Temperature dependence of the magnetization measured under field cooling (FC) for $Pr_{0.50}Sr_{0.475}Ba_{0.025}CoO_3$ (black open circles), $Pr_{0.50}Sr_{0.45}Ba_{0.05}CoO_3$ (red open circles) and $Pr_{0.50}Sr_{0.40}Ba_{0.10}CoO_3$ (blue open circles) at (a) 10Oe and (b) 10 KOe.

Table 4. 10. Magnetic details of the $Pr_{0.50}(Sr_{1-x}Ba_X)_{0.50}CoO_3$ family (x = 0.025, 0.05, 0.10). The magnetic saturation (M_S) and the coercive field (H_C) are extracted from the magnetization versus field measurements at 10 K, and the absolute or relative step-like jump ΔM are extracted from Figure 4. 53.

Sample	T_C (K)	T_{SI} (K)	M_S (μ_B/f.u) 10 K	H_C (μ_B/f.u) 10 K	$\Delta M(T)_{abs.}$ (μ_B/f.u) 10 Oe	$\Delta M(T)_{rel.}$ (%) 10 Oe	$\Delta M(T)_{abs.}$ (μ_B/f.u) 10 KOe	$\Delta M(T)_{rel.}$ (%) 10 KOe
$Pr_{0.50}Ba_{0.025}Sr_{0.475}CoO_3$	236	108	1.96	0.076	0.020	34.5	0.093	9
$Pr_{0.50}Ba_{0.05}Sr_{0.45}CoO_3$	231	116	1.94	0.074	-	-	0.16	16
$Pr_{0.50}Ba_{0.10}Sr_{0.40}CoO_3$	225	90	1.95	0.030	0.009	34	0.24	21

We have set the sign crossover of the step-like behavior in the magnetization curves at H_{cr} ~ 300 Oe for PSCO. For the new family the magnetic field crossover is smaller. In $Pr_{0.50}Sr_{0.40}Ba_{0.10}CoO_3$ this value is set at 160 Oe as Figure 4. 54(a) shows. The comparison of the resistivity measurements between the less and most doped sample reflect a higher resistivity value for PSBCO_10% ($\rho \sim 0.65 \cdot 10^{-4}$ Ω·m) than PSBCO_2.5% ($\rho \sim 0.37 \cdot 10^{-4}$ Ω·m) at T > T_C.

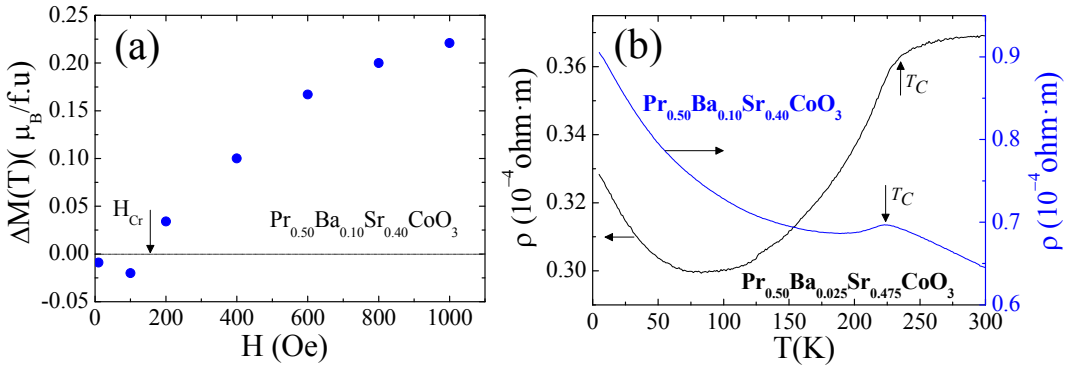

Figure 4. 54. (a) Magnetic field dependence of the step-like jump ΔM in the magnetization curves of $Pr_{0.50}Sr_{0.40}Ba_{0.10}CoO_3$ and (b) thermal evolution of the resistivity for $Pr_{0.50}Sr_{0.475}Ba_{0.025}CoO_3$ (black line) and $Pr_{0.50}Sr_{0.40}Ba_{0.10}CoO_3$ (blue line).

We have also performed the structural characterization as a function of temperature using NPD. In this case we will focus only in the extreme composition $Pr_{0.50}Sr_{0.40}Ba_{0.10}CoO_3$. NPD data have been collected from 10 K to 285 K at D1B (ILL, Grenoble) using a wavelength $\lambda = 2.52$ Å. The thermal evolution of the neutron-diffracted intensities is plotted in Figure 4. 55. One sharp and defined structural transition occurs at $T_{S1} \sim 100$ K as in $Pr_{0.50}Sr_{0.50}CoO_3$. The Curie point is $T_C \sim 220$ K.

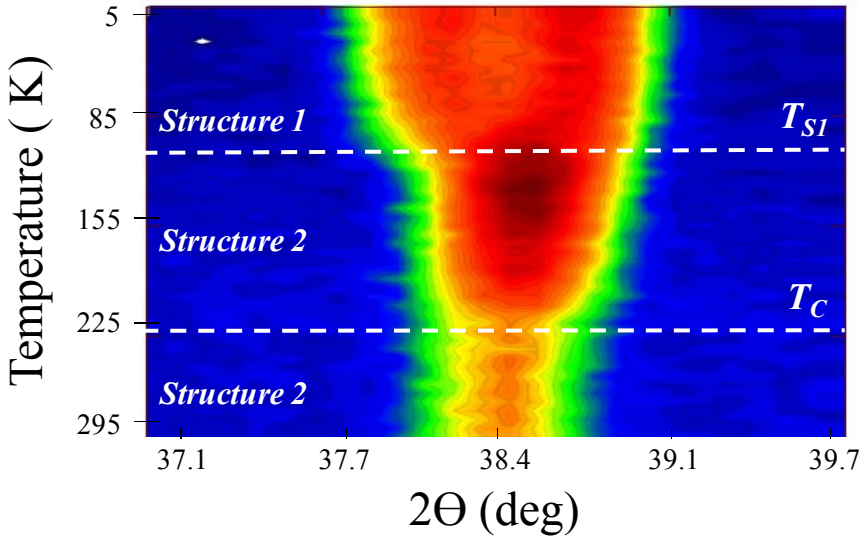

Figure 4. 55. Neutron diffraction intensities for characteristics reflections of the two successive crystal structures as a function of temperature for $Pr_{0.50}Sr_{0.40}Ba_{0.10}CoO_3$ measured at D1B beamline.

Figure 4. 56 shows the Rietveld refinements of NPD patterns for $Pr_{0.50}Sr_{0.40}Ba_{0.10}CoO_3$ at selected temperatures (285, 150 and 10 K). The good agreement between the experimental and calculated profile can be observed in panel (a), (b) and (c) for the *Imma* PM phase, the *Imma* FM2 phase and the *I4/mcm* FM1 phase, respectively. The magnetic models used in theses refinements are the same deduced for the ferromagnetic FM2 and FM1 phases in PSCO. FM2 develops below T_C ~ 220 K down to T_{SI} ~100 K with [100] FM domains, which (after a 45º rotation when adopting the *I4/mcm* symmetry) align parallel to the low temperature cell diagonals [110] FM.

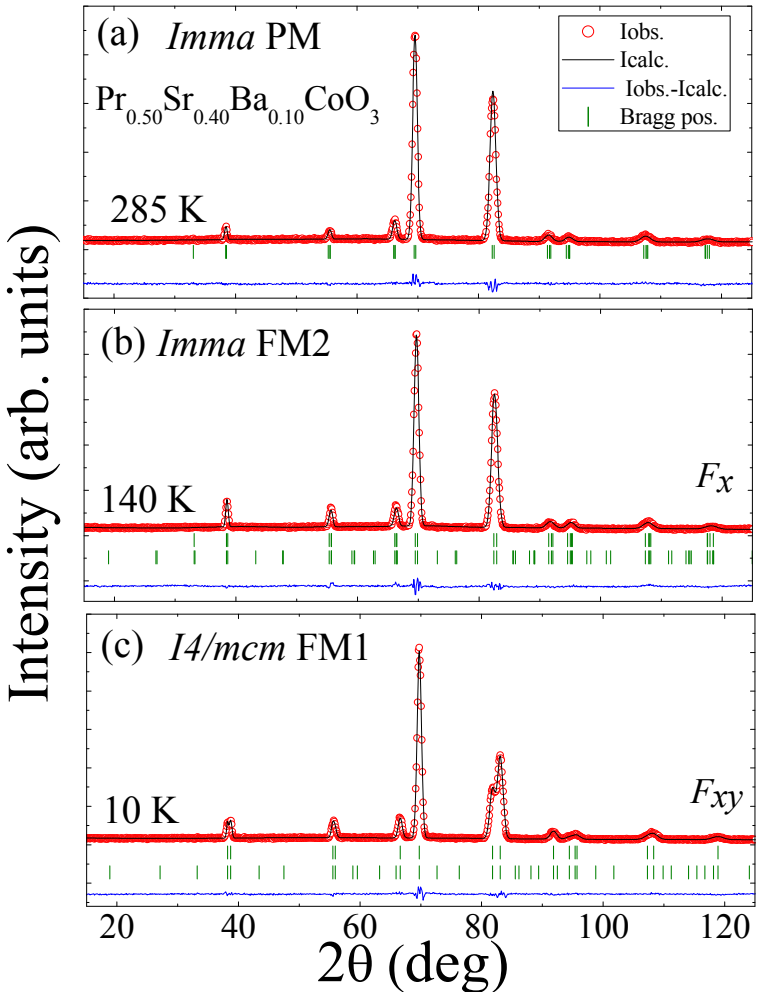

Figure 4. 56. Rietveld refinement (black line) of neutron diffraction patterns (red circles, experimental points; bottom blue line, difference) for $Pr_{0.50}Sr_{0.40}Ba_{0.10}CoO_3$ at selected temperatures. (a) 285 K, orthorhombic *Imma* paramagnetic phase. (b) 140 K, orthorhombic *Imma* ferromagnetic phase. (d) 10 K, tetragonal *I4/mcm* ferromagnetic phase (the second row of Bragg position is the magnetic phase).

In Figure 4. 57 it is plotted the thermal evolution (285, 140 and 10 K) of a selected angular region of the refined NPD patterns which contains a set of magnetic peaks at (101) and (020). On cooling, these two reflections split and transform into (002) and (110) in the *I4/mcm* phase. At low temperature the magnetic moment reaches a value of 1.78(3) μ_B/Co which is close to the moment found in PSCO. The structural details, the FM moment and the reliability factors of the Rietveld refinements for the three temperatures are listed in Table 4. 11.

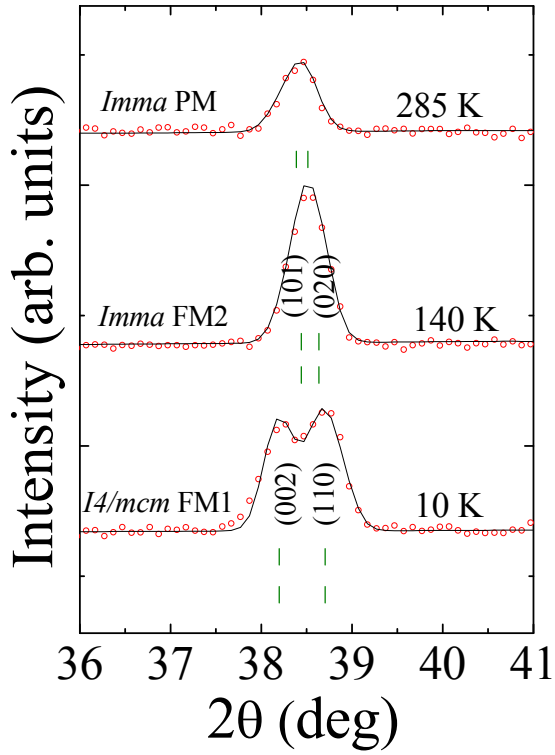

Figure 4. 57. Selected angular region of the refined neutron patterns for $Pr_{0.50}Sr_{0.40}Ba_{0.10}CoO_3$ measured at the indicated temperatures for each structural phase. Diffraction patterns have been shifted up for clarity and are indexed according to $\sqrt{2}a_0$ x $2a_o$ x $\sqrt{2}a_o$ at 140 K and $\sqrt{2}a_0$ x $2\sqrt{a_0}$ x $2a_0$ at 10 K.

We can thus conclude that in $Pr_{0.50}(Sr_{1-x}Ba_X)_{0.50}CoO_3$ the transformation *R-3c* → *Imma* → *I4/mcm* is maintained at least up to 10% Ba in *B*-site. The MS transition is preserved introducing the large Ba^{2+} cation while keeping a 50% of Pr in *A*-site. The Curie temperature hardly changes for x=0, 5% and 10%, and the decrease of T_{SI} is also very tiny, although the T_{SI} transition widen.

Table 4. 11. Crystal structures of $Pr_{0.50}Sr_{0.40}Ba_{0.10}CoO_3$ and reliability factors found by Rietveld refinements of Neutron Data at selected temperatures.

$Pr_{0.50}Sr_{0.40}Ba_{0.10}CoO_3$	285 K	140 K	10 K
Space group	*I mma* (No. 74)	*I mma* (No. 74)	*I 4/mcm* (No. 140)
a (Å)	5.4011(2)	5.3873(1)	5.3723(3)
b (Å)	7.6338(4)	7.6090(2)	5.3723(3)
c (Å)	5.4293(3)	5.4246(1)	7.6945(5)
Vol ($Å^3$)	223.853(2)	222.363(1)	222.08(3)
Pr/Sr/Ba	4*e*	4*e*	*4b*
x	0	0	0
y	0.25	0.25	0.5
z	0.0025(4)	0.0030(2)	0.25
B ($Å^2$)	1.129(6)	1.036(3)	0.586(1)
Co	4*b*	4*b*	*4c*
x	0	0	0
y	0	0	0
z	0.5	0.5	0
B ($Å^2$)	0.478(5)	0.162(1)	0.15384)
O1	4*e*	4*e*	*4a*
x	0	0	0
y	0.25	0.25	0
z	0.4636(3)	0.4631(1)	0.25
B ($Å^2$)	1.164(5)	1.077(2)	1.196(3)
O2	8*g*	8*g*	*8h*
x	0.25	0.25	0.2809(3)
y	0.0198(1)	0.0206(7)	0.7809(3)
z	0.75	0.75	0
β	1.531(1)	1.085(3)	1.00785)
Ordered FM moment (μ_B/Co)	-	1.406(3)	1.780(3)
χ^2	1.32	1.55	0.67
R_B (%)	4.55	6.80	1.60
R_{mag} (%)	-	3.39	4.81

4.12. Synthesis of $Pr_{0.50}Sr_{0.50}CoO_3$ single crystal

To go further in the characterization of the half-doped cobaltite $Pr_{0.50}Sr_{0.50}CoO_3$ and the evolution of the magnetic easy axis, we have grown single crystals of PSCO. As far as we know, our single crystal is the second one grown by an optical floating-zone method. The first crystal of PSCO was grown by S. Hirahara *et al.* in 2006 [32].

In our optical floating-zone furnace, the basic concept is that four ellipsoidal mirrors are used to focus the light from halogen lamp onto a vertically held rod shaped sample to produce a molten zone which is then moved along the sample in order to grow a single crystal. In our laboratory we have used a four mirror floating zone furnace (model: FZ-T-P1200_H-I-S-PC) from Crystal Systems Corporation.

$Pr_{0.50}Sr_{0.50}CoO_3$ powder was prepared by solid-state reaction and shaped into cylindrical bars of 3 mm in diameter and 100 mm in length by pressing at an isostastic pressure to form feed rods. The rods were sintered at 1170 ºC for 24h in air and then used for feed rods. A piece of the cylindrical bar was cut to serve as a first seed. The feed rod and the growing crystal were rotated at 25 rpm and 15 rpm in opposite directions, respectively. The grown crystal was annealed under oxygen pressure of 3 bar for 5h and we applied a growth rate of 4 mm/h. We obtained a growth length of 133 mm at the end of the procedure.

The magnetic measurements of the grown crystal resemble the polycrystalline compound and it shows a PM to FM transition at T_C ~ 220 K as Figure 4. 58 shows. In addition, the step like-behavior is also visible in the single crystal but a slightly lower temperature T_{SI} ~ 90 K than in the fully oxygenated pellets. Probably, an annealing process under oxygen will be needed to get an optimal oxygenation of the crystal. The first X-ray measurements using a diffractometer with an area detector confirms the high quality of the sample and only single crystal reflections were observed. In parallel to this thesis, the complete study of the single crystals are been carried out by our group.

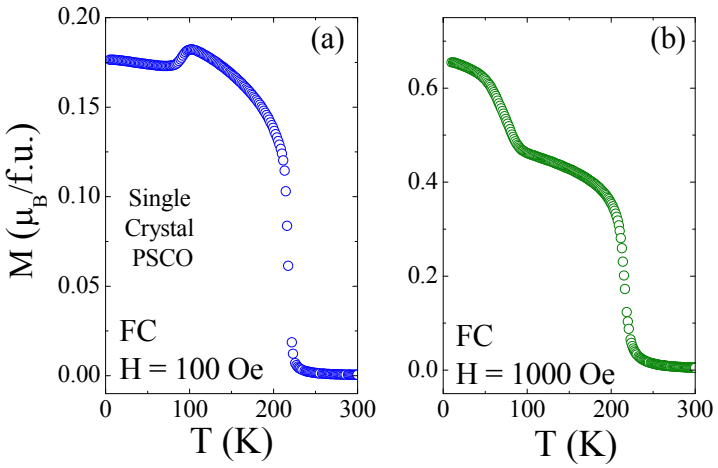

Figure 4. 58. Temperature dependence of the magnetization measured under field cooling (FC) for $Pr_{0.50}Sr_{0.50}CoO_3$ single crystal at (a) 100 Oe and (b) 1000 Oe.

4.13. Tentative T-r_A phase diagram of $Ln_{0.50}$(Sr, A)$_{0.50}CoO_3$ (A=Ba, Ca)

In order to complete our previous results, other compositions of the type $Ln_{0.50}(Sr_{1-x}A_x)_{0.50}CoO_3$ with A: Ba or Ca and x small were partially characterized. For this, apart from half-doped $Pr_{0.50}(Sr_{1-x}Ba_x)_{0.50}CoO_3$, other compounds such as $Pr_{0.50}(Sr_{0.50-x}Ca_x)CoO_3$ with $0.025 \leq x \leq 0.10$ or $(Pr_{0.50-x}Tb_x)Sr_{0.50}CoO_3$ with x=0 and 0.05 were very recently synthesized. However, for these last compounds a deep characterization is not presented in this manuscript and we only focus on the magnetic transition temperatures determined by means of magnetic measurements. We observed in the susceptibility measurements that most of the Sr-rich samples are FM metallic and they also exhibit a step-like behavior at low temperature like the half-doped PSCO. Similarly, to the half-doped PBSCO and NSCO cobaltites, the X-ray diffraction data of most of these compounds show *Imma* symmetry at RT. The smallest synthesized compound for the construction of a tentative phase diagram was the half-doped $Tb_{0.50}Sr_{0.50}CoO_3$ cobaltite which presents T_C = 120K and crystallizes in a different space group (*Pbnm*) [71].

In Table 4. 12 is detailed the transitions temperature for each cobaltite, the average A-cation radius $\langle r_A \rangle$ and the A-cation-size variance (σ^2). The last was calculated following: $\sigma^2 = \sum \chi_i r_i^2 - \langle r_A \rangle^2$, where χ_i is the fractional occupancy of the A-site by the i cation and r_i the corresponding ionic radii [44, 72, 73]. Standard ionic radii using IX-coordination [48] with values 1.179, 1.1263 and 1.095 Å for Ln^{3+} = Pr, Nd, and Tb, respectively, and 1.47, 1.31, and 1.18 Å for A^{2+}= Ba, Sr, and Ca, respectively, were used to calculate $\langle r_A \rangle$ and (σ^2).

Table 4. 12. Structural and magnetic transition temperatures for $Ln_{0.50}(Sr, A)_{0.50}CoO_3$ cobaltites (A=Ba, Ca). T_C: Curie temperature. T_{S2}: *R-3c* → *Imma* transition. T_{S1}: *Imma* → *I4/mcm* transition.

Sample	$\langle r_A \rangle$ (Å)	$\langle \sigma^2 \rangle$ (Å^2)	T_C (K)	T_{S2} (K)	T_{S1} (K)
$Pr_{0.50}Sr_{0.40}Ba_{0.10}CoO_3$	1.260	0.0087	225	300	90 (126)
$Pr_{0.50}Sr_{0.45}Ba_{0.05}CoO_3$	1.252	0.0065	231	310	116 (131)
$Pr_{0.50}Sr_{0.50}CoO_3$	1.244	0.0043	230	314	120 (130)
$Pr_{0.50}Sr_{0.475}Ca_{0.025}CoO_3$	1.241	0.0043	224	-	97
$Pr_{0.45}Tb_{0.05}Sr_{0.50}CoO_3$	1.240	0.0043	220	-	59
$Pr_{0.50}Sr_{0.45}Ca_{0.05}CoO_3$	1.238	0.0042	222	-	74
$Nd_{0.50}Sr_{0.50}CoO_3$	1.237	0.0054	228	340	-
$Pr_{0.50}Sr_{0.425}Ca_{0.075}CoO_3$	1.235	0.0042	221	-	28
$Pr_{0.50}Sr_{0.40}Ca_{0.10}CoO_3$	1.231	0.0041	216	-	23
$Sm_{0.50}Sr_{0.50}CoO_3$	1.221	0.00792	180 [74]	-	-
$Eu_{0.50}Sr_{0.50}CoO_3$	1.225	0.00903	162 [74]	-	-
$Gd_{0.50}Sr_{0.50}CoO_3$	1.209	0.0103	123[74]	-	-
$Tb_{0.50}Sr_{0.50}CoO_3$	1.202	0.01156	120	-	-

As a result in Figure 4. 59, we propose a tentative phase diagram that gathers the information of the table. Figure 4. 59 shows a reentrant region centered on PSCO where the half-doped Pr and Sr rich samples stabilize the *I4/mcm* structure. For these compositions (1.23 Å < r_A < 1.26 Å) the Curie temperature T_C hardly varies with the average distortion of the perovskite. T_C remains almost constant, which is in contrast with the strong variations of T_C in smaller perovskites presenting *Imma* or *Pbnm* symmetries at low temperatures.

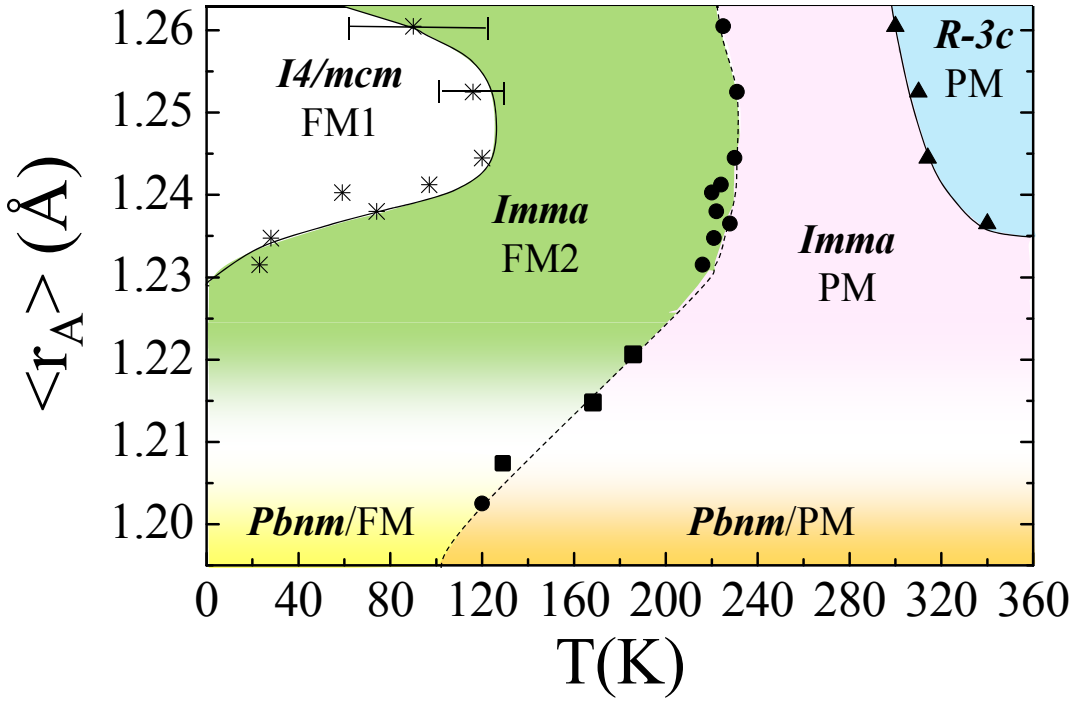

Figure 4. 59. Tentative T-r_A phase diagram of half-doped $Ln_{0.50}(Sr, A)_{0.50}CoO_3$ cobaltites (A = Ba, Ca) rich in Strontium.T_{S2} corresponds to black triangles, T_C corresponds to black circles and T_{S1} corresponds to crosses. Black squares are the T_C of $Ln_{0.50}Sr_{0.50}CoO_3$ cobaltites (Ln= Sm, Eu, Gd) extracted from Ref. [74].

4.14. Discussion and conclusions

To summarize, in this chapter we have presented a complete structural, magnetic and electronic characterization of the half-doped cobaltite $Pr_{0.50}Sr_{0.50}CoO_3$ by combining the data analysis from different techniques such as NPD and X-ray absorption spectroscopies.

$Pr_{0.50}Sr_{0.50}CoO_3$ (PSCO) notably differs from $Pr_{0.50}Ca_{0.50}CoO_3$ (PCCO) where a spin-state change has been proved in order to favor a partial Pr^{3+} to Pr^{4+} valence shift and a exotic metal-insulator transition at around 80 K. In contrast with the absence of a long-range magnetic order in PCCO, metallic $Pr_{0.50}Sr_{0.50}CoO_3$ is ferromagnetic (FM) below $T_C \sim 230$ K. Here, an unexpected step in magnetization at $T_{S1} \sim 120$ K takes place, which can be positive or negative depending on the applied field, with crossover at $H_{cr} \approx 30$ mT. In addition, another striking feature is that this second magnetic transition vanishes by substituting Pr with other lanthanides, indicating an active participation of the Pr ions.

During the last years, different hypothesis were proposed by different groups to explain its magnetic behavior at T_{S1}, such as: (i) a structural and magnetic transition; (ii) structural changes involving phase separation phenomena, (iii) ordering of the Pr moments, (iv) orbital ordering in the e_g orbitals of the Co^{3+} ions in IS state, (v) hybridization between the Pr *4f* orbitals and O *2p* orbitals, (vi) SS changes in the Co^{3+} ions, or (vii) a Co spin reorientation. The crystal structure at both sides of T_{S1} was also subject of debate.

Because two of the proposed mechanisms [(v) and (vi)], the first step in this work was to investigate the electronic configuration in Pr and Co ions by means of X-ray absorption spectroscopy. The first structural analysis in this compound was compatible with a possible hybridization between the Pr and O ions owing to the contraction in the $\langle \text{Pr-O} \rangle^{\text{VIII}}$ bond length at $T_{S1.}$ However, our XAS results at the Pr L_3 and $M_{4,5}$ edges did not reveal any Pr^{3+} to Pr^{4+} oxidation process across T_{S1}. Added to this, we have observed an stability of the average formal valence of cobalt ions at the Co $L_{2,3}$ and O *K* edges consistent with the invariable CoO_6 octahedra volume across T_{S1}. In addition, our findings discarded a large population of LS Co^{3+} ions below T_{S1}, pointing out a mixture of Co^{3+} ions in IS or HS, with Co^{4+} ions in LS or IS state. In order to determine the spin-state in this compound we have used complementary X-ray emission spectroscopic techniques, whose results indicate that this Pr-based cobaltite presents an effective spin state S=1at RT. Applying the constraint of the effective spin, charge-transfer multiplet calculations indicate that the most probable scenario involves mixed LS:HS states in Co^{3+} ions and also mixed LS:IS states in Co^{4+} ions, in contrast to the PCCO cobaltite.

To further clarify the puzzling properties of PSCO, it was also necessary to determine its structural properties. For this, using high-resolution neutron diffraction we have investigated and solve the structural evolution with temperature. Our analysis reveals four successive crystal symmetries, which follows the *Pm-3m* $\rightarrow$ *R-3c* $\rightarrow$ *Imma* $\rightarrow$ *I4/mcm* transformations with decreasing temperature. The study discarded previously proposed symmetries and reveals that this compound is single phased at low temperature. The possibility of a phase separation phenomena across T_{S1} previously proposed was also ruled out. So, from the structural analysis we conclude that the MS effects are induced by the *Imma* $\rightarrow$ *I4/mcm* symmetry changes, which are responsible for the second magnetic transition at T_{S1}, implying strong modifications in the strength of the double exchange coupling along the different directions. Although, the metallic character in PSCO is preserved in this transformation, a significant reorganization of the conducting band is expected because of the straightening of the Co-O1-Co bond angle and changes in the rotation system of the octahedra. The stretching deformation in the octahedron across T_{S1} is slight.

Another interesting output of this work is the confirmation of spin-lattice coupling in PSCO across its double ferromagnetic phase (FM1 for T < T_{S1} and FM2 for T > T_{S1}) by means of XMCD. We have found an orbital contribution to the magnetization (of around 1/3 of the spin component) and the results reveal that the temperature dependence of the orbital moment ordering is coupled to the ordering of the electronic spins, indicating the importance of the spin-orbital coupling term in this cobaltite, promoting a parallel alignment of both magnetic moments at both sides of the MS transition. In absence of an external field we consider that very likely a reorientation of the orbital moment is provoked by the *Imma* → *I4/mcm* symmetry changes, and as a consequence of the spin-orbit coupling, the ordered Co spins are rotated between the FM1 and FM2 phases.

This last issue has been also corroborated by the analysis of the magnetic structures using neutron diffraction. The different magnetic structures and magnetic symmetries of PSCO at both sides of T_{S1} were solved and determined. Above T_{S1} the FM2 phase is composed of [100] FM domains (F_x), with magnetic symmetry *Im'm'a* (m_y=0). Below T_{S1} there is a change in the magnetocrystalline axis. The coupled orbital and spin components of the moment rotate by 45º and the easy axis becomes parallel to the diagonal of the tetragonal unit cell (F_{xy}). The overall symmetry of the low temperature phase is *C2'/m'* (with $|m_x|=|m_y|$). Such a symmetry presents degeneration and two equivalent magnetic easy-axis, which are associated to the two conjugated magnetic domains with spin orientations [110] and [1-10]. So, the lost of magnetization (negative-step) under the low fields (H< H_{cr}) is produced by the emergence and coexistence of conjugated [110] and [1-10] ferromagnetic domains below the *Imma* → *I4/mcm* transition. A schematic view of magnetic ordering and magnetic domains above and below T_{S1} is shown in Figure 4. 60. On the other hand, the interpretation of the sudden positive jump under field is ascribed to a larger J_F/K_a ratio, with J_F and K_a being the double-exchange term and the magnetocrystalline energy, respectively. In the tetragonal phase the Co-O1-Co angle (apical angle) becomes completely flat (~180º) which enhances the coupling J_F (double-exchange).

This chapter is also filled out with the structural and magnetic characterization of other similar cobaltites. We have observed that the MS transition does not appear in $Nd_{0.50}Sr_{0.50}CoO_3$ or smaller cells, and even it is suppressed in epitaxial PSCO thin film. The latter example evidences the importance of the lattice degrees of freedom for the MS transition in the ceramic samples. However, we have recently found that the anomalous MS transition is preserved in bigger cells if, instead of Pr, we substitute Sr^{2+} by a bigger alkaline-earth ion such as Ba^{2+} or

when it is substituted by smaller ion such as Ca^{2+}. A tentative T-r_A phase diagram for $Ln_{0.50}(Sr_{1-x}A_x)_{0.50}CoO_3$ Sr rich cobaltites has been proposed.

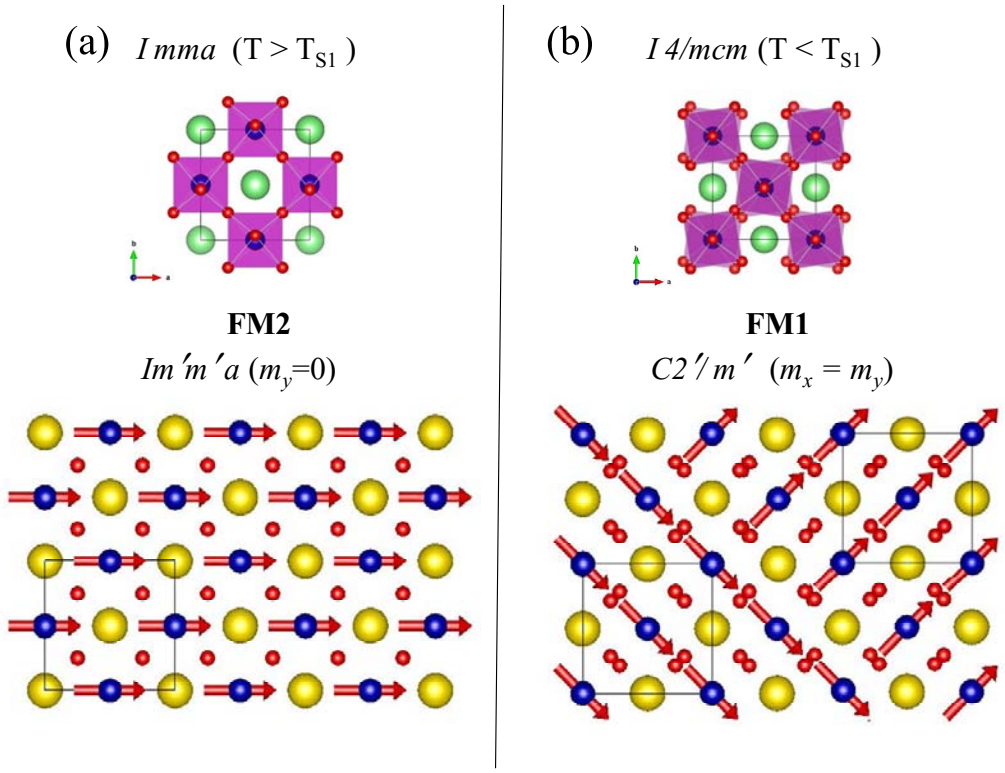

Figure 4. 60. Schematic view of the crystal and magnetic structures for (a) the ferromagnetic phase above T_{S1} (FM2) composed of [100] ferromagnetic domains and (b) the ferromagnetic phase below T_{S1} (FM1) showing the coexistence of conjugated [110] and [1-10] magnetic domains.

BIBLIOGRAPHY

[1] A. Podlesnyak, K. Conder, E. Pomjakushina, and A. Mirmelstein, "ChemInform Abstract: Layered Cobalt Perovskites: Current Topics and Future Promises," *ChemInform*, vol. 39, no. 40, Sep. 2008.

[2] B. Raveau and M. Motin Seikh, *Cobalt oxides. From Crystal Chemistry to Physics*. WILEY-VCH, 2012.

[3] N. B. Ivanova, S. G. Ovchinnikov, M. M. Korshunov, I. M. Eremin, and N. V. Kazak, "Specific features of spin, charge, and orbital ordering in cobaltites," *Uspekhi Fiz. Nauk*, vol. 52, pp. 789–810, 2009.

[4] A. Kundu, R. Sarkar, B. Pahari, a. Ghoshray, and C. N. R. Rao, "A comparative study of the magnetic properties and phase separation behavior of the rare earth cobaltates, $Ln_{0.5}Sr_{0.5}CoO_3$ (*Ln*=rare earth)," *J. Solid State Chem.*, vol. 180, pp. 1318–1324, 2007.

[5] C. Zener, "Interaction between the d-shells in the TM. Ferromagnetic compounds of Manganese with perovskite structure," *Phys. Rev.* vol. 82, no.3, pp. 403, 1951.

[6] J. B. Goodenough, "An interpretation of the magnetic properties of the perovskite-type mixed crystals $La_{1-x}Sr_xCoO_{3-\delta}$," *J. Phys. Chem. Solids*, vol. 6, pp. 287–297, 1958.

[7] J. B. Goodenough, A. Wold, R. J. Arnott, and N. Menyuk, "Relationship between crystal symmetry and magnetic properties of ionic compounds containing Mn^{3+}," *Phys. Rev.*, vol. 124, no. 2, pp. 373–384, 1961.

[8] R. Caciuffo, D. Rinaldi, G. Barucca, J. Mira, J. Rivas, M. Señarís-Rodríguez, P. Radaelli, D. Fiorani, and J. Goodenough, "Structural details and magnetic order of $La_{1-x}Sr_xCoO_3$ (x~0.3)," *Phys. Rev. B.*, vol. 59, no. 2, pp. 1068–1078, 1999.

[9] P. Ravindran, "Electronic structure , phase stability , and magnetic properties of La_{1-x} Sr_xCoO_3 from first-principles full-potential calculations," *Phys. Rev. B.*, vol. 60, no. 24, 1999.

[10] M. A. Senaris-Rodriguez and J. B. Goodenough, "Magnetic and Transport Properties of the System," *Journal of Solid State Chemistry*, vol. 118. pp. 323–336, 1995.

[11] S. Tsubouchi, T. Kyômen, and M. Itoh, "Calorimetric study of $La_{1-x}Sr_xCoO_{3-\delta}$ (0~x~0.5): Evidence for long-range ferromagnetic ordering for x~0.3," *Phys. Rev. B*, vol. 67, no. 094437, pp. 1–5, 2003.

[12] G. H. Kwei, D. Louca, J. L. Sarrao, J. D. Thompson, and H. Ro, "Correlation of local Jahn-Teller distortions to the magnetic / conductive states of $La_{1-x}Sr_xCoO_3$," *Phys. Rev. B.*, vol. 60, no. 14, pp. 378–382, 1999.

[13] D. Louca and J. L. Sarrao, "Dynamical disorder of spin-induced Jahn-Teller orbitals with the insulator-metal transition in cobaltites.," *Phys. Rev. Lett.*, vol. 91, no. 15, p. 155501, 2003.

[14] T. Takami, J.-S. Zhou, J. Goodenough, and H. Ikuta, "Correlation between the structure and the spin state in $R_{1-x}Sr_xCoO_3$ (*R*=La, Pr, and Nd)," *Phys. Rev. B.*, vol. 76, no. 144116, pp. 1–7, 2007.

[15] N. Sundaram, Y. Jiang, I. E. Anderson, D. P. Belanger, C. H. Booth, F. Bridges, J. F. Mitchell, and H. Zheng, "Local Structure of La," *Mater. Sci.*, vol. 2, pp. 1–5, 2009.

[16] Y. Okimoto, X. Peng, M. Tamura, T. Morita, K. Onda, T. Ishikawa, S. Koshihara, N. Todoroki, T. Kyomen, and M. Itoh, "Ultrasonic propagation of a metallic domain in $Pr_{0.5}Ca_{0.5}CoO_3$ undergoing a photoinduced insulator-metal transition," *Phys. Rev. Lett.*, vol. 103, no. 027402, pp. 1–4, 2009.

[17] S. Tsubouchi, T. Kyômen, M. Itoh, P. Ganguly, M. Oguni, Y. Shimojo, Y. Morii, and Y. Ishii, "Simultaneous metal-insulator and spin-state transitions in $Pr_{0.5}Ca_{0.5}CoO_3$," *Phys. Rev. B*, vol. 66, no.052418, pp. 3–6, 2002.

[18] A. J. Barón-González, C. Frontera, J. L. García-Muñoz, J. Blasco, and C. Ritter, "Role of A-site cations in the metal-insulator transition in $Pr_{0.5}Ca_{0.5}CoO_3$" *Phys. Rev. B.*, vol. 81, no. 054427, pp. 1–6, 2010.

[19] K. Knížek, J. Hejtmánek, P. Novák, and Z. Jirák, "Charge transfer, valence, and the metal-insulator transition in $Pr_{0.5}Ca_{0.5}CoO_3$" *Phys. Rev. B.*, vol. 81, no. 155113, pp. 1–5, 2010.

[20] J. L. García-Muñoz, C. Frontera, A. J. Barón-González, S. Valencia, J. Blasco, R. Feyerherm, E. Dudzik, R. Abrudan, and F. Radu, "Valence transition in (Pr,Ca)CoO_3 cobaltites: Charge migration at the metal-insulator transition," *Phys. Rev. B.*, vol. 84, no. 045104, pp. 3–8, 2011.

[21] J. Herrero-Martín, J. García-Muñoz, S. Valencia, C. Frontera, J. Blasco, A. Barón-González, G. Subías, R. Abrudan, F. Radu, E. Dudzik, and R. Feyerherm, "Valence change of praseodymium in $Pr_{0.5}Ca_{0.5}CoO_3$ investigated by X-ray absorption spectroscopy," *Phys. Rev. B*, vol. 84, no. 115131, pp. 1–6, 2011.

[22] J. Herrero-Martín, J. L. García-Muñoz, K. Kvashnina, E. Gallo, G. Subías, J. a. Alonso, and A. J. Barón-González, "Spin-state transition in $Pr_{0.5}Ca_{0.5}CoO_3$ analyzed by X-ray absorption and emission spectroscopies," *Phys. Rev. B.*, vol. 86, no. 125106, pp. 1–6, 2012.

[23] H. W. Brinks, H. Fjellvag, A. Kjekshys, and B. C. Hauback, "Structure and Magnetism of $Pr_{1-x}Sr_xCoO_3$" *Journal of Solid State Chemistry*, vol. 147. pp. 464–477, 1999.

[24] K. Yoshii and A. Nakamura, "Magnetic properties of $Pr_{1-x}Sr_xCoO_3$" *Phys. B*, vol. 282, pp. 514–515, 2000.

[25] R. Mahendiran and P. Schiffer, "Double Magnetic Transition in $Pr_{0.5}Sr_{0.5}CoO_3$," *Phys. Rev. B*, vol. 68, no. 024427, p. 18, 2003.

[26] I. O. Troyanchuk, D. V. Karpinsky, A. N. Chobot, d. G. Voisekhovic, and V. M. Dobryanskii, "Phase transformations in $Pr_{1-x}Sr_xCoO_3$" *JETP Lett.*, vol. 84, pp. 151–155, 2006.

[27] C. Leighton, D. D. Stauffer, Q. Huang, Y. Ren, S. El-Khatib, M. a. Torija, J. Wu, J. W. Lynn, L. Wang, N. a. Frey, H. Srikanth, J. E. Davies, K. Liu, and J. F. Mitchell, "Coupled structural/magnetocrystalline anisotropy transitions in the doped perovskite cobaltite $Pr_{1-x}Sr_xCoO_3$" *Phys. Rev. B., Phys.*, vol. 79, pp. 1–7, 2009.

[28] A. M. Balagurov, I. A. Bobrikov, D. V. Karpinsky, I. O. Troyanchuk, V. Y. Pomjakushin, and D. V. Sheptyakov, "Successive structural phase transitions in $Pr_{0.5}Sr_{0.5}CoO_3$ in the range 10–1120 K," *JETP Lett.*, vol. 88, pp. 531–536, 2008.

[29] I. O. Troyanchuk, D. V. Karpinsky, V. V. Efimov, E. Efimova, V. Sikolenko, and R. Yusupov, "Crystal structure and the magnetic state of $Pr_{0.5}Sr_{0.5}Co_{0.5}Fe_{0.5}O_3$" *JETP Lett.*, vol. 87, no. 6, pp. 306–310, 2008.

[30] A. M. Balagurov, I. A. Bobrikov, V. Y. Pomjakushin, E. V. Pomjakushina, D. V. Sheptyakov, and I. O. Troyanchuk, "Low-temperature structural anomalies in $Pr_{0.5}Sr_{0.5}CoO_3$" *JETP Lett.*, vol. 93, no. 5, pp. 263–268, 2011.

[31] M. Uchida, R. Mahendiran, Y. Tomioka, Y. Matsui, K. Ishizuka, and Y. Tokura, "Changes of magnetic domain structure induced by temperature-variation and electron-beam irradiation in $Pr_{0.5}Sr_{0.5}CoO_3$," *Appl. Phys. Lett.*, vol. 86, no. 131913, 2005.

[32] S. Hirahara, Y. Nakai, K. Miyoshi, K. Fujiwara, and J. Takeuchi, "Magnetic properties, thermal expansion and magnetostriction of $Pr_{0.5}Sr_{0.5}CoO_3$ single crystal," *J. Magn. Magn. Mater.*, vol. 310, pp. 1866–1867, 2007.

[33] K. Yoshii and H. Abe, "Doping effects of Ru in $Ln_{0.5}Sr_{0.5}CoO_3$ (*Ln*=La, Pr, Nd, Sm, and Eu)," *Phys. Rev. B*, vol. 67, no. 094408, pp. 1–8, 2003.

[34] R. Ganguly, A Maignan, C. Martin, M. Hervieu, and B. Raveau, "The magnetic properties of the half-doped cobaltites $R_{0.50}A_{0.50}CoO_3$ (R=La, rare earth and A= Ca, Sr, Ba)," *J. Phys. Condens. Matter*, vol. 14, pp. 8595–8604, 2002.

[35] P. Kumar and R. Mahendiran, "Influence of rare earth moment ordering on magnetic entropy change in $Nd_{0.5}Sr_{0.5}CoO_3$", *Appl. Phys. Lett.*, vol. 101, no. 2012, p. 042411, 2012.

[36] J. Rodríguez-Carvajal, "Recent advances in magnetic structure determination by neutron powder diffraction," *Phys. B Condens. Matter*, vol. 192, pp. 55–69, 1993.

[37] B. Thole and G. Van Der Laan, "Branching ratio in X-ray absorption spectroscopy," *Phys. Rev. B.*, vol. 38, no. 5, pp. 3158–3171, 1988.

[38] B. T. Thole, G. Van Der Laan, and J. C. Fuggle, "3*d* X-ray-absorption lines and the $3d^9 4f^{n+1}$' multiplets of the lanthanides," *Phys. Rev. B.*, vol. 32, no. 8, 1985.

[39] J. Hejtmánek, E. Šantavá, K. Knížek, M. Maryško, Z. J. T. Naito, H. Sasaki, and H. Fujishiro, "Metal-insulator transition and the Pr^{3+}/Pr^{4+} valence shift in $(Pr_{1-y}Y_y)_{0.7}Ca_{0.3}CoO_3$" *Phys. Rev. B.*, vol. 82, no. 165107, pp. 1–7, 2010.

[40] R. D. Cowan, *The theory of Atomic structure and Spectra*, 1981st ed. Berkeley,CA: University of California, 1981.

[41] Z. Hu, G. Kaindl, H. Ogarasawa, A. Kotani, and I. Felner, "*Ln*-4*f*/ligand-2*p* covalence in Ba*Ln*O_3 and Cs_3LnF_7 (*Ln* = Ce, Pr, Tb)," C*hem. Phys. Lett.,* vol. 325, pp. 241–250, 2000.

[42] A. L. Ankudinov, B. Ravel, J. J. Rehr, and S. D. Conradson, "Real-space multiple-scattering calculation and interpretation of X-ray-absorption near-edge structure," *Phys. Rev. B*., vol. 58, no. 12, pp. 7565–7576, 1998.

[43] F. Guillou, Q. Zhang, Z. Hu, C. Y. Kuo, Y. Y. Chin, H. J. Lin, C. T. Chen, A. Tanaka, L. H. Tjeng, and V. Hardy, "Coupled valence and spin-state transition in $(P_{0.7}Sm_{0.3})_{0.7}Ca_{0.3}CoO_3$" *Phys. Rev. B.*, vol. 87, no. 115114, 2013.

[44] F. Damay, C. Martin, M. Hervieu, a Maignan, B. Raveau, G. André, and F. Bourée, "Structural transitions in the manganite $Pr_{0.5}Sr_{0.5}MnO_3$," *J. Magn. Magn. Mater.*, vol. 184, pp. 71–82, 1998.

[45] T. Y. Tan, B. J. Kennedy, Q. Zhou, C. D. Ling, W. Miiller, C. J. Howard, M. A. Carpenter, and K. S. Knight, "Impact of Jahn-Teller active Mn^{3+} on strain effects and phase transitions in $Sr_{0.65}Pr_{0.35}MnO_3$" *Phys. Rev. B.*, vol. 85, no.104107, pp. 1–10, 2012.

[46] N. E. Brese and M. O'Keeffe, "Bond-valence parameters for solids," *Acta Crystallogr. Sect. B Struct. Sci.*, vol. 47, pp. 192–197, 1991.

[47] I. D. Z. Brown, *Kristallogr.*, vol. 199, pp. 255–272, 1992.

[48] B. Y. R. D. Shannon, M. H, N. H. Baur, O. H. Gibbs, M. Eu, and V. Cu, "Revised Effective Ionic Radii and Systematic Studies of Interatomie Distances in Halides and Chaleogenides" *Acta. Cryst*, A32, 751, 1976.

[49] G. Schütz, W. Wagner, W. Wilhelm, P. Kienle, R. Zeller, R. Frahm, and G. Materlik, "Absorption of Circularly Polarized X-Rays in Iron," *Phys. Rev. Lett.*, vol. 58, no. 7, pp. 737–740, 1987.

[50] C. T. Chen, F. Sette, Y. Ma, and S. Modesti, "Soft-X-ray magnetic circular dichroism at the $L_{2,3}$ edges of nickel," *Phys. Rev. B.*, vol. 42, no. 11, pp. 7262–7265, 1990.

[51] B. T. Thole, P. Carra, F. Sette, and G. Van Der Laan, "X-ray circular dichroism as a probe of orbital magnetization," *Phys. Rev. Lett.*, vol. 68, no. 12, pp. 1943–1946, 1992.

[52] P. Carra, B. T. Thole, M. Altarelli, and X. D. Wang, "X-ray magnetic circular and local magnetic fields," *Phys. Rev. Lett.*, vol. 70, no. 694, 1993.

[53] C. T. Chen, Y. U. Idzerda, H.-J. Lin, N. V. Smith, G. Meigs, E. Chaban, G. H. Ho, E. Pellegrin, and F. Sette, “Experimental confirmation fot he X-ray Magentic Circular Dicrhoism,” *Phys. Rev. Lett.*, vol. 75, no. 1, 1995.

[54] F. De Groot "*Core Level Spectroscopy in Solids.*” 2008.

[55] M. W. Haverkort, Z. Hu, J. C. Cezar, T. Burnus, H. Hartmann, M. Reuther, C. Zobel, T. Lorenz, a. Tanaka, N. B. Brookes, H. H. Hsieh, H. J. Lin, C. T. Chen, and L. H. Tjeng, “Spin state transition in $LaCoO_3$ studied using soft X-ray absorption spectroscopy and magnetic circular dichroism,” *Phys. Rev. Lett.*, vol. 97, no. 176405, pp. 38–41, 2006.

[56] M. Merz, P. Nagel, C. Pinta, A. Samartsev, H. V. Löhneysen, M. Wissinger, S. Uebe, A. Assmann, D. Fuchs, and S. Schuppler, “X-ray absorption and magnetic circular dichroism of $LaCoO_3$, $La_{0.7}Ce_{0.3}CoO_3$, and $La_{0.7}Sr_{0.3}CoO_3$ films: Evidence for cobalt-valence-dependent magnetism,” *Phys. Rev. B.* , vol. 82, no. 174416, pp. 1–9, 2010.

[57] L. M. García, J. Chaboy, F. Bartolomé, and J. B. Goedkoop, “Orbital magnetic moment instability at the spin reorientation transition of $Nd_2Fe_{14}B$,” *Phys. Rev. Lett.*, vol. 85, no. 2, pp. 429–432, 2000.

[58] Y. C. Tseng, N. M. Souza-Neto, D. Haskel, M. Gich, C. Frontera, A. Roig, M. Van Veenendaal, and J. Nogués, “Nonzero orbital moment in high coercivity ε-Fe_2O_3 and low-temperature collapse of the magnetocrystalline anisotropy,” *Phys. Rev. B.* , vol. 79, no. 094404, pp. 1–6, 2009.

[59] J. Störh and H. C. Siehmann, *Magnetism: from fundamentas to nanoscale dynamics*. Springer, 2006.

[60] J. M. Chen, J. M. Lee, S. C. Haw, S. a. Chen, V. Hardy, F. Guillou, S. W. Chen, C. Y. Kuo, C. W. Pao, J. F. Lee, N. Hiraoka, H. Ishii, K. D. Tsuei, and Z. Hu, “Evolution of spin and valence states of $(P_{0.7}Sm_{0.3})_{0.7}Ca_{0.3}CoO_3$ at high-tempearture and high-pressure" *Phys. Rev. B.*, vol. 90, no. 035107, 2014.

[61] J. Padilla-pantoja, J. Herrero-mart, P. Gargiani, S. M. Valvidares, V. Cuartero, K. Kummer, O. Watson, N. B. Brookes, and J. Luis, "Stability of the cationic oxidation state in $Pr_{0.50}Sr_{0.50}CoO_3$ across the magnetostructural transition by X-ray absorption spectroscopy *" Inorg. Chem.*, vol. 53, no. 403117j, pp. 8854–8858, 2014.

[62] G. Ehora, S. Daviero-Minaud, M. Colmont, G. André, and O. Mentré, "$Ba_2Co_9O_{14}$: New inorganic building blocks with magnetic ordering through super-super exchanges only," *Chem. Mater.*, vol. 19, no. 3, pp. 2180–2188, 2007.

[63] J. M. Perez-Mato, S. V. Gallego, E. S. Tasci, L. Elcoro, G. de la Flor, and M. I. Aroyo, "Bilbao Crystallographic Server. 2013.," *Annu. Rev. Mater. Res.*, 2015. [Online]. Available: http://www.cryst.ehu.es/.

[64] M. Sikora, K. Knizek, C. Kapusta, and P. Glatzel, "Evolution of charge and spin state of transition metals in the $LaMn_{(1-x)}Co_xO_3$ perovskite series," *J. Appl. Phys.*, vol. 103, no. 07C907, 2008.

[65] G. Vankó, J.-P. Rueff, A. Mattila, Z. Németh, and A. Shukla, "Temperature and pressure-induced spin-state transitions in $LaCoO_3$," *Phys. Rev. B.,* vol. 73, no. 024424, pp. 1–9, 2005.

[66] J. Herrero-Martín, A. Mirone, J. Fernández-Rodríguez, P. Glatzel, J. García, J. Blasco, and J. Geck, "Hard X-ray probe to study doping-dependent electron redistribution and strong covalency in $La_{1-x}Sr_{1+x}MnO_4$," *Phys. Rev. B.*, vol. 82, no. 075112, pp. 1–8, 2010.

[67] J. Kawai, C. Suzuki, H. Adachi, T. Konishi, and Y. Gohshi, "Charge-tranfer effect on the linewith of Fe *K*-alpha X-ray fluorescence spectra," *Phys. Rev. B.*, vol. 50, no. 16, 1994.

[68] X. Wang, F. de Groot, and S. Cramer, "Spin-polarized X-ray emission of 3*d* transition-metal ions: A comparison via $K\alpha$ and $K\beta$ detection," *Phys. Rev. B.*, vol. 56, no. 8, pp. 4553–4564, 1997.

[69] C. Suzuki, J. Kawai, J. Tanizawa, H. Adachi, S. Kawasaki, M. Takano, and T. Mukoyama, "Local spin moment of $LaCoO_3$ probed by a core hole," *Chem. Phys.*, vol. 241, pp. 17–27, 1999.

[70] G. Vankó, T. Neisius, G. Molnár, F. Renz, S. Kárpáti, A. Shukla, and F. De Groot, "Probing the 3D spin momentum with X-ray emission spectroscopy: The case of molecular-spin transitions," *J. Phys. Chem. B*, vol. 110, pp. 11647–11653, 2006.

[71] J. S. Srikiran and S. M. Yusuf, "Study of structure and magnetic properties of the perovskite $Tb_{0.5}Sr_{0.5}CoO_3$," *J. Alloys Compd.*, vol. 390, pp. 26–30, 2005.

[72] C. Autret, C. Martin, M. Hervieu, a Maignan, B. Raveau, G. Andre, F. Boure, and L. Le, "$Pr_{0.50}Sr_{0.50-x}Ba_xCoO_3$: Size and Mistmach effect on Structural and Magnetic Transitions," *Chem. Mater,* no. 15, pp. 1886–1896, 2003.

[73] J. A. Collado, J. L. García-Muñoz, and M. a G. Aranda, "Effects of the *A*-site cation number on the properties of $Ln_{5/8}M_{3/8}MnO_3$ manganites," *J. Solid State Chem.*, vol. 183, pp. 1083–1089, 2010.

[74] I. O. Troyanchuk, N. V. Kasper, D. D. Khalyavin, A. N. Chobot, G. M. Chobot, and H. Szymczak, "Magnetic and structural phase transitions in some orthocobaltites doped by Ba or Sr ions," *J. Phys. Condens. Matter*, vol. 10, pp. 6381–6389, 1998.

Chapter 5

The spin-lattice coupling in the *Ln*$BaCoO_2O_{5.50}$ (*Ln* = Pr, Gd, Y) layered

5.1. Motivation

The *Ln*$BaCo_2O_{5\pm\delta}$ layered cobaltites, whose structure is similar to that of superconducting $YBa_2Cu_3O_7$ cuprate, are considered good examples of systems where the interplay of the spin, orbital, lattice, and charge degrees of freedom is strongly pronounced. The presence of Ba favors alternate layers of Ln^{3+} and Ba^{2+} cations. Furthermore, a simultaneous ordering of the oxygen vacant in *Ln*$BaCo_2O_{5.5}$ takes place if the size difference between the Ln^{3+} and A^{2+} cations is large.

These layered cobaltites ("112") have attracted considerable attention after the discovery of an exceptionally high magnetoresistance in *Ln*$BaCo_2O_{5.4}$ by Martin *et al*. in 1997 [1] and potential thermoelectric ion conduction properties in many compounds [2]. They are considered important potential materials for spintronics, SOFC cells, and thermoelectricity. However, the understanding of these systems from a fundamental point of view is still deficient and there are contradictory descriptions in the literature which has created considerable confusion regarding the origin of their multifunctional physical properties such as: (i) ferromagnetism (FM) near and above room temperature, (ii) metal-insulator transitions (MITs), (iii) spin-state (SS) transitions, (iv) orbital order, (v) charge order, or (vi) spin blockade phenomena.

In this chapter we will emphasize the work carried out during this thesis on the nonstoichiometric $YBaCo_2O_{5.50}$ system covering its magnetic, metal-insulator, and structural transitions. The combination of different techniques has been the key to outline the physical phenomenology $YBaCo_2O_{5.50}$ displays. Synchrotron X-ray Powder Diffraction (SXRPD) has allowed to determine the symmetry of the crystal structure, previously unclear, and the spectroscopic measurements have led to the quantification/determination of the SS transition across the MIT. Besides, the study will be extended to other members or the family with bigger lanthanides such as $GdBaCo_2O_{5.50}$ and $PrBaCo_2O_{5.5+\delta}$, considered good representatives of moderate (Gd) and big (Pr) *Ln* atomic sizes.

5.2. Introduction

5.2.1. Crystal structures and oxygen content

The crystal structure of the $LnBaCo_2O_{5+\delta}$ ($0 \leq \delta \leq 1$) compounds consists of a sequence of $[CoO_2]$-[BaO]-$[CoO_2]$-$[LnO_\delta]$ layers along the *c*-axis, including a doubling of the original perovskite cell in *c* direction (a_0 x a_0 x $2a_0$, where a_0 is the cubic perovskite cell parameter). The wide allowed oxygen content can lead to several crystallographic structures at RT, with either pyramidal or octahedral (or both) environments for the Co ions. Next, the RT structures for differences values of δ will be presented.

The first series of 112 cobaltites corresponds to the general formula $LnBaCo_2O_5$ and they can exhibit a tetragonal (*P4/mmm*) or an orthorhombic symmetry (*Pmmm* or *Pmma*), with a_p x a_p x $2a_p$ cell parameters. This structure forms mixed-valence states Co^{2+} and Co^{3+} ions (ratio 1:1) and each cobalt is inside a pyramid with a square base [2–4].

In the opposite stoichiometric case we find the compounds described by the formula $LnBaCo_2O_6$. In this case, the Co^{3+} and Co^{4+} ions are also present in equal amounts but in an octahedral environment with a tetragonal unit cell a_0 x a_0 x $2a_0$ [2–4].

The third series of 112 cobaltites is the nonstoichiometric case with general formula $LnBaCo_2O_{5.5}$, more complex. Although, only Co^{3+} ions are present in this structure they are equally distributed in pyramidal and octahedral oxygen environment because of the oxygen vacancies ordering. In this case, firstly some authors assume an orthorhombic *Pmmm* symmetry with a_0 x $2a_0$ x $2a_0$ cell parameters [2–9], but later it was confirmed either in the space group *Pmmm* or in the *Pmma* by many reports [6, 10–15]. In Figure 5. 1 is displayed the perspective view of the 112 structure for these three stoichiometris.

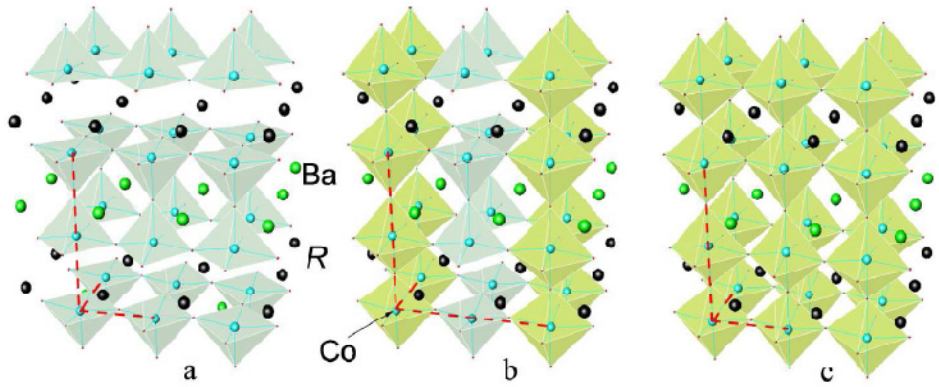

Figure 5. 1. Schematic crystal structure of $Ln BaCo_2O_{5+\delta}$ with (a) a_0 x a_0 x $2a_0$ (δ=0); (b) a_0 x $2a_0$ x $2a_0$ (δ=1); (c) a_0 x a_0 x $2a_0$ (δ=1) type unit cell extracted from Ref. [2], where the black balls are the rare earth (*R*) or lanthanide, the green balls are the Ba ion and the blue balls the Co ions.

Because of this structure is very sensitive to tiny variations in the oxygen content and the size of the Ln^{3+} cation, different long-range ordered superstructures or local distortions can be obtained, leading to variations in the magnetic and electric properties from one sample to the other. In addition, the oxygen content can strongly depend on the size of the Ln^{3+} cations as it was observed in the systematic synthesis of $Ln BaCo_2O_{5\pm\delta}$ (*Ln* = Pr, Nd, Sm, Eu, Gd, Tb, Dy, and Ho) samples in which their oxygen content decreases as the *Ln* decreases [9, 16].

Furthermore, it has been observed that a dependence of the lattice parameters, magnetic and electric properties exist, not only on the oxygen content, but also in the method of synthesis. Earlier studies have established clear correlations between the thermal treatment, oxygen content, vacant ordering and the observed physical properties [9, 15, 17–23].

So, for example the orthorhombic distortion depends on the synthesis history as S. Streule *et al.* reported [2], the lattice parameter *c* increased with δ, while *a* and *b* decreased as Figure 5. 2 (a),(b) shows. Besides, increasing the oxygen content $0 \leq \delta \leq 1$, it was observed a fast growing of the orthorhombic distortion, which reaches its maximum value near δ= 0.5 as shows Figure 5. 2(c). This is the signature of a strong tendency to oxygen vacancies order within the LnO_δ layers. The result is an alternation of oxygen-rich and -deficient *ac* layers, and consequently the doubling of the unit cell along the *b* direction.

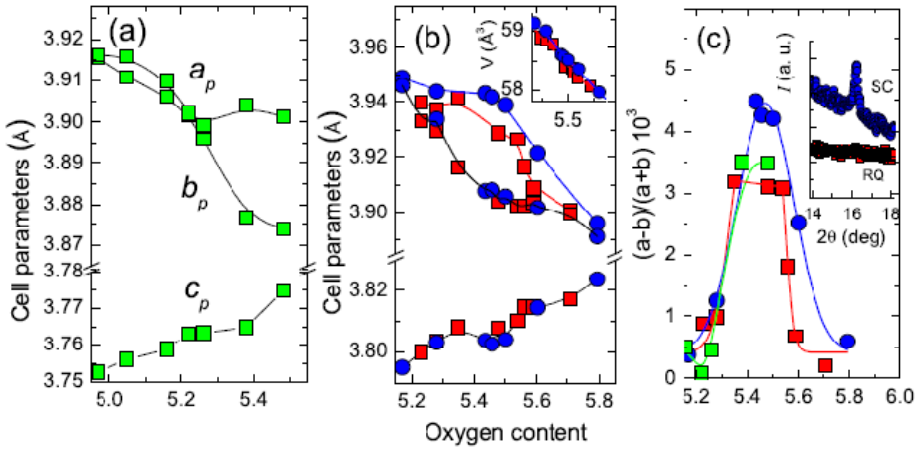

Figure 5. 2. Evolution of the lattice parameters with the oxygen content of (a) $GdBaCo_2O_{5+\delta}$ and (b) $PrBaCo_2O_{5+\delta}$. The inset shows the volume of the pseudocubic unit cell. (c) Orthorhombic distortion as a function of oxygen content for the slowly cooling (dots) and rapid quenching (squares) thermal treatment. The inset shows the X-ray diffraction pattern for each thermal treatment showing 2*b* periodicity in samples slowly cooled. The data is extracted from Ref. [2].

5.2.2. Magnetic and transport properties of $LnBaCo_2O_{5\pm\delta}$

We now turn to the discussion of the magnetic and transport properties of these materials. In this section we separate the analysis of the $LnBaCo_2O_5$ and the $LnBaCo_2O_{5+\delta}$ compounds because of the different complexity and controversy observed between both types of series.

$LnBaCo_2O_5$

$LnBaCo_2O_5$ undergo two magnetic transitions: (i) the first one is recognized as a paramagnetic (PM) to an antiferromagnetic (AFM) state at T_N ~340 K which is associated to a structural variation (*P4/mmm* $\rightarrow$ *Pmmm*) and (ii) the second one corresponds to a charge ordered state at T_{CO} ~210 K where a structural change (*Pmmm* $\rightarrow$ *Pmmb*) also takes place [22, 24–26]. Below T_{CO} an orbital ordering and a long-range Co^{2+}/Co^{3+} charge ordering occurs inducing a spin state transition in the Co ions. However, despite the fact that these compounds present a simple magnetic structure (named G-type AFM structure), the electronic configuration of the Co ions is still a controversial issue. Some examples are the $YBaCo_2O_5$ and $HoBaCo_2O_5$ samples reported by T. Vogt *et al.*[24] and F. Fauth *et al.* [22, 26] using neutron powder diffraction data (NPD), which can be interpreted with two possible spin state models: (a) Co^{3+} in IS ($S = 1$ t_{2g}^5 e_g^1) and Co^{2+} HS ($S = 3/2$ t_{2g}^5 e_g^2) or (b) Co^{3+} in HS ($S = 1$ t_{2g}^4 e_g^2) and Co^{2+} in HS

($S = 3/2\ t_{2g}^{5}\ e_g^{2}$). On the other hand, all $LnBaCo_2O_5$ compounds reported in the literature present an insulator behavior at T < 700 K.

Ln$BaCo_2O_{5\pm\delta}$

Since the materials investigated in this manuscript are mostly type *Ln*$BaCo_2O_{5.50}$, the discussion of the magnetic properties will be focus on these compounds. It has been observed the existence of successive magnetic transitions with decreasing temperature in the insulating phase which are interpreted as paramagnetic-ferromagnetic-antiferromagnetic (PM-FM-AFM) transitions and depending on the lanthanide size the PM-FM transition temperature ranges from T_C = 260-300 K. In addition, several publications using neutron diffraction evidenced a third magnetic transition (AFM → AFM) at T_{SSO} (SSO, spin state order) in compounds with small lanthanides (*Ln* = Tb and Y) [14, 27–30], but it is absent for larger lanthanides [30, 31]. A typical magnetic signal measured for *Ln*$BaCo_2O_{5.50}$ is plotted in Figure 5. 3.

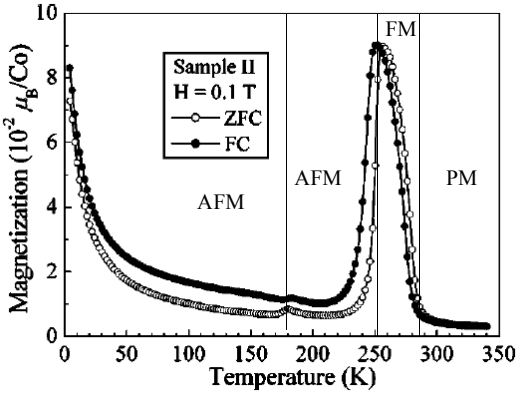

Figure 5. 3. Temperature dependent magnetization measurements for $TbBaCo_2O_{5.50}$ measured at 0.1 T. The data is extracted from Ref. [27].

However, the nature of the spontaneous magnetization within the temperature range T_N < T < T_C (the FM state) and the magnetic structure at temperatures T < T_N (the FM → AFM transition) is an open question and many authors have proposed different models of the magnetic ordering in the literature during the last years. One possible explanation associates the complex magnetic phase in *Ln*$BaCo_2O_{5.50}$ with a partial or full spin-state transition in which the Co^{3+} ions in the octahedral site (Co^{3+}_{oct}) changes from a HS (S = 2, $t_{2g}^{4}\ e_g^{2}$) to a LS (S = 0, $t_{2g}^{6}\ e_g^{0}$) and the Co^{3+} IS in the pyramidal site (Co^{3+}_{pyr}) remains unaltered. However, the establishment of the magnetic structure is needed for a better understanding of the magnetic

evolution. Distinct models for the magnetic ordering were proposed from the analysis of neutron powder diffraction (NPD) data. Next, will review some of the models proposed.

One of the earliest studies was done in $TbBaCo_2O_{5.4}$ by D. D. Khalyavin and coworkers in 2002 [32]. The authors suggested a model for the spontaneous magnetization below 245 K which involves an antiferromagnetic ordering with a small ferromagnetic component in the Co ions (ferrimagnetic ordering) due to the Dzyaloshinsky-Moriya type interactions. They also proposed an intermediate spin state for the trivalent cobalt ions.

Following this study, Plakhty *et al.* [27] later described the magnetic ordering in the three temperature regions with the magnetic moment aligned parallel to the *a*-axis shown in Figure 5. 4: (i) 255 K < T < 290 K, ferrimagnetic phase; (ii) 170 K < T < 255 K, AFM1 phase; and (iii) T < 170 K, AFM2 phase.

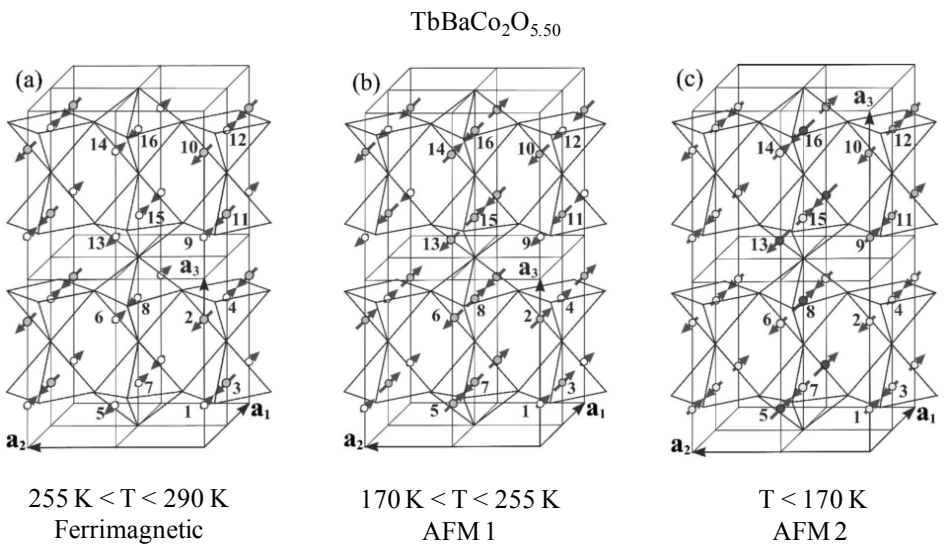

Figure 5. 4. Schematic representation of the magnetic structures proposed by Plakhty: (a) in the ferrimagnetic phase; (b) in the AFM1 phase; and (c) in the AFM2 phase for $TbBaCo_2O_{5.50}$. The circles shadowing and the arrow lengths reflect the different moment value for all 16 Co^{3+} ions in the unit cell. The data is extracted from Ref. [27].

In this case, the authors used the space group *Pmma* with unit cell $2a_0$ x $2a_0$ x $2a_0$ instead of the generally used group *Pmmm* with unit cell a_0 x a_0 x $2a_0$ for the ferrimagnetic and AFM1 phases. In contrast, the AMF2 phase was described by a *Pcca* symmetry with $2a_0$ x $2a_0$ x $4a_0$ magnetic unit cell. In the ferrimagnetic model the Co spins order antiparallel in the two nonequivalent pyramidal sites to explain the spontaneous magnetic moment, while in the AMF2 phase the two non equivalent octahedral sites adopt alternating antiparallel IS and HS states and the two non equivalent pyramidal sites adopt the IS state [27].

Another magnetic model for LnBaCo$_2$O$_{5.50}$ compounds was reported by D. D. Khalyavin *et al.* [7] who used a *Pmma* space group with $2a_0$ x $2a_0$ x $2a_0$ unit cell. The authors proposed for the temperature range $T_N < T < T_C$ that the Co ions in a pyramidal environment (Co1 and Co2 sites) has the same magnetic moment and the same spin state (in this case HS) and are AFM coupled, whereas the magnetic moments of the Co^{3+} ions in the octahedral position (Co3 and Co4 sites) are different: $m_{Co3} \sim 0$ and $m_{Co4} \sim 4\mu_B$/f.u and are FM coupling. This turn out a different spin-state at these positions, LS for Co3 site and HS for Co4 site. The magnetic model for this phase is shown in Figure 5. 5(a). The authors suggested for the phase below T_N that the Co magnetic moments in one half of the cell point in the opposite direction respect to the other half of the cell [see Figure 5. 5(b)].

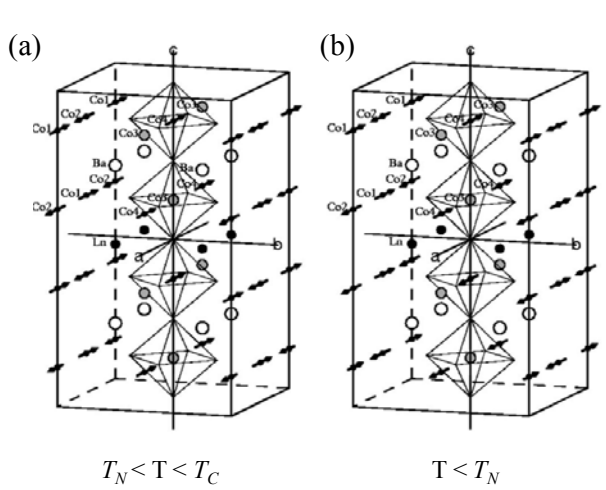

Figure 5. 5. Magnetic structure presented by Khalyavin *et al.* for LnBaCo$_2$O$_{5.50}$ in the (a) spontaneous magnetic moment phase and (b) the antiferromagnetic phase. The Cobalt ions in the low-spin state (Co3 site) are denoted by gray circles. The figure is extracted from Ref. [7].

In a different work HoBaCo$_2$O$_{5.50}$ (with heavy *Ln*) was characterized by NPD by J.-E. Jorgensen *et al.* [33]. They reported that this compound was PM above 265 K and can be described in space group *Pmma* with $2a_0$ x $2a_0$ x $2a_0$ unit cell. The structural study revealed abrupt changes in the cell parameters and the cell volume which were attributed to the metal-insulator transition (MIT, at $T_{MI} \sim 305$ K) and spin state variations in the Co^{3+} ions. In this report the authors proposed as a magnetic structure at 20K an AFM ordering with a $2a_0$ x $2a_0$ x $4a_0$ magnetic unit cell. The complex structure contains FM and AFM interactions and the magnetic moments arrange following this description: (i) Co ions in octahedral sites (Co4, referring to the nomenclature used by Khalyavin *et al.*) are HS (the refined moment was $m_{Co4} \sim 4\ \mu_B$/f.u) while Co3 site is mixed LS/IS state ($m_{Co3} \sim 1\ \mu_B$/f.u); and (ii) Co ions in the two

crystallographically different pyramidally sites (Co1/Co2) have the same magnetic moment ($m_{Co1,2} \sim 2\ \mu_B$/f.u) compatible with an IS state.

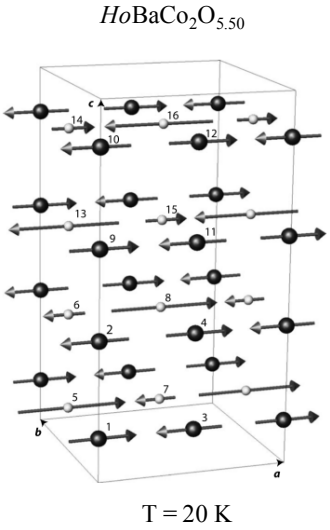

Figure 5. 6. Magnetic structure of HoBaCo$_2$O$_{5.50}$ at T =20 K [33]. Small and big balls represent Co ions in octahedral an pyramidal coordination, respectively. The numbers refer to the positions given for the all 16 Co ions. The length arrows indicate the magnitude of the magnetic moment.

So, it is evidenced that there is no consensus on the successive magnetic structures of the LnBaCo$_2$O$_{5.50}$ compounds. More single crystal studies would be desirable [5, 17, 34, 35] (Ln = Gd, Eu, Tb).

The compounds with $\delta \sim 0.5$ undergo a metal-insulator transition between 280 K and 400 K depending on the *Ln* (decrease with the size of the *Ln*) and as the structural/magnetic properties they are very sensitive to the oxygen stoichiometry. It should be noted that for Ln = Y or Ho, the TMI coincides with the Curie temperature and with the PM to FM transition. However, in other LnBaCo$_2$O$_{5.5}$ the MIT is rather higher than the temperature of the PM-FM transition.

One of the first transport studies in these cobaltites was done by Maignan *et al.* [9] in 1999. They reported the temperature dependence of the resistivity in different compounds synthesized with different atmospheres which can produce the suppression of MIT depending on the oxygen content. One of the series with different *Ln* was synthesized using an air atmosphere as Figure 5. 7(a) shows.

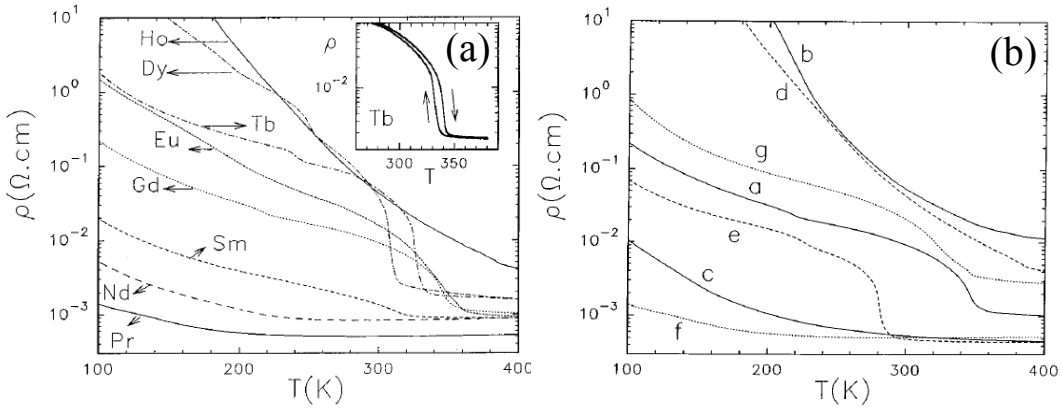

Figure 5. 7. Temperature dependence of the resistivity for (a) the air-synthesized $LnBaCo_2O_{5\pm\delta}$ cobaltites and (b) the air-synthesized $GdBaCo_2O_{5.4}$ [a], the argon annealed $GdBaCo_2O_5$ [b]; the oxygen annealed $GdBaCo_2O_{5.6}$ [c]; the air-synthesized [d] and the oxygen annealed [e] $HoBaCo_2O_{5\pm\delta}$; the air-synthesized [f] and the argon annealed [g] $PrBaCo_2O_{5\pm\delta}$. The graphics have been extracted from Ref.[9].

Here, one observes that the MIT only appeared for the intermediate lanthanides (*Ln* = Sm, Eu, Gd, Tb, Dy). In contrast, for large lanthanides (*Ln* = Pr, Nd) a semimetallic behavior was found, whereas for small lanthanides (*Ln* = Ho) a semiconductor behavior was observed.

As we mentioned the MIT is correlated with the oxygen stoichiometry, so in the same investigation [9] it was evidenced that samples annealed with Argon ($GdBaCo_2O_5$) or oxygen ($GdBaCo_2O_{5.6}$) the MIT is suppressed, meanwhile the air-synthesized $GdBaCo_2O_{5.4}$ exhibit the transition at $T_{MI} \sim 350$ K as it is plotted in Figure 5. 7(b). The same figure shows the evolution with temperature for the Ho sample annealed under an oxygen pressure, which exhibits the MIT at 290 K, whereas the air-synthesized sample does not. In conclusion, the MIT is associated to the 5.50 oxygen stoichiometry with oxygen vacancies well ordered.

5.2.3. The origin of the metal-insulator transition

As we have seen in the previous sections the fact that Co ions can stabilized in different electronic configurations (LS, IS, HS) is crucial for the physical properties. In this section we want to focus on the different mechanisms proposed for the MIT and the several Co spin-states models suggested in the literature for $LnBaCo_2O_{5.5}$ compounds. We have previously discussed in Section 5.2.2. the great controversy about the magnetic ground state in $LnBaCo_2O_{5.5}$ cobaltites, thus the spin state (SS) transition is also a matter of debate.

It is worth nothing that the IS state is widely accepted as aground state of the pyramidal Co^{3+} ions in the $LnBaCo_2O_{5.50}$ [12, 36, 37].

A long list of publications have addressed the question of the MIT in the layered perovskite cobaltites. The first proposal was by Maignan *et al.* [9] from his structural and magnetic characterization of different $LnBaCo_2O_{5.50}$. They suggested a coexistence of IS (pyramids) and LS (octahedra) for $T < T_{MI}$ and both spin states evolving to HS Co^{3+} at high temperatures in these oxides. On the other hand, Moritomo *et al*. [13] speculated for $TbBaCo_2O_{5.50}$ a spin state transition from full IS state to the HS state in both pyramidal and octahedral sites using structural data. From the magnetic characterization of $GdBaCo_2O_{5.50}$, C. Respaud and coworkers [36] suggested a coexistence of HS/IS state in the metallic phase**.**

In Ref. [12] our group used synchrotron X-ray data to prove a SS transition in $GdBaCo_2O_{5.5}$. C. Frontera *et al.* reported that the MIT was accompanied by an anomalous cell volume (V) expansion [12] [see Figure 5. 8(b)] produced by the increase of the volume of the octahedra (CoO_6) above T_{MI} while the volume of the pyramids (CoO_5) decreases as Figure 5. 8(a) shows. This behavior was attributed to a change in the spin state of Co^{3+} ions in the octahedral sites from LS to HS states on heating, meanwhile Co^{3+} ions in the pyramidal

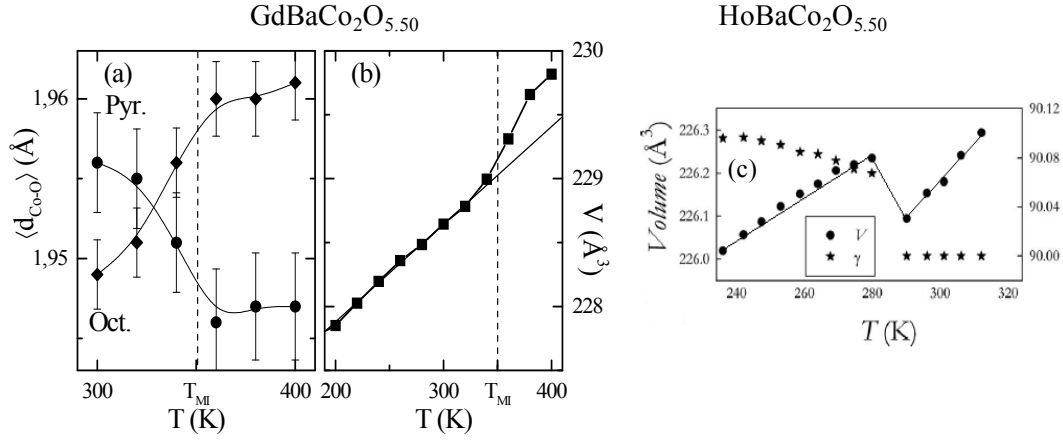

Figure 5. 8. Temperature dependence of (a) average Co-O distances for the CoO_6 and CoO_5 polyhedra and (b) unit-cell volume in $GdBaCo_2O_{5.50}$. The continuous straight line in (b) is a guide-to-the-eyes to highlight the anomalous volume expansion above T_{MI}. Evolution of the volume unit cell in $HoBaCo_2O_{5.50}$ across the structural transition and MIT. The graphics are extracted from Ref. [12, 39].

Based on this picture Maignan *et al.* [38] proposed a complementary model to explain the change in the electron mobility, based on the phenomenon of "spin blockade". It is schematized in Figure 5. 9. A mobile electron is represented by a HS Co^{2+} specie. Electron jumps are allowed to neighbour Co^{3+} HS or Co^{3+} IS sites. But not to neighbour Co^{3+} LS sites,

producing the insulating phase. Figure 5. 9(c) shows that the extra hole easily move to LS Co^{3+} ions.

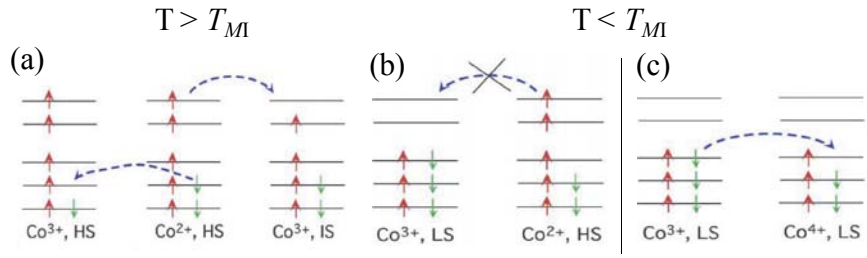

Figure 5. 9. Schematic diagram of possible electron (a), (b) and hole (c) hopping between the HS/IS Co^{3+} and LS Co^{3+} ion. (b) Illustrates the phenomenon of a "spin blockade". Panel (a) applies for the metallic phase and panel (b) and (c) for the insulating phase. Figure adapted from Ref. [38].

In contrast to the high number of structural and magnetic reports on the MIT in *Ln*$BaCo_2O_{5.50}$ cobaltites, only a few spectroscopic measurements are found in the literature for these compounds [40–42]. The first attempt to address the MIT using experimental spectroscopic techniques to clarify the electronic structure was done by M. Lafkioti *et al.* [40] in 2008. This report measured the orbital and spin contribution in $DyBaCo_2O_{5.50}$ by means of X-ray magnetic circular dichroism (XMCD). The observed large orbital moment below MIT was attributed to a Co^{3+} IS at pyramidal and octahedral sites, while above the MIT the octahedra was assigned to a Co^{3+} LS state and the pyramids would remains in the IS state. On the other hand, at the same time the recorded soft X-ray Absorption Spectroscopy (XAS) in $GdBaCo_2O_{5.50}$ and the theoretical calculations by M. García-Fernandez *et al.* [41] led to propose a HS state in the Co^{3+}_{pyr} and a Co^{3+} LS state in the octahedral site for the insulating phase. This last assumption was recently not corroborated by Z. Hu *et al.* who claimed mixed LS/HS in the Co^{3+}_{oct} from XAS results in $GdBaCo_2O_{5.50}$.

5.3. Sample synthesis and experimental details

Polycrystalline samples of $YBaCo_2O_{5.50}$ were prepared in collaboration with O. Castaño (ICMAB) by two different methods in the present thesis: by sol-gel method and solid-state reaction. The procedure followed in both methods is detailed below.

For the sol-gel sample, we dissolved yttrium acetate hydrate, barium acetate, and cobalt acetate tetrahydrate in suitable stoichiometric ratio in distilled water at 60 ºC for a few minutes. Then, an excess of citric acid monohydrate was added to the solution until saturation (~ 70 g of citric acid for 15 g of the sample).

The mix has held at 110 ºC in order to evaporate the water solvent and the resultant acetic acid. The final product was a dark violet gel, which was thermally fired at 550 ºC in a muffle furnace for 5 h in order to eliminate the organic material. The black powder obtained was pressed into pellets and calcined under air at 1050 ºC for 24 h. The bars were then cooled slowly (-60 ºC/h) to room temperature (RT). After regrinding and pressing again, the heat treatment was repeated under pure O_2 atmosphere.

For the solid-state reaction, we prepared stoichiometric amounts of yttrium oxide (Y_2O_3), barium carbonate ($BaCO_3$), and cobalt oxide (Co_3O_4). After a decarbonation process (18 h at 900 ºC), the mixture was pressed into pellets and the last annealing was done at 1100 ºC for 15 h at 60 ºC/h (under O_2 atmosphere).

The other two $LnBaCo_2O_{5.50}$ (*Ln* = Pr, Gd) samples were only prepared by solid-state reaction in our group. For both specimens, high purity powders of Pr_6O_{11}, Gd_2O_3, $BaCO_3$, and Co_3O_4 were mixed at stoichiometric weights. After a decarbonation process (15 h at 1000 ºC) the mixtures were pressed into pellets, $PrBaCo_2O_{5.50}$ ($GdBaCo_2O_{5.50}$) was annealed at 1100 ºC (1125 ºC) during 24 h in air and cooled down (100 ºC/h) to RT. This procedure was repeated several times. For the Pr-based cobaltite an annealing process was carried to improve the content of oxygen. The powdered precursor was finally annealed at 600 ºC in pure Argon during 24 h and quenching them in liquid nitrogen [43]. With Pr the absolute oxygen content 5.5 is difficult to obtain. The M(T) curve (Figure 5. 10) reproduced the expected transition temperatures. However, the transitions are not so abrupt like with smaller *Ln* cations. The oxygen content of these layered cobaltites controls not only the mean valence of Co ions, but also the coordination of Co (pyramidal or octahedral) and the possible disorder has therefore a strong influence on the spin-state of Co for large *Ln* such as La or Pr [10]. The transitions no very abrupt in $PrBaCo_2O_{5.50+\delta}$ can also indicate a lack of perfect vacant ordering. Our group proved that in a similar Pr sample he 80% of octahedral sites were truly occupied by octahedra, while the other 20% were occupied by pyramids [43].

The quality of the initial compounds obtained was tested by means of laboratory X-ray diffraction (using a Siemens D-5000 diffractometer) and we found that the samples were well-crystallized and single phase.

MAGNETOMETRY: The direct current (dc) magnetization measurements were performed using a Superconducting Quantum Interferometer Device (SQUID, Quantum Design) with an applied magnetic field of 0.5 T after cooling under the applied field for $YBaCo_2O_{5.50}$ and $GdBaCo_2O_{5.50}$ compounds On the other hand for the $PrBaCo_2O_{5.50+\delta}$ a small magnetic field was used (0.1 T). Figure 5. 10 displays the M(T) curves for the $LnBaCo_2O_{5.50}$

(*Ln* = Pr, Gd) where the magnetic transitions are labeled. These measurements evidence good quality of both samples. By using the labeling (+δ) in $PrBaCo_2O_{5.50+\delta}$ we means that a tiny deviation of the stoichiometry and a certain vacant disorder is possible with Pr. In the case of smaller lanthanides vacant disorder is negligible. The magnetic curves for $YBaCo_2O_{5.50}$ will be detailed in Section 5.4.

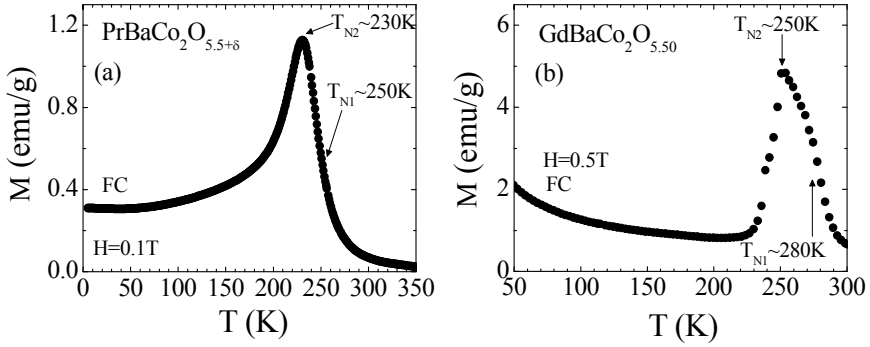

Figure 5. 10. Temperature dependence of the dc magnetization measured under an applied field of (a) 0.1 T for $PrBaCo_2O_{5.50+\delta}$ and (b) 0.5 T for $GdBaCoO_2O_{5.50}$.

Ac magnetic measurements in the Y-based cobaltite were also performed using a Physical Property Measurement System (PPMS, Quantum Design) at frequencies values γ=0.1, 1.1, and 9.9 kHz, an amplitude of 10 Oe, and zero field bias, on heating after a zero field cooling.

ELECTROMETRY: Resistivity measurements were done by the four probe method and Seebeck coefficient was measured using the thermal transport option of the PPMS under two probe configuration.

SYNCHROTRON X-RAY DIFFRACTION: In this chapter the structural characterization is only devoted to the $YBaCo_2O_{5.50}$ sample, thus the experimental details are related to this specific compound. The structural study was carried out using Synchrotron X-Ray Powder Diffraction (SXRPD) at ID22 (the old ID31 beamline) beamline of the European Synchrotron Radiation Facility (ESRF, Grenoble, France) in the 4-350 K temperature range. A short wavelength λ = 0.39978(25) Å, to reduce the absorption, was selected with a double-crystal Ge (111) monochromator and calibrated with Si NIST (*a* = 5.43094 Å). The sample was loaded in a borosilicate glass capillary (ϕ = 0.5 mm). The low temperature data was recorded placing the capillary in a continuous liquid-helium flow cryostat with rotating sample rod. On the other hand, measurements above RT were done by using a hot air blower.

Diffraction data was analyzed with the Rietveld method using FULLPROF suite of programs [44].

SYNCHROTRON X-RAY ABSORPTION: Soft X-ray absorption spectroscopy (XAS) measurements at the Co $L_{2,3}$ and O K edges from 200 K to 370 K were performed on the BL29-BOREAS beamline at the ALBA Synchrotron Light Facility for the three $LnBaCo_2O_{5.50}$ (Ln = Pr, Gd, Y) compounds. Data were recorded by means of surface-sensitive total electron yield (TEY). Proper bulk-pellet-sensitive measurements required in-situ scraping of the sample under ultrahigh vacuum (~10^{-9} mbar) conditions. A CoO pellet was simultaneously measured in the tail of the beam to correct for possible energy shifts. The nominal flux on the BL29-BOREAS beamline was on the order of 10^{12} photons/s with an energy resolution of about 50 meV. Flux and time exposure were selectively reduced in some cases in order to minimize Co ions photoreduction.

X-ray emission spectroscopy (XES) experiments on $LnBaCo_2O_{5.50}$ at 150 K and 300 K were carried out at beamline ID26 of the European Synchrotron Radiation Facility (ESRF). The incident energy ($E_{inc.}$ = 7800 eV) was tuned through the Co K-edge by means of a pair of cryogenically cooled Si(311) monochromator crystals and the overall resolution was 0.4 eV. A reference Co metallic foil was used to calibrate the monochromator energy.

The emitted X-rays were analyzed using a set of four spherically bent Ge(444) crystals that were arranged with the sample and photon detector (avalanche photodiode) in a vertical Rowland geometry (R = 1 m) at 90º scattering angle. In addition, high-energy resolution fluorescence-detected X-ray absorption near edge structure (HERFD-XANES) spectra at the Co K-edge were collected at the maximum of the Co $K\beta_{1,3}$ emission line. A continuous He-flow cryostat was used to carry out low temperature measurements.

5.4. Simultaneous paramagnetic-ferrimagnetic and metal-insulator transition in $YBaCo_2O_{5.50}$

As we earlier commented along the Introduction, only $LnBaCo_2O_{5.50}$ cobaltites using heavy Ln shows that the MIT coincides with the onset of the FM moment while for larger Ln, these two transitions are clearly separated. Figure 5. 11 displays some physical measurements done in $YBaCo_2O_{5.50}$ where it is possible to observe this effect, similar to the changes observed in $HoBaCo_2O_{5.50}$ [38]. The left panel shows that the upturn of the resistivity is concomitant with the apparition of ferromagnetism at $T_{MI} = T_C \sim 295$ K in $YBaCo_2O_{5.50}$.

The magnetic signal measured at 5 T, evidences also that the magnetic moment reaches its maximum value and it vanishes at T_{N1} ~ 265 K on cooling where the new magnetic phase (AFM) stabilizes. So, it is well observed the two magnetic transitions (PM $\rightarrow$ FM $\rightarrow$ AFM) typical for these compounds. However, the ac measurements applying three different frequencies proof another magnetic transition in which the cobalt magnetic moments rearrange in a second AFM structure at T_{N2} ~ 231 K. Figure 5. 11(b) displays the thermal evolution of the real part of the ac-magnetization together with the Seebeck coefficient. In the inset of this figure it is visible the apparition of a tiny peak in the magnetic data at low temperature, reflecting a new magnetic ordering at low temperature. From the Seebeck measurement we have seen an upturn of the Seebeck coefficient coinciding with the onset of the insulating phase, similar to that found for $HoBaCo_2O_{5.50}$., and reach a maximum value of S~300 μV/K. However, the Seebeck coefficient of the Ho-based cobaltite was reported to take small negative values above T_{MI} (S ~ -2 μV /K) [38], in contrast with our results in $YBaCo_2O_{5.50}$. It should be noticed that the sign of the Seebeck coefficient changes depending on the type-conduction band (if it is electron or hole- based). So, some tiny deviation from the 5.50 oxygen content can produce the presence of a small portion of Co^{4+} (Co^{2+}), leading the presence of holes (electrons) in the system.

Nevertheless, apart from the previous macroscopic magnetic characterization, the three magnetic transitions were previously confirmed by NPD. C. Frontera *et al*. [30] in 2008 reported the appearance of several magnetic peaks in NPD patterns at low temperature in $YBaCo_2O_{5.50}$. The integrated intensity of these peaks is plotted in Figure 5. 12. From this figure it can be seen that a new magnetic peak (½ 1 1) appears at T ~ 287 K a temperature close to the Curie temperature. On cooling, this peaks vanishes at T_{N1} ~ 260 K and a new magnetic reflection appears (½ 1 ½) at T_{N2} ~ 235 K. So, our magnetic data are consistent with the results obtained earlier by NPD.

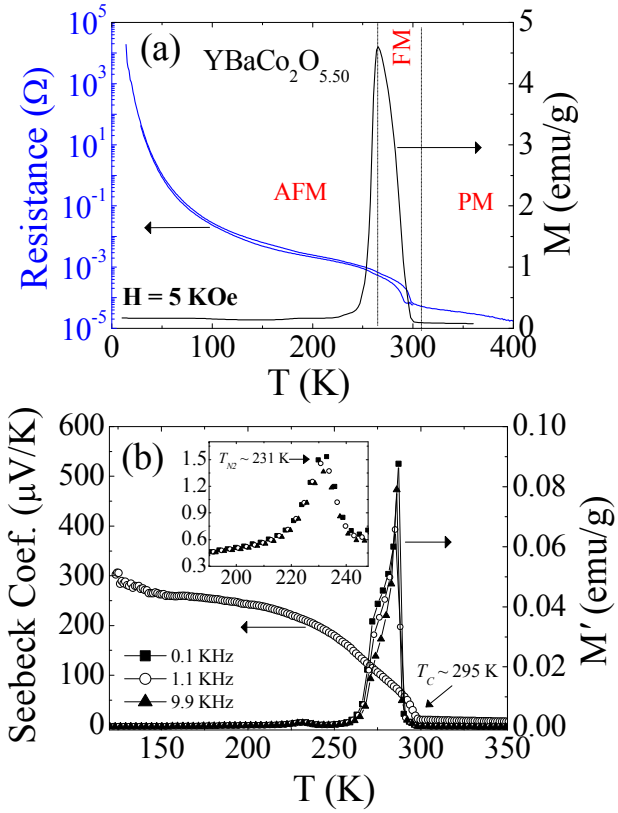

Figure 5. 11. (a) Temperature dependence of the dc resistivity (left axis) and dc magnetization measured under an applied field of 5 KOe (right axis) for the $YBaCoO_2O_{5.50}$ cobaltite where it is visible the three magnetic phases. (b) Temperature dependence of the Seebeck coefficient (left axis) and in-phase ac-magnetization (right axis) measured at different frequencies. The inset focuses on the second AFM transition at T_{N2} ~231 K.

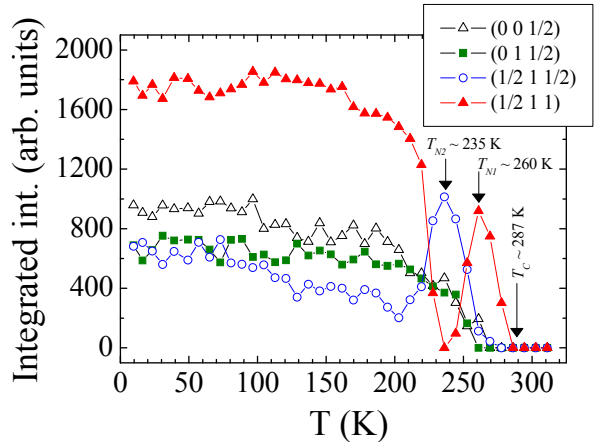

Figure 5. 12. Thermal evolution of the integrated intensity in the most intense magnetic peaks for $YBaCo_2O_{5.50}$. All reflections have been indexed according to a_0 x $2a_0$ x $2a_0$ cell.

5.5. Structural changes at the metal-insulator transition in $YBaCo_2O_{5.50}$

SXRPD patterns for $YBaCo_2O_{5.50}$ have been collected between 5 K and 350 K on the high resolution ID22 diffractometer at the ESRF (Grenoble). The data were recorded at the short wavelength of λ = 0.39978(25) Å. The left panel in Figure 5. 13 presents some selected experimental patterns collected in the temperature range from 320 K to 5 K. As can be appreciated, pattern collected starting from 290 K reveals a well-resolved splitting of (*h k l*) peaks with $h \neq 0$ and $k \neq 0$ such as the (1 2 0) reflection which transforms into (-120)-(120).

Moreover, the splitting is also observed in patterns collected at T = 270 K and 245 K as it has been also observed in a similar cobaltite $HoBaCo_2O_{5.50}$ [39]. However, on cooling the spontaneous splitting disappears at 210 K and it seems the structure come back into the RT phase. So, this behavior clearly indicates a first-order structural transition type.

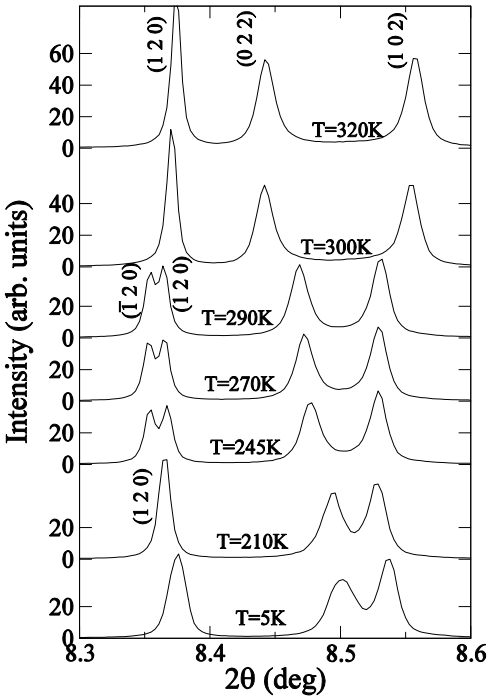

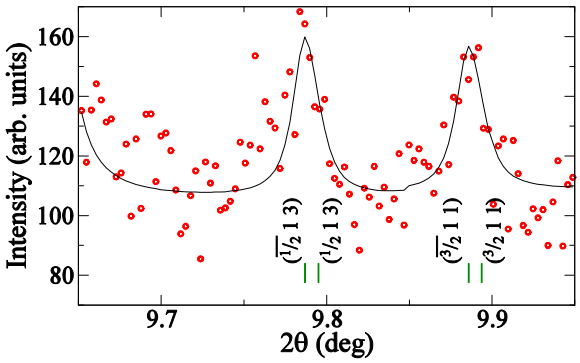

Figure 5. 13. (Left) Selected portion for the SXRPD measured at indicated temperatures. Diffraction patterns have been shifted up for clarity. (Right) Selected portion of the Rietveld refinement at 270 K. Reflections are indexed on the basis of the a_0 x $2a_0$ x $2a_0$ lattice.

Rietveld refinements have shown that the SXRPD patterns collected above RT can be refined using a single phase with a space group *Pmmm* (No. 47) with the standard a_0 x $2a_0$ x $2a_0$ lattice (where a_0 is the ideal cubic parameter), see Figure 5. 14(a). On the other hand, a suitable and complete description of the observed low-T structure has been obtained by using a

monoclinic symmetry. In the first attempt to solve the structure, we checked the monoclinic *P112/m* space group (No. 10) (and a_0 x $2a_0$ x $2a_0$ cell), reported in Ref. [39]. We obtained very good results (χ^2 = 4.0; R_B = 3.4 %), but we have carefully examined the diffractions patterns in the temperature range from 290 K to 245 K and we have observed a few tiny peaks in a small angle range (9.6º- 10º). So, we have proposed a new monoclinic S.G. *P112/a* (No. 13) with $2a_0$ x $2a_0$ x $2a_0$ lattice in which the obtained agreement parameters are almost identical to the first S.G. (χ^2 = 3.9; R_B = 3.4 %). Panel right in Figure 5. 13 displays the refined superstructures peaks at 270 K using the S.G. *P112/a* which evidences the doubling of the *a* cell parameter. The complete Rietveld refinement is shown in Figure 5. 14(b) at this selected temperature. The inset shows the good agreement between the simulated and the experimental diffraction pattern in the angle region where the monoclinic splitting is visible.

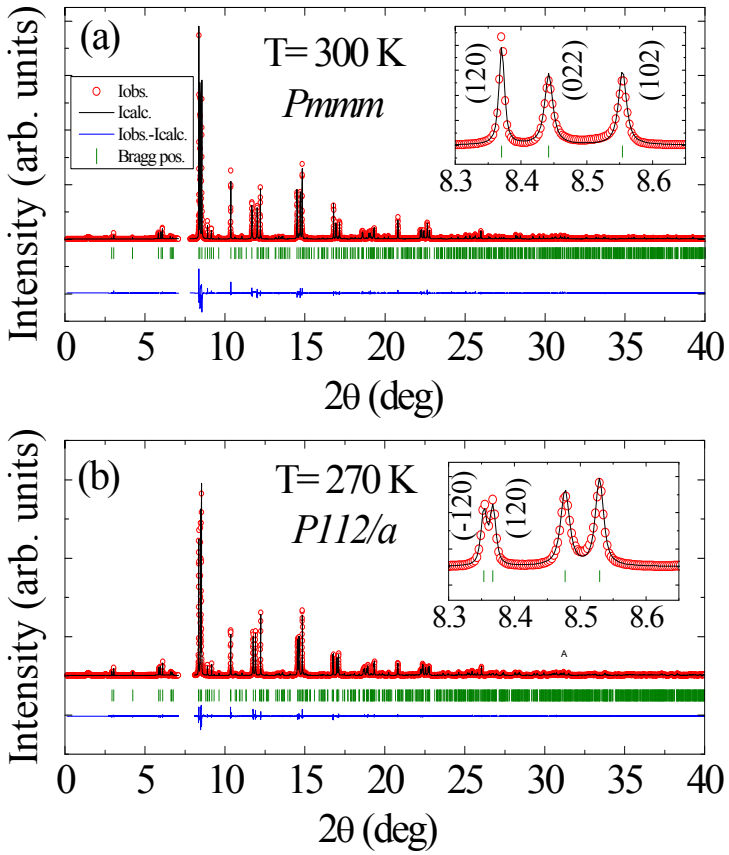

Figure 5. 14. SXRPD pattern of $YBaCo_2O_{5.50}$ refined by means of Rietveld refinement method (red circles, experimental points; blue line, difference; green symbols, Bragg positions) by assuming (a) an orthorhombic symmetry at 300 K and (b) a monoclinic symmetry at 270 K. The inset shows a selected portion of the Rietveld refinement at indicated temperatures. Reflections are indexed on the basis of the a_0 x $2a_0$ x $2a_0$ lattice.

Figure 5. 15(a) evidences that the observed splitting at 270 K can be refined by using a monoclinic cell ($\gamma = 90.09^{o}$, very close to 90^{o}) while it is not reproducible with an orthorhombic cell ($\gamma = 90^{o}$). So, it is well clear that two different structural transitions take place on cooling for $YBaCo_2O_{5.50}$, which can be described as a *Pmmm* $\rightarrow$ *P112/a* $\rightarrow$ *Pmmm* transformation. The interesting point is that, the first structural transition at $T_{S1} \sim 290$ K is concomitant to the PM $\rightarrow$ FM transition and the MIT for this compound unlike the compounds with large *Ln*. In addition, it should be note that the second structural transition between 245 K and 210 K (*P112/a* $\rightarrow$ *Pmmm*) occurs close to the second AFM magnetic transition ($T_{S2} = T_{N2} \sim 231$ K).

Figure 5. 15(b) displays a schematic view of the orthorhombic structure obtained from the Rietveld refinement at RT where it is possible to observe the different the sequence of $[CoO_2]$-[BaO]-$[CoO_2]$-$[YO_{0.5}]$ layers along the *c*-axis.

The spin-lattice coupling can be observed in the thermal evolution of the monoclinic angle together with the magnetic signal in Figure 5. 16(b). When the angle differs from 90^{o}, the FM phase takes place and on cooling, the monoclinic angle decrease up to 90^{o} during the AFM phase.

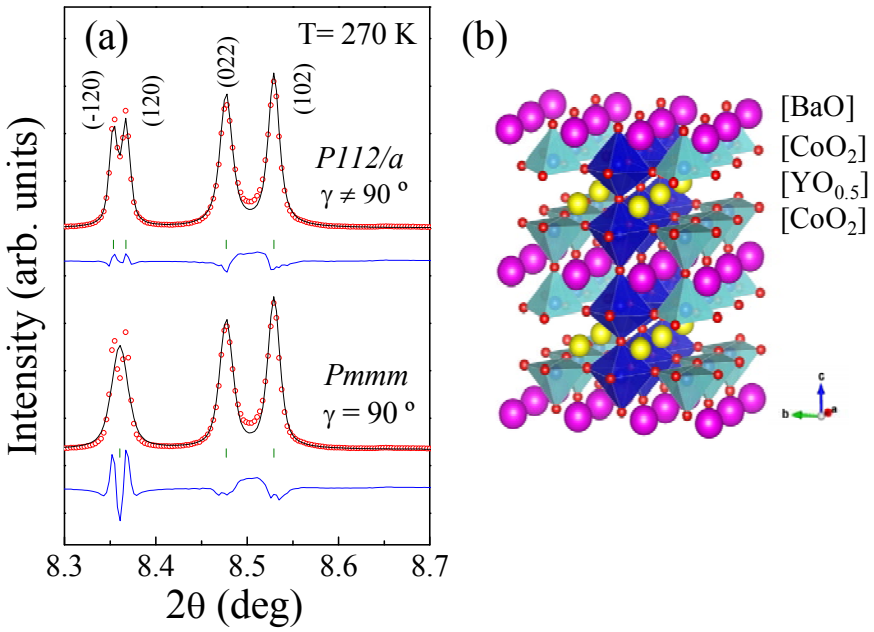

Figure 5. 15. (a) Selected portion of the Rietveld refinement of SXRPD pattern at 245 K by assuming a monoclinic phase (top) and an orthorhombic phase (bottom). (b) Schematic view of the orthorhombic perovskite structure of $YBaCo_2O_{5.50}$ where the sequence of $[CoO_2]$-[BaO]-$[CoO_2]$-$[YO_{0.5}]$ layers along the *c*-axis.

These structural changes are also observed in the thermal evolution of the cell parameters and the cell volume. Figure 5. 16(a) shows that on cooling the cell parameters suffer an abrupt change around 300 K, where *b* and *c* shrink and *a* increase at the same time. Moreover, it is observed that the cell volume enlarges when entering in the insulating phase (on cooling across T_{MI}). This behavior coincides with the reported $HoBaCo_2O_{5.50}$ but is opposite to that found for larger *Ln* (Pr, Gd, Tb, Nd…). However, the cell volume contracts on cooling when entering in the second AFM phase at T_{N2} ~ 231 K and the new orthorhombic phase.

Table 5. 1 and Table 5. 2 list the structural parameters and the agreement factors for the orthorhombic description at 300 K and the monoclinic description at 270 K, respectively.

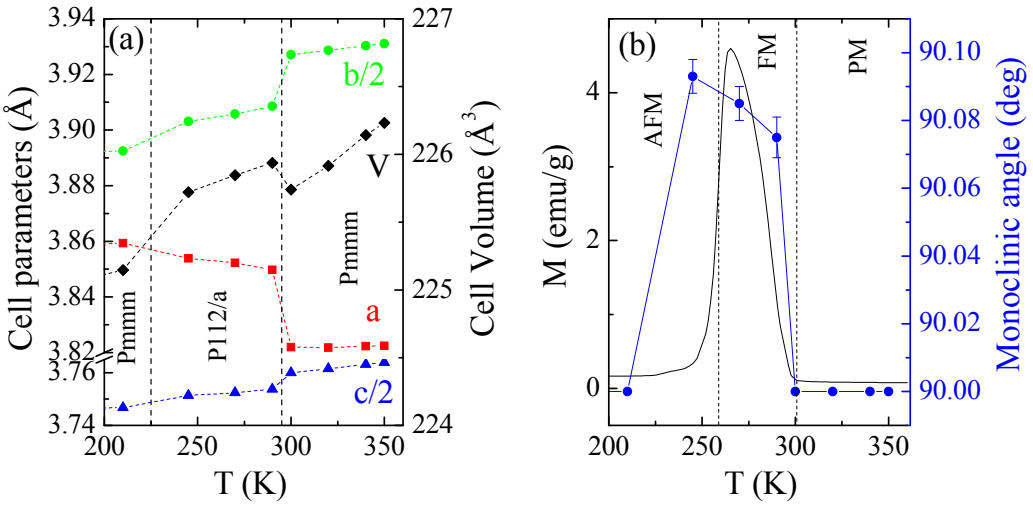

Figure 5. 16. (a) Evolution with temperature of cell parameters (left axis) and unit cell volume (right axis) obtained by Rietveld refinement of SXRPD patterns. Cell parameters are referred to of the a_0 x $2a_0$ x $2a_0$ setting.

Table 5. 1. Structure at 300 K refined using S.G. *Pmmm* (No. 47). Lattice parameters are a = 3.8219(1), b = 7.8545(2), c = 7.5198(1), and γ = 90.0º. Agreement parameters are χ^2 = 2.2 and R_B = 5.4%.

Atom	W. P.	*x/a*	*y/b*	*z/c*	$B_{iso.}$
Ba	*2o*	½	0.2487(11)	0	0.37(1)
Y	*2p*	½	0.2672(14)	½	0.45(2)
Co_{P1}	*2r*	0	½	0.2529(7)	0.25(3)
Co_{O1}	*2q*	0	0	0.2669(7)	0.25(3)
O1	*1a*	0	0	0	1.42(2)
O2	*1e*	0	½	0	1.42(2)
O3	*1c*	0	½	½	1.42(2)
O3*v**	*1g*	0	0	½	1.42(2)
O4	*2s*	½	0	0.3198(11)	0.59(2)
O5	*2t*	½	½	0.2791(12)	0.91(2)
O6	*4u*	0	0.2400(7)	0.2996(5)	0.39(2)

* It is the atomic parameter involving the oxygen vacant.

Table 5. 2. Structure at 270 K refined using S.G. *P112/a* (no. 13). Lattice parameters are a = 7.7046(1), b = 7.8120(1), c = 7.5052(1), and γ = 90.082º. Agreement parameters are χ^2 = 3.9 and R_B = 3.4%.

Atom	W. P.	*x/a*	*y/b*	*z/c*	$B_{iso.}$
Ba	*4g*	-0.0003(2)	0.2492(1)	-0.0010(5)	0.59(1)
Y	*4g*	0.0010(3)	0.2714(1)	0.4982(8)	0.73(2)
Co_{P1}	*2e*	¼	0	0.258(3)	0.5883)
Co_{P2}	*2e*	¼	0	0.743(3)	0.58(3)
Co_{O1}	*2f*	¼	½	0.249(3)	0.37(4)
Co_{O1}	*2f*	¼	½	0.743(3)	0.37(4)
O1	*2e*	¼	0	0.000(9)	1.3(2)
O2	*2f*	¼	½	0.000(9)	1.3(2)
O3*v*	*2f*	¼	½	0.500(9)	1.3(2)
O4	*4g*	-0.009(5)	0.014(5)	0.18(4)	0.8(2)
O5	*4g*	0.002(7)	0.488(5)	0.278(4)	0.8(2)
O6	*4g*	0.264(4)	0.235(5)	0.290(5)	0.8(2)
O7	*4g*	0.741(4)	0.244(5)	0.305(5)	0.8(2)

5.6. Competition between the orthorhombic-monoclinic phases at low temperature in $YBaCo_2O_{5.50}$

Following with the structural characterization detailed in the previous section, some extra diffraction data has been also recorded later from 300 K to 4.5 K, but including new temperatures inside the low temperature range (160 K-4.5 K). This new data were more carefully collected in ID22 using the same wave length but with temperature steps of about 10-20 K and waiting for temperature stabilization. We have commented in the previous section that below 245 K, the phase transforms again into an orthorhombic symmetry. The new measurements also reflect this effect, but on cooling below 55 K a new unexpected splitting of the same type-peaks [(*h k l*) reflections with $h \neq 0$ and $k \neq 0$] has been observed down to 4.5 K. This is the first evidence of a new splitting at low temperature in these cobaltites to the best of our knowledge. The evolution of the pattern diffractions are illustrated in Figure 5. 17(a, b), showing the splitting of (120) reflection below $T_{S3} \sim 55$ K. So, at low temperature we find a monoclinic phase *(P112/a*, doubling *a* lattice parameter) instead of an orthorhombic phase (*Pmmm*). The Rietveld refinements show that the crystal structure below $T < T_{S2}$ can be described by the coexistence of the orthorhombic-monoclinic phase but the majority phase in the different temperature ranges has been determined: (i) $T_{S3} < T < T_{S2}$, *Pmmm* symmetry, and (ii) $T < T_{S3}$, *P112/a* symmetry. To follow the evolution of both phases as a function of temperature, the weight fraction is plotted in Figure 5. 18(b). From these new data, we can conclude that three structural transitions are present for $YBaCo_2O_{5.50}$ on cooling: *Pmmm* $\rightarrow$ *P112/a* $\rightarrow$ *Pmmm* $\rightarrow$ *P112/a*. This reflects a competition with temperature between both symmetries.

The evolution of the cell parameters and the cell volume obtained in the Rietveld refinement of the new diffraction data between 200 K and 4.5 K exhibit an opposite evolution of the three cell parameters in this second *P112/a* $\rightarrow$ *Pmmm* transition at T_{S3} in front the first *P112/a* $\rightarrow$ *Pmmm* transition at $T_{S1.}$ At low temperature, *b* and *c* parameters lengthen, while *a* parameter shrinks across the structural transition. However, the cell volume increases on cooling as it happens when entering in the insulating phase at $T_{MI} \sim 295$ K from the metallic phase.

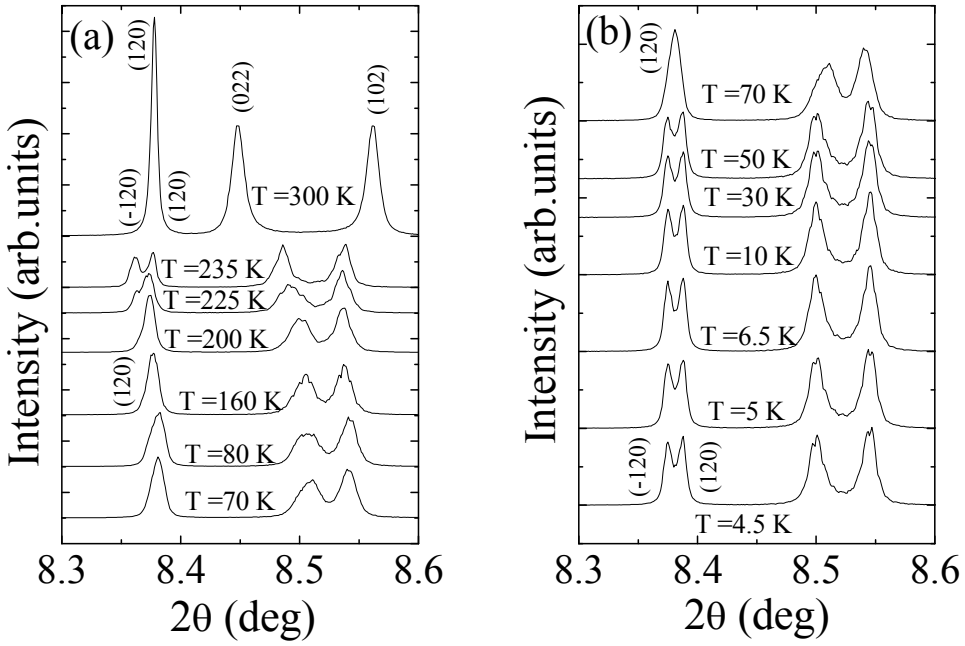

Figure 5. 17. Selected portion of the SXRPD as a function of temperature from 300 K to 5 K where it is visible the splitting of (*h k l*) peaks with $h \neq 0$ and $k \neq 0$. Diffraction patterns have been shifted up for clarity. Reflections are indexed on the basis of the a_0 x $2a_0$ x $2a_0$ lattice.

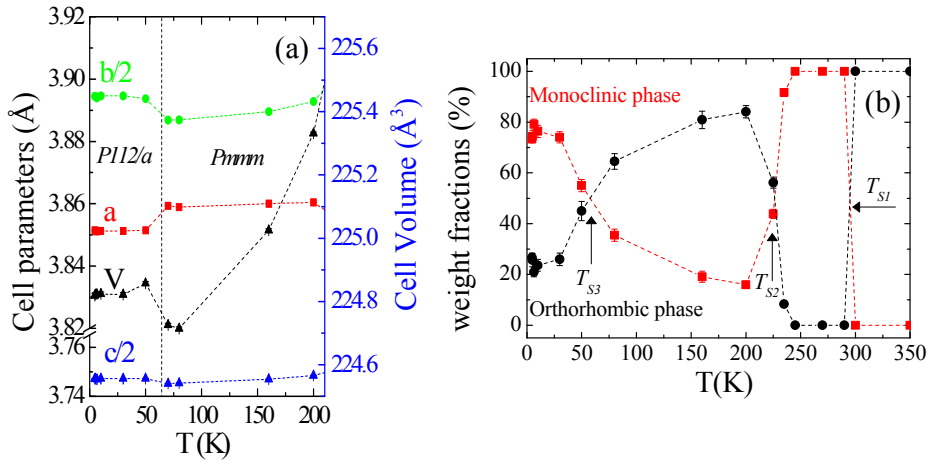

Figure 5. 18. (a) Evolution with temperature of cell parameters (left axis) and unit cell volume (right axis) obtained by Rietveld refinement of SXRPD patterns below 210 K. Cell parameters are referred to of the a_0 x $2a_0$ x $2a_0$ setting. (b) Thermal evolution of the weight fractions obtained by the Rietveld refinements for the two possible symmetries, monoclinic (red solid squares) and orthorhombic (black solid circles). The three transition temperature (T_{S1}, T_{S2}, T_{S3}) are indicated.

To summarize, we have elaborated a phase diagram as a function of the temperature for $YBaCo_2O_{5.50}$ using the physical and the structural properties observed along this work, see Figure 5. 19. On cooling we observe different features for this cobaltite:

(i) **$T > T_{S1} = 295$ K :** The sample is found in a metallic (M) and paramagnetic (PM) state. We have detected an orthorhombic (*Pmmm*) crystal structure with a_0 x $2a_0$ x $2a_0$ lattice.

(ii) **$T_{N1} = 260$ K $< T < T_{S1}$:** The sample changes to an insulator state (I) at T_{S1} = 295 K = T_C and at the same time becomes ferromagnetic (FM). In addition, we observe a change in the crystal structure from the SXRPD data in which the final phase is monoclinic (*P112/a*) with standard $2a_0$ x $2a_0$ x $2a_0$ lattice.

(iii) **$T_{N2}=T_{S2}=231$ K $< T < T_{N1}$** : The sample remains insulating, but we observe an AFM ordering (AFM1) from the magnetic measurements. However, in this temperature range the crystal structure remains in the same monoclinic symmetry.

(iv) **$T_{S3}= 55$ K $< T < T_{S2}$:** In this region a new AFM magnetic phase (AFM2) stabilizes and at the same time we found that the orthorhombic phase get back, but there is a coexistence of phases between the orthorhombic (majority) and the monoclinic (minority) structure.

(v) **$T < T_{S3}$:** The sample remains in the same magnetic and electric state, but there is a competition between both crystal structures. The recovery of the splitting of some peaks determines that the major phase is the monoclinic symmetry in this region.

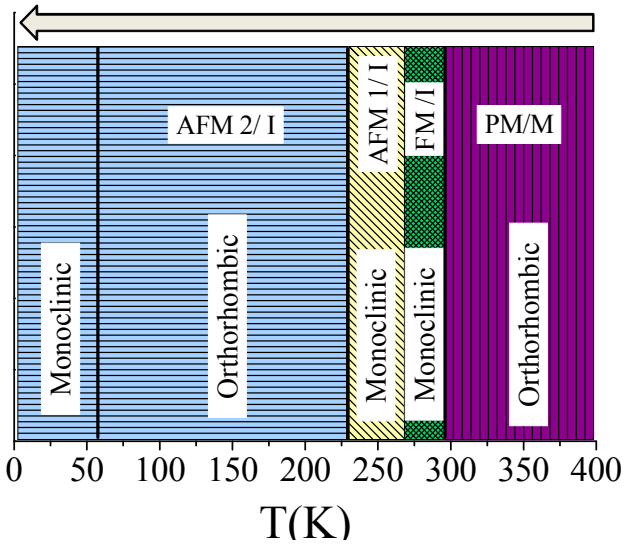

Figure 5. 19. Schematic phase diagram as a function of the temperature where it is possible to observe the evolution of the structure (*Pmmm* → *P112/a* → *Pmmm* → *P112/a*, on cooling) and the magnetic transition (PM → FM → AFM1 →AFM2) in $YBaCo_2O_{5.50}$

5.7. Investigation of the spin-state transition in $LnBaCo_2O_{5.50}$ (Ln= Pr, Gd, Y)

As it has been commented in Section 5.2.3 the origin of the metal-insulator transition in $LnBaCo_2O_{5.50}$ cobaltites is rather controversial. One of the most accepted mechanisms is a SS transition in the Co ions. However, the spin-state in the Co^{3+} ions in both octahedral (Co^{3+}_{oct}) and pyramidal (Co^{3+}_{pyr}) coordination is still a controversial issue. The contradictory scenarios that have been proposed include a full or partial LS→ IS or LS → HS state transition for the Co^{3+}_{oct} and an IS or HS stable configuration for the Co^{3+}_{pyr}. We have seen in the Introduction that there are only a few published spectroscopy works addressing the Co SS in these layered cobaltites with very different conclusions. As seen in Chapter 2, X-ray Absorption Spectroscopy (XAS) and X-ray Emission Spectroscopy (XES) are extremely sensitive, complementary techniques to probe the SS of transition metals, in particular $3d^6$ systems.

Therefore, we decided to combine them to study $YBaCo_2O_{5.50}$ (YBCO) and also other family systems such as $PrBaCo_2O_{5.5+\delta}$ (PBCO) and $GdBaCo_2O_{5.50}$ (GBCO). This has allowed us to correlate the SS changes with the *Ln* size. This comparison has been very helpful to ascertain the electronic configuration of these cobaltites.

5.7.1. XAS at the Co $L_{2,3}$ and O K edges

Firstly, we performed XAS at the Co $L_{2,3}$ edges ($2p \rightarrow 3d$ transitions) and the O K ($1s \rightarrow 2p$) edge between 200 K (temperature where all samples are in the insulating phase) and 370 K (temperature where almost all samples have crossed or are close to their MIT). As mentioned in Section 5.2.2., the T_{MI} shifts to low temperatures as the *Ln* radius size decreases: 370 K in PBCO, 340 K in GBCO, and 295 K in YBCO. Figure 5. 20 shows the evolution of the Co $L_{2,3}$ XAS spectra of $YBaCo_2O_{5.50}$ (the main studied compound in this chapter) as a function of temperature. The sharp and strong absorption features at 784 and 799 eV correspond to the M_5 and M_4 edges of Ba ($3d \rightarrow 4f$ transitions), respectively.

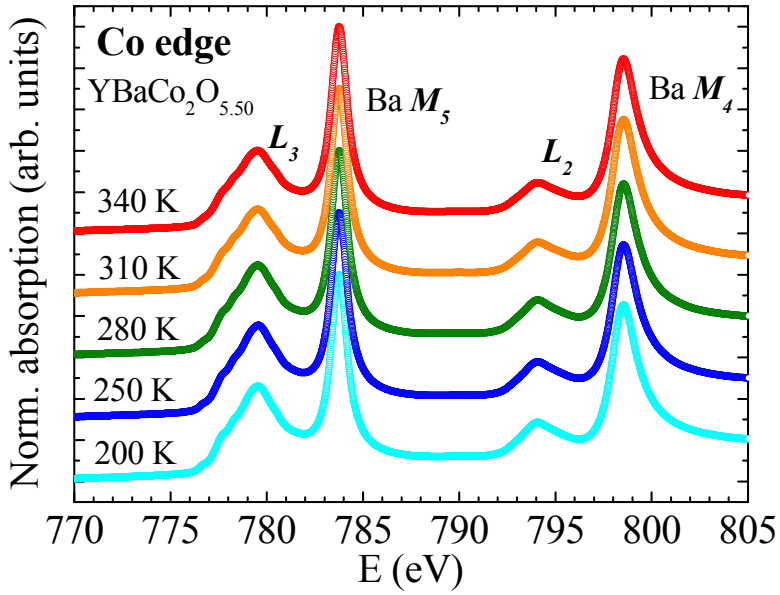

Figure 5. 20. Experimental Co $L_{2,3}$ XAS spectra as a function of temperature for $YBaCo_2O_{5.50}$. Spectra have been vertically shifted for clarity.

The XAS measurements here presented are similar to those earlier reported in Ref. [40–42], but with enhanced statistics: the set includes several temperatures across the MIT. As we can observe in the analysis of the complete spectrum, there are no appreciable changes in the whole temperature range studied which means that there is no relevant change in the filling of the Co 3*d* states. Nevertheless, a closer look at the L_3 edge as a function of temperature shows distinct features, which can be correlated with the SS changes. To facilitate it, we have compared the Co L_3 edge XAS measured at different temperatures for each system (PBCO, GBCO, and YBCO), as shown in Figure 5. 21(a, b, and c).

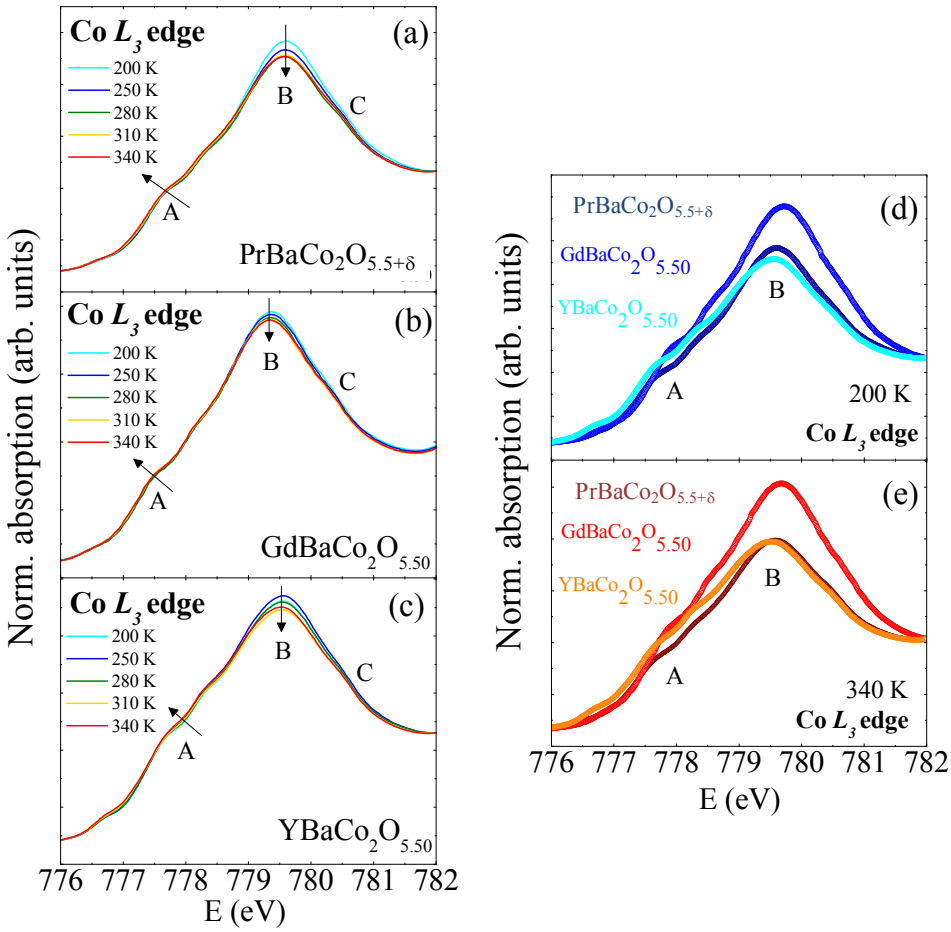

Figure 5. 21. Experimental Co L_3 XAS spectra as a function of temperature for (a) $PrBaCo_2O_{5.5+\delta}$; (b) $GdBaCo_2O_{5.50}$; and (c) $YBaCo_2O_{5.50}$. Comparison between the three cobaltites at (d) 200 K and (e) 340 K. Labels A, B and C mark features discussed in the text. The arrows indicate the evolution of the spectral intensity on increasing the temperature.

Starting from the largest *Ln* cation size, PBCO, we appreciate a shoulder (A) at the low-energy side (~ 778 eV) which gets more prominent and shifts to lower energies with the increase of the temperature. This is consistent with Co^{3+} ions in a dominant HS state at the octahedral sites. Moreover, this evolution is accompanied by a small drop of the intensity of peak B at the L_3 edge as the temperature increases. This trend tends to get stabilized when the temperature reaches 310 K. Another effect is also observed in feature C, which is the shoulder at the Co L_3 edge high-energy side (~ 780.5 eV). In this case, it shifts to low energies as the temperature increases. Similar variations are observed in the other two compounds studied, namely GBCO and YBCO. We should notice that the electronic structure of PBCO is not fully comparable with the other two samples because of the two effects early discussed in

Section 5.3. PBCO does not only contain Co^{3+}, but also a certain amount of Co^{4+} ions and some structural disorder: the octahedral sites are occupied by 80% octahedra and the other 20% by pyramids.

As a first conclusion from the previous results, we have found a modest SS variation in the Co $^{3+}$ ions with increasing temperature across the MIT which indicates that only a small number of LS Co^{3+} ions are changing into a HS state, in agreement with the results obtained by Z.Hu *et al.* in $GdBaCo_2O_{5.50}$. So, the common scenario in which a full LS $\rightarrow$ HS transition undergoes across the MIT can be rejected.

In order to complete the study about the nature of the SS in the family, we have also compared the Co L_3 edge spectra between the three systems at T < T_{MI} (200 K) and at T > T_{MI} (340 K), see Figure 5. 21(d, e). A 200 K the spectrum of YBCO is the most shifted to low energies, followed by the GBCO system, and PBCO. The same trend is observed in the 340 K data. Thus, this behavior is a strong indication that the SS in the smallest *Ln* cation-size compound is larger than in PBCO. Nevertheless, we have to take into account that due to the larger Co oxidation state ($Co^{3+\delta}$) in PBCO its XAS spectrum also shifts towards high energies. This effect makes difficult to compare it with the other two compounds, but the large A/B ratio in PBCO can be taken as a fingerprint of excited lower SS. So, we can be summarize as: $SS_{YBCO} \sim SS_{GBCO} > SS_{PBCO}$.

Another supporting data set in the analysis of the SS are the XAS measurements at the O *K* edge, which are also sensitive to the density of empty Co 3*d* t_{2g} and e_g states via hybridization to the O 2*p* states. The temperature evolution of the O *K* spectra for $YBaCo_2O_{5.50}$ is depicted in Figure 5. 22 together with the spectrum of $PrCoO_3$ at 10 K as a reference sample containing only Co^{3+} in a LS state (t_{2g}^6, *S*=0) in an octahedral environment. As we have done with the Co $L_{2,3}$ XAS spectra, we only show the complete data for the main studied compound, YBCO. Evaluating the pre-peak region (between 525 eV and 531 eV) and the comparison to $PrCoO_3$, we note the existence of a large density of 3*d* t_{2g}^{oct} empty states below T_{MI} = 295 K which indicates that a pure $Co^{3+}{}_{oct}$ LS is not expected in the insulating phase. The same interpretation can be applied for the other two systems (PBCO and GBCO) when the experimental O *K* edge is evaluated.

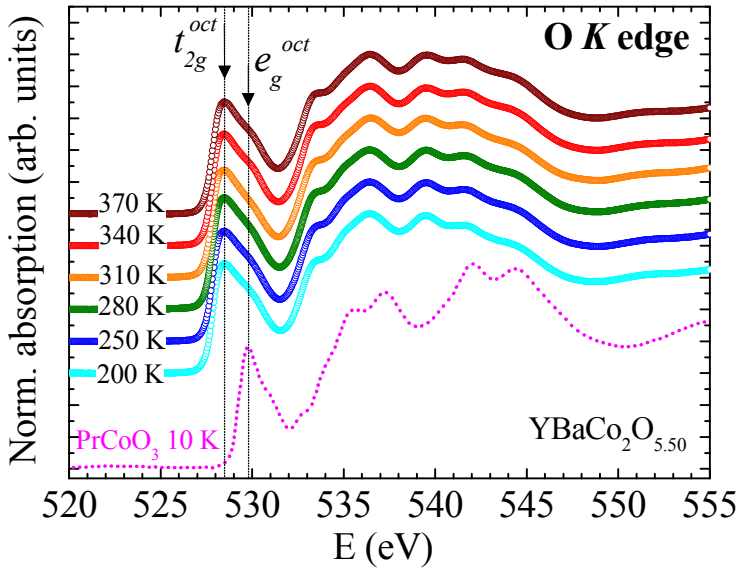

Figure 5. 22. Experimental O *K* XAS of $YBaCo_2O_{5.50}$ at different temperatures. The experimental spectrum of $PrCoO_3$ (pink dotted line) serves as a reference. The black dotted line indicates the energy of the t_{2g} and e_g states in octahedral sites.

So, the first conclusion extracted from these data reinforces the scenario of a LS:HS states mixture in the Co^{3+}_{oct} for the ground state in the $LnBaCo_2O_{5.50}$ series The possibility of having all Co^{3+}_{oct} in a LS state at low temperatures can be definitely discarded.

To shed more light to the SS transition, we have also plotted the pre-peak region of the O *K* edge measured at 200 K and 370 K for each system as Figure 5. 23(a,b,c) displays. We observe that as the temperature increases, in the three compounds, there is a transfer of spectral weight from the higher energy peak ~ 529.8 eV (unoccupied e_g^{oct} states, green arrow) to the lower energy peak ~ 528.5 eV (unoccupied t_{2g}^{oct} states, red arrow), and this is accompanied by a spectral energy shift to lower energies of the spectrum at 370 K. A similar transfer has been observed in $LaCoO_3$ and $PrCoO_3$ (as shown in Chapter 3) which is an additional support to the presence of a partial spin state transition involving Co^{3+}_{oct} ions. The comparison between the three systems allows us to establish that the release of the 3*d* states with t_{2g} symmetry is largest for the largest *Ln* cation size compound, PBCO. However, as we have mentioned for the Co $L_{2,3}$ edges this compound is not fully comparable with the other two systems. We also observe here that the pre-peak position is at ~ 528 eV, while for the other two is at ~ 528.5 eV, indicating that PBCO is more oxidized. The changes observed in GBCO and YBCO with temperature go in the same direction, but the overall variations are slightly larger for GBCO. The evolution at the O *K* pre-edge XAS appears clearer when the first derivative is calculated.

The partial transition of Co^{3+}_{oct} ions in LS+HS states into a predominance of HS states at $T > T_{MI}$ produces shift in the main peak of the first derivative of the O *K* edge XAS to low energies as the temperature increases. This can be determined by looking at the spectral centroid (the center of mass of the peak). The evolution is plotted in Figure 5. 23(d,e,f), where the metallic and the insulating phases have been delimited.

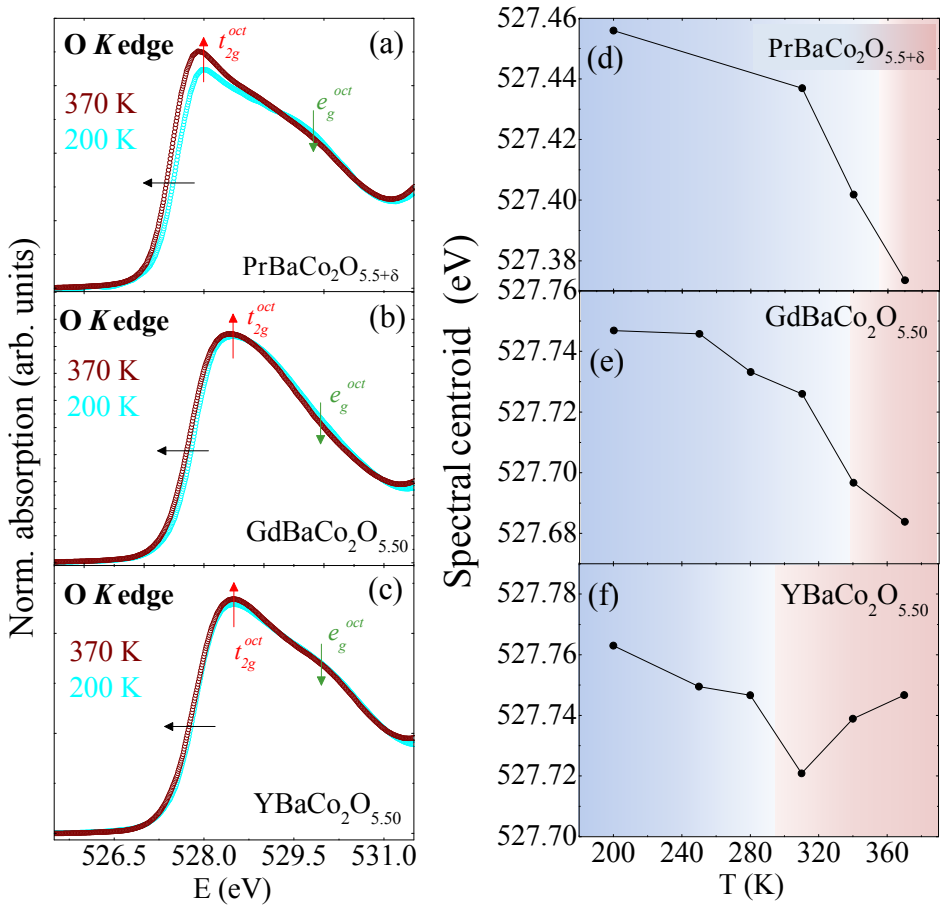

Figure 5. 23. Experimental O *K* XAS spectra at 200 K (blue circles) and 370 K (red circles) for (a) $PrBaCo_2O_{5.5+\delta}$, (b) $GdBaCo_2O_{5.50}$, and (c) $YBaCo_2O_{5.50}$. The black arrows indicate the evolution of the pre-peak edge on increasing the temperature and the red and green arrows indicate that of the empty t_{2g}^{oct} and e_g^{oct} states, respectively. (d), (e) and (f) show the temperature evolution of the calculated spectral centroid of the first derivative curve of the O *K* edge. The blue zone corresponds to the insulating phase and the red zone to the metallic phase.

The thermal evolution of the spectral centroid of the first derivative curve of the O *K* edge leads us to confirm that the SS evolution is monotonous with the temperature for all compounds. This means, there is a thermal electron promotion from t_{2g} to e_g orbitals which

indicates a large density of excited states in comparison to the ground state at low temperature. However, in the case of the Y-based cobaltite (where the MIT occurs at lower temperature) there is a minimum in the evolution of the spectral centroid [Figure 5. 23(f)] just when crossing the MIT (around 310 K), indicating a pronounced LS+HS $\rightarrow$ HS transition. But, the trend reverses at T< 310 K. This unexpected evolution is an evidence that the SS enhances up to the MIT, but when entering in the metallic regime the filling rate of excited states seems to be reduced, as if the SS got stabilized at T > T_{MI}. In the other compounds, this effect is not probably observable due to limitations in the experimentally accessible thermal region which did not completely cover the MIT in the Pr and Gd-based cobaltites.

In order to go further in the study of the electronic configuration of the Co^{3+} ions in the double-layered cobaltites, in Figure 5. 24 we have plotted the comparison between the experimental O *K* edge XAS difference spectra for $YBaCo_2O_{5.50}$ in different temperature ranges, as compared to the experimental O *K* edge spectrum for $PrCoO_3$ at 10 K, and the calculated unoccupied Co 3*d*-O 2*p* states partial density of states (DOS) in a pyramidal coordination (digitalized from Ref. [45]). It should be noticed that in the calculated unoccupied Co 3*d*-O 2*p* DOS, the lower energy structure at 528.5 eV consists of the unoccupied t_{2g} (dashed line) and the shoulder at 530.6eV corresponds to the x^2-y^2 levels (dotted line). On the other hand, the unoccupied $3z^2$-r^2 level (dash-dotted line) is pulled down to 1.6 eV from the x^2-y^2 and appears close to the unoccupied t_{2g} because of the missing apical oxygen in the CoO_5 coordination [45]. We focus in the Y-based cobaltite because it is the main studied compound in this chapter. The corresponding description for the other two compounds will be compiled in a future publication.

The total difference between the XAS spectra at 370 K and 200 K, which corresponds to the comparison between the metallic and insulating phases, reveals different positive shoulders due to the release of electronic density from different symmetry states. The first main peak at ~ 527.7 eV corresponds to the energy of t_{2g} levels in CoO_6 coordination, while the shoulder close to it at a higher energy (~ 528.5 eV) is related to the t_{2g} levels in CoO_5 coordination. On the other hand, a small negative shoulder is observed at 530.5 eV which indicates an occupation process of x^2-y^2 levels. So, this result suggests that in this extended temperature range there is a transfer of electrons from the t_{2g} to e_g states in the octahedrally-coordinated Co^{3+} ions and also in the Co^{3+} ions with pyramidal coordination. Said otherwise, these points to the existence of a SS transition that comprehends both all of Co ions in the cell, in contrast to the previously proposed variation of the electronic configuration only in the octahedrally-coordinated Co ions.

Let us now analyze the difference spectra for the different temperature intervals from bottom to top:

(1) 250 K-200 K spectra (insulating regime): a positive shoulder signals an inoccupation in t_{2g}^{oct} and t_{2g}^{pyr} orbitals. We ascribe these variations to thermal activations not because to a real SS transition. This evolution seems to be larger at octahedral sites.

(2) 340 K-280 K (across MIT): there are small variations compatible with a steady increase of the SS similarly as in (1), but the excitation rate is considerably reduced. The low lying $3z^2$-r^2 e_g orbital in piramidally coordinated Co ions gets populated.

(3) 370 K-310 K (metallic regime): the scenario is now completely different. There is a large deexcitation of Co 3*d* electrons at octahedral sites, which repopulate low energy t_{2g}^{oct} orbitals. The evolution is not that clear in Co^{3+}_{pyr}, but looking at the energy that corresponds to t_{2g}^{pyr} it seems that they are not that much affected. It is interesting to note that this interval coincides with the reversal spectral centroid position shown in Figure 5.23(f) when entering in the metallic phase.

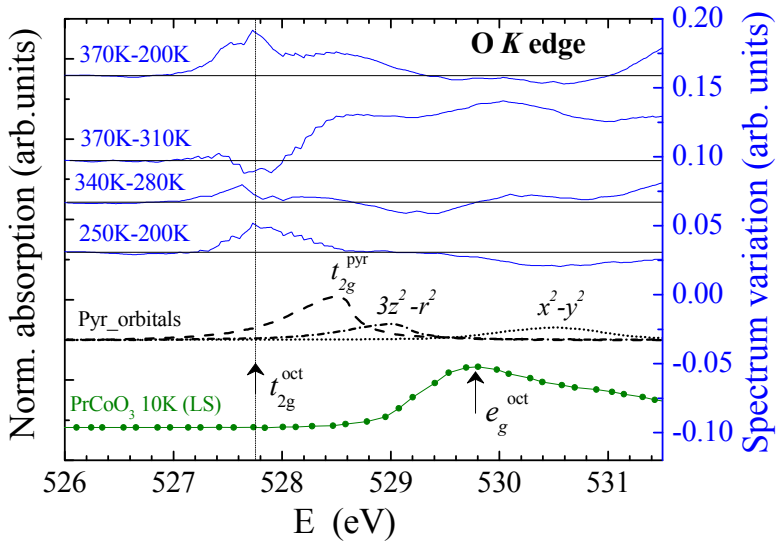

Figure 5. 24. Bottom to top: experimental O *K* XAS spectra of $PrCoO_3$ at 10 K (green curve); the dashed, dash-dotted, and dotted lines correspond to the unoccupied Co 3*d*-O 2*p* DOS calculations for the t^2_g, $3z^2$-r^2, and x^2-y^2 states, respectively, in a pyramidal coordination [45]; experimental O *K* XAS difference in $YBaCo_2O_{5.50}$ at different temperature ranges (blue curves).

It is now interesting to extend the main conclusions extracted for YBCO to the other two family compounds. In Figure 5. 25 we have plotted the experimental O *K* preedge XAS difference for the three compounds between 370 K and 200 K. Here, we observe that the largest changes are happening in the largest *Ln* cation size compound, PBCO, followed by GBCO, and finally the smallest *Ln*-based specimen, YBCO.

This allows to correlate the temperature-induced increment of Co ions in an excited electronic configuration with the size of the *Ln* ion radius ($\Delta SS_{PBCO} > \Delta SS_{GBCO} > \Delta SS_{YBCO}$). We also see that the difference spectrum of PBCO is slightly shifted to low energies, which is coherent with an excess of oxygen, i.e. $PrBaCo_2O_{5.5+\delta}$. As we previously commented, we should here find an unequal distribution of Co^{3+} ions in CoO_6 and CoO_5 coordination, namely a larger presence of octahedra. In any case, the three compounds show a similar electronic filling evolution when increasing temperature. There is a clear release of 3*d* states with t_{2g}^{oct} symmetry concomitant to the occupation of e_g^{oct} states, which leads to a higher spin-state. The O *K* preedge XAS pointed to a mixed LS:HS state in the Co^{3+}_{oct} for the ground state. Now, the difference curves in Figure 5. 25 reveal that this ratio is variable and evolves towards dominancy of the HS state at high temperatures. On the other hand, an inspection of the same figure at the energies corresponding to the orbitals with CoO_5 coordination indicates an occupation transfer from the t_{2g}^{pyr} into e_g^{pyr} states for the Y-based compound. This is a strong indication that in the smaller cobaltite (at least) the SS changes have a pyramidal contribution and not only the Co^{3+}_{oct} ions are changing. Our observations in YBCO are the first direct evidence that the Co^{3+}_{pyr} ions are also changing their SS across the MIT. Since the most accepted scenario for these Co ions is an IS configuration at $T < T_{MI}$ [9, 12, 36, 37], we assume that they get partially promoted into a HS configuration.

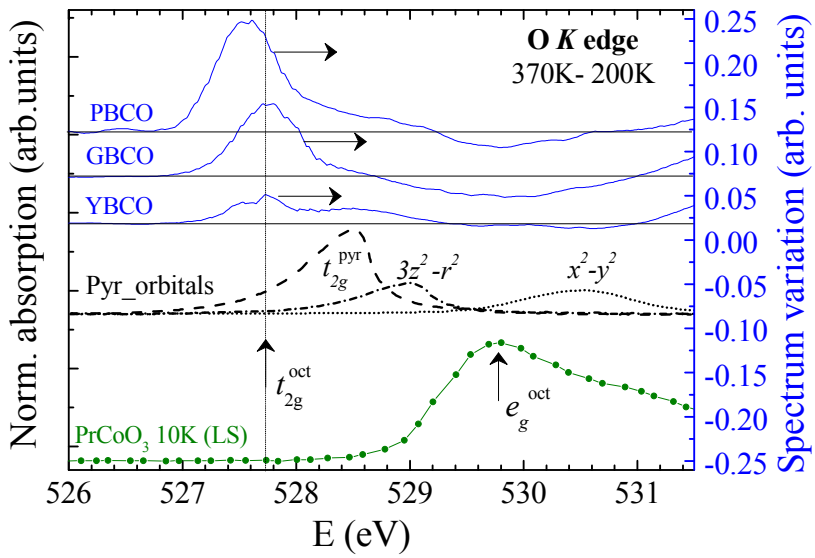

Figure 5. 25. Bottom to top: experimental O *K* XAS spectra of $PrCoO_3$ at 10 K (green curve), the LDA+ U calculations for the 2*p*-hybridized 3*d* t^2_g (dashed lines), $3z^2$-r^2 (dash-dotted lines), and x^2-y^2 (dotted lines)states, in a pyramidal coordination; experimental O *K* XAS difference between 370 K and 200 K for $PrBaCo_2O_{5.50}$, $GdBaCo_2O_{5.50}$ and $YBaCo_2O_{5.50}$ (blue curves).

5.7.2. $K\beta$ X-ray emission lines

As we did for the $LnCoO_3$ and $Pr_{0.50}Sr_{0.50}CoO_3$ compounds studied in this thesis, we decided to perform 1*s*3*p* nonresonant X-ray Emission Spectroscopy (XES) on the $LnBaCo_2O_{5.50}$ cobaltites with the aim to determine the effective Co spin and possible SS transitions. Since XES provides information about the effective number of unpaired 3*d* electrons, it becomes a complementary technique to XAS (see Section 2.5.3. in Chapter 2 for more information). The experimental data from polycrystalline samples of $PrBaCo_2O_{5.50}$, $GdBaCo_2O_{5.50}$, and $YBaCo_2O_{5.50}$ were recorded at the ID26 beamline of the ESRF at two different temperatures (150 K and 300 K). At the same time $PrCoO_3$ at 20 K (t_{2g}^6, S=0) and $LaMn_{0.98}Co_{0.02}O_3$, the latter only contains Co^{2+} in a HS state (t_{2g}^5 e_g^2, S=3/2) [46], were also measured as a reference compound. Figure 5. 26 summarizes the results.

The comparison of the shape and the position of the different spectra for the three samples with the references compounds allows us to determine that: (i) all $LnBaCo_2O_{5.50}$ samples are more spin polarized than $PrCoO_3$, regardless of temperature, (ii) the double-layered cobaltites are less spin polarized (S < 3/2) than $LaMn_{0.98}Co_{0.02}O_3$, and (iii) there is a slight variation of the effective spin in the $LnBaCo_2O_{5.50}$ samples between 150 K and 300 K. We should notice that room temperature measurements are insufficient to permit the analysis of the MIT, since it occurs at higher temperatures in PBCO and GBCO, and at 295 K in YBCO.

The XES measurements taken at 300 K are thus a limitation to observe changes resulting from a possible SS transition coupled to the MIT. Then, the small observed variations between 150 K and 300 K should be considered as thermal excitations from t_{2g} to e_g states.

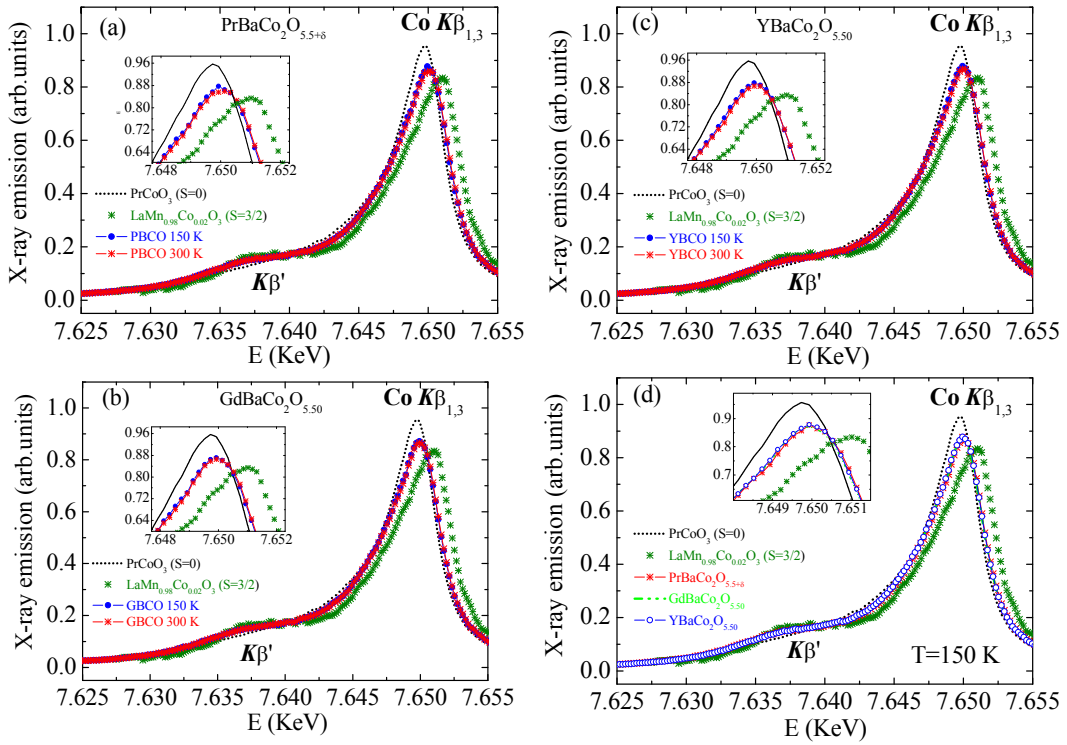

Figure 5. 26. Co *K*β main emission lines from polycrystalline samples of $LnBaCo_2O_{5.50}$ at 150 K and 300 K for (a) *Ln*=Pr, (b) *Ln*=Gd, and (c) *Ln*=Y; (d) comparison between the three compounds at 150 K. The spectra from $PrCoO_3$ (dotted black line) and $LaMn_{0.98}Co_{0.02}Co_3$ (data digitalized from Ref. [46]) are shown for comparison. The inset shows the maxima of the $K\beta_{1,3}$ peak.

After the qualitative inspection of the experimental spectra, we follow the procedure already presented in Chapter 3 to quantify the spectral changes by means of the integrals of the absolute values of the difference spectra (IAD). The results are shown in Figure 5. 27, added to the experimental points obtained from the previously studied cobaltites: $PrCoO_3$, $LaCoO_3$, $Pr_{0.50}Ca_{0.50}CoO_3$, and $Pr_{0.50}Sr_{0.50}CoO_3$. This leads to S=1.17, 0.99, and 0.97 for the Pr, Gd and Y-based cobaltite at 150 K, respectively. These values increase up S=1.26, 1.1, and 1.06 at 300 K. Surprisingly, the variation of the effective spin between 150 K and 300 K is almost identical for the three compounds: ΔS_{PBCO}= 0.09, ΔS_{GSCO}= 0.11, and ΔS_{YBCO}= 0.09.

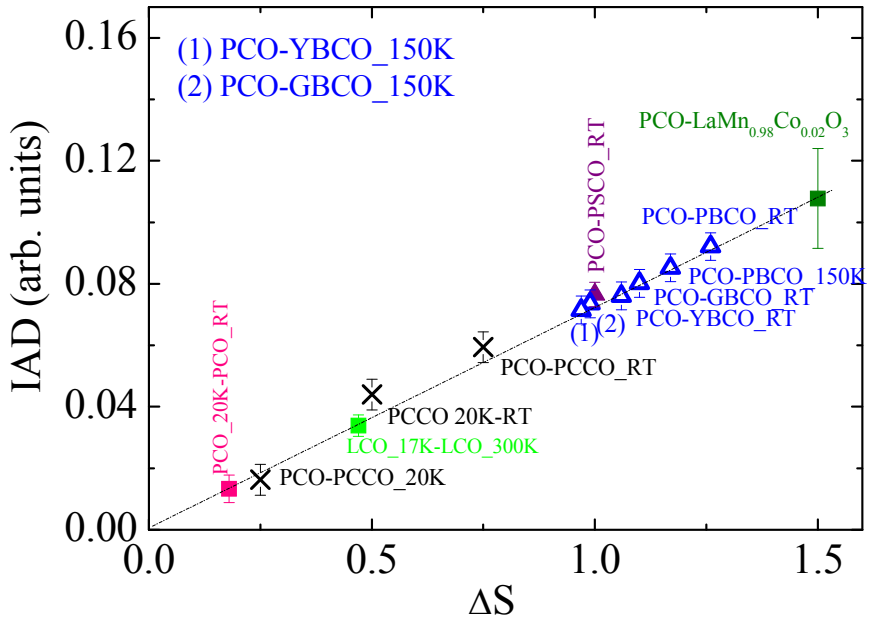

Figure 5. 27. Integrals of the absolute values of the difference spectra (IAD) for the Co *K*β main emission lines from polycrystalline samples with *Ln*=Pr, Gd, and Y (blue empty triangles). All other experimental points are extracted from Chapters 3 and 4: PrCoO3 (PCO), $LaCoO_3$ (LCO), $Pr_{0.50}Ca_{0.50}CoO_3$ (PCCO) and $Pr_{0.50}Sr_{0.50}CoO_3$ (PSCO).

At this point, we can build a possible scenario or model for the electronic configuration of these $LnBaCo_2O_{5.50}$ cobaltites considering the effective spin derived from the XES and the XAS results of this, and previous studies found in the literature. The most recent work on these double-layered perovskites was done by Z. Hu and coworkers [42] on a single crystal of $GdBaCo_2O_{5.50}$. After the analysis of experimental and calculated XAS spectra at the Co $L_{2,3}$ and O *K*-edges, they claimed a scenario where half of the Co^{3+} ions at the octahedral sites are in the LS state and the other half in the HS state, while the Co^{3+} ions at the pyramidal sites are in the HS configuration at low temperatures. Then, upon increasing temperature across the MIT, part of the octahedral Co^{3+} LS ions transform into the HS state. Although this scenario seems plausible, it is incompatible with our XES results. While, the Z. Hu *et al.* [42] model is based on an average *S*=1.5 value at 78 K for $GdBaCo_2O_{5.50}$, we have obtained S= 0.99 for the same compound also in the insulating region (150 K). Considering the very similar *S* value for YBCO at the same temperature, we can contemplate the following standard *S*=1 model for both GBCO and YBCO: Co^{3+} ions at octahedral sites in a 1:1 mixture of LS and HS states, and half of the Co^{3+} ions at pyramidal sites in an IS state, i.e. Co_{oct} LS:HS (1:1) +Co_{pyr} IS. Our XES

measurements simply do not support the piramidally-coordinated Co^{3+} ions in to be in the HS state in $GdBaCo_2O_{5.50}$ and $YBaCo_2O_{5.50}$.

5.8. Summary and conclusions

Along this chapter we have investigated the structural changes and physical properties of the double-layered $LnBaCo_2O_{5.50}$ family of compounds, focusing on the $YBaCo_2O_{5.50}$ cobaltite. This compound and the previously reported in the literature $HoBaCo_2O_{5.50}$ are the unique two known cases where the MIT coincides with the onset of the FM phase. In the case of the Y-based cobaltite $T_C = T_{MI} = 295$ K, exhibiting three successive magnetic transitions of the type PM $\rightarrow$ FM $\rightarrow$ AFM1 $\rightarrow$ AFM2 upon cooling. We have performed SXRPD to solve the crystal symmetry in this cobaltite, enabling the detection of the (*h k l*) peaks splitting with $h \neq 0$ and $k \neq 0$, and superstructure reflections. We have found three different structural transitions on cooling, which follow the *Pmmm* $\rightarrow$ *P112/a* $\rightarrow$ *Pmmm* $\rightarrow$ *P112/a* sequence. We have found that the evolution of the YBCO unit-cell volume is opposite to the large rare-earths case as it expands when cooling across the MIT, in agreement with the Ho case. In addition, the different structural transition temperatures coincide with the temperatures where the magnetic transitions take place. For temperatures below 200 K we have observed a competition between the orthorhombic and monoclinic phases; while the first one is majority at $55 < T < 231$ K, the latter dominates at $T \leq 55$ K.

One of the main mechanisms proposed in the literature for the MIT is a SS transition, in which the SS of Co^{3+} ions at the octahedral sites would change from HS to LS state. Meanwhile Co^{3+} ions at the pyramidal sites would remain in an IS state. In order to address this problem we have performed XAS and XES measurements. The analysis at the Co $L_{2,3}$ and O *K* edges reveals a modest SS evolution in the Co $^{3+}$ ions with increasing temperature across the MIT that indicates that only a small number of Co^{3+} LS ions are changing into a excited state. In addition, the large density of $3d\ t_{2g}{}^{oct}$ empty states indicates that a pure $Co^{3+}{}_{oct}$ LS state is not possible in the insulating phase. So, the simple scenario of a full LS $\rightarrow$ HS transition across the MIT can be rejected. The existence of mixed LS:HS states for $Co^{3+}{}_{oct}$ in the ground state of $LnBaCo_2O_{5.50}$ compounds that we propose agrees with the conclusions by Z. Hu *et al*. [42]. The deeper spectroscopic analysis here presented for the Y-based cobaltite evidences that not only the variations in the SS are ascribed to an octahedral coordination, but there is also a certain evolution in the electronic configuration of the Co^{3+} ions with O_5 coordination.

The comparison of XAS spectra with other compounds like $PrBaCo_2O_{5.5+\delta}$ and $GdBaCo_2O_{5.50}$, suggests that the average SS is larger in the small *Ln* cation size compounds and so $SS_{YBCO} \sim SS_{GBCO} > SS_{PBCO}$. However, the XAS spectra of PBCO are not fully comparable with those of the other two samples because of the different stoichiometry; the oxygen content in PBCO is slightly larger, leading to the appearance of Co^{4+} ions and also some disorder in the coordination (the octahedral sites are occupied by a 80% of octahedra and a 20% of pyramids).

On the other hand, a quantitative measure of the effective spin has been deduced for all compounds from XES measurements, confirming comparables small variations between 150 K and 300 K and a direct correlation of the average S with the *Ln* ion radius: $S_{PBCO} > S_{GBCO} > S_{YBCO}$. This had led us to propose a new electronic model for the $YBaCo_2O_{5.50}$ cobaltite: based on a LS:HS mixed state for Co^{3+}_{oct} ions and Co^{3+}_{pyr} in an IS state.

Finally, we note inconsistency arising between the XAS and XES results in the correlation of the SS as function of the *Ln* cation-size, that we believe to be related with the different probe-depth of the employed spectroscopic techniques. The soft XAS measurements were performed by TEY, highly surface sensitive, in contrast to the bulk-sensitive hard XES measurements. A gradient in the oxygen content with depth is likely to occur in $LnBaCoO_2O_{5.5}$, particularly in the oxygen-excess Pr-based cobaltite.

BIBLIOGRAPHY

[1] C. Martin, a. Maignan, D. Pelloquin, N. Nguyen, and B. Raveau, "Magnetoresistance in the oxygen deficient *Ln*$BaCo_2O_{5.4}$ (*Ln*=Eu, Gd) phases," *Appl. Phys. Lett.*, vol. 71, no 10, p. 1421, 1997.

[2] A. Podlesnyak, K. Conder, E. Pomjakushina, and A. Mirmelstein, "Layered Cobalt Perovskites: Current Topics and Future Promises," *Chem.Inform*, vol. 39, no. 40, 2008.

[3] B. Raveau and M. Motin Seikh, *Cobalt oxides. From Crystal Chemistry to Physics*. WILEY-VCH, 2012.

[4] N. B. Ivanova, S. G. Ovchinnikov, M. M. Korshunov, I. M. Eremin, and N. V. Kazak, "Specific features of spin, charge, and orbital ordering in cobaltites," *Uspekhi Fiz. Nauk*, vol. 52, pp. 789–810, 2009.

[5] Y. P. Chernenkov, V. P. Plakhty, V. I. Fedorov, S. N. Barilo, S. V. Shiryaev, and G. L. Bychkov, "X-ray Diffraction Study of Superstructure in $GdBaCo_2O_{5.5}$," *Phys. Rev. B.*, vol. 71, no.184105, p. 4, 2004.

[6] V. P. Plakhty, Y. P. Chernenkov, S. N. Barilo, a. Podlesnyak, E. Pomjakushina, D. D. Khalyavin, E. V. Moskvin, and S. V. Gavrilov, "Spin structure and magnetic phase transitions in $TbBaCo_2O_{5.5}$," *Phys. Rev. B.*, vol. 71, no. 214407,p. 13, 2004.

[7] D. D. Khalyavin, "Magnetic ground state of *Ln*$BaCo_2O_{5.5/5.44}$ cobalt oxides," *Phys. Rev. B.*, vol. 72, no. 134408, 2005.

[8] O. T. Chang, *Frontal semiconductor research*. 2006, pp. 171–209.

[9] A. Maignan, C. Martin, D. Pelloquin, N. Nguyen, and B. Raveau, "Structural and Magnetic Studies of Ordered Oxygen-Deficient Perovskites *Ln*$BaCo_2O_{5+\delta}$, Closely Related to the '112' Structure," *J. Solid State Chem.*, vol. 142, pp. 247–260, 1999.

[10] C. Frontera, J. L. García-Muñoz, A. E. Carrillo, C. Ritter, D. Martín Y Marero, and A. Caneiro, "Structural and magnetic study of $PrBaCo_2O_{5+\delta}$ (δ =0.75) cobaltite," *Phys. Rev. B.*, vol. 70, no. 184428, pp. 1–9, 2004.

[11] S. Streule, A. Podlesnyak, D. Sheptyakov, E. Pomjakushina, M. Stingaciu, K. Conder, M. Medarde, M. V. Patrakeev, I. A. Leonidov, V. L. Kozhevnikov, and J. Mesot, "High-temperature order-disorder transition and polaronic conductivity in $PrBaCo_2 O_{5.48}$" *Phys. Rev. B.*, vol. 73, no. 094203pp. 3–7, 2006.

[12] C. Frontera, J. García-Muñoz, A. Llobet, and M. Aranda, "Selective spin-state switch and metal-insulator transition in $GdBaCo_2O_{5.5}$," *Phys. Rev. B.*, vol. 65, no. 180405(R), pp. 3–6, 2002.

[13] Y. Moritomo, T. Akimoto, M. Takeo, A. Machida, E. Nishibori, M. Takata, M. Sakata, K. Ohoyama, and A. Nakamura, "Metal-insulator transition induced by a spin-state transition in $TbBaCo_2O_{5+\delta}$ (δ=0.5)," *Phys. Rev. B.*, vol. 61, no. 20, pp. R13325–R13328, 2000.

[14] D. D. Khalyavin, D. N. Argyriou, U. Amann, A. A. Yaremchenko, and V. V. Kharton, "Spin-state ordering and magnetic structures in the cobaltites $YBaCo_2O_{5+\delta}$ (δ=0.50 and 0.44)," *Phys. Rev. B.,* vol. 75, no. 134407, pp. 1–15, 2007.

[15] D. Akahoshi and Y. Ueda, "Oxygen Nonstoichiometry, Structures, and Physical Properties of $YBaCo_2O_{5+x}$ ($0.00<x<0.52$)," *J. Solid State Chem.*, vol. 156, pp. 355–363, 2001.

[16] S. Roy, I. S. Dubenko, M. Khan, E. M. Condon, J. Craig, N. Ali, W. Liu, and B. S. Mitchell, "Magnetic properties of perovskite-derived air-synthesized $RBaCo_2O_{5+\delta}$ (R=La-Ho) compounds," *Phys. Rev. B.*, vol. 71, no. 214421, pp. 1–8, 2005.

[17] A. A. Taskin, a. N. Lavrov, and Y. Ando, "Transport and magnetic properties of $GdBaCo_2O_{5+x}$ single crystals: A cobalt oxide with square-lattice CoO_2 planes over a wide range of electron and hole doping," *Phys. Rev. B.,* vol. 71, pp 1–28, 2005.

[18] D. Khalyavin, S. Barilo, S. Shiryaev, G. Bychkov, I. Troyanchuk, A. Furrer, P. Allenspach, H. Szymczak, and R. Szymczak, "Anisotropic magnetic, magnetoresistance, and electrotransport properties of $GdBaCo_2O5.5$ single crystals," *Phys. Rev. B.*, vol. 67, no. 214421, pp. 1–5, 2003.

[19] E. P. A. Podlesnyak, S. Streule, M. Medarde, K.Conder, "Effect of oxygen nonstoichiometry on structuraland magnetic properties of $PrBaCo_2O_{5+\delta}$," *Phys. B Condens. Matter*, vol. 1348, pp. 359–361, 2005.

[20] S. Streule, a Podlesnyak, J. Mesot, M. Medarde, K. Conder, E. Pomjakushina, E. Mitberg, and V. Kozhevnikov, "Effect of oxygen ordering on the structural and magnetic properties of the layered perovskites $PrBaCo_2O_{5+\delta}$," *J. Phys. Condens. Matter*, vol. 17, pp. 3317–3324, 2005.

[21] S. STREULE, "PhD Thesis: Neutron Diffraction Study of Cobaltite Systems," 2006.

[22] F. Fauth, E. Suard, V. Caignaert, and B. Domeng, "Interplay of structural , magnetic and transport properties in the layered Co-based perovskite $LnBaCo_2O_5$ (*Ln* = Tb, Dy, Ho)," *Phys. Journal. B.*,vol. 174, pp. 163–174, 2001.

[23] J. F. Mitchell, J. Burley, and S. Short, "Crystal and magnetic structure of $NdBaCo_2O_{5+\delta}$: Spin states in a perovskite-derived, mixed-valent cobaltite," *J. Appl. Phys.*, vol. 93, p. 7364, 2003.

[24] T. Vogt, P. M. Woodward, P. Karen, B. A. Hunter, P. Henning, and A. R. Moondenbaugh, "Low to high-spin transition indiced by charge ordering in $YBaCo_2O_5$," *Phys. Rev. Lett.*, vol. 84, no. 13, p. 2969, 2000.

[25] M. Soda, Y. Yasui, M. Ito, S. Iikubo, M. Sato, and K. Kakurai, "Magnetic Structures and Spin States of $NdBaCo_2O_5$," *J. Phys. Soc. Japan*, vol. 73, pp. 464–468, 2004.

[26] E. Suard, F. Fauth, V. Caignaert, I. Mirebeau, and G. Baldinozzi, "Charge ordering in the layered Co-based perovskite $HoBaCo_2O_5$," *Phys. Rev. B.*, vol. 61, no. R11871, 2000.

[27] V. P. Plakhty, Y. P. Chernenkov, S. N. Barilo, A. Podlesnyak, E. Pomjakushina, D. D. Khalyavin, E. V. Moskvin, and S. V. Gavrilov, "Spin structure and magnetic phase transitions in $TbBaCo_2O_{5.5}$," *Phys. Rev. B.*, vol. 71, no. 214407, 2005.

[28] J. Padilla-Pantoja, C. Frontera, O. Castaño, and J. L. García-Muñoz, "Simultaneous para-ferrimagnetic, metal-insulator, and orthorhombic-monoclinic transitions in $YBaCo_2O_{5.50}$," *Phys. Rev. B.*, vol. 81, no. 132405, pp. 1–4, 2010.

[29] J. Padilla-Pantoja, C. Frontera, J. Herrero-Martín, and J. García-Muñoz, "Spin state and structural changes at the metal-insulator transition in $YBaCo_2O_{5.5}$ by synchrotron X-rays," *J. Appl. Phys.*, vol. 111, p. 07D710, 2012.

[30] C. Frontera, J. L. Garcia-Munoz, and O. Castaño, "Influence of *R*-ion size on spin state of Co and magentic properties of $RBaCo_2O_{5.50}$ cobaltites," *J. Appl. Phys.*, vol. 103, no. 07F713, 2008.

[31] C. Frontera, J. L. García-Muñoz, O. Castaño, C. Ritter, and a Caneiro, "The effect of oxygen disorder on magnetic properties of $PrBaCo_2O_{5.50}$ layered cobaltite," *J. Phys. Condens. Matter*, vol. 20, p. 104228, 2008.

[32] D. D. Khalyavin, D. D. Khalyavin, I. O. Troyanchuk, I. O. Troyanchuk, N. V. Kasper, N. V. Kasper, Q. Huang, Q. Huang, J. W. Lynn, J. W. Lynn, H. Szymczak, and H. Szymczak, "Magnetic structure of $TbBaCo_2O_{5.4}$ perovskite," *J. Mater. Res.*, vol. 17, no. 4, pp. 838–843, 2002.

[33] J.-E. Jørgensen and L. Keller, "Magnetic ordering in $HoBaCo_2O_{5.5}$," *Phys. Rev. B*, vol. 77, no. 024427, pp. 1–7, 2008.

[34] V. I. Gatalskaya, M. Baran, R. Szymczak, H. Szymczak, S. N. Barilo, G. L. Bychkov, and S. V. Shiryaev, "Anisotropy of magnetic properties of a twin-free $EuBaCo_2O_{5.5}$ single crystal," *Phys. Solid State*, vol. 49, no. 1, pp. 107–112, 2007.

[35] M. Baran, V. I. Gatalskaya, R. Szymczak, S. V. Shiryaev, S. N. Barilo, K. Piotrowski, and H. Szymczak, "Magnetic phase transitions in $TbBaCo_2O_{5.50}$ single crystals," *J. Phys. Condens. Matter*, vol. 15, 8853, 2003.

[36] M. Respaud, C. Frontera, J. García-Muñoz, M. Aranda, B. Raquet, J. Broto, H. Rakoto, M. Goiran, A. Llobet, and J. Rodríguez-Carvajal, "Magnetic and magnetotransport properties of $GdBaCo_2O_{5+\delta}$: A high magnetic-field study," *Phys. Rev. B.*, vol. 64, no. 214401, pp. 1–7, 2001.

[37] F. Fauth, E. Suard, V. Caignaert, and I. Mirebeau, "Spin-state ordered clusters in the perovskite $NdBaCo_2O_{5.47}$," *Phys. Rev. B.*, vol. 66, no. 184421, 2002.

[38] A. Maignan, V. Caignaert, B. Raveau, D. Khomskii, and G. Sawatzky, "Thermoelectric power of $HoBaCo_2O_{5.5}$: Possible evidence of the spin blockade in cobaltites," *Phys. Rev. Lett.*, vol. 93, no. 2, pp. 026401–1, 2004.

[39] L. Malavasi, M. Brunelli, Y. Diaz-Fernandez, B. Pahari, and P. Mustarelli, "Charge ordering driven metal-insulator transition in the layered cobaltite $HoBaCo_2O_{5.5}$," *Phys. Rev. B.*, vol. 80, no. 153102, pp. 5–8, 2009.

[40] M. Lafkioti, E. Goering, S. Gold, G. Schütz, S. N. Barilo, S. V. Shiryaev, G. L. Bycnkov, P. Lemmens, V. Hinkov, J. Deisenhofer, and A. Loidl, "Spin state and orbital moments across the metal-insulator-transition of $REBaCo_2O_{5.5}$ investigated by XMCD," *New J. Phys.*, vol. 10, 2008.

[41] M. Garcia-Fernandez, V. Scagnoli, U. Staub, a. M. Mulders, M. Janousch, Y. Bodenthin, D. Meister, B. D. Patterson, a. Mirone, Y. Tanaka, T. Nakamura, S. Grenier, Y. Huang, and K. Conder, "Magnetic and electronic Co states in layered cobaltate $GdBaCo_2O_{5.5-x}$," *Phys. Rev. B.*, 78, no. 054424, pp. 1–13, 2008.

[42] Z. Hu, H. Wu, T. C. Koethe, S. N. Barilo, S. V Shiryaev, G. L. Bychkov, C. Schüßler-Langeheine, T. Lorenz, a Tanaka, H. H. Hsieh, H.-J. Lin, C. T. Chen, N. B. Brookes, S. Agrestini, Y.-Y. Chin, M. Rotter, and L. H. Tjeng, "Spin-state order/disorder and metal–insulator transition in $GdBaCo_2O_{5+\delta}$: experimental determination of the underlying electronic structure," *New J. Phys.*, vol. 14, p. 123025, 2012.

[43] C. Frontera, J. García-Muñoz, A. Carrillo, M. Aranda, I. Margiolaki, and A. Caneiro, "Spin state of Co^{3+} and magnetic transitions in $R BaCo_2O_{5.50}$(R=Pr,Gd): Dependence on rare-earth size," *Phys. Rev. B.*, vol. 74, no. 054406, pp. 1–11, 2006.

[44] J. Rodríguez-Carvajal, "Recent advances in magnetic structure determination by neutron powder diffraction," *Phys. B Condens. Matter*, vol. 192, pp. 55–69, 1993.

[45] Z. Hu, H. Wu, M. W. Haverkort, H. H. Hsieh, H. J. Lin, T. Lorenz, J. Baier, A. Reichl, I. Bonn, C. Felser, a. Tanaka, C. T. Chen, and L. H. Tjeng, "Different look at the spin state of Co^{3+} ions in a CoO_5 pyramidal coordination," *Phys. Rev. Lett.*, vol. 92, no. 20, pp. 207402–1, 2004.

[46] M. Sikora, K. Knizek, C. Kapusta, and P. Glatzel, "Evolution of charge and spin state of transition metals in the $LaMn_{(1-x)}Co_xO_3$ perovskite series," *J. Appl. Phys.*, vol. 103, no. 07C907, 2008.

Chapter 6

Effects of spin-state instabilities on the properties of the $Ba_2Co_9O_{14}$ cobaltite

6.1. Motivation

As it was previously mentioned in this work, the metal-insulator transitions (MIT) in Co oxides are a fundamental topic due to the importance of the Co spin state in the field of strongly correlated oxides. We have investigated the spin-state (SS) in Co^{3+} ions and their effects on selected compounds of different families such as $Ln_{1-x}A_xCoO_3$ and $LnBaCo_2O_{5.50}$ cobaltites (*Ln* = lanthanide, A: alkaline earth). We could observe that both compounds present remarkable magnetic and transport properties due to the ability of Co ions to adopt different oxidations states and electronic configurations at the valence band. In an effort to find new strongly correlated Cobalt systems with appealing non conventional properties due to spin-sate instabilities, we decided to investigate $Ba_2Co_9O_{14}$ (BCO). This chapter is devoted to the study of this Co system, recently synthesized, with a completely different structure. It has attracted much attention due to their promising thermoelectric and catalytic properties from a technical point of view in the field of new materials as a cathode for solid oxide fuel cells (SOFCs). A SOFCs is an electrochemical device that generates chemical energy directly into electrical energy with low environment impact and good fuel flexibility.

6.2. Introduction

Recently, new cobalt oxides have been synthesized as potential candidates for thermoelectric materials, like the hexagonal perovskite-related oxides with general formula $A_{3n+3m}A'_nB_{3m+n}O_{9m+6n}$ (with n, m = integers, *A* = alkaline earth, A', *B* = metals, alkaline earth and rare earth metals) and the misfit layered cobaltites [which consist of CdI_2-type oxide layers (CoO_2) and rock-salt-type layers]. The most interesting layered cobaltite investigated by many groups from both the basic physic and applications viewpoint the layered sodium Na_xCoO_2 which exhibits a high thermopower and low resistivity. This cobalt oxide is considered as a cathode operating on the Co(IV)/Co(III) redox couple with the highest oxygen reduction reaction (ORR) activity for SOFCs in the 500 ºC < T < 800 ºC temperature range. Then, looking for new cathodes operating in the Co(III)/Co(II) couple a new intergrowth series of cobaltites with general formula $Ba_{n+1}Co_nO_{3n+3}(Co_8O_8)$ have been synthesized. The first attempt to synthesize these new Barium cobaltite series was done by J. Sun *et al.* [1] in 2006 who reported the first structural details for the single crystals of $Ba_2Co_9O_{14}$ (n = 1) and $Ba_3Co_{10}O_{17}$ (n = 2). Shortly after, G. Ehora *et al.* [2] presented a deeper structural and magnetic study using neutron powder diffraction (NPD) at room temperature (RT) and at low temperature (1.5 K).

This system is a mixed-valence Co^{2+}/Co^{3+} oxide and presents a rhombohedral (*R-3m*) crystal unit cell in the whole temperature range [1–4]. In contrast to the other families studied in this manuscript presenting a perovskite structure, BCO shows a more complex structural symmetry. Its structure can be described as an intergrowth of CdI_2-type $CoO_{6/3}$ layers and Co_3O_{12} octahedral trimers that are connected by corner sharing CoO_4 tetrahedra, as shown in Figure 6.1. There are five crystallographically independent Co sites (*Coi*), with octahedral (*i=1,2,4,5*) and tetrahedral (*Co3*) local coordination.

The *Co2* octahedron shares its opposite triangular faces with two *Co1* octahedra, forming the Co_3O_{12} octahedral trimer; the *Co4* and the *Co5* octahedra share edges to form the CdI_2-type $CoO_{6/3}$ layers; and the *Co3* tetrahedron shares corners with both the Co_3O_{12} trimers and the CdI_2-type $CoO_{6/3}$ layers.

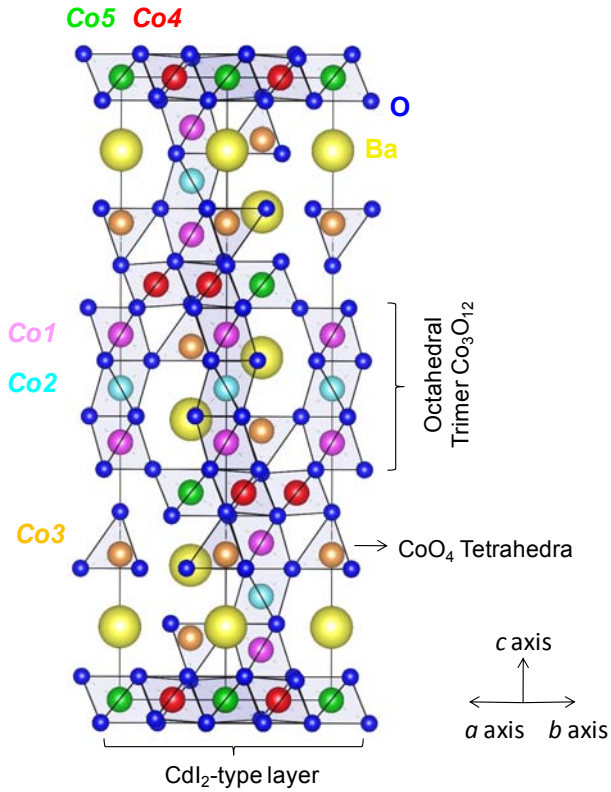

Figure 6.1. Crystal structure of $Ba_2Co_9O_{14}$ in which its 5 crystallographically independent Co sites are shown with different colors. The different coupled structures are indicated: Co_3O_{12} octahedral trimer, the CdI_2-type $CoO_{6/3}$ layers and the tetrahedron shares corners.

The electric and magnetic characterization done by several authors in $Ba_2Co_9O_{14}$ shows an antiferromagnetic (AFM) order below T_N ~ 40 K and it is insulating in the whole temperature range [1–3]. The bond valence sum (BVS) calculation done by J. Sun *et al.* suggests that cobalt ions are mainly Co^{3+} at the *Co2*, *Co3* and *Co4* sites, whereas *Co1* and *Co5* sites are mainly Co^{2+}. However, the BVS calculation from neutron diffraction (ND) data measured by Ehora *et al.* [2] reveals a slightly different scenario. *Co3* and *Co5* sites were found to be divalent (Co^{2+}), while *Coi* (i=1, 2, 4) sites would be trivalent (Co^{3+}). In addition, the effective magnetic moment (μ_{eff}) obtained from the temperature dependence of the magnetization and also the ND data at 1.5 K suggest different spin-states for the Co ions. So, the long-range AFM order is attributed to the *Co3* and *Co5* sites with HS configuration (S = 3/2, $t_{2g}^{5}\ e_g^{2}$). Meanwhile, *Coi* (i=1, 2, 4) sites are considered to be in a LS configuration (S = 0, $t_{2g}^{6}\ e_g^{0}$). In spite of its insulating behavior, Ehora *et al.* [2] reported an insulator-insulator transition at high temperatures (T_t ~ 540 K) from resistivity measurements up to 900 K.

The origin of this particular transition is a matter of debate and requires further investigations. Different mechanisms can be invoked to explain the change observed in conductivity. Among them, (i) a spin-state (SS) transition from LS to HS in the Co^{3+} ions at high temperature, like in $LaCoO_3$, or (ii) a possible melting of the charge ordering at *Co4* and *Co5* sites within the CdI_2-type layers. The first hypothesis was checked by J.-G. Cheng *et al.* [4] by measuring X-ray absorption spectroscopy (XAS) at the Co $L_{2,3}$ edges and the temperature dependence of the Co-O bond length using synchrotron X-rays. These authors checked the valence state and the spin states of Co ions at RT by the comparison between the experimental Co $L_{2,3}$ XAS spectrum of BCO and the experimental spectra of some reference compounds. Unquestionably, the simulated spectrum confirms that all Co^{3+} ions are in LS and Co^{2+} ions are in HS at RT. In addition, the measurements at the O *K*-edge reveal temperature-dependent spectral changes due to a spin-state transition of Co^{3+} ions. In the same report, high-resolution synchrotron X-ray powder diffraction (SXRPD) between 300 and 900 K also indicate changes around T_t in the Co-O bond distances, mainly for *Co1* and *Co2* sites.

In order to shed more light on the insulator-insulator transition and its origin we have carried out the first neutron powder diffraction (NPD) study up to $T_t \sim 570$ K to determine the structural changes at the five cobalt positions. NPD data is needed to clarify the evolution and changes in the individual Co-O bond lengths and also to explore emerging distortions from a possible Co^{3+} IS above the transition. We expect that our results will be more reliable than previously published ones at high temperatures because of the higher sensitivity to oxygen atoms displacements that ND presents. Moreover, to confirm the electronic configuration of each crystallographic independent Co site at RT we have used different X-ray spectroscopic techniques like XAS, XES, HERFD-XANES and theoretical calculations. Finally, the magnetic structure and the analysis of magnetic interactions at play in this cobaltite will be discussed using ND data measured at low temperatures.

6.3. Synthesis and characterization of $Ba_2Co_9O_{14}$: experimental details

Bulk polycrystalline samples of $Ba_2Co_9O_{14}$ were prepared by solid-state reaction of appropriate amounts of Co_3O_4 and $BaCO_3$ powders. The cobalt oxide was dried at 900 ºC during 18 h and the carbonate was de-carbonated at 850 ºC during 12 h and later at 900 ºC during 15 h. After the de-carbonation process, the mixture was pressed into a pellet (d ~ 2.5 cm) and

annealed during 24 h at 800 ºC in air. After a regrinding of the resulting pellet, the compression and the annealing (850 ºC during 24 h, later 890 ºC during 24 h, and slowly cooled down to RT at a rate of 120 ºC/h in air) processes were repeated several times.

The quality of the sample was checked using a Siemens D-5000 diffractometer tuned at Cu *Kα* emission. We found the sample to be single phased and without impurities. Rietveld refinements show that the sample presented a certain degree of preferred orientation (needle-like) at room temperature.

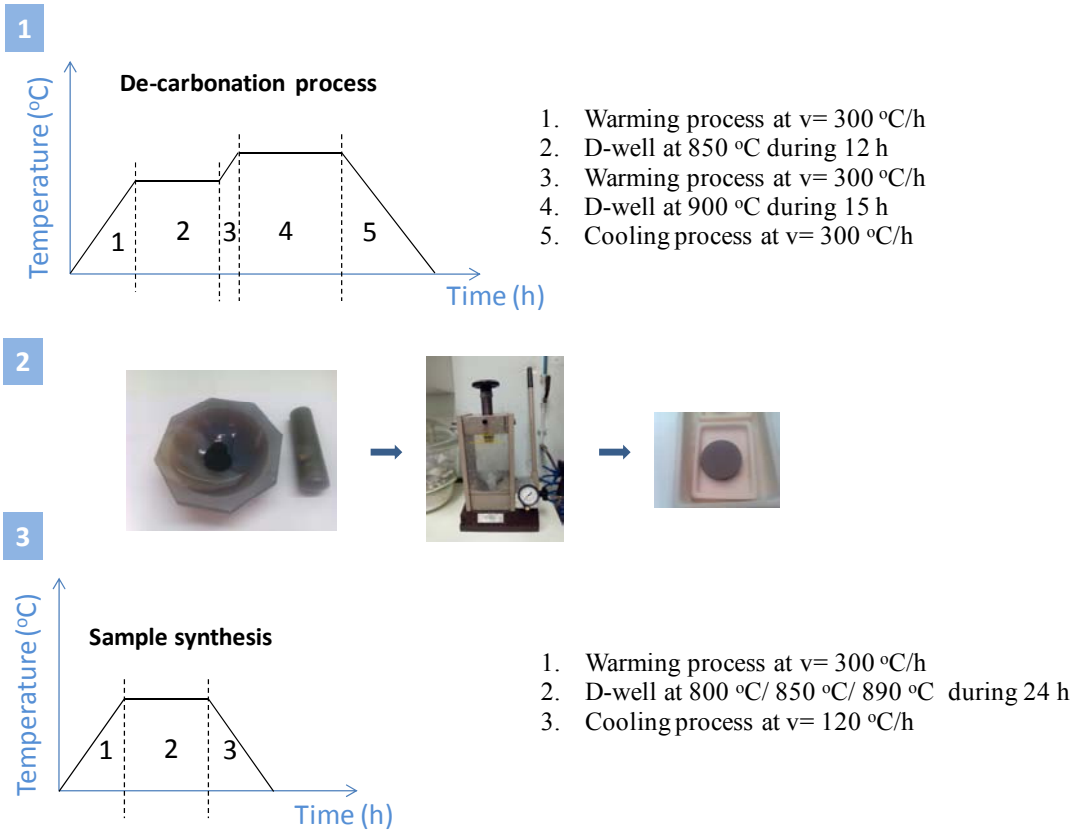

Figure 6.2. Scheme of the synthesis procedure followed to prepare ceramic $Ba_2Co_9O_{14}$. Step 1 shows the de-carbonation process of the precursors. Step 2 shows the grinding process, and finally step 3 shows the annealing process at its respective velocities (v).

MAGNETOMETRY: The direct current (dc) magnetization was measured using a superconducting quantum interferometer device (SQUID, Quantum Design) under different magnetic fields after zero-field cooling (ZFC) and field cooling (FC) processes. The ac-magnetization was measured using a Physical Property Measurement System (PPMS, Quantum Design) at frequency values γ= 1.1, 3.3 and 9.9 kHz, and an amplitude of 10 Oe.

ELECTROMETRY: In order to perform transport measurements in the sample, metallic silver (Ag) electrodes (500 nm) were deposited on the top of the surface using a physical mask. A thermal treatment to fix Ag on the pellet was done at 450º C for 1 hour under O_2 atmosphere. Contacts were done with platinum wiring (25 μm) and dc resistivity was measured at temperatures ranging from 300 K down to 10 K via the four-probe method using a PPMS.

The temperature dependence of the Seebeck coefficient and the electrical conductivity measurements were recorded at high temperatures using a commercial setup from Linseis LSR-3 with the collaboration of Dr. Sebastian Reparaz from the "Institut Català de Nanociència i Nanotecnologia" (ICN2). The samples were cut into square bars of approximately 1 cm length. A temperature gradient of about 50 K was applied across the sample, and the Seebeck coefficient was measured using two Alumel thermocouples. All measurements were calibrated against a calibration standard constant.

NEUTRON POWDER DIFFRACTION: The crystalline structure of $Ba_2Co_9O_{14}$ was studied as a function of temperature by means of NPD on the high-resolution D2B diffractometer of the Institute Laue-Langevin (ILL, Grenoble), while warming up the sample in a furnace from RT to 800 K. Data were recorded at a neutron wavelength $\lambda = 1.594$ Å using the high-intensity mode of the instrument. On the other hand, the magnetic structure was investigated on the D1B diffractometer at 60 K and 5 K using a neutron wavelength $\lambda = 2.52$ Å. All data were analyzed with the Rietveld method using the FULLPROF suite of programs [5].

SYNCHROTRON X-RAY ABSORPTION: Soft X-ray absorption spectroscopy (XAS) measurements at the Co $L_{2,3}$ edges were performed on the BL29-BOREAS beamline at the ALBA Synchrotron. Data were recorded by means of surface-sensitive total electron yield (TEY). Proper bulk-pellet-sensitive measurements required in-situ scraping of the sample under ultrahigh vacuum (~10^{-9} mbar) conditions. CoO was simultaneously measured as an energy calibration reference. The nominal flux on the BL29-BOREAS beamline was of the order of 10^{12} photons/s with an energy resolution of about 100 meV.

X-ray emission spectroscopy (XES) was carried out at beamline ID26 of the European Synchrotron Radiation Facility (ESRF). The incident energy was tuned through the Co *K*-edge (the incident energy was 7800 eV) by means of a pair of cryogenically cooled Si(311) monochromator crystals, being the overall resolution about 0.4 eV. A reference Co metallic foil was used to calibrate the monochromator energy. The emitted X-rays were analyzed using a set of four spherically bent Ge(444) crystals that were arranged with the sample and photon detector (avalanche photodiode) in a vertical Rowland geometry (R = 1 m) at 90º scattering angle.

In addition, high-energy resolution fluorescence-detected X-ray absorption near edge structure (HERFD-XANES) spectra at the Co *K*-edge were collected at the maximum of the Co $K\beta_{1,3}$ emission line. A continuous He-flow cryostat was used to carry out low temperature measurements.

6.4. Magnetic and transport properties characterization

6.4.1. Magnetic properties below room-temperature

Figure 6.3 shows the temperature dependence of direct current (dc) magnetization measured at 10 kOe under zero-field (ZFC) and field cooling (FC). The M(T) curve exhibits a paramagnetic behavior (PM) above 40 K. Below this temperature an anomaly is observed indicating that the sample presents an antiferromagnetic (AFM) order below T_N ~ 41.2 K. The magnetization totally agrees with the previous characterization reported in recent literature. This allows us to confirm the good quality of our sample.

The susceptibility of the sample obeys the Curie-Weiss (C-W) law, $\chi(T) = C/(T-\theta)$, where χ is the molar magnetic susceptibility, C is the Curie constant, and θ is the Weiss temperature. The inset of Figure 6.3 shows a lineal Curie-Weiss (C-W) behavior of χ^{-1} with temperature at $T > T_N$, deviating below the AFM transition [2–4], where the red straight line represents the fit to the C-W law. The effective magnetic moment per Co ion, μ_{eff}, can be obtained from the Curie constant applying the following equation:

$$\mu_{eff} = \sqrt{\frac{3kC}{N}} = \sqrt{8C}\mu_B \qquad \text{(Eq. 6.1)}$$

where, *k* is the Boltmann's constant (1.38 x 10^{-16} erg/K), *N* is the Avogradro's number, and μ_B is the Bohr magneton.

Thus, from the fitting we have obtained that the χ^{-1} values match the Curie-Weiss law with C = 14.90 emu· K/ mol · Oe within the 50 K < T < 200 K temperature interval (near 225 K we have observed a weak deviation in the C-W law) and the effective paramagnetic moment takes the value μ_{eff} = 10.8 μ_B/f.u.

As G. Ehora *et al.* and J.-G. Cheng *et al.* reported, we have found a very large value for μ_{eff} as compared with the expected spin-only 6.7 μ_B/f.u. theoretical value for the divalent Co ions (*Co3* and *Co5* sites) being in HS (S= 3/2). This significant deviation supports an orbital contribution or some contribution from the Co^{3+} ions being in a higher spin-state and not in LS.

However, several investigations in other families such as $SeCoO_3$ [μ_{eff} (Co^{2+}_{oct})= 5.32 μ_B] and Co_3O_4 [μ_{eff} (Co^{2+}_{tet})= 5.4 μ_B] spinel reflected that its experimental effective magnetic

moments were significantly larger than the theoretical value of 3.87 μ_B. In those cases, the discrepancies were assigned to an important unquenched orbital contribution ($J \neq S$). Likewise, our obtained effective moment $Ba_2Co_9O_{14}$ would be consistent with an important orbital contribution.

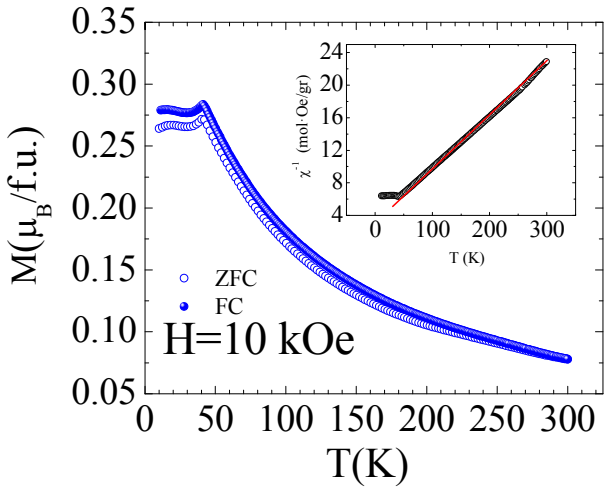

Figure 6.3. Temperature dependence of magnetization of $Ba_2Co_9O_{14}$ measured at 10 kOe using direct current (dc). Open and solid circles refer to measurements under the zero-field cooling (ZFC) and field cooling (FC) conditions, respectively. The inset shows the inverse magnetic susceptibility as a function of temperature at 10 kOe. The Curie-Weiss fitting is shown by the red solid line.

Figure 6.4 displays the M(H) data measured at different temperatures for $Ba_2Co_9O_{14}$. The hysteresis loop shows a linear variation at 100 and 300 K as it is expected for a PM material. However, the curve at 5 K shows a slightly deviation from the linear evolution which it is common for a canted AFM state. This confirms that the material is a pure AFM without any FM component at $T < T_N$. We have also observed that the curves do not saturate at high fields, H > 7 T being needed to force all of the magnetic domains to be aligned, and there is no residual magnetization, which means there is no hysteretic behavior.

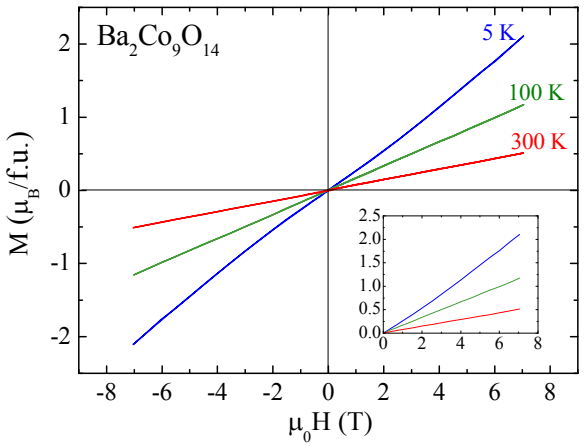

Figure 6.4. Magnetic field dependence of magnetization for $Ba_2Co_9O_{14}$ measured at 5 K, 100 K and 300 K under FC conditions.

6.4.2. Transport properties up to 800 K

Figure 6.5 shows the temperature dependence of the Seebeck coefficient (S_b) (left axis) and the electrical resistivity (right axis) measured between room temperature and 780 K. $Ba_2Co_9O_{14}$ exhibits an exceptionally high thermopower of 180 μV/K at RT, reaching ~ 236 μV/K around T_S = 535 K, and rapidly drops beyond this temperature. This decrease in S_b indicates that the high energy levels (excited states) are more occupied by mobile charge carriers than the low energy levels pointing to a possible spin-state change. A positive Seebeck coefficient only reflects the presence of positive mobiles charges (electron holes), thus $Ba_2Co_9O_{14}$ is considered as a *p*-type conductor. Unfortunately, its resistivity is high precluding this oxide to be an effective potential thermoelectric material for energy conversion at high temperature. Its high resistivity does not favor a large figure of merit, $Z = S_b^2/\rho K$ (ρ and K standing for the resistivity and thermal conductivity, respectively) for high temperature thermoelectric applications in spite of its high thermopower.

Summarizing, the Seebeck curve could be divided into three different regions:

(i) zone I (T < 450K): in this region we find that S_b is approximately constant. This behavior is typical for tunneling assisted polaronic conductor;

(ii) zone II (450 K ≤ T ≤ T_S): in this region we find the peaked S_b(T) curve. Its large thermopower around T_S seems related to an anomalous high spin or/and orbital degeneracy. These strong correlations probably exist between the spin entropy carried by the holes and the density of mobile holes;

(iii) zone III (T > T_t): in this region we find a drop of S_b indicating a sudden increase in the density of *p*- type mobile carriers.

As we have mentioned, the resistivity values are rather high confirming an insulator behavior in BCO as reported by Ehora *et al*. We also observe a large variation on cooling in accordance with a broad insulator-insulator development between 415 K to 610 K. In order to determine the transition temperature (T_t) we have plotted d[ln(ρ)]/d(1/T) against 1/T (see inset of Figure. 6.5) which allows us to establish T_t ~567 K.

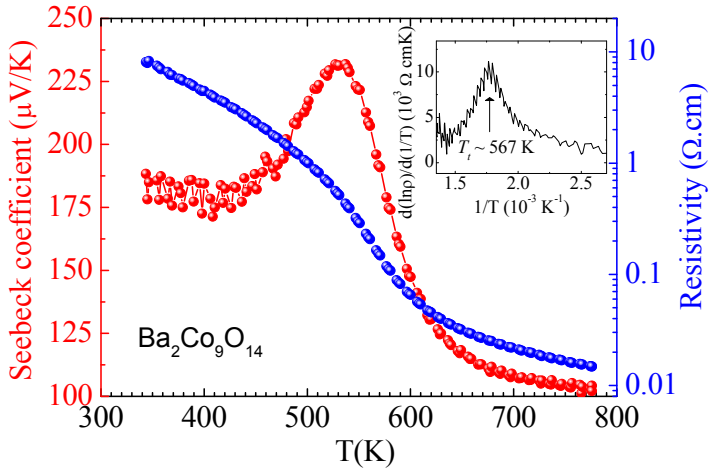

Figure 6.5. Temperature dependence of the Seebeck coefficient (left axis) and the resistivity (right axis). The inset shows the d[(lnρ)]/d(1/T) vs 1/T curve peaking at T_t ~567 K.

To get deeper into the transport properties we have studied different mechanisms for the electronic conductivity. In many materials, the thermal energy is large enough to allow electrons or small polarons into jump to the nearest neighbors at high temperatures. It is well known that most of the oxides that present metal-insulator transitions fullfill the following conductivity expression:

$$\sigma(T) = \sigma_0 \exp\left[-\left(\frac{T_0}{T}\right)^n\right] \qquad \text{(Eq. 6.2)}$$

where σ_0 is the conductivity at temperature T_0 and *n* can take different values depending on the model describing the conductivity: for the Arrhenius model *n*=1, for the Nearest Neihgbour Hopping (NNH) model *n*=1/2, and for the Variable Range Hopping (VRH) model *n*=1/4. The lineal approximation of the log (ρ) vs $(T_0/T)^n$ can establish which model fits better the experimental data, and it allows to calculate the activation energy (E_a). In this case, we decided to divide resistivity measurements into two different zones (Zone I for T > T_t and Zone II for T < T_t):

I. Arrhenius model → log (ρ) vs 1/T → $E_a(T) = k_\beta T_0$ (Eq. 6.3)

II. NNH model → log (ρ) vs $1/T^{1/2}$ → $E_a(T) = k_\beta T_0^{1/2} T^{1/2}$ (Eq. 6.4)

III. VRH model → log (ρ) vs $1/T^{1/4}$ → $E_a(T) = k_\beta T_0^{1/4} T^{3/4}$ (Eq. 6.5)

So, in order to check if these models can reproduce our transport data, we have plotted the log (ρ) vs (1/T) in Figure 6.6, where the two selected zones to calculate the activation energy are indicated.

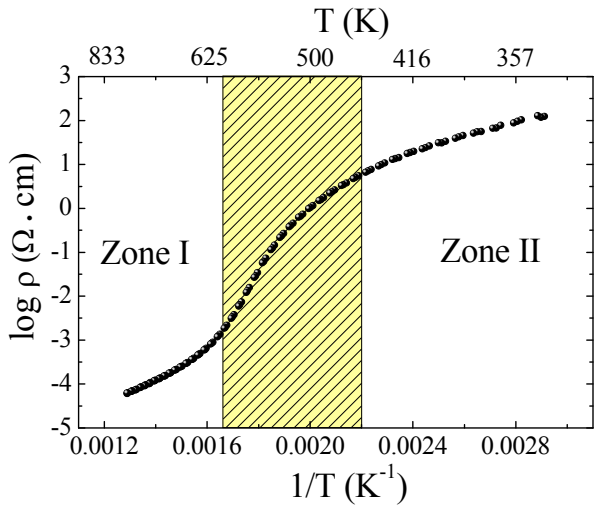

Figure 6.6. Temperature dependence of log (ρ) versus 1/T indicating two linear zones selected to determine the activation energy. The yellow zone demarcates the broad transition area between 430 K and 610 K.

Figure 6.7 shows the comparison of the log (ρ) vs $1/T^n$ for two of the models previously presented with their corresponding linear fitting. Panel (a) compares the Arrhenius and VRH models for Zone I and panel (b) compares the Arrhenius and VRH models, for Zone II. The comparison between the NNH and the Arrhenius models is not shown because of the good agreement between the fitting and the experimental data for both models. So, we cannot discern which approximation matches better the experimental measurements. However, we have selected the Arrhenius model due to the fact that at low temperatures (for Zone I) and at high temperatures (for Zone II) it seems to work better than the NNH model.

So, we can observe that the Arrhenius approximations fit better the experimental data for the whole temperature range in the two studied zones than VRH model. Applying this approximation (Eq. 6.3), we have obtained the activation energies E_a = 0.25 eV for T > T_t and E_a = 0.14 eV for T < T_t.

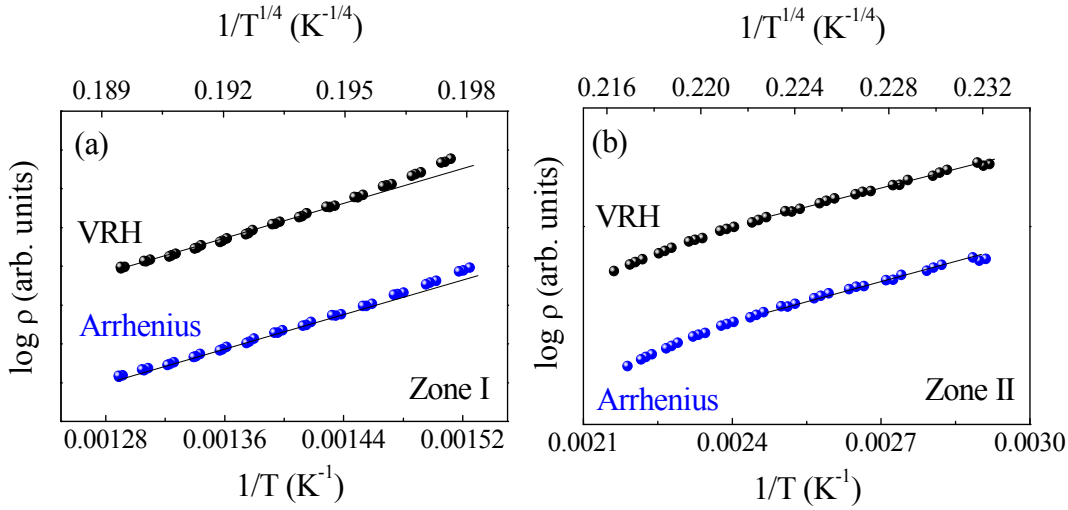

Figure 6.7. Comparative temperature dependence of log (ρ) versus $1/T^n$ for the (a) Arrhenius and VRH models in Zone I, and (b) Arrhenius and VRH models in Zone II. The experimental data poimts have been vertically shifted for clarity reasons.

To complete the study on the transport properties of $Ba_2Co_9O_{14}$ we have performed electrical conductivity measurements below 300 K. In Figure 6.8 we show measurement above and below 300 K, where low temperature data have been normalized to high temperature ones for comparison. We notice that the resistivity increases from 1.5 x 10^{-3} Ω·cm at 800 K to 6 x 10^6 Ω·cm at T ~ 40 K, which confirms the insulating behavior of the compound in accordance with the report by Ehora *et al* [2]. However, they reported an anomaly in the resistivity of their sample below 200 K of unclear origin which is absent in our measurements.

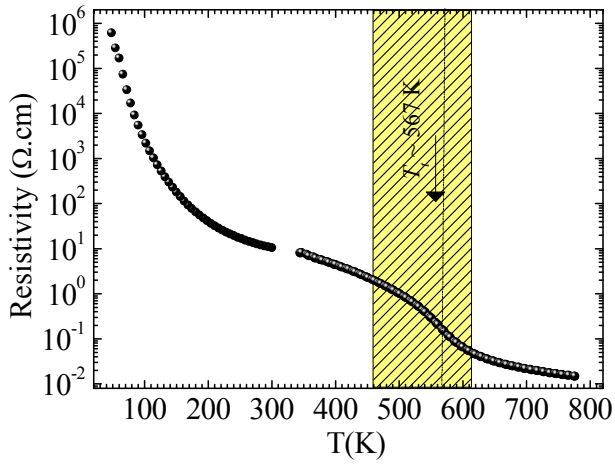

Figure 6.8. Temperature dependence of electrical resistivity in the whole temperature range. Measurements below 300 K are normalized to the high temperature data.

6.5. Structural anomalies at high temperature studied by neutron powder diffraction

NPD patterns measured at D2B (λ = 1.594 Å) for $Ba_2Co_9O_{14}$ have been successfully refined using a single phase with space group *R3-m* (No. 166) for all studied temperatures between RT and 800 K. The refined NPD data at RT are shown in Figure 6.9 and the structural details as a function of temperature together with the agreement factors are reported in Table 6.1.

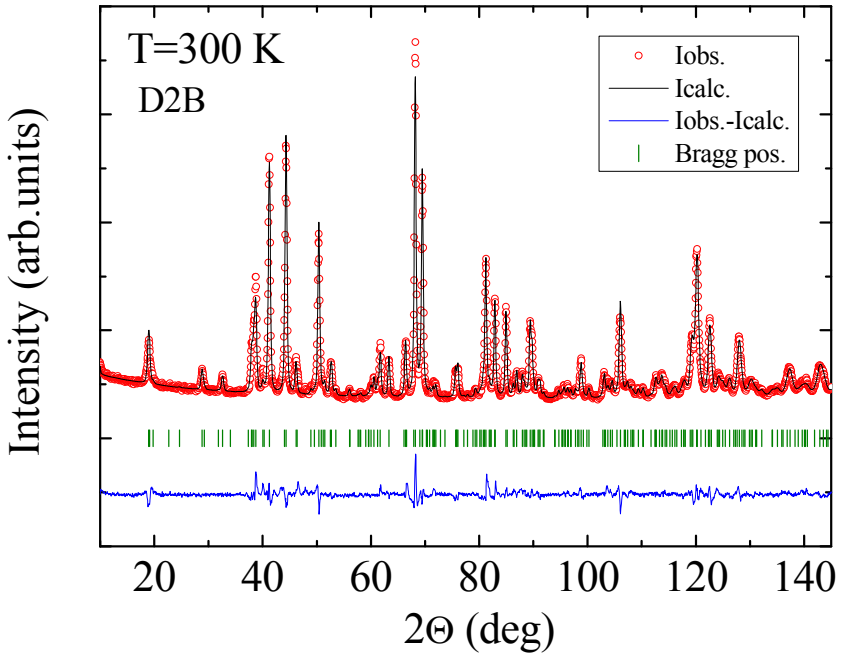

Figure 6.9. Rietveld refinement neutron diffraction pattern from D2B for $Ba_2Co_9O_{14}$ at RT.

Table 6.1. Structural parameters of $Ba_2Co_9O_{14}$ as a function of temperature. The employed space group for refinements is *R-3m* (S.G. 166).

T(K)	800 K	600 K	420 K	300 K
a (Å)	5.7516(4)	5.7277(4)	5.7003(4)	5.6921(7)
b (Å)	5.7516(4)	5.7277(4)	5.7003(4)	5.6921(7)
c (Å)	29.4996(5)	29.2459(4)	28.9577(4)	28.8936(4)
γ (deg)	120	120	120	120
Atom coordinates: Ba *6c*(1/3, 2/3, *z*), *Co1 6c*(0, 0, *z*), *Co2 3b*(0, 0, 1/2), *Co3 6c*(2/3, 1/3, *z*), *Co4 9e*(5/6, 1/6, 2/3), *Co5 3a*(1/3, 2/3, 2/3), O1 *18h*(*x, y, z*), O2 *6c*(0, 0, *z*), O3 *18h*(*x, y, z*)				
Ba (*z*)	0.5492(3)	0.5515(2)	0.5502(2)	0.5502(8)
Ba, B_{iso} (Å^2)	1.54(2)	1.12(1)	0.40(9)	0.30(8)
Co1 (*z*)	0.5870(6)	0.5881(5)	0.5884(5)	0.5884(4)
Co1, B_{iso} (Å^2)	1.05(6)	0.74(6)	0.41(5)	0.21(3)
Co2, B_{iso} (Å^2)	1.05(6)	0.74(6)	0.41(5)	0.21(3)
Co3 (*z*)	0.5682(5)	0.5694(4)	0.5663(3)	0.5663(2)
Co3, B_{iso} (Å^2)	1.05(6)	0.74(6)	0.41(5)	0.21(3)
Co4, B_{iso} (Å^2)	1.05(6)	0.74(6)	0.41(5)	0.21(3)
Co5, B_{iso} (Å^2)	1.05(6)	0.74(6)	0.41(5)	0.21(3)
O1 (*x*)	0.3130(2)	0.3087(1)	0.3025(1)	0.3012(5)
O1 (*y*)	0.1565(2)	0.1542(9)	0.1512(6)	0.1506(7)
O1 (*z*)	0.5453(1)	0.5453(1)	0.5440(8)	0.5437(7)
O1, B_{iso} (Å^2)	1.46(7)	0.94(5)	0.45(4)	0.31(4)
O2 (*z*)	0.6994(2)	0.6993(2)	0.6996(1)	0.6996(6)
O2, B_{iso} (Å^2)	0.817(2)	0.86(1)	0.75(8)	0.60(7)
O3 (*x*)	0.9814(2)	0.9749(1)	0.9706(1)	0.9701(6)
O3 (*y*)	0.4907(1)	0.4874(8)	0.4852(6)	0.4851(6)
O3 (*z*)	0.7035(1)	0.7040(1)	0.7046(9)	0.7046(8)
O3, B_{iso} (Å^2)	1.25(6)	0.75(5)	0.57(4)	0.41(1)
Agreement parameters:				
χ^2 (%)	0.77	0.78	0.71	0.74
R_B(%)	6.62	5.20	4.19	3.80

The evolution of the *a, c* cell parameters and the hexagonal unit cell-volume with temperature are plotted in Figure 6.10(a, b). We can observe an anomaly in the evolution of the three structural parameters at T_t ~ 567 K, where *a* and *c* exhibit a sudden shrink on cooling by 1.05 % and 2.1 %, respectively. The insulator-insulator transition is also found at this temperature value by taking the maximum of *dV/dT* which is plotted in panel (b). The transition temperature T_t perfectly matches that determined from transport measurements.

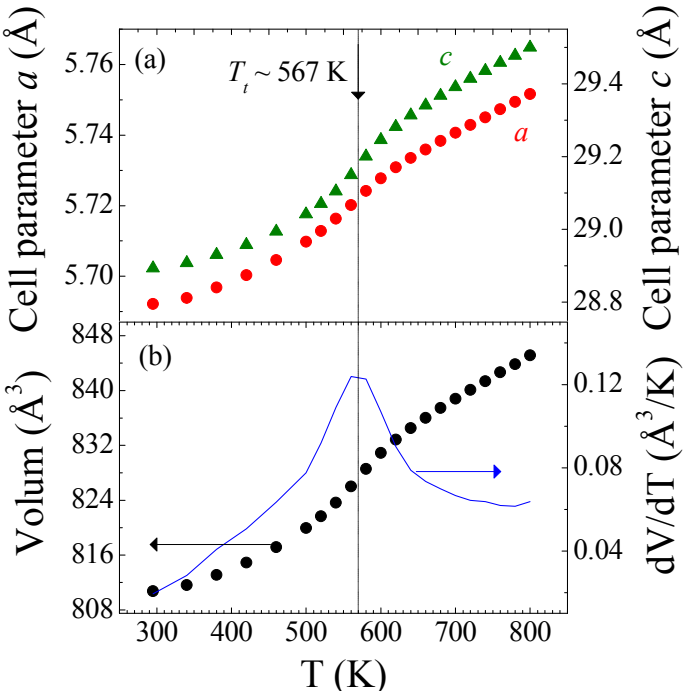

Figure 6.10. Temperature dependence of (a) cell parameters (*a*, left axis and *c*, left axis), and (b) the unit-cell volume (left axis) and its respective *dV/dT* derivative.

The obtained Co_i-O bond distances from NPD and the calculated bond-valence sum (BVS) at selected temperatures are reported in Table 6.2. The obtained values are the most reliable up to now due the fact that neutron diffraction is a technique very sensitive to the oxygen positions, while the reported data from other authors works were acquired by high-resolution synchrotron X-ray powder diffraction (SRXPD) [4]. The BVS parameters have been calculated taking into account the data reported in reference [6] by N. E. Breese and M. O'Keeffe. The valence, v_{ij} of a bond between two atoms *i* and *j* is defined as the sum of all the valences from a given atom *i* with valence V_i and it obeys:

$$\sum_j v_{ij} = V_i \qquad \text{(Eq. 6.6)}$$

The common empirical expression for the variation of the length d_{ij} of a bond with valence V_i is defined as:

$$v_{ij} = exp\left[(R_0 - d_{ij})/b\right] \quad \text{(Eq. 6.7)}$$

where R_0 = 1.700 Å(Co^{3+}) and 1.692(Co^{2+}) for *Coi*-Oj distances extracted from Ref. [6], *dij* are the experimental *Coi*-Oj bond distances obtained from refinements, and *b* is a universal constant with value 0.37 Å.

At first sight, we can observe that *Coi*-O*j* distances with an octahedral environment (*i=1, 2, 4*) increase on heating, while the *Co5*-O*j* bond distances decrease. Around tetrahedral *Co3* sites the bond lengths decrease with temperature but they recover at T > 600 K, approximately. The BVS calculations for all *Coi* ions at RT are similar to the expected theoretical values, but it seems that on heating the formal valence of the Co^{3+} ions (*Co1*, *Co2* and *Co4*) decreases, unlike Co^{2+} ions (*Co3* and *Co5*) whose valence increases at high temperatures. A valence of ~ 3.4^+ is found for *Co4* site at RT indicating that this Co ion is strongly linked to the oxygen neighbors in contrast to the rest of Co ions.

Table 6.2. Evolution for the nearest neighbour *Coi*-O bond lengths as calculated from the bond-valence sum for Co ions.

	800 K	600 K	420 K	300 K
$d_{Co1\text{-}O1}$ (Å) x3	1.986(2)	1.974(7)	1.970(1)	1.968(4)
$d_{Co1\text{-}O3}$ (Å) x3	2.012(8)	1.947(9)	1.902(9)	1.896(6)
Calculated BVS	2.676	2.969	3.184	3.220
$d_{Co2\text{-}O1}$ (Å) x6	2.054(6)	2.025(7)	1.964(7)	1.949(7)
Calculated BVS	2.305	2.492	2.939	3.061
$d_{Co3\text{-}O1}$ (Å) x3	1.887(5)	1.910(4)	1.911(9)	1.916(3)
$d_{Co3\text{-}O2}$ (Å)	1.939(2)	1.890(1)	1.948(1)	1.948(1)
Calculated BVS	2.284	2.250	2.160	2.138
$d_{Co4\text{-}O2}$ (Å) x2	1.903(4)	1.909(9)	1.903(3)	1.899(5)
$d_{Co4\text{-}O3}$ (Å) x4	1.944(8)	1.933(5)	1.923(6)	1.918(3)
Calculated BVS	3.232	3.267	3.344	3.387
$d_{Co5\text{-}O3}$ (Å) x6	2.064(7)	2.086(4)	2.101(8)	2.100(5)
Calculated BVS	2.195	2.068	1.986	1.997

It is well known that changes in the distances are a fingerprint of spin-state transitions as it has already reported in other compounds such as $LaCoO_3$ or $GdBaCo_2O_{5.50}$ [7, 8]. So, to discuss possible changes in the spin-state for Co ions in $Ba_2Co_9O_{14}$ the evolution of Co-O distances of Co ions with octahedral and tetrahedral coordination (*Co3* site*)* have been plotted in Figures 6.11 and 6.12, respectively. We found some discontinuities in the bondlengths around the transition temperature $T_t \sim 567$ K, which is marked by dotted lines: (i) the average Co-O distances for *Co1* and *Co2* sites expand across the SS transition (+ 1.3% and + 1.37 %, respectively); (ii) the *Co4-O* bond distance suffers slight changes (~ + 0.33%), so that we can consider that it remains constant; (iii) *Co5*-O bondlengths shrink on heating around -0.76 %, unlike the SXRPD reported data showing no changes at this Co site; and (iv) bondlengths in *Co3*-O tetrahedra decrease (~ -1.10 %) on heating. In the structural analysis by Cheng *et al*. the specific sites where the SS transition (from LS to HS) takes places is at the *Co1* and *Co2*. However, our results show that a SS transition in the Co^{2+} sites is possible and not only in the Co^{3+} sites with octahedral coordination. The most likely spin-states in $Ba_2Co_9O_{14}$ are discussed in the Section 6.7.

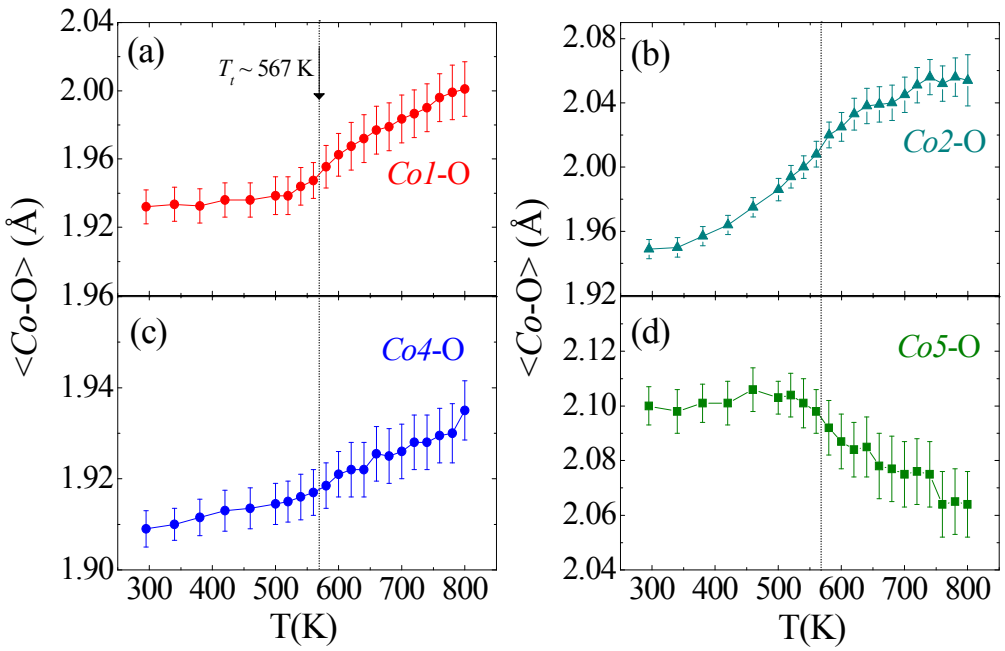

Figure 6.11. Temperature evolution of the average Co_i-O distances (Co_i = 1, 2, 4, 5) for the Co ions with octahedral coordination.

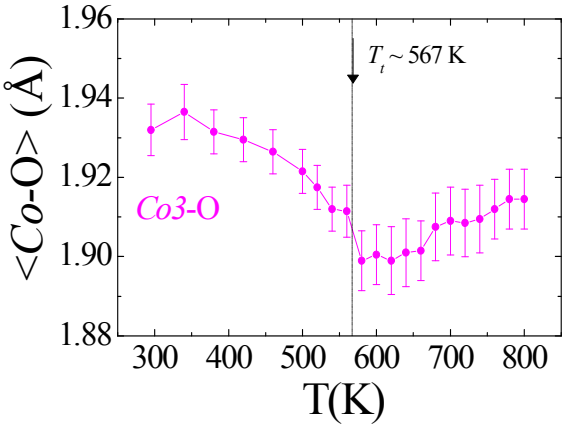

Figure 6.12. Temperature dependence of the average *Co3*-O distance (tetrahedral coordination).

6.6. The magnetic structure at low temperature

In this section we discuss the magnetic structure at low temperatures. Neutron diffraction data below and above the Néel temperature were acquired at D1B using a wavelength λ = 2.52 Å. Figure 6.13 shows the pattern on cooling. As it can be seen, various magnetic peaks in the 5 K pattern (blue) are not present at 60 K (black pattern). All new peaks were indexed considering a doubled cell parameter along the *c* – axis and a propagation vector *k* = (0 0 3/2).

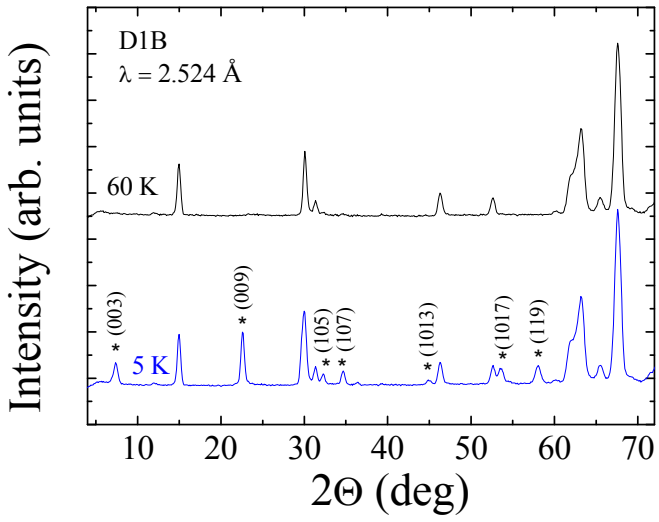

Figure 6.13. Neutron diffraction patterns from D1B measured at 60 K and 5 K. (*) Indicates the new magnetic peaks that appear in the AFM phase (on cooling).

The analysis of the magnetic structure was realized taking into account different magnetic subgroups derived from the structural space group (*R-3m*). Only two models have been found compatible with our neutron diffraction data. Both descriptions show that only the divalent cobalt (*Co3*, *Co5*) positions are magnetic (see Figure 6.17(b) for the crystal structure where the magnetic and non-magnetic Co ions are represented in red and green balls, respectively). The description of the magnetic structure has been investigated using the BNS setting which refers to the Belov-Neronova-Smirnova notation [9]. The first solution, called Model 1, is described using the magnetic S.G. C_c2/c (BNS 15.90) where the magnetic moment for *Co3* and *Co5* ions corresponds to $m = (m_x, 2m_x, m_z)$ with m_z converging to zero. The second solution found, called Model 2, is described using the magnetic S.G. C_c2/m (BNS 12.63) in which the magnetic moment only has one component, $m = (m_x, 0, 0)$. Figure 6.14 displays the refined NPD data at 5 K using the two commented models. The refined parameters obtained from the two possible models are listed in Table 6.3 together with the agreement parameters. It must be highlighted that *Co3* ion presents a magnetic moment $m_{Co3} \sim 2.9\ \mu_B$ while *Co5* moments are antiparallel to *Co3* ones and their magnetic moment takes a value $m_{Co5} \sim 1.8\ \mu_B$ in both models. These numbers raise a question on the actual spin state and the real oxidation state of these divalent cobalt ions. As we mentioned at the introduction of this chapter (Section 6.2) it has been assumed that *Co3* and *Co5* sites are Co^{2+} ions in a HS state. However, the different ordered magnetic moment that they present could suggest a different electronic configuration. So, X-ray absorption spectroscopy (XAS) was employed to analyze the spin state for each specific Co site in $Ba_2Co_9O_{14}$.

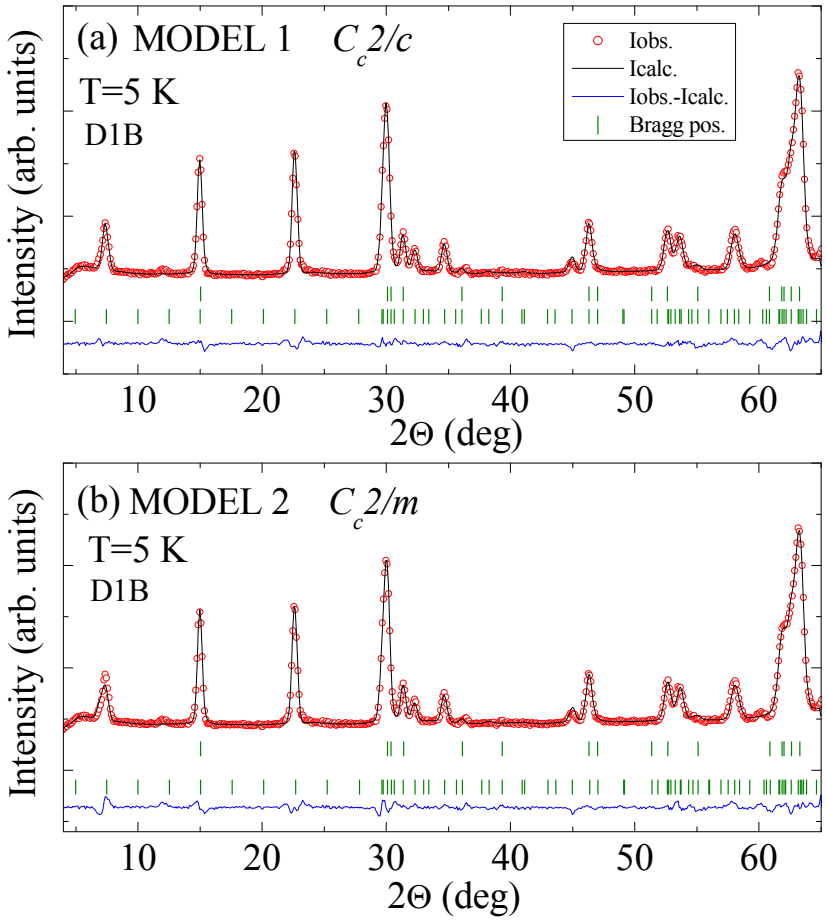

Figure 6.14. Rietveld refinements of the neutron patterns from D1B measured at 5 K for (a) the first proposed magnetic structure with $m = (m_x, 2m_x, m_z)$ and (b) the second magnetic structure with $m = (m_x, 0, 0)$.

Table 6.3. Refined parameters for the two magnetic structure models proposed at 5 K. The only Co ions with magnetic contribution are *Co3* and *Co5* sites.

Cell parameters: $a = b = 5.6928(4)$ Å, $c = 57.7200(2)$ Å, $\gamma = 120^{o}$			
Atomic coordinates: *Co3* (0, 0, 0.1164(7)); *Co5*: (0, 0, 0)			
Propagation vector **k** = (0, 0, 3/2)			
C_c2/c, MODEL 1 (BNS 15.90)		C_c2/m, MODEL 2 (BNS 12.63)	
Co3		***Co3***	
$(m_x, 2m_x, m_z)$	(1.62(2), 3.24(2), 0.53(9))	$(m_x,0,0)$	(2.88(7), 0,0)
m_T (μ_B/f.u.)	2.85(3)	m_T (μ_B/f.u.)	2.88(7)
Co5		***Co5***	
$(m_x, 2m_x, m_z)$	(1.03(2), 2.06(4), -0.53(9))	$(m_x,0,0)$	(1.76(5), 0,0)
m_T (μ_B/f.u.)	1.86(4)	m_T (μ_B/f.u.)	1.76(5)
χ^2	16.2	χ^2	21.6
R_B (%)	2.61	R_B (%)	2.81
R_{mag} (%)	6.23	R_{mag} (%)	6.48

Schematic representations of the two discussed models are depicted in Figure 6.15 and Figure 6.16, the first one showing the projection along the *c* axis, and the latter showing the projection along the *ab* plane. We see that both models indexed with different S.G. describe identical magnetic structures but rotated by 90 degrees. In Figure 6.16(b) we can view how the magnetic moments arrange in AFM order forming triple layered blocks, [see Figure 6.17(a) for a better understanding].

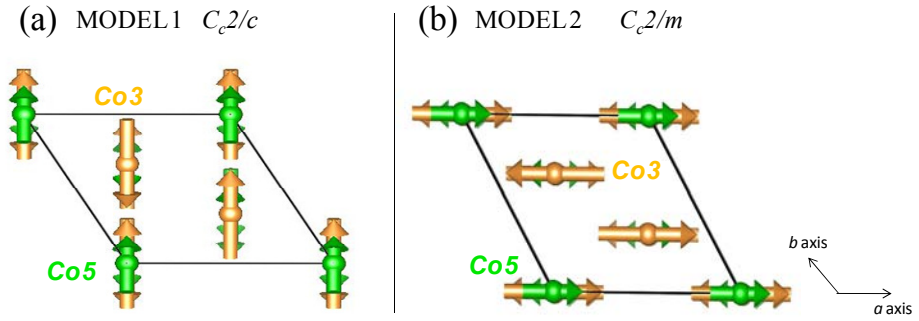

Figure 6.15. Projection along the *c* axis of the two possible magnetic structures for $Ba_2Co_9O_{14}$. Green and yellow arrows represent spins for the *Co5* and *Co3* sites, respectively.

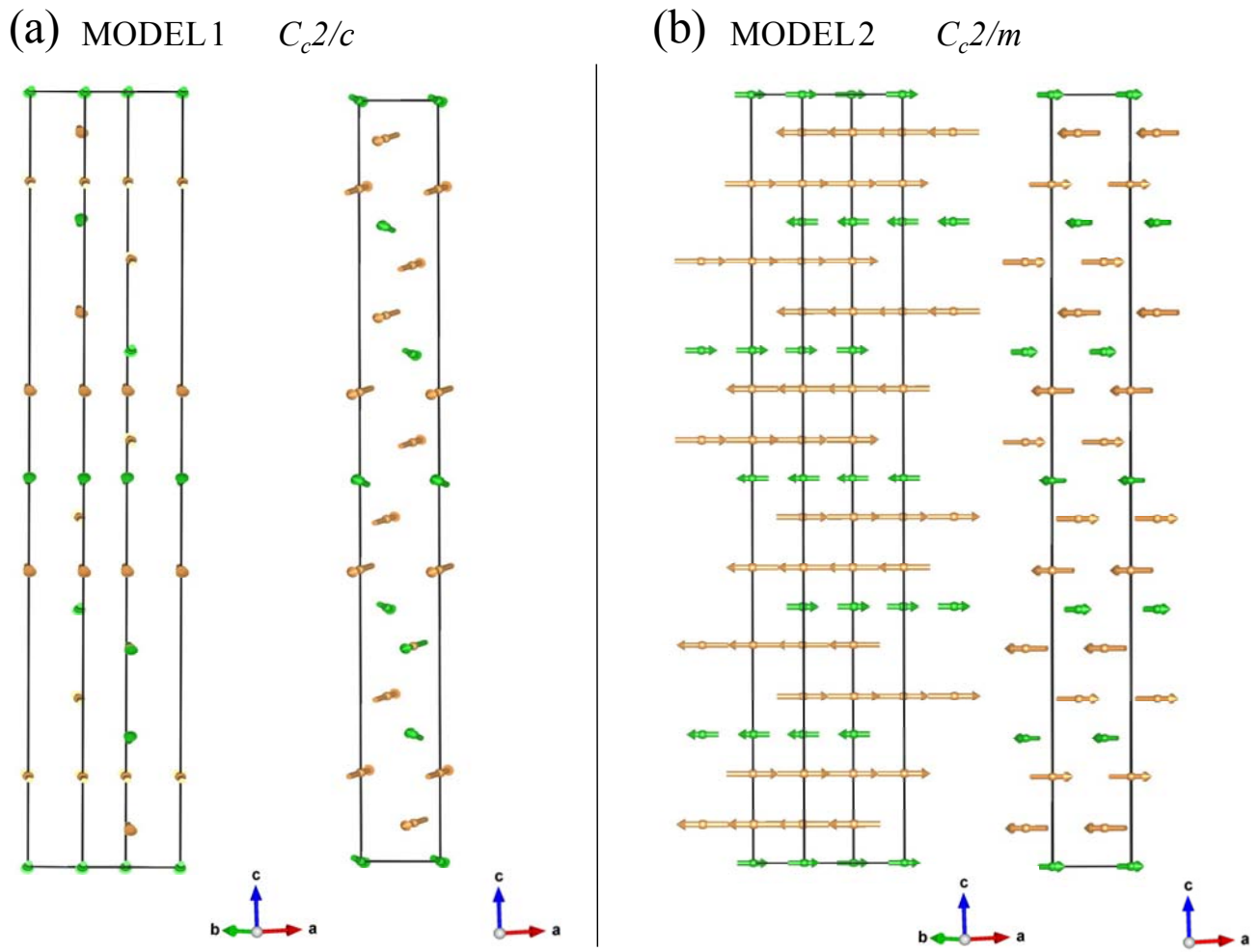

Figure 6.16. Projection along the *ab* plane of the two possible magnetic structures for $Ba_2Co_9O_{14}$. Green and yellow arrows represent spins for the *Co5* and *Co3* sites, respectively.

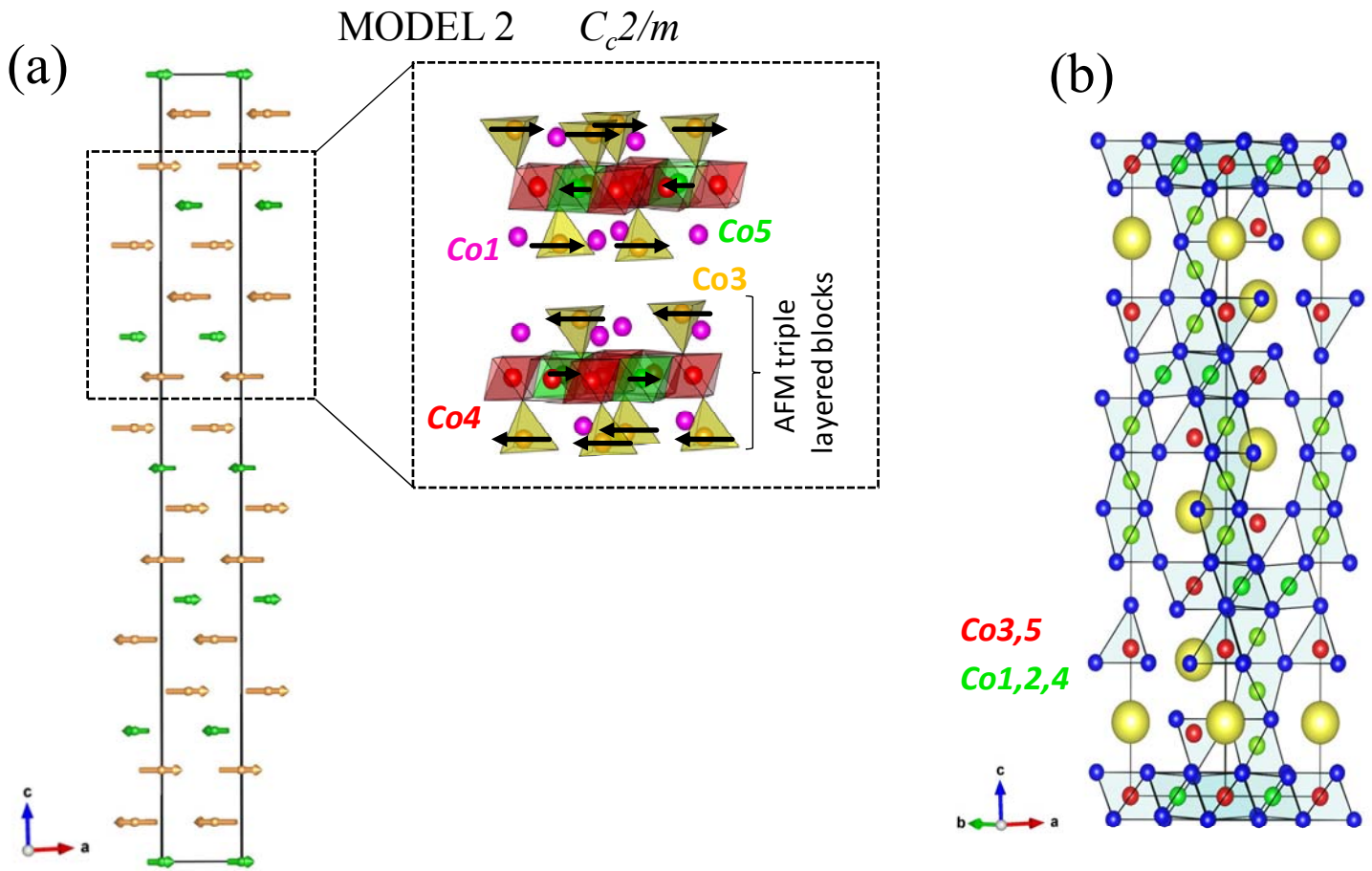

Figure 6.17. (a) Projection along the *ab* plane for the magnetic structure BNS 1263 where the zoom shows the arrangement of the magnetic moments in the AFM triple layered blocks for $Ba_2Co_9O_{14}$; (b) schematic view of the crystal structure pointing out the positions of the magnetic Co ions (red balls) and the non-magnetic Co ions (green balls).

6.7. Spin state-transition analyzed by XAS and XES

As we mentioned in Section 6.5, a spin-state transition at Co sites with trivalent Co ions (*Co1* and *Co2* sites) is expected at $T_t \sim 567$ K and probably for divalent Co ions (*Co3* and *Co5* sites) too. We found that *Co1*-O and *Co2*-O bondlengths take values between 1.93-1.95 Å at $T < T_t$, which are compatible with the expected theoretical values for Co^{3+} ions in a LS configuration [$d(Co^{3+}\text{-}O)^{VIII}$ (LS)= 1.945 Å and $d(Co^{3+}\text{-}O)^{VIII}$ (HS)= 2.01 Å)] [10]. On the other hand, at $T > T_t$ bondlengths take values around 2.00-2.05 Å which fit a Co^{3+} HS model. The same hypothesis can be used to determine the Co^{2+} spin-state. The *Co5*-O bondlengths at $T < T_t$ are rather compatible with a HS configuration (S = 3/2, $t_{2g}^5\ e_g^2$) than with a LS because theoretically the $d(Co^{2+}\text{-}O)^{VIII}$ (HS) distance should be ~ 2.145 Å, while for a LS configuration we get 2.05 Å [10]. So, despite of the observed reduction at this Co site a spin-state transition would not be possible when at low temperatures seem to be in a HS state. On the other hand the *Co3*-O bondlengths at low temperature seems to better fit the LS state (S = 1/2, $e_g^4\ t_{2g}^3$), which also means a lower magnetic contribution than that of *Co5*.

However, as we previously observed when studying the magnetic structure in Section 6.6, the only Co ions which give some magnetic contribution to the structure are the *Co3* and *Co5* sites. Moreover, the proposed models reveal that m_{Co3} is larger than m_{Co5}. Thus, the *Co3* site should be in a HS state while the magnetic study suggests a different scenario for *Co5* than for *Co3*, like a LS or mixed LS/HS state. If one considers Co^{2+} HS (S = 3/2, $e_g^3\ t_{2g}^4$) in a tetrahedral coordination, we obtain $\mu_{eff} = g \cdot S \sim 3\ \mu_B$/f.u. in good agreement with the experimental moment obtained for *Co3*. On the other hand, a Co^{2+} LS (S = 1/2, $t_{2g}^6\ e_g^1$) in octahedral coordination yields $\mu_{eff} \sim 1\ \mu_B$/f.u. in disagreement with the magnetic moment obtained for *Co5*. Then, the most likely scenario for this Co site would be a mixed LS/HS (2/3:1/3) state.

In order to shed more light about the valence and spin states of Co ions in $Ba_2Co_9O_{14}$, we have carried out XAS at the Co $L_{2,3}$ ($2p \rightarrow 3d$ transitions) edges at room temperature measured in BL-29 BOREAS beamline (ALBA Synchrotron). The experimental spectrum of this compound has different multiplet structures [see Figure 6.19(a)] due to the presence of different valence, coordination, and electronic configuration in the Co ions.

So, it is rather tricky to distinguish each separate contribution from the experimental spectrum. Then, we decided to use charge-transfer multiplet (CTM) calculations using the CTM4XAS program (based on the Cowan code) [11, 12] for the experimental XAS spectra and explore the spin state of each Co ions contribution. As we discussed previously, the expected electronic configuration for each site at room temperature is: (i) a LS state for the trivalent ions in CoO_6 octahedra (*Co1*, *Co2* and *Co4*); (ii) a HS state for the divalent tetrahedra (*Co3*); and (iii) a mixed LS /HS for the divalent octahedra (*Co5*).

Concerning the Co^{2+} LS, the multiplet theory demonstrates that the crystal field effect of oxygen is too weak in Co^{2+} in an octahedral environment (O_h) to favor a LS ground state [13]. So, this is rather unlikely to occur in octahedral oxides as shown in Figure 6.18(b). Moreover, looking at the energy level diagram for Co^{2+} in a tetrahedral crystal field (T_d) [see, Fig. 6.18(a)] a HS appears to be consistent as ground state where the first order e_g subshell is completely filled and the t_{2g} subshell is half-filled giving $S = 3/2$. Namely, there is only one possibility to distribute seven electrons in the 3*d* orbitals following the Hund's Rules for this local symmetry. Low spin states can only exist by a violation of the first Hund's Rule. This fact is also applied to Co^{3+} in a tetrahedral crystal field, where the LS ($S = 0$, $t_{2g}^{\ 6}\ e_g^{\ 0}$) state never becomes the ground state [see, Fig. 6.18 (c)]. In contrast, Co^{3+} systems in an octahedral local symmetry are typically close to the HS/LS crossover point and thus both configurations may exist [Figure 6.18(d)] [13].

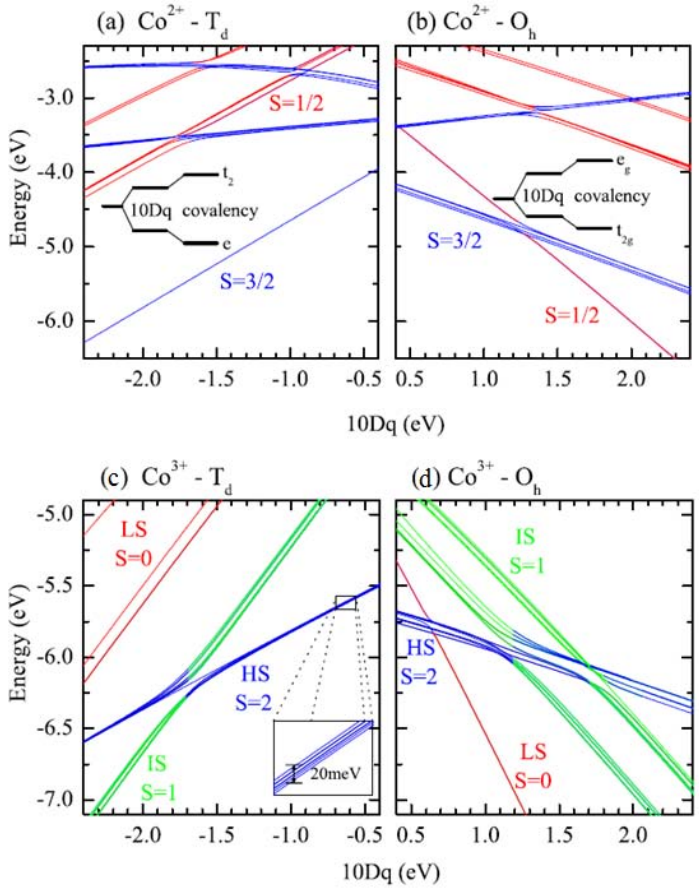

Figure 6.18. Energy level diagrams for (a) Co^{2+} in a tetrahedral crystal field, (b) Co^{2+} in an octahedral crystal field, (c) Co^{3+} in a tetrahedral crystal field, and (d) Co^{3+} in an octahedral crystal field [13].

In summary, *Co3* and *Co5* positions should present the same SS despite the different magnitude of the magnetic moment. In addition, *Coi* (i = 1, 2, 4) are in a LS state at RT, but *Co1* and *Co2* transform into a HS state at T > T_r.

Figure 6.19 shows the room-temperature Co $L_{2,3}$ XAS spectrum of $Ba_2Co_9O_{14}$ together with the calculated ones for Co^{3+} O_h in LS , Co^{2+} O_h in HS, and Co^{2+} T_d ions in HS. In addition, the weighted sum of calculated spectra with a composition of 6/9 Co^{3+} O_h + 1/9 Co^{2+} O_h + 2/9 Co^{2+} T_d as a simulation for $Ba_2Co_9O_{14}$ is also plotted (the relative weights are defined according to the different multiplicities of the Co Wyckoff positions in the structure). In Table 6.4 we list all the parameters used for the CTM calculations.

As we observe in Figure 6.19(b), the simulated spectrum excellently matches the experimental one. This result represents a new evidence that the *Co5* site is in a HS electronic configuration like the *Co3* site as earlier reported. At the same time it raises the question about the origin of the differences found in the ordered magnetic moments at both Co ions. Figure 6.20 shows a schematic view of the crystal structure below and above the SS transition.

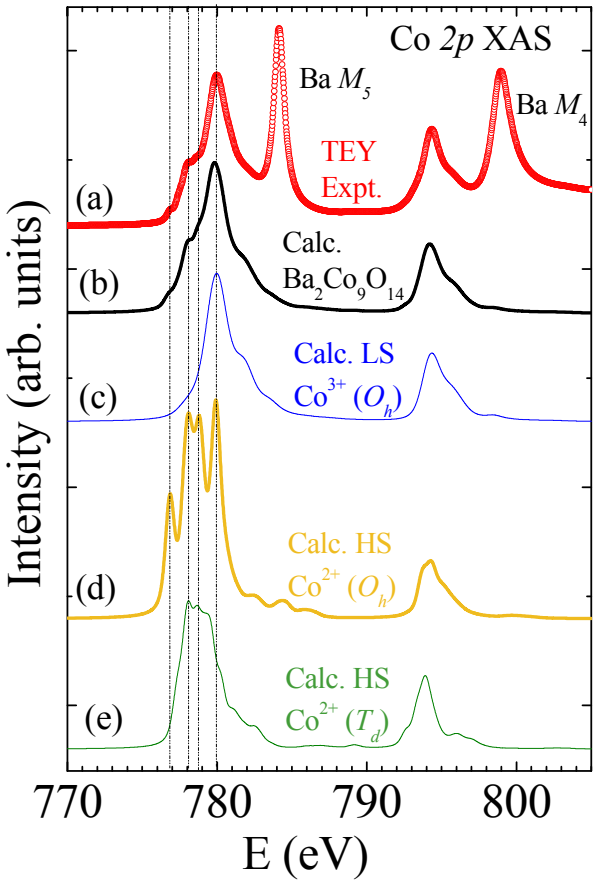

Figure 6.19. (a) Experimental total-electron yield (TEY) Co $L_{2,3}$ XAS spectrum of $Ba_2Co_9O_{14}$ measured at room temperature; (b) weighted sum of the calculated spectra; (c) calculated spectrum for octahedral Co^{3+} in LS; (d) calculated spectrum for octahedral Co^{2+} in HS; and (e) calculated spectrum for tetrahedral Co^{2+} in HS. All spectra have been vertically shifted for clarity. Vertical dotted lines are eye-guides.

Despite the fact that we ascertained the electronic configuration for *Co5* site, we found illustrative to calculate the XAS spectrum of Co^{2+} LS in octahedral symmetry to compare with the Co^{2+} HS and create the corresponding weighted sum of the calculated spectra using Co^{2+} (O_h) in LS. We can observe in Figure 6.21 (b) that there are slight differences between the calculated spectra of $Ba_2Co_9O_{14}$ using Co^{2+} (O_h) in HS or LS, the main ones being the new

structures at ~778 and ~778.9 eV from Co^{2+} LS appearing in the simulated spectra. These new calculations confirm the absence of Co^{2+} LS in the structure.

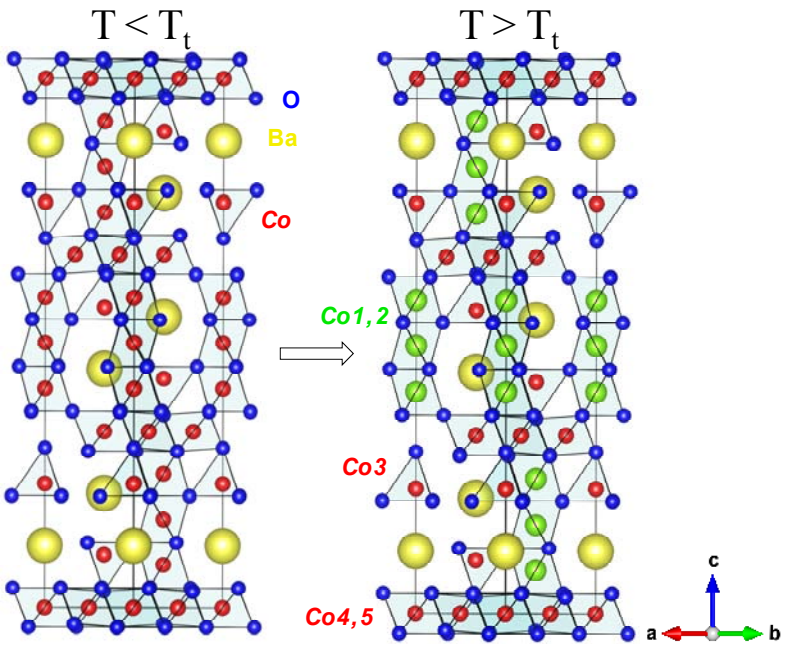

Figure 6.20. Schematic view of the crystal structure below and above the SS transition, where it can be seen which Co sites are involved in the transition. The ionic radius size for each electronic configuration is: Co^{3+VIII} (LS)= 0.545 Å and Co^{3+VIII} (HS)= 0.61 Å.

Table 6.4. Parameters employed in the charge-transfer multiplet calculations with CTM4XAS.

Parameter	Co^{3+} LS	Co^{2+} HS	Co^{2+} LS	Co^{2+} HS
Symmetry	O_h	O_h	O_h	T_d
Crystal field (*10Dq*) (eV)	+1.6	+0.8	+2	-0.3*
Charge transfer energy (Δ) (eV)	+3.0	+3.0	+3.0	7
U_{dd} (eV)	6.2	6	6	6
U_{pd} (eV)	7.5	8	8	8
Hopping e_g electrons (T_{eg}) (eV)	2.0	2.0	2.0	1.0
Hopping t_{2g} electrons (T_{t2g}) (eV)	1.0	1.0	1.0	2.0
Spin-orbit coupling (S.O)	1.0	1.0	1.0	1.0
Slater's integrals (F_{dd}, F_{pd}, G_{pd})	1.0	1.2	1.0	1.2

(*) For T_d symmetry we used a negative value for the crystal field parameter (*10Dq*) that represents the crystal inversion between the low energy twofold e_g and the high energy threefold t_{2g} orbitals with respect to the O_h symmetry.

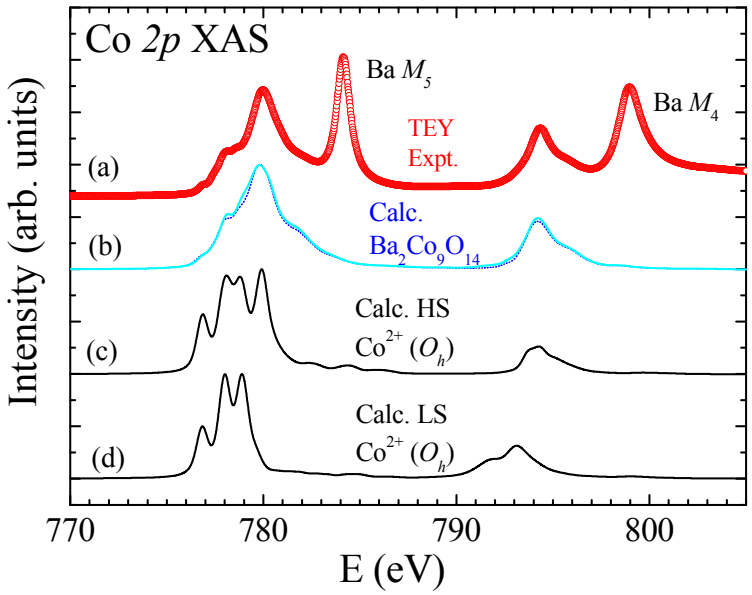

Figure 6.21. (a) Experimental TEY Co $L_{2,3}$ XAS spectrum of $Ba_2Co_9O_{14}$ measured at RT; (b) the weighted sum of the calculated spectra using Co^{2+} (O_h) in HS state (blue dotted line) and Co^{2+} (O_h) in LS state(blue solid line); (c) calculated spectrum for Co^{2+} (O_h) in HS state, and (d) calculated spectra for Co^{2+} (O_h) in LS state. Spectra have been vertically shifted for clarity.

Moreover, to get deeper into the study of the electronic configuration of Co ions in $Ba_2Co_9O_{14}$ we decided to undertake 1*s*3*p* nonresonant X-ray emission spectroscopy (XES). This experiment was recorded at the ID26 beamline of the ESRF (Grenoble) with the collaboration of Dr. Sara Lafuerza (beamline scientist). Various reference compounds were also measured such as $PrCoO_3$, $Pr_{0.50}Ca_{0.50}CoO_3$, or $Pr_{0.50}Sr_{0.50}CoO_3$. This technique is sensitive to the electron density localized on the absorbing ion, more in particular to the effective number of unpaired 3*d* electrons (effective spin). The $K\beta_{1,3}$ main emission line responds to the recombination of the 1*s* core hole with a 3*p* electron that follows the photoabsorption process, while the $K\beta'$ satellite feature reflects the exchange interaction of the secondary hole appearing in the 3*p* orbitals with the electrons located in the 3*d* band. Figure 6.22 shows the experimental $K\beta_{1,3}$ main lines of $Ba_2Co_9O_{14}$ at 300 K, $PrCoO_3$ at 20 K (S = 0), $Pr_{0.50}Ca_{0.50}CoO_3$ (PCCO) at 20 K and 300 K (S = 0.25 and S = 0.75, respectively) and $Pr_{0.50}Sr_{0.50}CoO_3$ (PSCO) at 300 K (S = 1). As we observe, all compounds have similar emission spectra and the main differences arise from the

intensity and position of the $K\beta_{1,3}$ lines. Qualitatively speaking, $Ba_2Co_9O_{14}$ seems to show a kind of intermediate XES spectrum between that of PCCO at low temperature and RT. Since we have derived the spin-state of each type of Co ion from XAS results, the total spin can be determined as $S = 6/9 \cdot 0 + 1/9 \cdot 3/2 + 2/9 \cdot 3/2 = 1/2$ for $Ba_2Co_9O_{14}$. We notice that this quantitative determination fits with the qualitatively comparison of BCO to previously studied compounds presented in the manuscript (see final Figure 7.1 in Chapter 7).

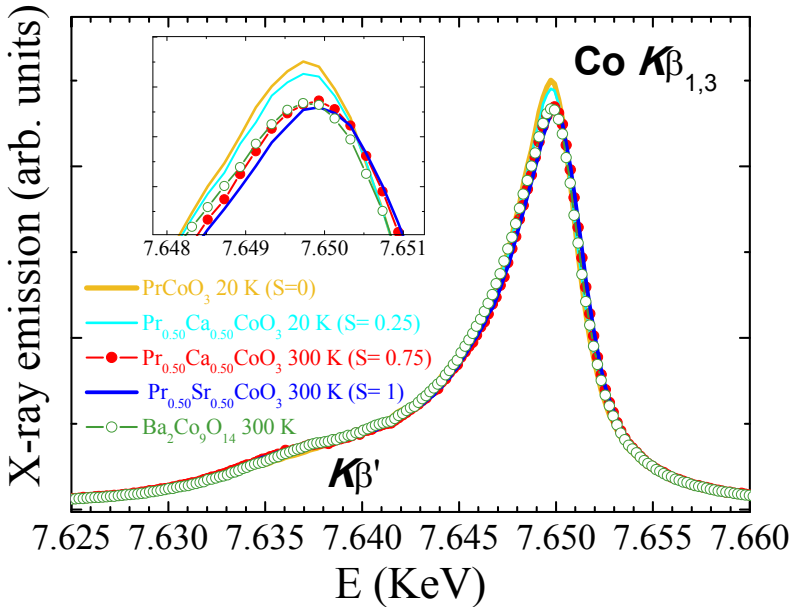

Figure 6.22. Co $K\beta$ emission lines spectrum of $Ba_2Co_9O_{14}$ at RT, as compared to $PrCoO_3$, $Pr_{0.50}Ca_{0.50}CoO_3$ and $Pr_{0.50}Sr_{0.50}CoO_3$ spectra.

Figure 6.23 provides the high energy resolution fluorescent detection - X-ray absorption near-edge spectra (HERFD-XANES) Co K edge spectra of $Ba_2Co_9O_{14}$ and reference compounds (CoO, $CaBaCoZnFe_2O_7$ at room temperature, and $PrCoO_3$ at low temperature). As we previously mentioned BCO is a Co^{2+}/Co^{3+} mixed-valence oxide with different local-geometry contributions. This fact produces different structures in the XANES spectra of the BCO due to the presence of many unoccupied states resulting from other contributions with different symmetries like Co^{2+} HS (T_d, $CoFe_2O_4$), Co^{2+} (O_h, CoO), and Co^{3+} (O_h, $PrCoO_3$). XANES spectra of the references samples are also plotted in Fig.6.23 to understand the complexity of this analysis. The qualitative analysis shows that: (i) feature B is attributed to CoO and $CaBaCoZnFe_2O_7$, (ii) feature C is characteristic of Co^{3+} LS, and (iii) feature D is the result of the presence of Co^{2+} ions HS in octahedral coordination.

The inset shows the pre-peak region (A) between 7707 and 7714 eV which reflects the density of empty Co 3*d* orbitals due to the hybridization with the O 2*p* states (dipole-allowed transitions). The experimental pre-edge can be interpreted as the result of three contributions: the lowest-energy feature corresponds to Co^{2+} states with t_{2g} symmetry, and that centered at ~7711.5 eV is originated from Co^{2+} and Co^{3+} states with e_g symmetry. Indeed, we have carried out a simulation using the weighted addition of the experimental XAS spectra of the measured reference samples (see inset of Figure 6.23). The resultant spectrum presents two features at the pre-edge region corresponding to the different contributions just commented. However, this empirical simulation is far from perfect due to the crudeness of the approximation performed.

Then, the main information we can extract from HERFD-XANES measurements is that it is well evidenced the presence of different valence states and local geometrical coordination for the Co ions $Ba_2Co_9O_{14}$ in agreement with the conclusions obtained from CTM calculations. The complex structure of BCO does not allow us to extract more conclusive results about the total electronic configuration.

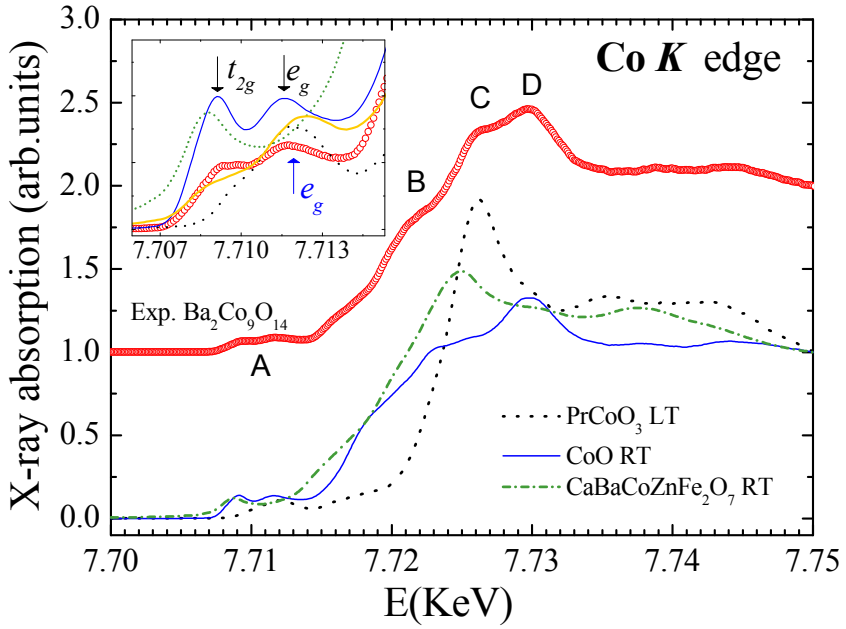

Figure 6.23. HERFD spectra at the Co K edge of $Ba_2Co_9O_{14}$ at RT, as compared to $PrCoO_3$, $CaBaCoZnFe_2O_7$, and CoO. The inset shows the pre-edge region sensitive to the occupation of the Co 3*d* states. The black arrows indicate the empty states resulting from the t_{2g} and e_g states attributed to Co^{2+} ions, and the blue arrow indicates the e_g empty states ascribed to Co^{3+} LS. The yellow solid line is the calculated spectra obtained from adding the reference compounds spectra.

6.8. Super-superexchange interaction and the effect of covalence

As we have mentioned in Section 6.6 the magnetic moments at *Co3* and *Co5* sites arrange in an AFM order forming triple layered blocks. One of these blocks is composed of three FM layers coupled as shown in Figure 6.24. In the same figure a schematic view of the magnetic structure (taking the basic model, Model 2) can be observed. Here, the length of the arrows represents the magnitude of the ordered magnetic moment found in the tetrahedral Co^{2+} ions (m_{Co3} = 2.88 μ_B/f.u.) and the octahedral Co^{2+} ions (m_{Co5} = 1.76 μ_B/f.u.). These AFM triple layered blocks are coupled antiferromagnetically to each other, but the magnetic interactions inside the individual blocks are expected to be larger than between the AFM triple layered blocks as we will see later.

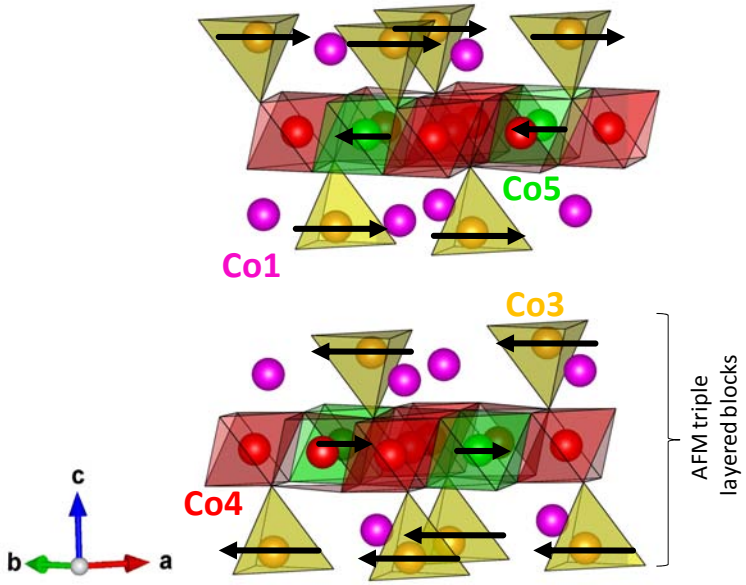

Figure 6.24. Part of the magnetic unit cell of $Ba_2Co_9O_{14}$ showing the arrangement of the magnetic moments in the AFM triple layered blocks. Some diamagnetic Co ions have been removed from the structure for clarity reasons.

For a better understanding of the magnetic interactions in this compound we must pay attention to the spin exchange interactions through M-O-M superexchange (SE) paths, where M is a transition metal ion, in our case Cobalt. However, G. Ehora *et al.* [2] realized that in this system M-O···O-M super-superexchange (SSE) interactions could be more determinant that

superexchange coupling for the low temperature magnetic ordering. Our results concerning the distribution of LS diamagnetic Cobalts are totally consistent with this idea.

A main feature of the ground state of $Ba_2Co_9O_{14}$ is that all the SE paths involve magnetic and diamagnetic Co ions (*Co1*, *Co2*, *Co4* sites) whereas interactions between two magnetic ions (*Co3* and *Co5* sites) are only possible through SSE paths.

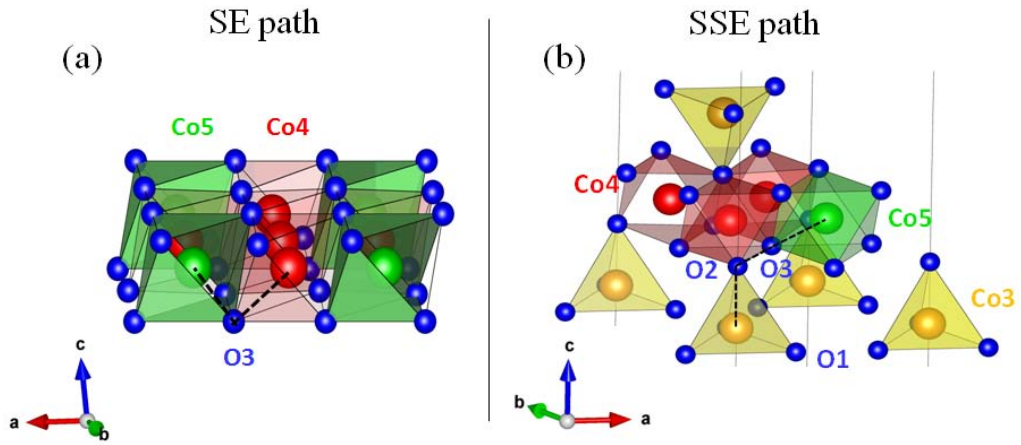

Figure 6.25. Schematic view of (a) the CdI_2-type layer from the crystal structure of $Ba_2Co_9O_{14}$ involving M-O-M SE interactions between a magnetic and a diamagnetic ion, in this case *Co5* and *Co4* sites respectively; and (b) central part of the crystal structure of $Ba_2Co_9O_{14}$, which includes M-O···O-M SSE interactions between two magnetic ions, in this case *Co5* and *Co3* positions. Some Co and O ions have been removed from the structure for a better understanding. Dashed lines depict the *Co5*-O3-*Co4* and *Co5*-O3···O2-*Co3* paths.

In contrast with the SE interactions (determined by the Goodenough-Kanamori rules [14, 15]), there is no general rule a priori for the SSE interactions. However, two different conditions have been inferred from the study of other compounds which regulate the SSE. So, it has been reported in other magnetic oxides like $Ba_2Cu(PO_4)_2$, $Sr_2Cu(PO_4)_2$, $BaCuP_2O_7$ or $(VO)_2P_2O_7$ that the strength of a M-O···O-M interaction is mainly based on the O···O distance and the M-O···O angle rather than the M···O distance [2]. The SSE interactions are stronger when the O···O distance is shorter than the Van der Waals distance [d(O···O) ~ 2.8 Å] [16–19]. For longer O···O distances (> 2.8 Å) the associated SSE coupling is negligible in the most of compounds.

It is also of interest to recall that indirect interactions (M-O···O-M) can be stronger than any direct interaction (M-O-M) in a given magnetic compound. So, in $Ba_2Co_9O_{14}$ the arrangement of the magnetic moments in the FM layers inside each block can be induced by SSE couplings between different layers rather than by the M-O-M SE paths within a given layer (see Figure 6.25). So, following the same methodology proposed by G. Ehora *et al.* [2] we have

analyzed in detail the structural features involved in main SSE paths within the structure. We have performed the analysis using the structural parameters and information obtained from our high resolution neutron diffraction data measured at D2B beamline.

After considering the different possible SSE paths in $Ba_2Co_9O_{14}$, we have detailed in Table 6.5 the Co-O···O-Co distances and Co-O···O angles between magnetic-magnetic Co ions. Later, it will be discussed the implications of the Co(magnetic)-O-Co(diamagnetic) paths listed in Table 6.6 for the distinct magnetic features of Co^{2+} sites.

Table 6.5. Detailed M-O···O-M bondlenghts and the M-O···O bond angles related to the SSE interactions between magnetic-magnetic Co ions.

Magnetic-Magnetic SSE path	d_{13} (*Co*-O···O) (Å)	d_{23} (O···O)(Å)	d_{14} (*Co*-O···O-*Co*) (Å)	angle *Co*-O···O (deg)	angle O···O-*Co* (deg)
			Co3-O···O-*Co3* path		
Co3-O1-O1-*Co3* *(antiferro)*	4.180(3)	2.879(6)	4.880(5)	118.4(13)	24.4(5)
Co3*-O1-O1-*Co3 ***(ferro)***	**4.198(2)**	**2.423(8)**	**5.693(4)**	**146.38(7)**	**15.0(3)**
			Co5-O···O-*Co3* path		
Co5-O3-O1-*Co3*	4.556(10)	2.860(6)	4.460(5)	136.3(6)	88.21(10)
Co5-O3-O2-*Co3*	3.434(7)	2.844(3)	4.460(5)	87.8(5)	87.8(4)
Co5*-O3-O2-*Co3	**3.434(7)**	**2.64(2)**	**4.460(5)**	**93.6(6)**	**87.8(4)**
			Co5-O···O-*Co5* path		
Co5-O3-O3-*Co5*	4.439(9)	2.733(1)	5.693(4)	136.6(5)	18.4(3)

As we can observe only some SSE paths, with O···O distances shorter than 2.8 Å, can be considered as strong interactions. Some indirect Co-Co couplings between two magnetic Co ions are: *Co5*-O3-O2-*Co3* [see Fig. 6.25(b)] *or Co3*-O1-O1-*Co3* SSE paths. Table 6.5 shows the existence of SSE paths which have O···O distances exceeding 2.8 Å. Magnetic interactions associated to them can be neglected (effective spin exchange parameter $J \sim 0$). Some examples are the *Co5*-O3-O1-*Co3* or FM *Co3*-O1-O1-*Co3* distances.

Another interesting observation in $Ba_2Co_9O_{14}$, firstly suggested by G. Ehora *et al.* [2], is the existence of covalence effects. As we have seen in Section 6.6 and 6.7, the refined moments are (m_{Co3} ~2.9 μ_B/f.u.) and (m_{Co3} ~2.9 μ_B/f.u.) for the tetrahedral *Co3* site and the octahedral *Co5* site (m_{Co5} ~1.8 μ_B/f.u.), respectively. These values are in agreement with the values proposed in

Ref. [2]. One possibility for the strong reduction in the *Co5* site moment could be a different spin state of Co^{2+} ions. However, our investigation has revealed the same SS for both Co^{2+} ions. Another, possibility is the hypothesis of covalence effects in this system suggested by G. Ehora *et al.* [2].

In order to check this possibility we have searched differences in the coordination and different type of SE paths within the structure around *Co5* respect to *Co3* positions involving interactions between magnetic-diamagnetic Co ions. The first evidence favoring different covalence is that *Co5* and *Co3* positions have different local coordination: the *Co5* site is surrounded by 6 oxygen atoms while the *Co3* site is only surrounded by just 4 oxygens. So, at first sight this can make the *Co5* site more covalent than the *Co3* site. Apart from this fact, an additional main cause of the magnetic moment reduction in *Co5* is the different type of SE paths involving magnetic-diamagnetic Co ions. Then, we have analyzed the structural features involved in SE paths from our neutron diffraction data measured at D2B beamline. In Table 6.6 we detail the possible Co-O-Co bond distances and Co-O-Co bond angles between magnetic-diamagnetic Co ions. We observe that the Co-O-Co bond angles in the three SE paths for the *Co3* site involve small values (less than 155 º), while the *Co5* presents one SE path (*Co5*-O3-*Co1*) with an angle close to 180º. This situation could favor a $Co^{2+} \rightarrow$ O covalent magnetic transfer inside the *Co5*-O3-*Co1* paths and as a consequence the observed reduction of the magnetic moment in the *Co5*.

Table 6.6. Detailed M-O-M bond distances and the M-O-M bond angles related to the SE interactions between magnetic-diamagnetic Co ions.

Magnetic-Diamagnetic SE path	d_{13} (*Co*-O) (Å)	d_{23} (O-*Co*)(Å)	d_{13} (*Co*-O-*Co*) (Å)	angle *Co*-O-*Co* (deg)
		Co5-O-*Co1* path		
Co5-O3-*Co1*	2.03(2)	2.036(1)	4.058(7)	**174.2(2)**
		Co5-O-*Co4* path		
Co5-O3-*Co4* x 2	1.955(9)	2.036(9)	2.844(4)	90.9(4)
		Co3-O-*Co1* path		
Co3-O1-*Co1*	1.82(1)	1.961(4)	3.342(8)	124.1(9)
		Co3-O-*Co2* path		
Co3-O1-*Co2*	1.88(9)	1.96(4)	3.745(7)	154.1(11)
		Co3-O-*Co4* path		
Co3-O2-*Co4* x 3	2.00(4)	1.925(2)	3.43(3)	121.5(2)

6.9. Summary and conclusions

To summarize, in this chapter we have presented a combined structural, magnetic and electric/electronic characterization of the recently prepared oxide $Ba_2Co_9O_{14}$ by means of neutron diffraction and spectroscopic analysis. This compound was initially considered as a promising material to be used as a cathode for SOFCs due to the high thermopower values it reaches at RT. However, the high values observed in the electrical resistivity do not favor a large figure of merit rendering it incompatible with being an effective thermoelectric material. Furthermore, the positive sign in the Seebeck coefficient indicates a *p*-type conductor nature. The insulator-insulator transition at high temperature observed in the resistivity measurements is relevant from an electronic point of view due to the capability of some Co ions to change their spin-state. On the other hand, the magnetic characterization revealed a long range antiferromagnetic order below T < 41.2 K and an effective moment ($\mu_{eff.}$ = 10.8 μ_B/f.u.), which differs from the expected theoretical values, indicating orbital contributions or some contribution from Co^{3+} ions with a higher spin-state.

Our investigation using neutron powder diffraction confirms the complex crystallographic structure reported by G. Ehora *et al.* [2] where five Co sites with different valence and coordination are involved. Three of them are considered to be octahedral Co^{3+} ions (*Co1*, *Co2*, *Co4* sites) whereas the rest are divalent ions with differentiated local environments: tetrahedral at the *Co3* site and octahedral at the *Co5* site. Our structural refinements reveal changes in the cell parameters and, as a consequence, in the cell volume just at the insulator-insulator transition (T_t ~ 567 K). We have detected from the structural study that only two Co sites (*Co1* and *Co2*) are suffering changes in the Co-O bond length across the transition. This fact is a hallmark, as in other cobalt oxides, of a spin-state transition taking place at high temperatures in $Ba_2Co_9O_{14}$.

In addition, we have performed a detailed investigation of the magnetic order, which follows an earlier study by G. Ehora *et al.* The neutron diffraction pattern at 5 K revealed the presence of new magnetic peaks related to the AFM phase and they were successfully indexed using the k = (0 0 3/2) propagation vector, implying a cell doubling along the *c*-axis. We also observed that only two Co sites turned out to be magnetic (*Co3* and *Co5* sites), while the others were diamagnetic at low temperatures. The refinements together with the symmetry analysis determined that both the conjugated C_2/c and C_2/m magnetic groups give perfect account of the experimental magnetic intensities. They correspond to the same AFM phase with the anisotropy axis rotated by 90º, and therefore the anisotropy in the *ab* plane cannot be determined.

In both, the magnetic moments arrange in the structure giving AFM triple layered blocks where *Co3* and *Co5* sites are antiparallel with different amplitude (m_{Co3} ~ 2.9 μ_B/f.u. and m_{Co5} ~ 1.8 μ_B/f.u.). The magnetic interactions inside the individual blocks are expected to be larger than between the AFM triple layered blocks. The analysis of the magnetic ordering at low temperature reflects that: (i) the M-O···O-M SSE interaction is more decisive than the M-O-M SE coupling and (ii) the presence of covalence effects in one of the magnetic cobalt (*Co5* site).

The main conclusion extracted from the characterization of $Ba_2Co_9O_{14}$ is that undergoes an insulator-insulator transition at T_t ~ 567 K, which arises from a spin-state transition, mainly in the Co^{3+} ions. The enhancement of specific Co-O distances (*Co1* and *Co2* sites) across T_t corroborates the LS state to HS state transition in these Co^{3+} ions. This result has been also supported by the magnetic structure and XAS characterization, confirming the non-magnetic behavior (S=0, LS) in three (*Co1*, *Co2* and *Co4*) out of the five cobalt ion types below T_T .

.

BIBLIOGRAPHY

[1] J. Sun, M. Yang, G. Li, T. Yang, F. Liao, Y. Wang, M. Xiong, and J. Lin, "New barium cobaltite series $Ba_{n+1}Co_nO_{3n+3}(Co_8O_8)$: Intergrowth structure containing perovskite and CdI_2-type layers," *Inorg. Chem.*, vol. 45, no. 23, pp. 9151–9153, 2006.

[2] G. Ehora, S. Daviero-Minaud, M. Colmont, G. André, and O. Mentré, "$Ba_2Co_9O_{14}$: New inorganic building blocks with magnetic ordering through super-super exchanges only," *Chem. Mater.*, vol. 19, no. 3, pp. 2180–2188, 2007.

[3] T. Takami, S. Saiki, J. Cheng, and J. B. Goodenough, "Magnetic and transportproperties of $Ba_2Co_9O_{14}$ and $Ba_{1.9}A_{0.1}Co_9O_{14}$ (A= La or Na)," *J. Phys. Soc. Japan*, vol. 79, no. 11, p. 114713, 2010.

[4] J. G. Cheng, J. S. Zhou, Z. Hu, M. R. Suchomel, Y. Y. Chin, C. Y. Kuo, H. J. Lin, J. M. Chen, D. W. Pi, C. T. Chen, T. Takami, L. H. Tjeng, and J. B. Goodenough, "Spin-state transition in $Ba_2Co_9O_{14}$," *Phys. Rev. B*, vol. 85, no.094424, pp. 1–6, 2012.

[5] J. Rodríguez-Carvajal, "Recent advances in magnetic structure determination by neutron powder diffraction," *Phys. B Condens. Matter*, vol. 192, pp. 55–69, 1993.

[6] N. E. Brese and M. O'Keeffe, "Bond-valence parameters for solids," *Acta Crystallogr. Sect. B Struct. Sci.*, vol. 47, pp. 192–197, 1991.

[7] P. G. Radaelli and S.-W. Cheong, "Structural phenomena associated with the spin-state transition in $LaCoO_3$," *Phys. Rev. B*, vol. 66, no. 094408, p. 33, 2002.

[8] C. Frontera, J. García-Muñoz, a. Llobet, and M. Aranda, "Selective spin-state switch and metal-insulator transition in $GdBaCo_2O_{5.5}$," *Phys. Rev. B*, vol. 65, no. 180405(R) pp. 3–6, 2002.

[9] N. Belov, *Sov. Phys. Crystallogr.*, vol. 2, pp. 311–322, 1957.

[10] B. Y. R. D. Shannon, M. H, N. H. Baur, O. H. Gibbs, M. Eu, and V. Cu, "Revised Effective Ionic Radii and Systematic Studies of Interatomie Distances in Halides and Chaleogenides"*Acta. Cryst.*, 1976].

[11] R. D. Cowan, *The theory of Atomic structure and Spectra*, 1981st ed. Berkeley, CA: University of California, 1981.

[12] F. De Groot and A. Kotani, "*Core level spectroscopy of solids"*. 2008.

[13] N. Hollmann, Z. Hu, M. Valldor, a. Maignan, a. Tanaka, H. H. Hsieh, H.-J. Lin, C. T. Chen, and L. H. Tjeng, "Electronic and magnetic properties of the kagome systems $YBaCo_4O_7$ and $YBaCo_3MO_7$ (M=Al, Fe)," *Phys. Rev. B*, vol. 80, no. 085111, pp. 3–7, 2009.

[14] J. B. Goodenough, *J. Phys- Chem. Solids*, vol. 6, no. 287, 1958.

[15] J. Kanamori, *J. Phys- Chem. Solids*, vol. 10, no. 87, 1959.

[16] M. H. Whangbo, H. J. Koo, and D. Dai, "Spin exchange interactions and magnetic structures of extended magnetic solids with localized spins: Theoretical descriptions on formal, quantitative and qualitative levels," *J. Solid State Chem.*, vol. 176, pp. 417–481, 2003.

[17] H. J. Koo, M. H. Whangbo, P. D. VerNooy, C. C. Torardi, and W. J. Marshall, "Flux growth of vanadyl pyrophosphate, $(VO)_2P_2O_7$, and spin dimer analysis of the spin exchange interactions of $(VO)_2P_2O_7$ and vanadyl hydrogen phosphate, $VO(HPO_4)\cdot_{0.5}H_2O$," *Inorg. Chem.*, vol. 41, no. 18, pp. 4664–4672, 2002.

[18] D. Dai, M. H. Whangbo, H. J. Koo, X. Rocquefelte, S. Jobic, and a. Villesuzanne, "Analysis of the spin exchange interactions and the ordered magnetic structures of lithium transition metal phosphates $LiMPO_4$ (M = Mn, Fe, Co, Ni) with the olivine structure," *Inorg. Chem.*, vol. 44, no. 7, pp. 2407–2413, 2005.

[19] M. H. Whangbo, D. Dai, and H. J. Koo, "Spin dimer, electronic band structure and classical spin analyses of spin exchange interactions and ordered magnetic structures of magnetic solids," *Solid State Sci.*, vol. 7, pp. 827–852, 2005.

Chapter 7

General conclusions

In this thesis, we have investigated the relevance and effects of spin state instabilities in cobalt oxides with spin-lattice coupling. The thesis focuses primarily on the study of cobalt oxides with structural, electronic and spin instabilities, in strongly correlated cobaltites having different crystallographic structures. The four analyzed systems, $LnCoO_3$, $Pr_{0.50}Sr_{0.50}CoO_3$, $LnBaCoO_{5.50}$, and $Ba_2Co_9O_{14}$, were characterized combining X-ray spectroscopies and neutron and synchrotron diffraction. Along this manuscript each chapter has been dedicated to a different system, addressing structural, electronic, magnetic, magnetostructural or metal-insulator transitions. The main conclusions obtained in this work have already been presented in the last section of each chapter. However, an overall view of the major highlights is summarized in this brief chapter.

Chapter 3: Spin-state crossover in lanthanide $LnCoO_3$ cobaltites: $PrCoO_3$ versus $ErCoO_3$

With the aim of determining the nature and evolution of the spin-state transitions in $LnCoO_3$ cobaltites as a function of the *Ln* size, structural and electronic state investigations were mainly focused on two family members with different distortion: *Ln*= Pr representing moderate distortions and Er presenting a higher distortion. Some conclusions were reached concerning the nature of the spin-state (SS) regarding the two most likely scenarios

[(i) LS → LS+HS → HS and (ii) LS → IS → HS], and the phase diagram evolution increasing the structural distortion in the system:

- The SS transition temperatures (T_{SS1} and T_{SS2}) shift to higher values as the *Ln* size decreases. The onset of the SS transitions has been determined and monitored for: $LaCoO_3$ (T_{SS1} ~ 50 K and T_{SS2} ~ 480 K), $PrCoO_3$ (T_{SS1} ~ 200 K and T_{SS2}~ 400 K), and $ErCoO_3$ (T_{SS} ~ 450 K).
- The spectral similarities between the La and Pr-based perovskites in the XAS and XES measurements indicate that the origin of the first (on warming) transition is a progressive or gradual low-spin to high-spin state change up to an approximately 90:10 LS:HS mixed state.
- The IS or HS spin state excitations in $ErCoO_3$ bring about an expansion of the CoO_6 octahedron producing modifications in structural parameters such as the cell dimensions and volume, orthorhombic strain, Co-O bond distances, or the Co-O-Co bond angles. They reflect a broad SS crossover from LS to excited states that begins at T_{SS} ~ 450 K and extends up to temperatures higher than 800K, without signs of activated static Jahn-Teller distortion.
- A systematic study done to fix the width of the electronic transitions in the $LnCoO_3$ series of cobaltites as function of the distortion in the structure demonstrates the existence of three different regions or electronic configurations between transitions: PH1 ($T \leq T_{SS1}$), PH2 ($T_{SS1} < T < T_{SS2}$), and PH3 ($T \geq T_{SS2}$) with PH1 referring to the LS state, PH2 to a LS+HS/IS state, and PH3 for the high temperature metallic phase with the majority of Co ions in HS configuration. While for the light $LnCoO_3$ compounds ($\langle r_A \rangle \geq 1.079$ Å) the three phases are well separated, in the heavy compounds ($\langle r_A \rangle < 1.079$ Å) the intermediate PH2 phase becomes thermodynamically unstable or gets suppressed.

Chapter 4: Magnetostructural effects and spin-lattice coupling in $Pr_{0.50}Sr_{0.50}CoO_3$

$Pr_{0.50}Sr_{0.50}CoO_3$ (PSCO) notably differs from $Pr_{0.50}Ca_{0.50}CoO_3$ (PCCO) where a spin-state change favors a partial Pr^{3+} to Pr^{4+} valence shift and an exotic metal-insulator transition at around 80 K. The PSCO mixed Co^{3+}/Co^{4+} perovskite also presents unexpected properties which are detailed below:

- $Pr_{0.50}Sr_{0.50}CoO_3$ is metallic and FM below 230 K (FM2). On cooling an unexpected step in magnetization at T_{S1} ~ 120 K takes place, which can be positive or negative depending on the applied field. Another ferromagnetic phase develops at T_{S1} coinciding

with marked structural changes. We showed that this unexpected m*agnetostructural* (MS) transition vanishes by substituting Pr with other lanthanides, being absent in other compositionally similar systems such as $Nd_{1/3}La_{1/6}Sr_{0.50}CoO_3$ or $Nd_{0.50}Sr_{0.50}CoO_3$ (as well as in $Pr_{0.50}Sr_{0.50}CoO_3$ thin films). A possible active participation of the Pr ions was investigated.

- We have solved the structural evolution with temperature. Our analysis reveals four successive crystal symmetries, which follows the *Pm-3m* $\rightarrow$ *R-3c* $\rightarrow$ *Imma* $\rightarrow$ *I4/mcm* transformations with decreasing temperature. The last transformation being responsible for the unexpected second magnetic transition (FM1). Despite of the strong contraction of the average $\langle \text{Pr-O} \rangle^{\text{VIII}}$ bond length, our XAS results at the Pr L_3 and $M_{4,5}$ edges did not reveal any Pr^{3+} to Pr^{4+} oxidation process across T_{S1}, nor changes in the formal valence of cobalt ions (unlike $Pr_{0.50}Ca_{0.50}CoO_3$).
- The magnetic characterization by means of XMCD demonstrates the key role of the *spin-orbit* coupling for the stabilization of two distinct FM phases in this cobaltite. We have found an orbital contribution to the magnetization and the orbital moment ordering is coupled to the ordering of the electronic spins across T_{S1} . Very likely a reorientation of the orbital moment is provoked by the *Imma* $\rightarrow$ *I4/mcm* symmetry changes, and helped by the spin-orbit coupling the ordered Co spins rotate between the FM1 and FM2 phases.
- This was corroborated by neutron diffraction. The different magnetic structures and magnetic symmetries of PSCO at both sides of T_{S1} were determined. Above T_{S1} the FM2 phase is composed of [100] FM domains (F_x), with magnetic symmetry *Im'm'a* (m_y=0). Below T_{S1} the coupled orbital and spin components of the moment rotate by 45º into two conjugated ferromagnetic domains [110] and [1-10] (F_{xy}). The overall symmetry of the low temperature phase is *C2'/m'* (with $|m_x|=|m_y|$). The striking magnetization was understood.
- The unusual magnetostructural changes are preserved in bigger cells if, instead of Pr, we substitute Sr^{2+} by a bigger alkaline-earth ion such as Ba^{2+} or by smaller ion such as Ca^{2+}. A T-r_A phase diagram for $Ln_{0.50}(Sr_{1-x}A_x)_{0.50}CoO_3$ Sr rich cobaltites has been proposed.
- The spectroscopic (XAS, XES) measurements and charge-transfer multiplet calculations in $Pr_{0.50}Sr_{0.50}CoO_3$ indicate that the average SS of Co is basically

insensitive to the temperature and the electronic configuration can be described by a mixture of Co^{3+} ions in LS:HS state and Co^{4+} ions in a LS:IS state (17.5% Co^{3+} LS+ 32.5% Co^{3+} HS + 40% Co^{4+} LS + 10% Co^{4+} IS with S=1).

Chapter 5: The spin-lattice coupling in the *Ln*$BaCo_2O_{5.50}$ (*Ln*=Pr, Gd, Y) layered cobaltites

- $YBaCo_2O_{5.50}$ is composed of an equilibrated ratio of Co^{3+} ions in pyramidal and octahedral coordination forming an ordered pattern. It undergoes on cooling a PM $\rightarrow$ FM and metal-insulator transitions at $T_C = T_{MI} \sim 295$ K. On further cooling, it suffers two additional magnetic transitions into AFM phases (AFM1, AFM2) at T_{N1}~265 K and T_{N2}~231K, respectively.
- The crystalline structure evolution of $YBaCo_2O_{5.50}$ has been described by means of synchrotron X-ray powder diffraction. Concomitantly with the MIT, an orthorhombic-monoclinic transition takes place at T_{S1} ~295 K. The splitting of some (*hkl*) peaks with $h\neq0$ and $k\neq0$ and the appearance of new superstructure peaks evidences the crystal transformation from *Pmmm* to *P112/a*, doubling the *a* cell parameter. On cooling, a second structural transition (*P112/a* $\rightarrow$ *Pmmm*) has been detected at $T_{S2}=T_{N2}$. However, the crystal structure can be here described by the coexistence of the orthorhombic-monoclinic phases. On the other hand, the monoclinic cell reappears, becoming the majority phase below T_{S3} ~55 K. Signaling that at low temperatures there exists a competition between the orthorhombic-monoclinic phases.
- In the first structural transition (at T_{MI}), it has been found that the evolution of the unit-cell volume is opposite to the larger rare-earths case (Pr and Gd) as it expands when entering the insulating phase, in agreement with $HoBaCo_2O_{5.50}$.
- The anomalous cell volume expansion and structural changes on cooling across the MIT has been attributed to a change in the SS of Co^{3+} ions at the octahedral sites (LS $\rightarrow$ HS states, warming), while the Co^{3+} ions in a pyramidal coordination remain in an IS state. The spectroscopy has allowed to quantitatively describe the electronic occupation in the *3d* valence band. Surprisingly, the deeper spectroscopic analysis done for the Y-based cobaltite evidences that not only the variations in the SS are ascribed to the Co^{3+} ions in a CoO_6 coordination, but there is also a certain evolution in the electronic configuration of the Co^{3+} ions with CoO_5 coordination.

Chapter 6: Effects of spin state instabilities on the properties of the $Ba_2Co_9O_{14}$ cobaltite

In the search of new strongly correlated cobalt systems with non-conventional properties due to spin-state instabilities, we decided to investigate $Ba_2Co_9O_{14}$ (BCO). This charge-ordered Co^{2+}/Co^{3+} oxide has attracted much attention due to their promising catalytic and thermoelectric properties. It presents a complex rhombohedral *R-3m* structure with five crystallographically independent Co sites (octahedrally and tetrahedrally coordinated).

- This compound is AFM below 41 K and it undergoes an insulator-insulator transition at T_t ~ 567 K, which arises from a spin-state transition.
- By means of neutron diffraction, we have described the influence of the spin-state changes on the anomalous structural evolution across T_t. We have observed an increase in some specific Co-O bond distances (mainly at the *Co1* and *Co2* sites), suggesting a SS transition from LS to HS at the octahedrally coordinated Co^{3+} sites.
- The structural results relative to the electronic configuration have been confirmed by the magnetic and XAS characterization, proving the non-magnetic behavior (S=0, LS) in three (*Co1*, *Co2* and *Co4* sites) out of the five cobalt ion types below T_t. In contrast, the Co^{2+} ions with tetrahedral (*Co3* site) and octahedral (*Co5* site) coordination have been found to be magnetic, being in a HS state.
- The study of the magnetic order has revealed that the AFM order at low temperatures can be described with the k=(3/2, 0, 0) propagation vector and the magnetic moments arrange in AFM triple-layered blocks where *Co3* and *Co5* are antiparallel to each other and show very different magnetization values (m_{Co3} ~2.9 μ_B/f.u. and m_{Co5} ~1.8 μ_B/f.u.).
- It is also evidenced that covalence effects give rise to covalent magnetic transfer ($Co^{2+} \rightarrow O$) and as a consequence the magnetic moment in the *Co5* site is reduced. Moreover, in this compound the super-superexchange magnetic interactions (M-O···O-M) are more prevalent than the superexchange mechanism (M-O-M).

As a final summary of the investigation done in this work, we present Figure 7.1, which contains all the $K\beta$ XES data taken for all compounds presented in this manuscript.

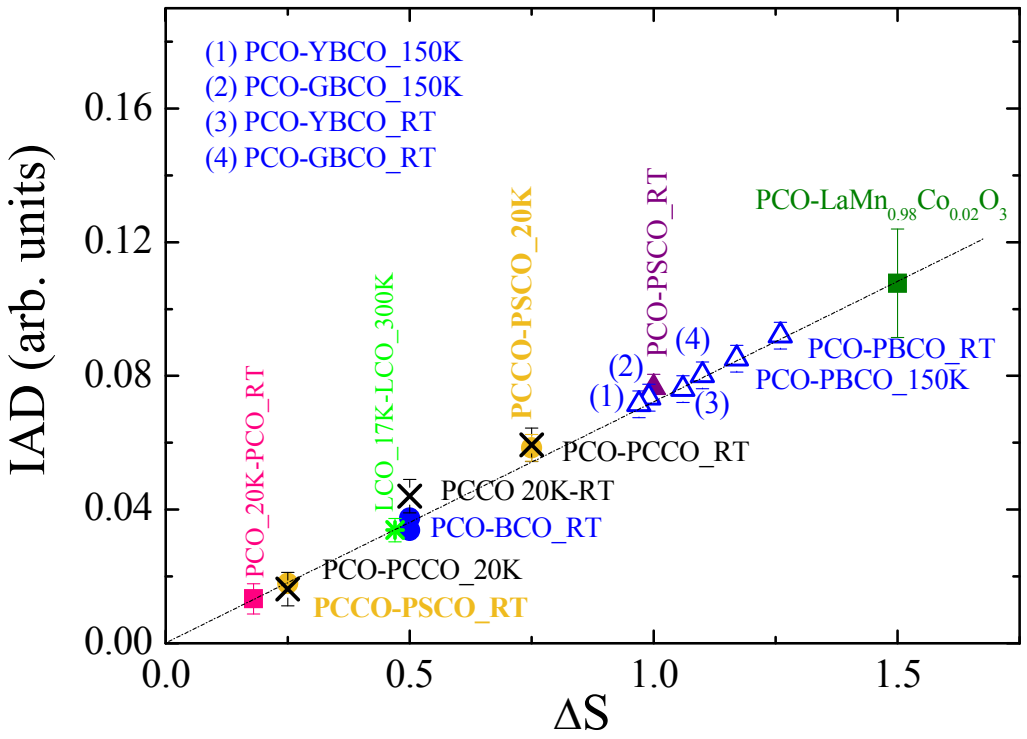

Figure 7. 1. IAD analysis of Co Kβ emission curves for all compounds studied in this thesis at different temperatures: $LaCoO_3$ (LCO), $PrCoO_3$ (PCO), $Pr_{0.50}Ca_{0.50}CoO_3$ (PCCO), $Pr_{0.50}Sr_{0.50}CoO_3$ (PSCO), $PrBaCo_2O_{5.50}$ (PBCO), $GdBaCo_2O_{5.50}$ (GBCO), $YBaCo_2O_{5.50}$ (YBCO), and $Ba_2Co_9O_{14}$ (BCO).

Publications

- *Simultaneous paraferrimagnetic, metal-insulator, and orthorhombic-monoclinic transitions in $YBaCo_2O_{5.5}$.*
  J. Padilla-Pantoja, C. Frontera, O. Castaño, J.L. García-Muñoz.
  Physical Review B, 81, 1 (2010).

- *Spin State and structural changes at the metal-insulator transition in $YBaCo_2O_{5.5}$ by synchrotron X-rays.*
  J. Padilla-Pantoja, C. Frontera, J. Herrero-Martin, and J.L. García-Muñoz.
  Journal Applied of Physics, 111, 234291 (2012).

- *The low temperature magnetostructural transition in $Pr_{0.50}Sr_{0.50}CoO_3$: bulk versus thin film behavior.*
  J. Padilla-Pantoja, J. Herrero-Martin, X. Torrelles, B. Bozzo, J. Blasco, C. Ritter, and J.L. García-Muñoz.
  Journal Applied of Physics, 115, 17D721, (2014).

- *Role of Pr cations and the low temperature transition in $Pr_{0.50}Sr_{0.50}CoO_3$: a comparison to $Pr_{0.50}Ca_{0.50}CoO_3$.*
  J. Padilla-Pantoja, A.J. Barón-González, B. Bozzo, J. Blasco, C. Ritter, J. Herrero-Martin, and J.L. García-Muñoz.
  Physica B, 455, 56-59 (2014).

- *Stability of the cationic oxidation states in $Pr_{0.50}Sr_{0.50}CoO_3$ across the magnetostructural transition by X-ray absorption spectroscopy.*
  J. Padilla-Pantoja, J. Herrero-Martin, P.Gargiani, M. Valvidares, V. Cuartero, K. Kummer, O. Watson, N. Brookes, and J.L. García-Muñoz.
  Inorganic Chemistry, 53, 8854-8858 (2014).

- *Structural Properties and Singular Phase Transitions of Metallic $Pr_{0.50}Sr_{0.50}CoO_3$ Cobaltite.*
  J. Padilla-Pantoja, J. L. García-Muñoz, B. Bozzo, Z. Jirák and Javier Herrero-Martín.
  Inorganic Chemistry, 53, 12297-12304 (2014).

- *Structural effects of the spin-state crossover at high temperature in the distorted $ErCoO_3$ cobaltite.*
  J. Padilla-Pantoja, J. L. García-Muñoz, J. A. Alonso, and M. T. Fernández-Díaz.
  Journal of physics: Conference series 663,012005 (2015).

- *Spin-lattice coupling across the singular magnetostructural transition in $Pr_{0.50}Sr_{0.50}CoO_3$ by X-ray magnetic circular dichroism.*
  J. Padilla-Pantoja, J. Herrero-Martín, E. Pellegrin, P. Gargiani, S. M. Valvidares, A. Barla, and J. L. García-Muñoz.
  Physical Review B, accepted (2015).

- *Magnetic properties of metallic $Pr_{0.50}Sr_{0.50}CoO_3$ cobaltite.*
  J. L. García-Muñoz, J. Padilla-Pantoja, *et al.*
  In advanced state of preparation.

- *Study of the spin-state in $Pr_{0.50}Sr_{0.50}CoO_3$ analyzed by X-ray emission and absorption spectroscopies.*
  J. Padilla-Pantoja, J. Herrero-Martín, J. L. García-Muñoz, *et al.*
  In advanced state of preparation.

Agradecimientos/acknowledgments

Han pasado muchos años desde que emprendí esta aventura en el Icmab. De hecho ya hace unos 6 años!!!, parece que no, pero el tiempo vuela. En este tiempo han pasado cosas buenas y otras no tan buenas, pero las cuales siempre he podido compartir con diferente gente. Gente nueva que se ha cruzado en el camino o gente que ya estaba en él. Así que en este punto, en el que esta aventura se acaba me gustaría agradecer a cada uno ellos por haberme ayudado llegar hasta aquí.

Primeramente, me gustaría empezar con mis directores de tesis, José Luis y Javier, por haberme dado la oportunidad de iniciarme en el mundo de la investigación. A José Luis por haber depositado la confianza en mí desde el primer día y saber transmitirme su pasión por la Ciencia. Gracias también, por las innumerables preguntas con respuesta y valorar en muchas ocasiones mi esfuerzo y trabajo. A Javier por ser más que un director, por ser también un compañero de viajes y largos experimentos en el Sincrotrón, con sus incasables horas. Gracias también por adentrarme en el mundillo de la espectroscopia, nunca imaginé que sería tan interesante. Por los miles de e-mails respondiendo mis dudas (que han sido muchas!), los cuales siempre has intentado explicar con paciencia.

A Carlos Frontera, porque a pesar de que no hemos acabado juntos esta aventura, sí que la iniciamos. Para mí has contribuido en gran parte de mi formación, desde el primer día no has dudado en explicarme, aconsejarme y orientarme en diferentes aspectos. Parte de este trabajo te pertenece a ti también, así que a pesar de no ser oficialmente director, yo me llevo el recuerdo cómo si realmente lo hubieras sido. Gracias por ser además un gran amigo.

A Javier Blasco, por su importante contribución a esta tesis. Sin tus muestras tan bien sintetizadas, los resultados no habrían sido lo que son. Por tu amabilidad en los diferentes encuentros durante estos años e incluso via e-mail. Nunca has dudado en atender mis preguntas o dudas. A pesar de la distancia entre Zaragoza y Barcelona, ha sido un placer trabajar junto a ti.

A Xavier Torrelles, por sus explicaciones sobre difracción de capas. Sin ellas, parte de este trabajo no hubiera salido a la luz. Gracias por adentrarme en este mundo tan diferente al "bulk".

A Eric Pellegrin, por su amabilidad y saber solventar nuestras dudas sobre diferentes aspectos relacionados con la absorción y el dicroísmo. Por el interés mostrado cuando nos has encontrado en BOREAS haciendo algún experimento.

A Cinthia Piamonteze y Frank De Groot por su ayuda y soporte en las simulaciones con CTM4XAS. En especial a Cinthia, la cual no ha dudado en responder todos mis e-mails con dudas y además de ser siempre muy accesible.

A Jose Antonio Alonso, por las muestras de *Ln*CoO_3. Gracias a ellas, hay un gran trabajo presentado en esta tesis.

A Aura Janeth Barón, por los meses que compartimos como doctorandas en el Icmab. Gracias por acogerme en el grupo cuando llegué y por tus explicaciones referentes a la síntesis de las muestras en el laboratorio. Por ser más que una compañera, una amiga. Y aunque en la lejanía estamos, sé que algún día nos volveremos a encontrar con nuestras pequeñas.

A las diferentes personas que me he ido encontrado en el mundo "sincrotronero", o de los neutrones: Pierluigi Gargiano y Manu Valvidares de BOREAS (ALBA), Juan Rubio de BM25 (ESRF), Vera Quartero y Sara Lafuerza de ID26 (ESRF). En especial a Vera y Sara, por ayudarme con algunas medidas de XANES y XES en CLÆSS y ID26, sin ellas parte de los resultados de esta tesis no habrían sido posibles. Gracias también a las dos por esos pequeños ratos compartidos en ALBA o en alguna reunión de AUSE.

A todos los técnicos de los servicios generales del Icmab: a Bernat Bozzo por su ayuda con las medidas magnéticas y de resistividad, a Nico Dix por su ayuda en el crecimiento de capas con el PLD, a Anna Crespi y Joan Esquius por sus medidas y explicaciones en difracción de rayos X, a Luigi Morrone y Edgar Leon por las horas que habéis dedicado a soldar los contactos en mis muestras con el Wire Bonding, a Andrés Gómez y Mayte Simón por las imágenes de AFM en las capas crecidas. A Roberta, por el tiempo compartido en la síntesis de muestras como casi compañeras de grupo. Pero en especial a Anna, Roberta y Joan! A Oriol Sabater por su disponibilidad para ayudarme cuando algo no funcionaba, eres el hombre manitas del Icmab.

A la gente de administración, en especial a Pietat, María y Vicente. A Pietat por su ayuda en el papeleo cuando estuve de baja de maternidad, a María por esos desayunos a las 8. y a Vicente por todos los viajes y experimentos que me "has pagado". Vicente, se te echa mucho d menos en el instituto, sobretodo todas la batallitas que siempre nos contabas a la hora de comer. Y a tu pregunta: Pero tú cuando acabas la tesis?. Ya tiene respuesta: Vicente por fin acabé!!!!!!!!

A todas esas personas que han compartido espacio en nuestro pequeño despacho, de cada una de ellas me llevo un recuerdo: Roque, Kathy, Greta, Fanmao y Matheus (la última incorporación). A los vecinos de despacho: David Pesquera y Diego. Se os ha echado de menos estos últimos meses.

Y por último, y no menos importante a ese equipo COMILONA: Anna, Mariona, Regina, Ignasi, Roberta, Joan y Marixa. Gracias por todas nuestras conversaciones, celebraciones de cumpleaños, celebraciones de embarazos, celebraciones de incorporación de las bajas, amigos invisibles. Ahora me doy cuenta que lo celebramos todo!!!!

Por esas personas que en su día también formaron parte de este equipo: Silvia y Noemí. Gracias a Roxanna también por endulzarme la vida con bombones, chocolates y mimarme a Paula.

A mis amig@s de toda la vida, los cuales a pesar de estar un poco desaparecida últimamente, han entendido y se han preocupado en saber cómo iba la escritura. A vosotros Miriam, Marta y Alan. Porque siempre estáis ahí, en los buenos y malos momentos.

A mis amig@s de la uni. Porque muchos de vosotros habéis tenido una aventura científica parecida a la mía y que por cierto hemos SOBREVIVIDO!!!!: Sandra, Jou, Jordi, Dani, Son, Pau, Anneta y en especial a mi Zape (Mar). A pesar de estar a miles de Km, siempre como el primer dia!

Y por último, ahora si que de verdad. A mi familia. Sin ellos y su ayuda en estos últimos meses, esto no hubiera sido posible. En primer lugar a mi madre, por confiar en mí y enseñarme a ser la persona que soy. Porque donde he llegado ha sido gracias a ti. Supongo que has sabido transmitirme tu valentía, para no tirar la toalla en muchas ocasiones. A Jepi por confiar también en mí y estar cada día orgulloso de la Doctora que tendréis en casa. Animarme cuando todo lo veía negro. Gracias a los dos por las innumerables ocasiones en las que habéis tenido que hacer de iaia y avi (sobretodo estos últimos meses).

Gracias a la bisa, por las insistentes llamadas, por las broncas de que no me ve.pero eso refleja lo importante que soy para ti.

Al Tito Andrés, porque más que un tito es como un hermano. Gracias, por hacerme sentir siempre tan especial. Este año los bordamos, tú Licenciado y yo Doctora!

A ti Sensi, aunque no hay palabras. Simplemente, porque algún día volvamos a encontrarnos.

A ti Wapi, por aguantar mi mal humor en mis épocas de estrés, por apoyarme en los diferentes momentos de mi vida. Nadie aguanta tan fácilmente a una científica a su lado. Pero sobre todo GRACIAS, por el gran proyecto que hemos creado juntos. Paula es lo más bonito que hemos podido hacer.

Y por último, a mi petita, Paula. Porque con solo una sonrisa tuya todo parece más fácil. Me has sabido dar tranquilidad cuando más lo he necesitado. Además parte de este trabajo también es gracias a ti. Se puede decir que has sido una muy buena “sincrotronera” aguantando como una campeona los largos experimentos. T’estimu.

Asimismo, debo agradecer al Consejo Superior de Investigaciones Científicas (CSIC) la otorgación de la beca JAE-Predoc que me fue concedida en el año 2011. Así como a las diferentes grandes instalaciones como ALBA Syncrhotron Light Source, ILL, ESRF, SINQ, SLS y Helmholtz-Zentrum Berlin Synchrotron, por el tiempo de haz concedido.